This thesis has been reviewed by

Ao. Univ. Prof. Dipl.-Ing. Dr. techn. Günter Fafilek

Assoc. Prof. Dipl.-Chem. Dr. rer. nat. Bernhard Gollas

TECHNISCHE UNIVERSITÄT WIEN
Vienna University of Technology

DISSERTATION

THE CATHODE

Hydrogen evolution and oxygen reduction on polycrystalline platinum

carried out for the purpose of obtaining the academic degree of Doctor of Natural Sciences under the direction of

Ao. Univ. Prof. Dipl.-Ing. Dr. techn. Günter Fafilek

E164 - Institute of Chemical Technologies and Analytics

submitted at the Technical University of Vienna

Faculty of Technical Chemistry

by

Ing. Dipl.-Ing. Stefan Wibihal, BSc

Matrikelnummer: 0126331

Gerasdorferstraße 84

1210 Vienna

Vienna, January 31, 2016

Stefan Wibihal

Ing. Dipl.-Ing. Stefan Wibihal, BSc

ABSTRACT

The oxygen reduction reaction (ORR) and the hydrogen evolution reaction (HER) were investigated using a rotating ring disc electrode (RRDE) made of polycrystalline platinum in a pH range between 1 and 13. The cathodic polarization curves were measured at rotation rates between 100 rpm and 2000 rpm in aerated and N_2 purged aqueous electrolytes. These current-potential curves were analyzed using a multi-curve fit. With this new implemented method it is possible to obtain the kinetic data of the whole cathodic polarization curves from the beginning of the ORR to the HER. Therefore it is necessary to consider up to five reactions.

The ORR follows two reaction paths. The first path takes place at the same potential at which the platinum surface gets reduced under nitrogen and is a complete reduction of oxygen to hydroxide. While in literature the first electron transfer is generally accepted as the rate determining step for the ORR it is shown that there are several reasons why it is more likely that the first reaction path is limited by the reduction of platinum hydroxide adsorbed at the platinum surface.

At more negative potentials a second ORR path becomes rate determining. The simultaneous measured peak in the ring current indicates the formation of hydrogen peroxide as an intermediate in the second path. The ring currents due to the oxidation of this hydrogen peroxide are very small. The reason for this is that the main part of the peroxide intermediate is reduced at the disc electrode before it can desorb and reach the ring electrode. The kinetic parameters of both ORR paths are given in this work.

The limited current density caused by the diffusion controlled oxygen reduction becomes smaller in the hydrogen adsorption region due to the formation of hydrogen peroxide. It is assumed that adsorbed hydrogen blocks the free platinum sides on the surface which are required for the catalyzed breaking of the oxygen-oxygen bond. This hydrogen peroxide was measured at the ring electrode. The kinetic parameters of this effect have been determined.

Only in the solution with a pH-value of 1 the HER follows a Tafel mechanism. In all other electrolytes the Tafel slopes indicate a Heyrovský mechanism and a change in the kinetic of the HER was observed. This change in the kinetic is explained by the reversibility of the hydrogen electrode on platinum. At high positive overpotentials platinum would be only covered by adsorbed atomic hydrogen while at high negative overpotentials a platinum electrode would be mainly covered by molecular hydrogen. For low overpotentials the reversible reaction {1.13} has to be considered and the concentration of the adsorbed species is given by the Nernst equation. A new equation was deduced theoretically to calculate the current-potential relation of a reversible reaction in which only the product is initially in the solution. Using this equation the kinetic data of the HER were interpreted.

With the kinetic data presented in this work the whole polarization curves can be calculated for platinum in several aerated or deaerated electrolytes.

KURZFASSUNG

Die Sauerstoffreduktion (ORR) und die Wasserstoffentwicklung (HER) wurden mit Hilfe einer rotierenden Ring-Scheiben-Elektrode aus polykristallinem Platin gemessen. Dafür wurden kathodische Polarisationskurven unter Luft und Stickstoff in wässrigen Elektrolytlösungen aufgenommen. Aus diesen wurden mithilfe einer Multikurven-Anpassung die kinetischen Daten ausgewertet. Mit dieser neuen Methode der Datenauswertung für rotierende Scheibenelektroden war es möglich die kinetischen Daten aller Reaktionen vom Beginn der ORR bis hin zur HER zu bestimmen. Dafür mussten, je nach Elektrolyt, bis zu fünf Reaktionen berücksichtigt werden.

Die ORR folgt zwei unterschiedlichen Reaktionswegen. Die erste Reaktion beginnt im selben Potentialbereich bei dem auch die Reduktion der Platinoberfläche unter Stickstoff einsetzt und führt zu einer vollständige Reduktion von Sauerstoff zu Hydroxid. Der erste Elektronentransfer zum Sauerstoffmolekül ist weitgehend als reaktionslimitierender Schritt akzeptiert, allerdings deuten mehrere Gründe darauf hin, dass die Reduktion des Platinhydroxides geschwindigkeitsbestimmend für diesen ersten Reaktionsweg ist.

Bei negativeren Potentialen wird die Reaktionskinetik der ORR durch einen zweiten Reaktionsweg bestimmt. Der dabei detektierbare Ringstrom lässt auf die Bildung von Wasserstoffperoxid als ein Zwischenprodukt der ORR schließen. Die geringen Ringströme, die dabei gemessen wurden, zeigen, dass ein Großteil des gebildeten Peroxids an der Scheibe weiter reduziert wird und nur ein sehr geringer Anteil desorbiert. Die kinetischen Parameter beider Reaktionswege wurden in dieser Arbeit bestimmt.

Durch die Adsorption von Wasserstoff an Platin kommt es zu einer Verringerung des Grenzstromes der ORR auf Grund der Bildung von Wasserstoffperoxid. Der adsorbierte Wasserstoff blockiert dabei die freien Stellen am Platin, welche für die katalytische Trennung der Sauerstoff-Sauerstoff-Bindung notwendig wären. Ein ähnlicher Effekt kann auch bei anderen Adsorbaten beobachtet werden. Das dadurch gebildete Wasserstoffperoxid konnte an der Ringelektrode gemessen werden. Die kinetischen Daten dieses Effekts wurden ausgewertet.

Bei pH 1 folgt die HER einem Tafel-Mechanismus. In allen anderen Elektrolyten mit höheren pH-Werten deuten die Tafelsteigungen auf einen Heyrovský-Mechanismus hin. In diesen Elektrolyten wurde eine Änderung der Kinetik beobachtet, welche auf die Reversibilität der Wasserstoffelektrode an Platin zurückgeführt werden konnte. Bei hohen positiven Überspannungen ist an Platin nur atomarer Wasserstoff adsorbiert, während bei hohen negativen Überspannungen vor allem molekularer Wasserstoff vorliegt. Bei geringen Überspannungen muss die reversible Reaktion {1.13} berücksichtigt werden. Die Konzentration der adsorbierten Stoffe wird durch die Nernst-Gleichung bestimmt. Eine neue Gleichung zur Berechnung von Strom-Spannungs-Kurven für reversible Reaktionen, in denen nur das Produkt vorliegt, wurde hergeleitet. Mithilfe dieser Gleichung konnten die kinetischen Daten der HER ermittelt werden.

Mit den kinetischen Daten in dieser Arbeit ist es möglich vollständige Polarisationskurven für Platin in verschiedenen mit Luft oder Stickstoff gespülten, wässrigen Elektrolytlösungen zu berechnen.

ACKNOWLEDGMENTS

Content

Symbols

Latin-scribt symbols

A	m^2	area
a	-	activity
c	mol m^{-3}	concentration
C	F m^{-2}	electrical capacitance
C_{DL}	S s^{cp} m^{-2}	electrical capacitance of the double layer
cp	-	correction factor for a constant phase element
D	m^2 s^{-1}	diffusion coefficient
E	V	potential
E^0	V	standard potential
E_Ω	V	measured potential without ohmic drop compensation
F	C mol^{-1}	Faraday constant (F = 96485.3399 C mol^{-1} [1])
g_{Temk}	-	adsorption constant according to Temkin
h_{Temk}	-	evaporation constant according to Temkin
I	A	current
i	A m^{-2}	current density
i_{eq}	A m^{-2}	exchange current density at equilibrium potential
i^{RE}	A m^{-2}	pre-exponential current density at E = 0 vs. reference electrode
i^{RHE}	A m^{-2}	pre-exponential current density at E = 0 vs. RHE
i^{ROE}	A m^{-2}	pre-exponential current density at E = 0 vs. ROE
i^{SHE}	A m^{-2}	pre-exponential current density at E = 0 vs. SHE
i_L	A m^{-2}	diffusion limiting current density calculated by Levich equation
J	mol s^{-1}	flux of a substance
j	mol m^{-2} s^{-1}	flux of a substance per unit of surface
K_{Sech}	m^3 mol^{-1}	Sechenov coefficient
k	various	rate constant
k^0	various	potential independent rate constant
k_H	Pa m^3 mol^{-1}	volatility constant according to Henry's law
M_g	g mol^{-1}	molecular weight
N	-	collection efficiency of a RRDE
N_A	mol^{-1}	Avogadro constant (N_A = 6.02214179·10^{-23} mol^{-1} [1])
p	Pa	pressure or partial pressure
n	-	number of electrons involved in a chemical reaction
R	m	radius
R_g	J mol^{-1} K^{-1}	gas constant (R_g = 8.314472 J mol^{-1} K^{-1} [1])
R_Ω	Ω	ohmic resistance
r, z, ϕ	m,m,rad	cylindrical coordinate system
S	%	salinity
s	V^{-1}	exponential slope
T	K	temperature
t	s	time
t_s	V dec^{-1}	Tafel slope with a logarithm to base 10
E_{off}	V	offset potential
v	m s^{-1}	velocity
$\overline{x}$	m	mean distance
x, y, z	m,m,m	cartesian coordinate system
Z	Ω	electrical impedance

Greek symbols

α	-	charge transfer coefficient
α_0	-	fraction of molecules adsorbed on an unoccupied surface
α_{Lang}	-	fraction of molecules adsorbed according to Langmuir
α_{Temk}	-	fraction of molecules adsorbed according to Temkin
δ_N	m	Nernst diffusion layer
η	Pa s	dynamic viscosity
Θ_{Lang}	-	covered surface fraction according to Langmuir
Θ_{Temk}	-	covered surface fraction according to Temkin
μ_{cof}	-	coefficient of friction
μ_{Lang}	-	molecules impinging on a surface
ν	$m^2\,s^{-1}$	kinematic viscosity
ν_1	-	rate of evaporation of adsorbents from a fully covered surface
ν_{Lang}	-	rate of evaporation of adsorbents according to Langmuir
ν_{Temk}	-	rate of evaporation of adsorbents according to Temkin
ρ	$kg\,m^{-3}$	density
ω	$rad\,s^{-1}$	angular speed
ω_{AC}	$rad\,s^{-1}$	angular speed of the alternating current
∇	-	Nabla operator

Indices

A	adsorbed		eq	equilibrium
AC	alternating current		f	forward
ads	adsorption		i	species i
atm	gas/liquid interface		kin	kinetically controlled
B	bulk		lim	limiting
b	backward		R	ring
D	disc		S	catalyst/electrode surface
des	desorption		sat	saturation
DL	double layer		sex	surface exchange

Standard Abbreviations

CE	counter electrode		RRDE	rotating ring disc electrode
HER	hydrogen evolution reaction		RE	reference electrode
HOR	hydrogen oxidation reaction		Red	reduced species
Int	intermediate		RHE	reversible hydrogen electrode
M	active site of a heterogeneous catalyst		ROE	reversible oxygen electrode
OCP	open circuit potential		SCE	saturated calomel electrode
ORR	oxygen reduction reaction		SHE	standard hydrogen electrode
Ox	oxidized species		WE	working electrode
RDE	rotating disc electrode			

INTRODUCTION

A very important area of electrochemistry is electrochemical corrosion. In this kind of corrosion the anodic metal dissolution is accompanied by a cathodic counter reaction. In the atmosphere of the earth this cathodic reaction is usually the oxygen reduction reaction (ORR) while the hydrogen evolution reaction (HER) is only of importance for ignoble materials.

The ORR is also of importance for power supplies. Batteries were invented at the beginning of the 19th century [2] and have been the most important voltage source for a long time. Their development remains an important research field in electrochemistry. An alternative power supply, the fuel cell, was simultaneous developed by Grove [3] and Schönbein [4] about 40 years later. In a fuel cell the potential between oxygen and hydrogen dissolved in water is used.

Thus a fundamental understanding of the ORR is of great importance for the development of fuel cells and metal-air batteries and for the clarification of the galvanic corrosion mechanism. Although it has been researched for over a century its mechanism is only partly understood. The goal of this work is therefore to model whole cathodic polarization curves obtained on polycrystalline platinum caused by the oxygen reduction and hydrogen evolution.

The measurements were carried out with a polycrystalline platinum ring-disc electrode since this material is the most promising catalyst for the ORR. The great amount of literature about the ORR on this material provides the opportunity to compare the obtained data with the published results.

As the oxygen reduction depends on the mass transport a rotating ring disc electrode (RRDE) is used. It provides a well-known diffusion profile so that the mass transport limitation can be eliminated from the measured current and the reaction kinetic parameters can be determined.

In literature the kinetic parameters are obtained using the Koutecký-Levich plot [5] but the equation is very ill conditioned [6] when the charge transfer or the mass transport limitation is dominant. For this reason the kinetic data in this work was determined using a least squares fitting of a set of curves measured at different rotation rates. As the polarization curves are caused by several reactions, each reaction was optimized separately by minimizing the least squares.

The diffusion limiting current densities were analyzed using the Levich-equation [7] which requires several physical values. An extensive literature research was done to obtain these values. It was found that chloride solutions were most extensively studied and therefore in this work most measurements were carried out in 0.1 M chloride and 0.05 M sulfate electrolytes with a varying pH from 1 to 9.5. One set of data was measured in 0.1 M sodium hydroxide (pH 13). The measurements at pH 4.5 and pH 9.5 were buffered with 0.01 M potassium hydrogen phthalate respectively 0.01 M sodium borates. Except one measurement all electrolytes were saturated with air to study the ORR or nitrogen to investigate the HER. The oxygen concentration was also varied by increasing the salt concentration.

With the kinetic data given in this work complete polarization curves of platinum cathodes in a pH range from 1 to 13 can be calculated.

MATHEMATICAL MODELS

1.1 ADSORPTION ON THE ELECTRODE SURFACE

In the first step of heterogeneous catalyzed reactions at least one of the reactants must be adsorbed on the surface or in case of an electrochemical reaction at the electrode. Under steady state conditions the rate of desorption v_{Lang} of the adsorbents must be equal to the rate at which these molecules adsorb. Their adsorption depends on the rate at which they impinge μ_{Lang} on the surface and the fraction of these molecules which remain α_{Lang} there (1.1). [8, 9]

$$\alpha_{\mathrm{Lang}} \cdot \mu_{\mathrm{Lang}} = v_{\mathrm{Lang}} \tag{1.1}$$

The rate of desorption is assumed to be equal to that of a complete monolayer v_1 multiplied by the covered surface fraction Θ_{Lang} (1.2). The fraction of molecules, which get adsorbed at the electrode surface, can be calculated by the fraction of molecules which would be adsorbed on an unoccupied surface α_0 multiplied by the rate at which they impinge on the surface and the uncovered surface fraction (1.3). [8, 9]

$$v_{\mathrm{Lang}} = v_1 \cdot \Theta_{\mathrm{Lang}} \tag{1.2}$$

$$\alpha_{\mathrm{Lang}} \cdot \mu_{\mathrm{Lang}} = \alpha_0 \cdot \mu_{\mathrm{Lang}} \cdot \left(1 - \Theta_{\mathrm{Lang}}\right) \tag{1.3}$$

Therefore the Langmuir-isotherm for adsorption can be calculated by equation (1.4). [8, 9]

$$\Theta_{\mathrm{Lang}} = \frac{\alpha_0 \cdot \mu_{\mathrm{Lang}}}{v_1 + \alpha_0 \cdot \mu_{\mathrm{Lang}}} \tag{1.4}$$

The Langmuir-isotherm is valid for adsorption of a monolayer on a homogeneous surface when the interaction of the adsorbents can be neglected. [8, 9]

In case of an associative desorption (1.5) and dissociative adsorption (1.6) two sites on the adsorbent are necessary. Since all physical values have to be positive only one solution for these equations under steady state conditions exists (1.7).

$$v_{\mathrm{Lang}} = v_1 \cdot \Theta_{\mathrm{Lang}}{}^2 \tag{1.5}$$

$$\alpha_{\mathrm{Lang}} \cdot \mu_{\mathrm{Lang}} = \alpha_0 \cdot \mu_{\mathrm{Lang}} \cdot \left(1 - \Theta_{\mathrm{Lang}}\right)^2 \tag{1.6}$$

$$\Theta_{\mathrm{Lang}} = \frac{\left(\alpha_0 \cdot \mu_{\mathrm{Lang}}\right)^{1/2}}{v_1{}^{1/2} + \left(\alpha_0 \cdot \mu_{\mathrm{Lang}}\right)^{1/2}} \tag{1.7}$$

The desorption and the adsorption are not always proportional to the covered fraction and might follow an exponential relationship. In this case the desorption can be described by equation (1.8) [10] while the adsorption follows equation (1.9). The Temkin-isotherm (1.10) can be obtained from these two equations. [11]

$$v_{\mathrm{Temk}} = k_{\mathrm{des}} \cdot \exp\left(h_{\mathrm{Temk}} \cdot \Theta_{\mathrm{Temk}}\right) \tag{1.8}$$

$$\alpha_{\mathrm{Temk}} = k_{\mathrm{ads}} \cdot p \cdot \exp\left(g_{\mathrm{Temk}} \cdot \Theta_{\mathrm{Temk}}\right) \tag{1.9}$$

$$\Theta_{\text{Temk}} = \frac{\ln\left(\frac{k_{\text{ads}}}{k_{\text{des}}} \cdot p\right)}{(h_{\text{Temk}} - g_{\text{Temk}})} \tag{1.10}$$

This exponential approach works only for the middle range of adsorption. Even without adsorbates on the surface this model still predicts desorption.

1.2 DIFFUSION IN AN ELECTROLYTE WITHOUT CONVECTION

To get adsorbed, a molecule must be transported to the electrode surface. Without convection the only way of transportation to a static electrode is by diffusion or migration. In this context migration is the mass transport caused by the influence of an electric field on charged particles. Oxygen and water have no electric charge and therefore they won't be affected by migration. Only the transport of hydroxide, as a product of the HER and the ORR, from the vicinity of the electrode into the bulk would be increased by migration. The change of the pH in the diffusion layer was beyond the scope of this work but its effect on the reaction kinetics might be an interesting topic for further investigations.

Adolf Fick published the fundamental law of diffusion (1.11) which is similar to the heat flux proposed by other authors before. [12]

$$\frac{\partial c}{\partial t} = D \cdot \left(\frac{\partial^2 c}{\partial x^2} + \frac{1}{A} \cdot \frac{\mathrm{d}A}{\mathrm{d}x} \cdot \frac{\partial c}{\partial x}\right) \tag{1.11}$$

If the cross sectional area, which is normal to the diffusion flux is constant, the equation can be simplified to the "second Fick's law" for 1-dimensional (1.12) and 3-dimensional (1.13) diffusion in an isotropic media.

$$\frac{\partial c}{\partial t} = D \cdot \frac{\partial^2 c}{\partial x^2} \tag{1.12}$$

$$\frac{\partial c}{\partial t} = D \cdot \left(\frac{\partial^2 c}{\partial x^2} + \frac{\partial^2 c}{\partial y^2} + \frac{\partial^2 c}{\partial z^2}\right) \tag{1.13}$$

Under steady state conditions the concentration is independent of time and the diffusion flux can be calculated by the "first Fick's law" for 1-dimensional (1.14) and 3-dimensional (1.15) diffusion.

$$j = D \cdot \frac{\partial c}{\partial x} \tag{1.14}$$

$$j = D \cdot \left(\frac{\partial c}{\partial x} + \frac{\partial c}{\partial y} + \frac{\partial c}{\partial z}\right) \tag{1.15}$$

Albert Einstein provided the thermodynamic background for the law of diffusion. The arithmetic mean distance $\bar{x}$ a particle can move depends on time and is given by equation (1.16). In solutions, the diffusion coefficient depends on the radius of the particle R and the coefficient of friction of the fluid μ_{cof} (1.17). [13]

$$\bar{x} = \sqrt{2 \cdot D \cdot t} \tag{1.16}$$

$$D = \frac{R_\mathrm{g} \cdot T}{N_\mathrm{A}} \cdot \frac{1}{6 \cdot \pi \cdot \mu_\mathrm{cof} \cdot R} \tag{1.17}$$

The solution for the diffusion equation (1.13) depends on the initial and boundary conditions. To describe a static disc electrode with a radius R under steady state conditions where the r-axis is the radial distance from the center of the disc and the z-axis is normal to the center, equation (1.18) must be solved.

$$\left(\frac{\partial^2 c}{\partial r^2} + \frac{1}{r} \cdot \frac{\partial c}{\partial r} + \frac{\partial^2 c}{\partial z^2} \right) = 0 \tag{1.18}$$

The following boundary conditions are assumed [14]:

1. For a diffusion limited reaction at a disc electrode, the concentration is zero at the surface:

$$z = 0 \qquad\qquad r \leq R \qquad\qquad c = 0$$

$$z = 0 \qquad\qquad r > R \qquad\qquad \frac{\partial c}{\partial z} = 0$$

2. Far away from the disc electrode a bulk concentration can be assumed:

$$z = \infty \qquad\qquad r \geq 0 \qquad\qquad c = c_\mathrm{B}$$

$$z \geq 0 \qquad\qquad r = \infty \qquad\qquad c = c_\mathrm{B}$$
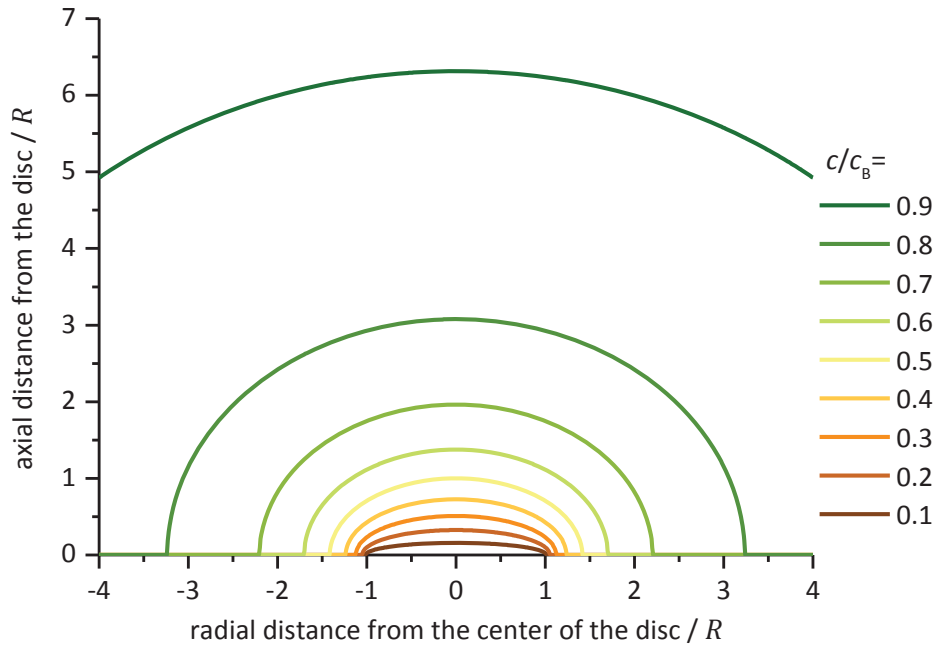

Figure 1: Concentration profile of a stationary disc electrode according to equation (1.19)

Equation (1.18) can be converted into a Bessel function. Its solution is given by equation (1.19) [15] and shown in Figure 1.

$$c_\mathrm{B} - c(r,z) = \frac{2 \cdot c_\mathrm{B}}{\pi} \cdot \tan^{-1} \frac{r}{\langle \frac{1}{2} \cdot \{r^2 + z^2 - R^2 + [(r^2 + z^2 - R^2)^2 + 4 \cdot z^2 \cdot R^2]^{1/2}\}\rangle^{1/2}} \tag{1.19}$$

1.3 ROTATING ELECTRODES

1.3.1 ROTATING DISC ELECTRODES

To study the reaction kinetics independent of the diffusion it is necessary to increase the mass transport by forced convection. This can be realized by stirring the solution but this makes it difficult to estimate the influence of the convection. For this reason rotating electrodes were developed. The most popular is the rotating disc electrode (RDE).

Considering a steady state current on a RDE with a sufficient low Reynolds number of the solution ($Re \leq 10^5$) the Navier-Stokes equation describing the motion of fluid substances can be expressed by the following equations in a cylindrical coordinate system [7]:

$$v_\mathrm{r} \cdot \frac{\partial v_\mathrm{r}}{\partial r} - \frac{v_\varphi^2}{r} + v_\mathrm{z} \cdot \frac{\partial v_\mathrm{r}}{\partial z} = \nu \cdot \left(\frac{\partial^2 v_\mathrm{r}}{\partial z^2} - \frac{v_\mathrm{r}}{r^2}\right) - \frac{1}{\rho} \cdot \frac{\partial p}{\partial r} \tag{1.20}$$

$$v_\mathrm{r} \cdot \frac{\partial v_\mathrm{r}}{\partial r} - \frac{v_\mathrm{r} \cdot v_\varphi}{r} + v_\mathrm{z} \cdot \frac{\partial v_\varphi}{\partial z} = \nu \cdot \left(\frac{\partial^2 v_\varphi}{\partial z^2} - \frac{v_\varphi}{r^2}\right) \tag{1.21}$$

$$v_\mathrm{r} \cdot \frac{\partial v_\mathrm{r}}{\partial r} + v_\mathrm{z} \cdot \frac{\partial v_\mathrm{z}}{\partial z} + v_\mathrm{z} \cdot \frac{\partial v_\varphi}{\partial z} = \nu \cdot \frac{\partial^2 v_\mathrm{z}}{\partial z^2} - \frac{1}{\rho} \cdot \frac{\partial p}{\partial z} \tag{1.22}$$

The continuity equation is (1.23).

$$\frac{\partial v_\mathrm{r}}{\partial r} + \frac{v_\mathrm{r}}{r} + \frac{\partial v_\mathrm{z}}{\partial z} = 0 \tag{1.23}$$

For a rotating disc electrode the following boundary conditions can be assumed [7]:

1. At the surface of the electrode the radial and axial velocity are zero and only the angular velocity is relevant:

$$z = 0 \qquad v_\mathrm{r} = 0 \qquad v_\varphi = r \cdot \omega \qquad v_\mathrm{z} = 0$$

2. Far away from the electrode a constant current of fluid is flowing to the disc:

$$z = \infty \qquad v_\mathrm{r} = 0 \qquad v_\varphi = 0 \qquad v_\mathrm{z} = -\mathrm{const.}$$

Under steady state conditions the diffusion must be equal to the convection (1.24). [7]

$$D \cdot \left(\frac{\partial^2 c}{\partial r^2} + \frac{1}{r} \cdot \frac{\partial c}{\partial r} + \frac{\partial^2 c}{\partial z^2}\right) = v_\mathrm{r} \cdot \frac{\partial c}{\partial r} + \frac{1}{r} \cdot v_\varphi \cdot \frac{\partial c}{\partial \varphi} + v_\mathrm{z} \cdot \frac{\partial c}{\partial z} \tag{1.24}$$

The solution of equation (1.24) by Veniamin G. Levich gives the thickness of the diffusion boundary layer (1.25). [7]

$$\delta_\mathrm{N} = 1.61 \cdot D^{1/3} \cdot \nu^{1/6} \cdot \omega^{-1/2} \tag{1.25}$$

The diffusion limiting current density, if the surface concentration is zero, can be obtained as a function of the rotation rate (1.27) as can be seen by combining equation (1.25) and the one dimensional first Fick's law (1.26).

$$j = D \cdot \frac{c_B - c_S}{\delta_N} \tag{1.26}$$

$$i_L = 0.62 \cdot n \cdot F \cdot D^{2/3} \cdot v^{-1/6} \cdot \omega^{1/2} \cdot c_B \tag{1.27}$$

D. P. Gregory and A. C. Riddiford offer a more exact solution for the diffusion layer under the same assumptions (1.28). [16]

$$\delta_N = 1.805 \cdot D^{1/3} \cdot v^{1/6} \cdot \omega^{-1/2} \cdot \left[0.8934 + 0.316 \cdot \left(\frac{D}{v} \right)^{0.36} \right] \tag{1.28}$$

The difference of the diffusion layer thickness calculated by equation (1.25) and (1.28) in Figure 2 increases at lower rotation rates. Levich states that the experimental values are given more closely by equation (1.25) than by the more exact solution from Gregory. This implies that there are other unconsidered effects such as the outer rim of the disc, natural convection or turbulences which influence the experimental results. [17]
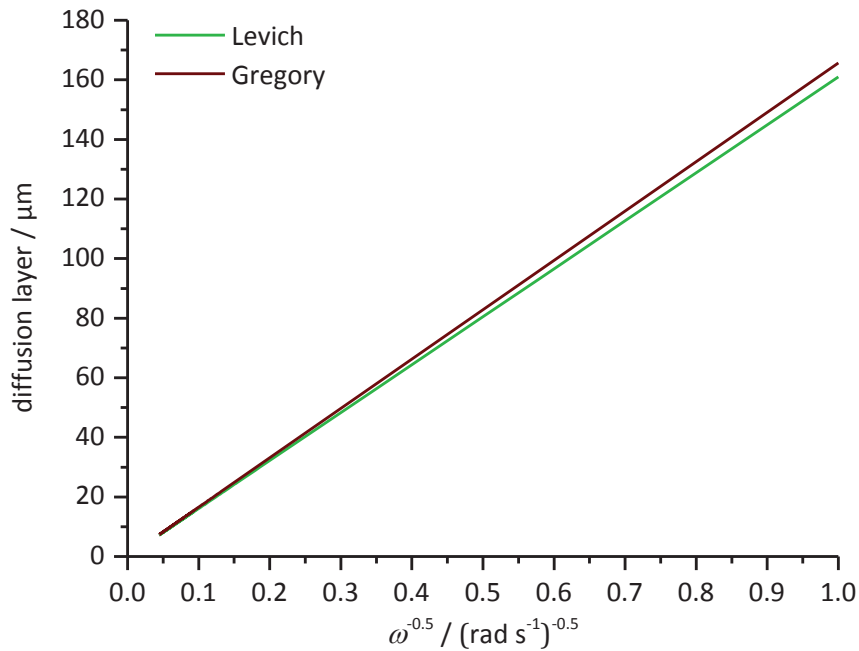
Figure 2: Diffusion layer calculated according to Levich [7] and Gregory [16]
(input parameter: $D = 10^{-9} \, \mathrm{m^2 \cdot s^{-1}}$; $v = 10^{-6} \, \mathrm{m^2 \cdot s^{-1}}$)

William H. Smyrl calculated the influence of the radial diffusion for a disc electrode with a diameter of 0.25 cm and a rotation speed of 300 rpm. In this case the difference between the limiting current calculated according to Levich and the one calculated by Smyrl was only 0.116 %. [18]

The current can also be influenced by the reaction kinetic. The effective current density of a first-order reaction (1.29) is given by equation (1.30). [5, 17]

$$i_{\text{kin}} = n \cdot F \cdot k \cdot c_{\text{S}} \tag{1.29}$$

$$\frac{1}{i} = \frac{1}{i_{\text{kin}}} + \frac{1}{i_{\text{L}}} \tag{1.30}$$

The Koutecký-Levich equation (1.30) is widely used for the interpretation of RDE measurements because it can be used to separate the kinetics from the mass transport limitation. Equation (1.31) shows how a relative error in the measured current density affects the relative error in the calculated kinetic current density. [6]

$$\frac{\Delta i_{\text{kin}}}{i_{\text{kin}}} = \frac{1+m}{1-m} \cdot \frac{\Delta i}{i} \tag{1.31}$$

$$m = \frac{i}{i_{\text{L}}} \tag{1.32}$$

The condition number is small for currents which are much smaller than the mass transport limiting current ($i \ll i_{\text{L}}$) and the Koutecký-Levich equation (1.30) is therefore well conditioned.

$$\lim_{m \to 0} \frac{1+m}{1-m} = 1$$

By increasing the current to the mass transport limitation ($i = i_{\text{L}}$) the condition number increases and the equation becomes ill conditioned.

$$\lim_{m \to 1} \frac{1+m}{1-m} = \infty$$

Another way to estimate the condition number is to show that the Koutecký-Levich equation is a Lipschitz continuous function. Therefore equation (1.30) can be transformed into equation (1.33) in which the kinetic current is expressed as a function of the current.

$$i_{\text{kin}}(i) = \frac{i \cdot i_{\text{L}}}{i_{\text{L}} - i} \tag{1.33}$$

The relative condition number for Lipschitz continuous functions can be estimated by equation (1.34). [19]

$$\kappa_{\text{rel}} \approx \frac{f'(x)}{f(x)} \cdot x \tag{1.34}$$

If the function (1.33) is Lipschitz continuous a Lipschitz constant $L > 0$ which satisfies condition (1.35) must exist. [20] The current can have values between zero and the limiting current. If the measured current reaches the limiting current the kinetic current becomes infinite and equation (1.33) is not longer Lipschitz continuous.

$$|i_{\text{kin}}(i_1) - i_{\text{kin}}(i_2)| \leq L \cdot |i_1 - i_2| \tag{1.35}$$

In the interval $0 \leq i < i_{\text{L}}$ the function (1.35) is continuous and differentiable so that the Lipschitz constant can be calculated by the mean value theorem (1.37) [20]. The supremum of the function

(1.36) and therefore the Lipschitz constant depends on how close the interval is set to the limiting current.

$$i_{kin}'(i) = \frac{i_L{}^2}{(i_L - i)^2}$$

(1.36)

$$L = \sup[i_{kin}'(i)]$$

(1.37)

The Koutecký-Levich equation (1.30) is Lipschitz continuous in the interval $0 \leq i < i_L$ and the relative condition number can be estimated by equation (1.38). At low current densities the condition number becomes 1 while the equation gets ill conditioned for current densities close to the diffusion limiting current.

$$\kappa_{rel} \approx \frac{i_L}{i_L - i}$$

(1.38)

Using the same way it can be shown that the Koutecký-Levich (1.30) equation is also ill conditioned for current densities close to the pure kinetically controlled current density.

The Koutecký-Levich equation (1.30) only considers an irreversible first order reaction. For reversible reactions {1.1} equation (1.39) is obtained by the combination of the diffusion limitation and the electrode kinetics. [21]

$$Ox + n\,e^- \underset{k_b}{\overset{k_f}{\rightleftharpoons}} Red$$

{1.1}

$$i = \frac{n \cdot F \cdot (k_f \cdot c_{Ox,0} - k_b \cdot c_{Red,0})}{1 + \frac{k_f \cdot \delta_{Ox}}{D_{Ox}} + \frac{k_b \cdot \delta_{Red}}{D_{Red}}}$$

(1.39)

1.3.2 ROTATING RING DISC ELECTRODES
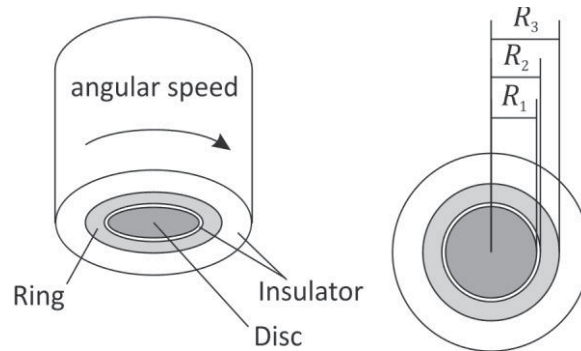

Figure 3: Rotating ring disc electrode

A reaction product or intermediate previously formed on the disc electrode {1.2} can be detected by a ring electrode around the disc (Figure 3). The product is transported by convective diffusion to the ring were it can be further oxidized or reduced {1.3}.

$$A \pm n\,e^- \rightarrow B$$

{1.2}

$$B \pm n\,e^- \rightarrow C$$

{1.3}

If the reaction rate on the ring electrode is infinitely fast the detectable ring current depends on the amount of the previously formed species at the disc and a geometrical factor called the collection efficiency (1.40). [22]

$$N = \frac{I_R}{I_D} \tag{1.40}$$

Considering a further reaction of the intermediate at the disc electrode the ring current would be also influenced by the diffusion boundary layer and the reaction rate at the disc electrode (1.41). [17]

$$I_R = \frac{I_D \cdot N}{1 + \frac{k_D \cdot \delta_N}{D}} \tag{1.41}$$

The flux density of the product reaching the ring is given by equation (1.42). [17]

$$j_R(r) = 0.4 \cdot \frac{j_D}{1 + \frac{k_D \cdot \delta_N}{D}} \cdot \frac{R_1^2 \cdot R_2}{r^3} \cdot \frac{\left(1 - \frac{3 \cdot R_1^3}{4 \cdot R_2^3}\right)^{1/3}}{\left(1 - \frac{R_2^3}{r^3}\right)^{1/3} \cdot \left(1 - \frac{3 \cdot R_1^3}{4 \cdot r^3}\right)} \tag{1.42}$$

In case of a very thin isolation between the disc and the ring $(R_2 - R_1 \ll R_1)$ and a small ring $(R_3 - R_2 \ll R_2)$ equation (1.42) can be reduced to (1.43). [17]

$$j_R(r) \approx \frac{j_D}{1 + \frac{k_D \cdot \delta_N}{D}} \cdot \frac{R_1^2 \cdot R_2}{r^3 \cdot \left(1 - \frac{R_2^3}{r^3}\right)^{1/3}} \tag{1.43}$$

The total amount of the species reacting on the ring electrode is given by equation (1.44). [17]

$$J_R = 2 \cdot \pi \cdot \int_{R_2}^{R_3} j_R(r) \cdot r \cdot dr \tag{1.44}$$

A comprehensive theoretical and experimental investigation of the RRDE was carried out by Wyndham John Albery. [22-36] By using the same boundary conditions as Levich the collection efficiency derived by Albery is given by equation (1.45). [22]

$$N = 1 - f\left(\frac{\alpha}{\beta}\right) + \beta^{2/3} \cdot [1 - f(\alpha)] - (1 + \alpha + \beta)^{2/3} \cdot \left\{1 - f\left[\frac{\alpha}{\beta} \cdot (1 + \alpha + \beta)\right]\right\} \tag{1.45}$$

$$\alpha = \left(\frac{R_2}{R_1}\right)^3 - 1 \tag{1.46}$$

$$\beta = \left(\frac{R_3}{R_1}\right)^3 - \left(\frac{R_2}{R_1}\right)^3 \tag{1.47}$$

$$f(x) = \frac{1}{4} + \frac{3^{1/2}}{4 \cdot \pi} \cdot \ln \frac{\left(1 + x^{1/3}\right)^3}{1 + x} + \frac{3}{2 \cdot \pi} \cdot \tan^{-1} \frac{2 \cdot x^{1/3} - 1}{3^{1/2}} \tag{1.48}$$

Albery stated that the values of the collection efficiency calculated according to Levich are up to 25 % too large. [22]

A. Damjanovic, M. A. Genshaw and J. O'M. Bockris studied the ORR and postulated a mechanism at which two parallel reactions take place at the disc electrode, the complete reduction to the reduced species (Red) {1.4} and the formation of an intermediate (Int) {1.5}. If the intermediate is reduced at the ring electrode {1.6}, the ratio of the disc and ring current can be calculated by equation (1.49). It is a function of the current forming the reduced species I_1 {1.4} and the current due to the formation of the intermediate I_2 {1.5}. [37]

$$Ox + m\ e^- \xrightarrow{k_1} Red \qquad \{1.4\}$$

$$Ox + (m-n)\ e^- \xrightarrow{k_2} Int \qquad \{1.5\}$$

$$Int + n\ e^- \xrightarrow{k_3} Red \qquad \{1.6\}$$

$$\frac{I_D}{I_R} = \frac{\frac{I_1}{I_2} + 1}{N} + \frac{\left(\frac{I_1}{I_2} + 2\right) \cdot k_3 \cdot \delta_N}{N \cdot D} \qquad (1.49)$$

The previous models only consider convection, diffusion and reaction kinetics but neglect migration. The effect of migration on the concentration profile at a rotating RRDE was studied by Sirshednu Guha [38] using a finite difference numerical technique. He showed that the migration can be very important for the transport of ionic species in electrolytes with low concentrations.
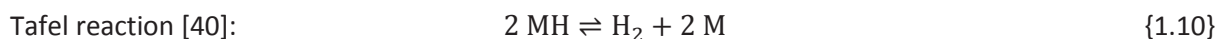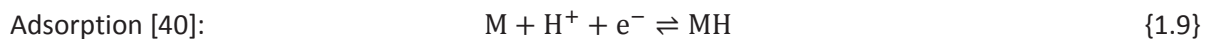
1.4 HYDROGEN EVOLUTION

The pH dependency of the hydrogen evolution reaction (HER) is determined by the equilibrium {1.7} in acidic electrolytes and by the equilibrium {1.8} in alkaline electrolytes.

$$H_2 \rightleftharpoons H^+ + 2\ e^- \qquad \{1.7\}$$

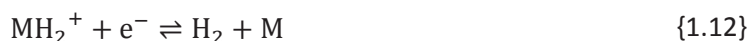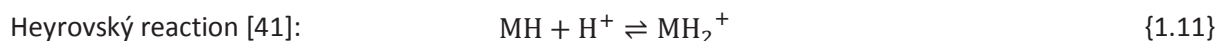$$H_2 + 2\ OH^- \rightleftharpoons 2\ H_2O + 2\ e^- \qquad \{1.8\}$$

C. A. Knorr defined the following steps for the HER [39]:

1. Transport of the hydrated hydrogen ions to the electrode surface
2. Dehydration, discharge and adsorption of the hydrogen
3. Recombination of the hydrogen atoms to molecules
4. Transport of the hydrogen molecules from the electrode surface into the bulk solution

The initial step of the hydrogen evolution is the adsorption of hydrogen ions on the electrode surface {1.9}. Two such adsorbed hydrogen atoms can combine to the H_2-molecule {1.10} which results in a Tafel slope of -29 mV dec[-1]. Another possibility is the reaction of an adsorbed atom with a hydrogen ion from the solution {1.11}. The further reduction {1.12} causes a Tafel slope of -118 mV dec[-1]. [40] A Tafel slope of -118 mV dec[-1] might also indicate that reaction {1.9} is rate determining, which is not considered in literature.

Adsorption [40]: $\qquad\qquad M + H^+ + e^- \rightleftharpoons MH \qquad \{1.9\}$

Tafel reaction [40]: $\qquad\qquad 2\ MH \rightleftharpoons H_2 + 2\ M \qquad \{1.10\}$

Heyrovský reaction [41]:
$$\text{MH} + \text{H}^+ \rightleftharpoons \text{MH}_2{}^+ \qquad\qquad \{1.11\}$$

$$\text{MH}_2{}^+ + \text{e}^- \rightleftharpoons \text{H}_2 + \text{M} \qquad\qquad \{1.12\}$$

Julius Tafel [42, 43] investigated the kinetic of the hydrogen evolution at different materials and none showed the expected slope from the Nernst equation (1.50) [44, 45].

$$E_{\text{eq}} = E^0 + \frac{R_{\text{g}} \cdot T}{n \cdot F} \cdot \ln \frac{a_{\text{Ox}}}{a_{\text{Red}}} \qquad\qquad (1.50)$$

This is due to the different catalytic properties of materials for the HER [42, 43]. The linear correlation between the electrode potential and the logarithmic current (1.51) or (1.52) is called Tafel equation.

$$E - E_{\text{eq}} = \frac{R_{\text{g}} \cdot T}{\alpha \cdot n \cdot F} \cdot \ln \frac{i}{i_{\text{eq}}} \qquad\qquad (1.51)$$

$$i = i_{\text{eq}} \cdot \exp\left[\frac{\alpha \cdot n \cdot F}{R_{\text{g}} \cdot T} \cdot \left(E - E_{\text{eq}} \right) \right] \qquad\qquad (1.52)$$

Tafel's investigations were carried out under significant hydrogen evolution. For such a high potential without mass transport limitation the Tafel equation is sufficient, but close to the equilibrium potential the anodic and the cathodic parts of the reversible reaction have to be considered. This is done by the Butler-Volmer equation (1.53). It was first published by T. Erdey-Grùz and M. Volmer [40] in 1930 who introduced the charge transfer coefficient. Independent of this work J. A. V. Butler [46] published one year later a similar equation. Both authors based their work on the experiments done by F. P. Bowden and E. K. Rideal [47, 48].
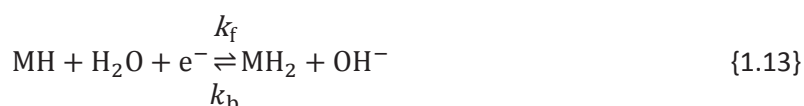
$$i = i_{\text{eq}} \cdot \left\{ \exp\left[\frac{\alpha \cdot n \cdot F}{R_{\text{g}} \cdot T} \cdot \left(E - E_{\text{eq}} \right) \right] - \exp\left[\frac{(1 - \alpha) \cdot n \cdot F}{R_{\text{g}} \cdot T} \cdot \left(E - E_{\text{eq}} \right) \right] \right\} \qquad (1.53)$$

Different types of Tafel lines for the cathodic hydrogen evolution have been published by J. O'M. Bockris and E. C. Potter. Three of these are free of vitiating influences but only the "ideal type" shows the expected linear Tafel behavior. The "silver type" and the "platinum type", with its hysteresis between forward and reverse scan, show two different Tafel slopes. [49]

These two Tafel slopes are not explained by either the Tafel equation nor by the Butler Volmer equation. For this reason a new approach is proposed in this work.

If the volume of the solution is large enough the reaction has no influence on the composition of the electrolyte. Therefore water and the formed hydroxide ions were neglected in the further consideration. It is also assumed that the electrolyte is initially free of molecular hydrogen.

For a reversible Heyrovský reaction {1.13} in combination with the desorption reaction {1.14} the steady state approximation is given by equation (1.54). The surface activity of adsorbed hydrogen can be calculated by equation (1.55).

$$\text{MH} + \text{H}_2\text{O} + \text{e}^- \underset{k_{\text{b}}}{\overset{k_{\text{f}}}{\rightleftharpoons}} \text{MH}_2 + \text{OH}^- \qquad\qquad \{1.13\}$$

$$\mathrm{MH_2 \rightarrow M + H_2} \tag{1.14}$$

$$k_\mathrm{f} \cdot a_\mathrm{MH} = k_\mathrm{b} \cdot a_\mathrm{MH_2} + \nu_\mathrm{Lang} \cdot a_\mathrm{MH_2} \tag{1.54}$$

$$a_\mathrm{MH_2} = \frac{k_\mathrm{f}}{k_\mathrm{b} + \nu_\mathrm{Lang}} \cdot a_\mathrm{MH} \tag{1.55}$$

Under steady state conditions capacitive currents can be neglected and the only contribution to the current is the desorption of molecular hydrogen from the surface (1.56) into the bulk which leaves a free surface site. At this surface site the electrochemical hydrogen adsorption reaction {1.9} and in a further step the reversible Heyrovský reaction {1.13} will take place.

$$i = n \cdot F \cdot \nu_\mathrm{Lang} \cdot \frac{k_\mathrm{f}}{k_\mathrm{b} + \nu_\mathrm{Lang}} \cdot a_\mathrm{MH} \tag{1.56}$$

The rate constants of an electrochemical partial reaction can be expressed by equation (1.57) and (1.58) [50]. The equilibrium potential cannot be calculated by the Nernst equation (1.50) if there is no hydrogen in the electrolyte. Therefore the potentials and the pre-exponential factors can be given with respect to an arbitrary chosen reference potential. In this work the pre-exponential current densities are given with respect to the SHE, the RHE or the ROE.

$$k_\mathrm{f} = k_\mathrm{f}^0 \cdot \exp\left[-\frac{(1-\alpha) \cdot n \cdot F}{R_\mathrm{g} \cdot T} \cdot E \right] \tag{1.57}$$

$$k_\mathrm{b} = k_\mathrm{b}^0 \cdot \exp\left[\frac{\alpha \cdot n \cdot F}{R_\mathrm{g} \cdot T} \cdot E \right] \tag{1.58}$$

$$i = i_\mathrm{f}^0 \cdot \frac{\exp\left[-\frac{(1-\alpha) \cdot n \cdot F}{R_\mathrm{g} \cdot T} \cdot E \right]}{1 + \frac{k_\mathrm{b}^0}{\nu_\mathrm{Lang}} \cdot \exp\left[\frac{\alpha \cdot n \cdot F}{R_\mathrm{g} \cdot T} \cdot E \right]} \cdot a_\mathrm{MH} \tag{1.59}$$

Figure 4 compares the current density calculated by the new equation (1.59), by a simple Tafel equation and by the Butler-Volmer equation in which the educts and the products are initially in the solution. At large cathodic overpotentials all three models show the same current density. The Tafel slope considers only the forward reaction without taking into account the adsorbed hydrogen atoms necessary according to the Nernst equation (1.50) for reaction {1.13}. This results in a current density which is too high. At positive overpotentials the Butler-Volmer equation shows an anodic reaction. This is only possible if hydrogen molecules are initially in the electrolyte. The proposed model according to equation (1.59) shows a change in the Tafel slope close to the equilibrium potential of the Butler-Volmer equation. If reaction {1.9} is assumed to be rate determining the change in the reaction rate compared to the straight Tafel line is due to the increase of the proton activity at the surface according to Nernst equation (1.50).
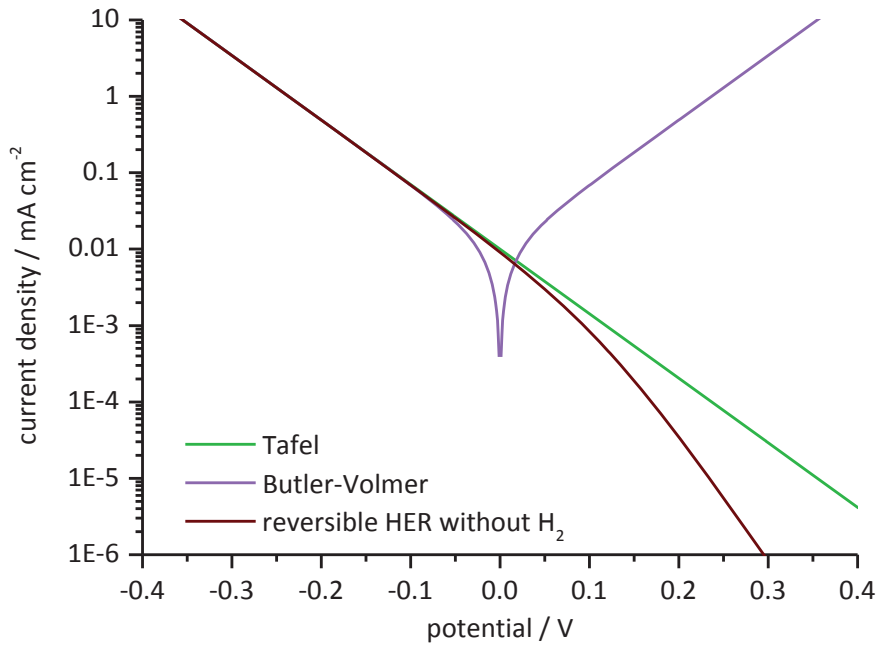
Figure 4: Current densities of for the HER calculated by the Tafel equation (1.52), the Butler-Volmer equation (1.53) and the reversible HER without H_2 (1.59) (input parameter: $E_{eq} = 0$ V; $T = 298.15$ K; $\alpha = 0.5$; $i_{eq} = i_f^0 = 0.01$ mA cm^{-2}; $n = 1$; $\frac{k_b^0}{v_{Lang}} = 0.1$)

Another interesting fact is the influence of the diffusion on the hydrogen evolution as has been reported by Kandler et al. [51] and was also found by other authors [52-55]. According to J. O'M. Bockris [39] the HER is diffusion controlled at Pt, Rh or Pd under some conditions. The effect of the diffusion on the hydrogen evolution (1.62) can be calculated according to Kandler et al. [51] by the combination of the steady state current from the first Fick's law (1.60) with the Nernst equation (1.61). Equation (1.62) gives the influence of the hydrogen diffusion on the potential between a platinum electrode and a hydrogen reference electrode.

$$j_{H_2} = \frac{D}{\delta_N} \cdot \left(c_{B,H_2} - c_{S,H_2} \right) \tag{1.60}$$

$$E = -0.029 \cdot \log \frac{c_{S,H_2}}{c_{RE,H_2}} \tag{1.61}$$

$$E = -0.029 \cdot \log \frac{c_{B,H_2} - \frac{j_{H_2} \cdot \delta_N}{D}}{c_{RE,H_2}} \tag{1.62}$$

Since the use of a hydrogen reference electrode is very uncommon today this approach can be more generalized using the Nernst equation (1.63).

$$E_{eq} = E^0 + \frac{R_g \cdot T}{n \cdot F} \cdot \ln\left(a_{S,H^+}^2\right) - \frac{R_g \cdot T}{n \cdot F} \cdot \ln\left(c_{B,H_2} - \frac{j_{H_2} \cdot \delta_N}{D} \right) \tag{1.63}$$

The current density of such a diffusion controlled reaction can be calculated using the rate constant from equation (1.57).

$$i = -n \cdot F \cdot k^0 \cdot \left(c_{\mathrm{B,H_2}} - \frac{j_{\mathrm{H_2}} \cdot \delta_{\mathrm{N}}}{D} \right) \cdot \exp\left[\frac{(1-\alpha) \cdot n \cdot F}{R_{\mathrm{g}} \cdot T} \cdot E \right] \tag{1.64}$$

1.5 OXYGEN REDUCTION

The pH dependency of the oxygen reduction reaction (ORR) is determined by equilibrium {1.15} in acidic electrolytes and by equilibrium {1.16} in alkaline electrolytes.

$$O_2 + 4\,H^+ + 4\,e^- \rightleftharpoons 2\,H_2O \tag{1.15}$$

$$O_2 + 2\,H_2O + 4\,e^- \rightleftharpoons 4\,OH^- \tag{1.16}$$

Wroblowa [56] published the mechanism of the oxygen reduction reaction (ORR) shown in Figure 5.

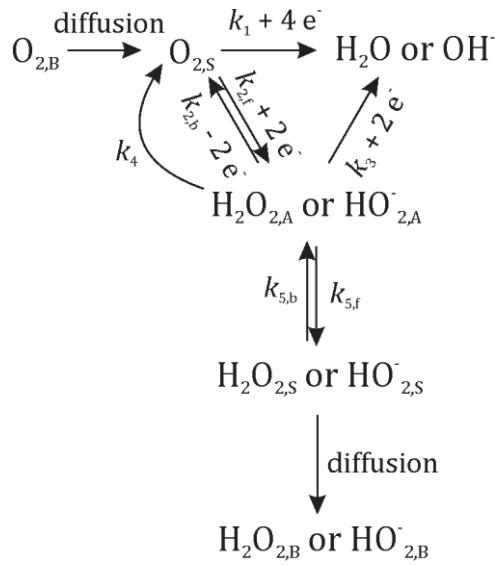Figure 5: Mechanism of the ORR by Wroblowa [56]

The indices of the rate constants k represent the following reactions:

1. Irreversible 4 e⁻ reduction of oxygen to water
2. Reversible 2 e⁻ reduction of oxygen to hydrogen peroxide
3. Consecutive, irreversible 2 e⁻ reduction to hydrogen peroxide
4. Catalytic decomposition of hydrogen peroxide to oxygen
5. Desorption of hydrogen peroxide from the electrode; $H_2O_{2,S}$ remains in the vicinity of the electrode surface

Further two diffusion controlled steps, the mass transport of oxygen to the electrode surface and the transport of hydrogen peroxide from the surface into the bulk electrolyte have to be considered. Depending on the pH in the vicinity of the catalyst, the ORR consumes H^+-Ions or forms OH^- increasing the pH.

To calculate the current of a reaction limited by mass transport such as the ORR the limiting current density has to be included in the previous models. At high overpotential the equation (1.65), which can be transformed into equation (1.66), is sufficient. This is just another form of the Koutecký-Levich equation (1.30). The current densities for different rotation rates of a RDE can be calculated by equation (1.66) using the diffusion limiting current densities according to Levich equation (Figure 6). [57]

$$E - E_{eq} = \frac{R_g \cdot T}{\alpha \cdot n \cdot F} \cdot \ln \frac{i_0}{i_{lim}} + \frac{R_g \cdot T}{\alpha \cdot n \cdot F} \cdot \ln \left(\frac{i_{lim}}{i} - 1 \right) \tag{1.65}$$
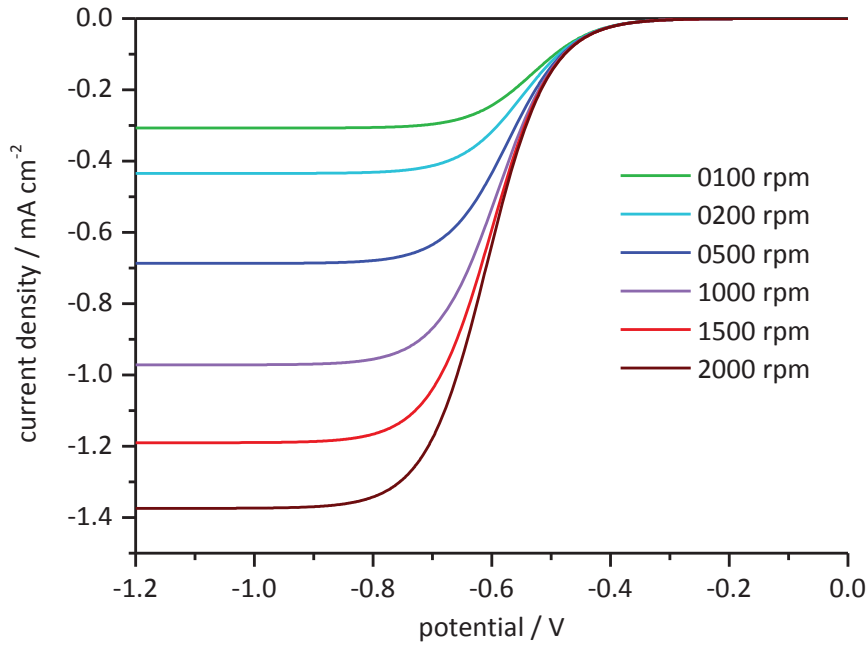

Figure 6: Current density caused by the ORR calculated by equation (1.66) (input parameter: $D = 10^{-9} \text{ m}^2 \text{ s}^{-1}$; $v = 2 \cdot 10^{-6} \text{ m}^2 \text{ s}^{-1}$; $c_B = 0.25 \text{ mol m}^{-3}$; $T = 298.15 \text{ K}$; $\alpha = 0.5$; $i_{eq} = 0.1 \text{ mA m}^{-2}$; $n_{slope} = 1$; $n_{lim} = 4$)

$$i = \frac{i_{eq} \cdot \exp \left[\frac{\alpha \cdot n \cdot F}{R_g \cdot T} \cdot \left(E - E_{eq} \right) \right]}{1 + \frac{i_{eq}}{i_{lim}} \cdot \exp \left[\frac{\alpha \cdot n \cdot F}{R_g \cdot T} \cdot \left(E - E_{eq} \right) \right]} \tag{1.66}$$

The complexity of the oxygen reduction reaction is shown in Table 1. It shows 16 possible reaction paths for the ORR. The estimated Tafel slopes for each electrochemical reaction are calculated under consideration of the previous reactions. [58]

$$-b_c = \frac{2.303 \cdot v_j}{n_c + \beta_c \cdot n_j} \cdot \frac{R_g \cdot T}{F} \tag{1.67}$$

$$-b'_c = \frac{2.303}{\sum_i Z_{IP} \cdot f_{IP} + \beta_c \cdot Z_{PQ} \cdot f_{PQ}} \cdot \frac{R_g \cdot T}{F} \tag{1.68}$$

The two Tafel slopes in Table 1 are calculated by equation (1.67) [58, 59] and (1.68) [58]. The symbols used in these two equations are not given in the symbol index.

v_j Number of times the rate determining step must occur for the overall reaction
n_c Number of electrons transferred in the rate determining step
β_c Symmetry factor of the rate determining step (assumed value $\beta_c = 0.5$)
n_j Total number of electrons transferred before rate determining step
Z Charge of a particle between two indicated states
f Fraction of the total electrical potential difference at the metal-solution interface for indicated states

Indices:

I   Initial state

P   State before highest energy barrier

Q   State after highest energy barrier

Table 1: Oxygen reaction paths and cathodic Tafel slopes [58]

Reaction Path	$-b_c$ mV dec^{-1}	$-b'_c$ mV dec^{-1}
I. Oxide Path		
$2\,M + O_2 \rightarrow 2\,MO$	-	-
$MO + MH_2O \rightarrow 2\,MOH$	-	-
$MOH + H^+ + e^- \rightarrow M + 2\,H_2O$	118	118
II. Electrochemical Oxide Path		
$2\,M + O_2 \rightarrow 2\,MO$	-	-
$MO + MH_2O + H^+ + e^- \rightarrow MOH + M + H_2O$	118	118
$MOH + H^+ + e^- \rightarrow M + H_2O$	39	39
III. Hydrogen Peroxide Path		
$M + O_2 + MH_2O \rightarrow MOH + MO_2H$	-	-
$MHO_2 + MH_2O \rightarrow MOH + MH_2O_2$	59	59
$M + MH_2O_2 \rightarrow 2\,MOH$	30	30
$MOH + H^+ + e^- \rightarrow M + H_2O$	118	118
IV. Metal Peroxide Path		
$M + O_2 + MH_2O \rightarrow MOH + MO_2H$	-	-
$M + MHO_2 \rightarrow MO + MOH$	59	59
$MO + MH_2O \rightarrow 2\,MOH$	30	30
$MOH + H^+ + e^- \rightarrow M + H_2O$	118	118
V. Electrochemical Metal Peroxide Path		
$M + O_2 + MH_2O \rightarrow MOH + MHO_2$	-	-
$MHO_2 + H^+ + e^- \rightarrow MO + H_2O$	39	39
$MO + MH_2O \rightarrow 2\,MOH$	30	30
$MOH + H^+ + e^- \rightarrow M + H_2O$	71	71
VI. Hoar Alkaline Path		
$M + O_2 + 2\,e^- \rightarrow MO_2{}^{2-}$	59	118
$M + MO_2{}^{2-} + 2\,H_2O \rightarrow 2\,MH_2O_2{}^-$	30	59
$MH_2O_2{}^- \rightarrow MOH + OH^-$	59	79
$MOH + e^- \rightarrow M + OH^-$	39	39
VII. Conway and Bourgault Path		
$O_2 + M + MH_2O \rightarrow MOH + MO_2H$	-	-
$MHO_2 + M \rightarrow MO + MOH$	59	59
$MO + H^+ + e^- \rightarrow MOH$	24	24
$MOH + H^+ + e^- \rightarrow M + H_2O$	71	71
VIII. Alternative Conway and Bourgault Path		
$M + O_2 + MH_2O \rightarrow MOH + MHO_2$	-	-
$MHO_2 + H^+ + e^- \rightarrow MO + H_2O$	39	39
$MO + H^+ + e^- \rightarrow MOH$	24	24
$MOH + H^+ + e^- \rightarrow M + H_2O$	39	39
IX. Riddiford Path		
$MH_2O + O_2 + H^+ + e^- \rightarrow MHO_2 + H_2O$	118	118
$MHO_2 + H^+ + e^- \rightarrow MO + H_2O$	39	39
$MO + MH_2O \rightarrow 2\,MOH$	30	30
$MOH + H^+ + e^- \rightarrow M + H_2O$	39	39

X. Krasilshchikov Path

Reaction		
$2\,M + O_2 \rightarrow 2\,MO$	-	-
$MO + e^- \rightarrow MO^-$	118	236
$MO^- + H^+ \rightarrow MOH$	59	79
$MOH + H^+ + e^- \rightarrow M + H_2O$	39	39

XI. Wade and Hackerman Path

Reaction		
$2\,M + O_2 + MH_2O + 2\,e^- \rightarrow 2\,MOH^- + MO$	59	118
$MO + MH_2O + 2\,e^- \rightarrow 2\,MOH^-$	20	30

XII. Damjanovic Path 1

Reaction		
$M + O_2 + H^+ + e^- \rightarrow MHO_2$	118	118
$MHO_2 + H^+ + e^- \rightarrow MO + H_2O$	39	39
$MO + H^+ + e^- \rightarrow MOH$	24	24
$MOH + H^+ + e^- \rightarrow M + H_2O$	39	39

XIII. Damjanovic Path 2

Reaction		
$2\,M + O_2 \rightarrow 2\,MO$	-	-
$MO + H_2O \rightarrow MO - H - OH$	-	-
$MO - H - OH + e^- \rightarrow MO - H - OH^-$	118	236
$MO - H - OH^- + H^+ \rightarrow MOH + H_2O$	59	79
$MOH + H^+ + e^- \rightarrow M + H_2O$	39	39

XIV. Damjanovic Path 3

Reaction		
$M + O_2 + H^+ + e^- \rightarrow MHO_2$	118	118
$MHO_2 + e^- \rightarrow MO + OH^-$	39	39
$MO + H_2O \rightarrow MO - H - OH$	30	30
$MO - H - OH + e^- \rightarrow MO - H - OH^-$	24	26
$MO - H - OH^- \rightarrow MOH + OH^-$	20	21
$MOH + H^+ + e^- \rightarrow M + H_2O$	17	17

XV. Hoare Path

Reaction		
$M + O_2 \rightarrow MO_2$	-	-
$MO_2 + e^- \rightarrow MO_2{}^-$	118	236
$MO_2{}^- + H^+ \rightarrow MO_2H$	59	79
$MHO_2H + e^- \rightarrow MHO_2^-$	39	47
$MHO_2^- + H^+ \rightarrow MH_2O_2$	30	34
$2\,H_2O_2 \xrightarrow{\text{catalytic}} H_2O + O_2$	30	30

XVI. Ives Path

Reaction		
$M + O_2 + e^- \rightarrow MO_2{}^-$	118	236
$MO_2{}^- + H^+ \rightarrow MHO_2$	59	79
$MHO_2H + e^- \rightarrow MHO_2^-$	39	47
$MHO_2^- + H^+ \rightarrow MH_2O_2$	30	34
$MH_2O_2 + e^- \rightarrow MOH + OH^-$	24	24
$MOH + e^- \rightarrow M + OH^-$	17	17

1.6 OXYGEN REDUCTION IN THE HYDROGEN ADSORPTION REGION

Several authors [60-71] found a decrease in the diffusion limited current density of the ORR with the onset of the hydrogen evolution on platinum electrodes. According to Damjanovic et al. [61] the platinum sites which are blocked by hydrogen may not be any longer accessible for the adsorption of oxygen and therefore the reaction {1.17} can take place. Since different authors [61, 63, 67, 72, 73] found also an increase in the yield of hydrogen peroxide formation during the ORR in the presence of different other adsorbents it is more likely that the breaking of the oxygen-oxygen bond requires a second platinum site.

$$2\,H_{ads} + O_2 \rightarrow H_2O_2 \qquad \{1.17\}$$

In this case the fraction of free catalyst sites $\Theta_{\text{Lang}}^{\text{free}}$ would depend on the fraction of adsorbed oxygen $\Theta_{\text{Lang}}^{O_2}$ and the fraction of catalyst sites blocked by other adsorbents $\Theta_{\text{Lang}}^{\text{ads}}$. Assuming Langmuir adsorption it can be calculated by equation (1.69).

$$\Theta_{\text{Lang}}^{\text{free}} = 1 - \Theta_{\text{Lang}}^{O_2} - \Theta_{\text{Lang}}^{\text{ads}} \qquad (1.69)$$

The reaction rate of this bond breaking mechanism $j_{O_{ads}}$ depends on the number of free surface sites on the catalyst and can be expressed by equation (1.70).

$$j_{O_{ads}} = k_{O_{ads}} \cdot \Theta_{\text{Lang}}^{O_2} \cdot \Theta_{\text{Lang}}^{\text{free}} \qquad (1.70)$$

The reaction rate of the ORR j_{ORR} is the sum of the amount of oxygen which gets reduced to hydroxide and the amount of oxygen getting reduced to peroxide and can be expressed by equation (1.71).

$$j_{\text{ORR}} = k_{OH^-} \cdot \Theta_{\text{Lang}}^{O_2} \cdot \Theta_{\text{Lang}}^{\text{free}} + k_{H_2O_2} \cdot \Theta_{\text{Lang}}^{O_2} \qquad (1.71)$$

Combining equation (1.69) with (1.71) the reaction rate of the ORR can be calculated by equation (1.72).

$$j_{\text{ORR}} = k_{OH^-} \cdot \Theta_{\text{Lang}}^{O_2} \cdot \left(1 - \Theta_{\text{Lang}}^{O_2} - \Theta_{\text{Lang}}^{\text{ads}}\right) + k_{H_2O_2} \cdot \Theta_{\text{Lang}}^{O_2} \qquad (1.72)$$

In case of the hydrogen adsorption reaction {1.18} the amount of hydrogen blocking the surface sites can be calculated by the Nernst equation (1.73) or (1.74).

$$M + H^+ + e^- \rightarrow MH_{ads} \qquad \{1.18\}$$

$$E = E_{\text{RHE}} - \frac{R_g \cdot T}{n \cdot F} \cdot \ln\left(\Theta_{\text{Lang}}^{H_{ads}}\right) \qquad (1.73)$$

$$\Theta_{\text{Lang}}^{H_{ads}} = \exp\left(-\frac{n \cdot F}{R_g \cdot T} \cdot (E - E_{\text{RHE}})\right) \qquad (1.74)$$

1.7 GAS/LIQUID SURFACE EXCHANGE KINETIC AS A LIMITING FACTOR

In the previous chapters only the heterogeneous reaction kinetics and the mass transport from the bulk solution to the catalyst surface have been considered. If the reactant comes from the atmosphere, e. g. the oxygen for corrosion, air batteries or fuel cells, the surface exchange kinetic between the atmosphere and the solution can be another limiting factor.

If the size of the catalyst surface, or in case of an electrochemical reaction the electrode, is much larger than the thickness of the electrolyte layer the flux of the educts to the surface can be described by the first Fick's law (1.26) under steady state conditions. Effects from the edges can be neglected if the area of the catalyst is large enough.
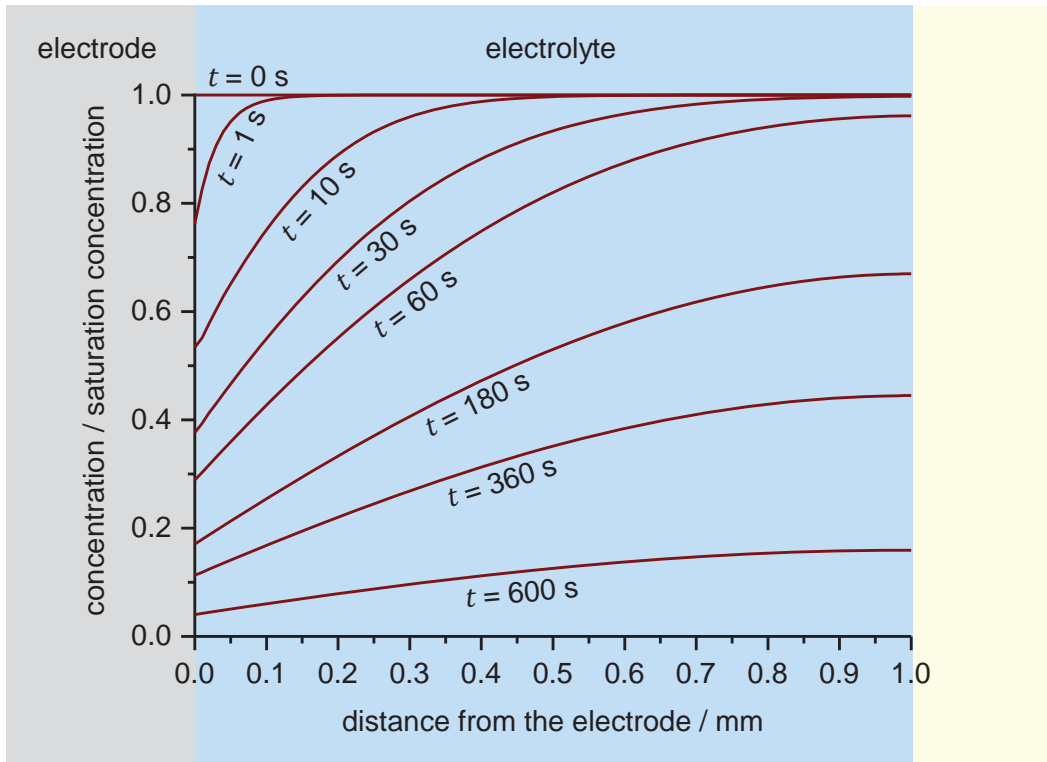
Figure 7: 1D concentration profile at different times after the reaction takes place at the electrode for an electrolyte thickness of 1 mm without gas/liquid exchange; calculated by Crank-Nicolson method [74] using the central difference (input parameters: $D = 2 \cdot 10^{-9}$ m^2 s^{-1}; $k_{kin} = 1$; $k_{sex} = 1$)

If a limited electrolyte thickness without an exchange between the gas/liquid interface is assumed equation (1.26) must be replaced by the time depending second Fick's law (1.12) since no steady state condition can be achieved (see Figure 7) and the concentration in the electrolyte drops during the reaction. In this calculation the heterogeneous catalyst, or in case of an electrochemical reaction the electrode surface, is infinite large compared to the thickness of the electrolyte layer. In this case the concentration depends only on the distance from the catalyst surface.

This surface exchange kinetic can be described by a first order reaction [75, 76] (1.75) which depends on the difference between the saturation concentration c_{sat} and the concentration at the gas/liquid interface c_{atm}.

$$j_{sex} = k_{sex} \cdot (c_{sat} - c_{atm}) \tag{1.75}$$

Under steady state conditions the reaction rate at the electrode, the diffusion from the gas/liquid interface to the electrode and the surface exchange between the atmosphere and the electrolyte must be equal (1.76). How long it will take until steady state conditions are reached depends on the thickness of the electrolyte. In Figure 8 it takes more than 10 minutes to reach steady state conditions but the surface exchange takes place after just 30 seconds.

$$j = k_{kin} \cdot c_S = D \cdot \frac{c_{atm} - c_S}{\delta_N} = k_{sex} \cdot (c_{sat} - c_{atm}) \tag{1.76}$$

The steady state educt concentration at the gas/liquid interface can be expressed by equation (1.77).

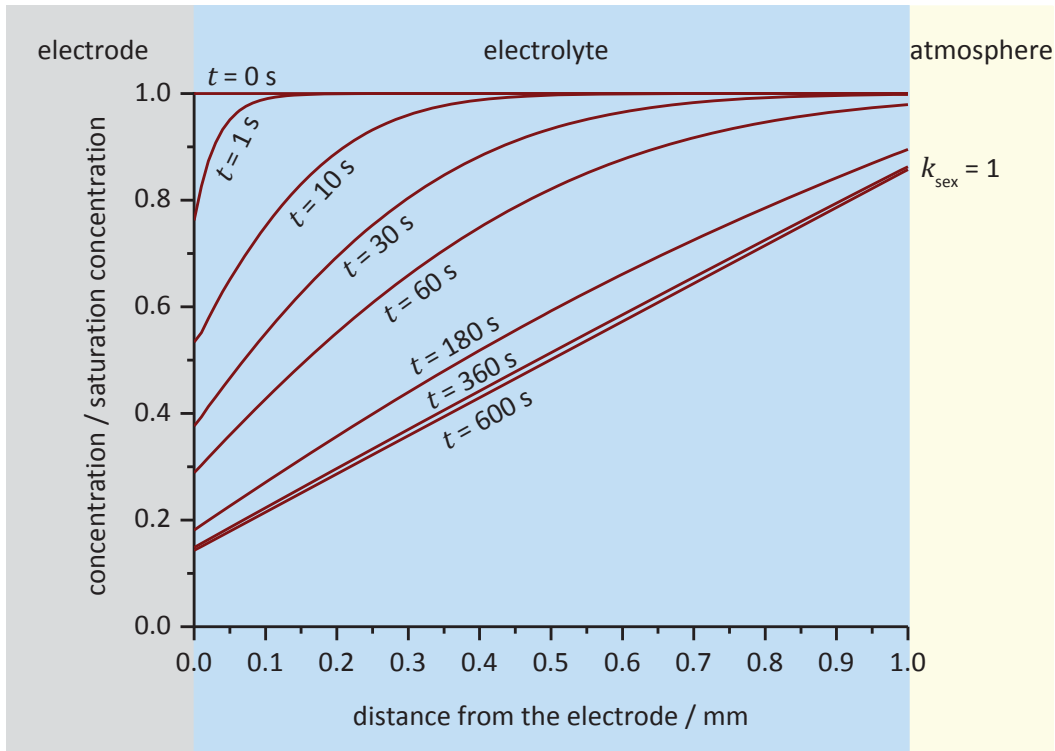$$c_{atm} = \frac{j \cdot \delta_N}{D} + c_S \tag{1.77}$$

Figure 8: 1D concentration profile at different times after the reaction takes place at the electrode for an electrolyte thickness of 1 mm with gas/liquid exchange; calculated by Crank-Nicolson method [74] using the central difference (input parameters: $D = 2 \cdot 10^{-9}$ m^2 s^{-1}; $k_{kin} = 1$; $k_{sex} = 1$)

The combination of equation (1.75) and (1.77) leads to (1.78).

$$(c_{sat} - c_S) = j \cdot \left(\frac{1}{k_{sex}} + \frac{\delta_N}{D} \right) \tag{1.78}$$

The limiting currents can be expressed by equation (1.79) and (1.80) so that (1.78) can also be written as (1.81).

$$j_{sex,lim} = k_{sex} \cdot c_{sat} \tag{1.79}$$

$$j_{diff,lim} = D \cdot \frac{c_{sat}}{\delta_N} \tag{1.80}$$

$$\frac{c_S}{c_{sat}} = 1 - j \cdot \left(\frac{1}{j_{sex,lim}} + \frac{1}{j_{diff,lim}} \right) \tag{1.81}$$

The substitution of the electrode concentration in equation (1.81) with the flux divided by the kinetic reaction rate constant leads to equation (1.82) which is similar to the Koutecký-Levich equation (1.30).

$$\frac{j}{k_{kin} \cdot c_{sat}} = 1 - j \cdot \left(\frac{1}{j_{sex,lim}} + \frac{1}{j_{diff,lim}} \right) \tag{1.82}$$

$$\frac{1}{j} = \frac{1}{k_{kin} \cdot c_{sat}} + \frac{1}{j_{sex,lim}} + \frac{1}{j_{diff,lim}} \tag{1.83}$$
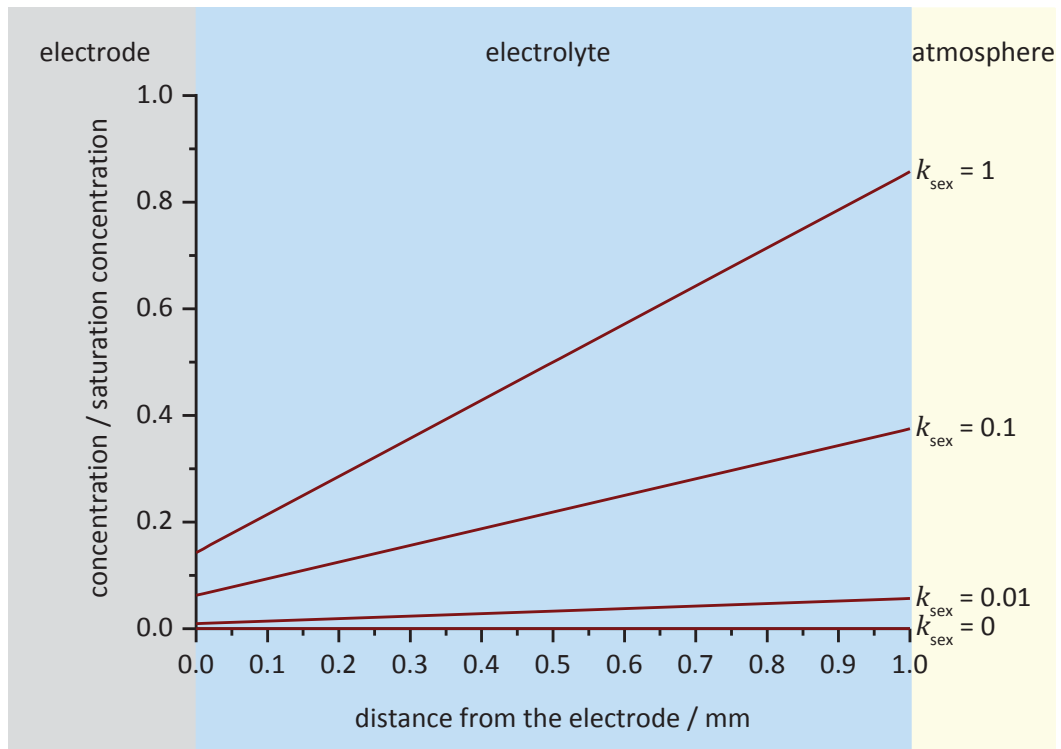
Figure 9: 1D concentration profile after the reaction takes place at the electrode for an electrolyte thickness of 1 mm with different gas/liquid exchange rates after 1 hour; calculated by Crank-Nicolson method [74] using the central difference (input parameters: : $D = 2 \cdot 10^{-9}$ m^2 s^{-1}; $k_{kin} = 1$; $k_{sex} = 1$)

Figure 9 shows the concentration profile after one hour in a 1 mm thick electrolyte layer with different surface exchange rates of the educt at the gas/liquid interface.

ELECTROCHEMISTRY OF PLATINUM

2.1 EQUILIBRIUM POTENTIALS

The most stable oxidation states of platinum are two and four but others exist as well. It is possible to produce monovalent platinum although it is very instable [77]. Hexavalent platinum was produced by L. Wöhler [78] under anodic oxygen evolution as PtO_3. The trivalent platinum is easily oxidized to an oxidation number of four and it can disproportionate into a platinum ion with oxidation state two and another one with oxidation state four [77].

The expected standard potential of equilibrium {2.1} (+1.23 V vs. SHE) can only be found when the platinum is oxidized. It was first reported by K. Bornemann [79] in 1909 on platinum pretreated by hydrogen peroxide.

$$O_2 + 4\,H^+ + 4\,e^- \rightleftharpoons 2\,H_2O \hspace{4cm} \{2.1\}$$
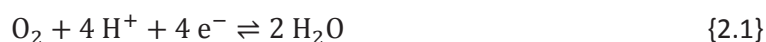
Anodized platinum has an open circuit potential of +1.00 V vs. SCE in 1 M sulfuric acid and of +0.22 vs. SCE in 1 M sodium hydroxide in a 1 atm oxygen atmosphere at 25°C [80]. Both potentials are close to the potential of the reversible oxygen electrode.

Platinum without pre-oxidation shows open circuit potentials more negative than the reversible oxygen potential [80-84]. These measured potentials are close to the reversible Pt/PtO potential [80]. The oxide film on platinum at the reversible oxygen potential was quantified by dissolution of PtO and PtO_2 in hydrochloric acid [85]. By spectroscopic measurements of the corresponding H_2PtCl_4 and H_2PtCl_6 a ratio of $PtO/PtO_2=6/1$ was found [85]. Under open circuit conditions in oxygen saturated sulfuric acid only 30 % of the platinum surface is covered by atomic oxygen [86, 87]. The surface coverage can be increased by adding nitric acid to form a complete oxide monolayer [86, 87]. During anodic polarization in sulfuric acid the oxygen chemisorption reaches a maximum at +2.3 V vs. SHE and a PtO_2-monolayer is formed [88, 89]. The oxygen adsorption at rhodium and iridium is four times higher than at platinum and palladium [90, 91].

The OCP change is -60 mV pH^{-1} [82, 90-93] and +30 mV per decade oxygen concentration [82, 91, 94-97] according to the Nernst equation (1.50). At very low pH-values (<1.5) [90, 91, 97, 98] and at pH 11.7 [99] this slope increases to +60 mV per decade oxygen concentration. The influence of hydrogen peroxide on the OCP is uncertain [82, 100]. Grube reported a shift of the OCP to lower potentials by increasing the peroxide concentration [84] but other authors [92, 101] found no influence. Below 10^{-3} M it was found that the potential shifts -30 mV per decade peroxide concentration but it remains stable at higher concentrations [94, 96]. A platinum electrode under hydrogen atmosphere usually shows the expected reversible H_3O^+/H_2 potential and therefore a slope of -30 mV per decade hydrogen pressure [97].

For the double layers between platinum and different electrolytes, capacities of 200 µF cm^{-2} in 0.5 M sulfuric acid, 300 µF cm^{-2} in pH 6.8 buffered solution (0.2 M KH_2PO_4 + 0.2M Na_2HPO_4) and 500 µF cm^{-2} in 1 M sodium hydroxide have been reported [102]. Other authors [103] found, depending on the potential of the platinum electrode, values between 16 and 33 µF cm^{-2} in sulfuric acid and between 10 and 60 µF cm^{-2} in neutral electrolytes.

Izaak M. Kolthoff [104] measured current-voltage curves using a platinum wire electrode in oxygen free electrolytes with different pH-values between 1 and 13. Cathodic polarized platinum shows prior to the oxygen evolution a small anodic current step due to the formation of a platinum oxide film in 0.1 M deaerated perchlor acid [85, 102, 105-107]. Anodically prepolarized electrodes have a cathodic current wave with a starting potential of +0.67 V vs. SCE in 0.1 M $HClO_4$ respectively -0.03 V vs. SCE in 0.1 M NaOH [104]. Both electrodes show similar potentials, depending on the pH, for the HER and the ORR [104]. The onset of the hydrogen evolution is at a potential of -0.2 V vs. SCE in 0.1 M $HClO_4$ and -0.9 V vs. SCE in 0.1 M NaOH [104]. The oxygen evolution on the other hand starts at +1.2 V vs. SCE in 0.1 M $HClO_4$ and at +0.5 V vs. SCE in 0.1 M NaOH [104]. In perchloric acid the anodic current of the platinum dissolution overlaps with the cathodic ORR above 1.0 V vs. SHE [108].
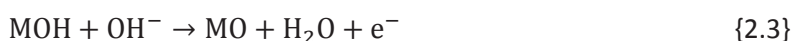
2.2 ANODIC REACTIONS IN WATER

2.2.1 OXYGEN EVOLUTION

In water the oxygen evolution limits the usable potential range in the anodic direction. It starts at +0.87 V vs. SCE in acidic solution, at +0.50 V vs. SCE in neutral solution and at +0.06 V vs. SCE in alkaline solution [102].
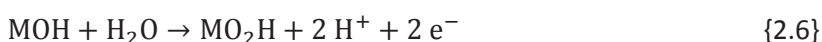
J. O'M. Bockris [109] postulated reaction {2.2} as the rate determining step for the oxygen evolution on platinum anodes in sulfuric acid. The experiments showed only a stoichiometric number of 3.7 instead of the expected four electrons [109].

The oxygen evolution path postulated by Bockris [109] is:

$$M + OH^- \rightarrow MOH + e^- \qquad \{2.2\}$$

$$MOH + OH^- \rightarrow MO + H_2O + e^- \qquad \{2.3\}$$

$$2\,MO \rightarrow O_2 + 2\,M \qquad \{2.4\}$$

Using chronopotentiometry and chronoamperometry at a platinum electrode in different concentrations of perchloric acid a different mechanism for the oxygen evolution was found on bare platinum and on oxide covered Pt (equation {2.5} to {2.7}) [110].

The oxygen evolution path postulated by Laitinen [110] is:

$$M + H_2O \rightleftharpoons MOH + H^+ + e^- \qquad \{2.5\}$$

$$MOH + H_2O \rightarrow MO_2H + 2\,H^+ + 2\,e^- \qquad \{2.6\}$$

$$MO_2H \rightarrow M + O_2 + H^+ + e^- \qquad \{2.7\}$$

The currents of the anodic oxygen evolution and cathodic oxygen reduction show an intercept at +1.23 V vs. SHE in 1 M $HClO_4$ [59] and sulfuric acid [98, 109] shows an exchange current density of $4 \cdot 10^{-10}$ A cm^{-2} at +1.23 V vs. RHE [59]. The stoichiometric number of 3.5 electrons in perchloric acid [59] is lower than the value of 3.7 measured in sulfuric acid [109].
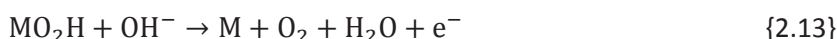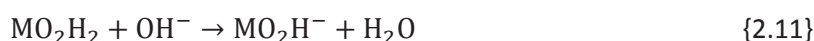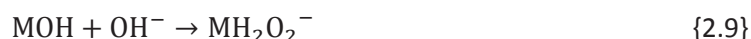
In 1 M KOH the stoichiometric number of electrons is 1.8 [59]. The intercept of the extrapolated anodic and cathodic Tafel lines is 50 mV more positive than for acidic condition and the exchange current density is $1 \cdot 10^{-11}$ A cm^{-2} at +1.23 V vs. RHE [59]. Tafel slopes of 55 mV dec^{-1} for current densities below 10^{-5} A cm^{-2} (1.6 V vs. RHE) and 110 mV dec^{-1} above 10^{-5} A cm^{-2} have been found for

the oxygen evolution [59]. Scarr [111] published a Tafel slope of 47 mV dec^{-1} between 10^{-6} A cm^{-2} and 10^{-4} A cm^{-2}.

The first charge-transfer steps of path I, III or IV given in Table 1 are supposed to be the rate determining step of the oxygen evolution in acidic electrolytes [59]. Under alkaline condition the second steps of path VI, X or XIII in Table 1 are assumed to be rate determining for the first part of the oxygen evolution [59]. At higher overpotentials the first discharge of path VI can be rate determining or the first or third step of path X or XIII [59]. An additional mechanism for the oxygen evolution was proposed by Scarr [111] for alkaline solutions.

The oxygen evolution path according to Scarr [111] is:

$$M + OH^- \rightarrow MOH + e^- \qquad\qquad \{2.8\}$$

$$MOH + OH^- \rightarrow MH_2O_2{}^- \qquad\qquad \{2.9\}$$

$$MH_2O_2{}^- \rightarrow MO_2H_2 + e^- \qquad\qquad \{2.10\}$$

$$MO_2H_2 + OH^- \rightarrow MO_2H^- + H_2O \qquad\qquad \{2.11\}$$

$$MO_2H^- \rightarrow MO_2H + e^- \qquad\qquad \{2.12\}$$

$$MO_2H + OH^- \rightarrow M + O_2 + H_2O + e^- \qquad\qquad \{2.13\}$$

2.2.2 OXIDATION OF HYDROGEN PEROXIDE

Hydrogen peroxide can be a stable product of the oxygen reduction as well as of the water oxidation.

Its acid dissociation constant is 11.62 at 25 °C [1].

Peroxide oxidation path by Berl under alkaline conditions [112]:

$$HO_2{}^- + OH^- \rightarrow O_2 + H_2O + 2\,e^- \qquad\qquad \{2.14\}$$
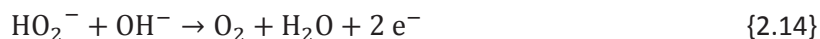
A. Hickling [113] investigated the oxidation of hydrogen peroxide on different electrode materials in 1 M KOH, 0.2 M KH$_2$PO$_4$ + 0.2M Na$_2$HPO$_4$ and 0.5 M sulfuric acid solution containing 0.01 to 0.5 M H$_2$O$_2$. The onset of the anodic decomposition of peroxide under alkaline conditions is at +0.09 V vs. SCE on platinum [113] (+0.06 V vs. SCE gold and at +0.16 V vs. SCE on nickel). The oxidation of hydrogen peroxide on platinum starts at +0.49 V vs. SCE in neutral solution and at +0.84 V vs. SCE under acidic conditions [113]. Gold and nickel showed only small irreproducible currents in neutral or acidic solution [113]. The experimental results in alkaline solutions are in good agreement with the previous mechanism postulated by W. G. Berl [113].

The peroxide oxidation on platinum starts in the same potential range in which the platinum forms its oxide film [85, 113]. With the onset of the oxygen evolution, platinum becomes passive for the hydrogen peroxide oxidation [100]. The reason might be the formation of an oxide layer. The charge transfer coefficient for the peroxide oxidation is 0.69 [100].

The peroxide oxidation path postulated by Hickling [113] is:

$$M + 2\,OH^- \rightleftharpoons MO + H_2O + 2\,e^- \qquad\qquad \{2.15\}$$

$$MO + H_2O_2 \rightleftharpoons M + O_2 + H_2O \qquad\qquad \{2.16\}$$
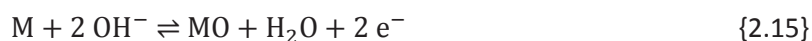
J. O'M. Bockris and L. F. Oldfield [92] studied the reduction and oxidation of hydrogen peroxide in a pH range between 0 and 13.5 at different electrodes with concentrations between 5 M and 10^{-6} M.

The potential of bright platinum was +0.84 V vs. SHE at pH 0 with a slope of -59 mV pH^{-1} and independent of the peroxide concentration [92] but the influence of the hydrogen peroxide concentration on the OCP is inconsistent in literature. Slopes of -60 mV dec^{-1} in perchloric acid [114] and -30 mV dec^{-1} in 1 M KOH [96] were found, while Gerischer [100] found an influence of the hydrogen peroxide concentration on the rest potential only in alkaline electrolytes. In 1 M KOH solutions a decrease of the slope at concentrations above 10^{-4} M hydrogen peroxide has been reported by Urbach and Bowen [96]. The results for oxygen are similar ambiguous and range from no influence [92] to +30 mV per decade oxygen partial pressure [96].
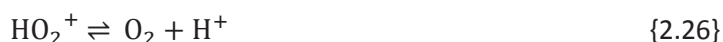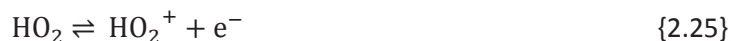
The peroxide oxidation path given by Bockris [92] is:

$$H_2O_2 \; \rightarrow \; HO_2 + H^+ + \; e^- \qquad \{2.17\}$$

$$HO_2 \rightarrow \; O_2 + H^+ + \; e^- \qquad \{2.18\}$$

The peroxide oxidation path postulated by Winkelmann [82] is:

$$H_2O_2 \rightleftharpoons \; H_2O_2{}^+ + e^- \qquad \{2.19\}$$

$$H_2O_2{}^+ \rightleftharpoons HO_2 + H^+ \qquad \{2.20\}$$

$$HO_2 \rightleftharpoons O_2^- + H^+ \qquad \{2.21\}$$

$$O_2{}^- \rightleftharpoons O_2 + e^- \qquad \{2.22\}$$

or

$$H_2O_2 \rightleftharpoons HO_2{}^- + H^+ \qquad \{2.23\}$$

$$HO_2{}^- \rightleftharpoons HO_2 + e^- \qquad \{2.24\}$$

$$HO_2 \rightleftharpoons HO_2{}^+ + e^- \qquad \{2.25\}$$
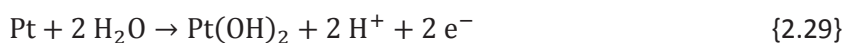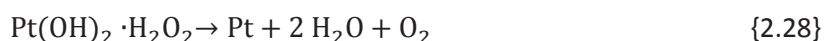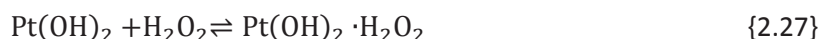
$$HO_2{}^+ \rightleftharpoons \; O_2 + H^+ \qquad \{2.26\}$$

A further extensive study of the electrochemical oxidation of hydrogen peroxide at platinum electrodes was carried out by Simon B. Hall [115-119]. The reaction was studied in a 0.1 M phosphate buffered solution with pH 7.26 containing up to 80 mM hydrogen peroxide. By using chronoamperometric measurements at a platinum RDE a linear relation between the current and the concentration of peroxide was found. The slope of this relation depends on rotation speed and is 0.6 mA cm^{-2} mM^{-1} at 630 rpm and 1.75 mA cm^{-2} mM^{-1} at 10000 rpm. This indicates a diffusion controlled reaction. The diffusion coefficients analyzed by the Koutecký-Levich equation depend on the peroxide concentration with a minimum of 0.6·10^{-9} m^2 s^{-1} at the lowest and highest concentration and a maximum of 1.40·10^{-9} m^2 s^{-1} at 0.03 M peroxide. A Michaelis-Menten mechanism according to reaction {2.27} to {2.29} was developed by Hall. [115]

The peroxide oxidation path postulated by Hall [115] is:

$$Pt(OH)_2 + H_2O_2 \rightleftharpoons Pt(OH)_2 \cdot H_2O_2 \qquad \{2.27\}$$

$$Pt(OH)_2 \cdot H_2O_2 \rightarrow Pt + 2\,H_2O + O_2 \qquad \{2.28\}$$

$$Pt + 2\,H_2O \rightarrow Pt(OH)_2 + 2\,H^+ + 2\,e^- \qquad \{2.29\}$$

At low anodic potentials the reduced binding sites of pure Pt dominate. The coverage of Pt(OH)$_2$ or Pt(OH)$_2$·H$_2$O$_2$ increases rapidly up to +0.33 V vs. sat. Ag/AgCl and remains almost constant for higher potentials. The reduced binding sites decrease with an increase of the potential. The amount of the

coverage inhibiting species $Pt(OH)_2 \cdot O_2$ and $Pt(OH)_2 \cdot H_2O_2 \cdot H^+$ show a constant increase with potential. In this work low diffusion coefficients of $0.55 \cdot 10^{-9}$ m^2 s^{-1} were obtained. [116]

At +0.60 V vs. sat. Ag/AgCl a change in the rate of reaction {2.29} appears due to a faster reoxidation of the Pt surface at higher potentials. Higher temperatures increase the rate of reaction {2.28}. A precursor site Pt_{PS} which is in equilibrium with $Pt(OH)_2$ was introduced. The equilibrium constant of $Pt_{PS}/Pt(OH)_2$ depends on the potential. [116, 117] The increase of the $H_2PO_4^-$ buffer concentration increases the rate of the peroxide oxidation. [118]

Chloride concentrations up to 115 mM inhibit the hydrogen peroxide oxidation. Two inhibition mechanisms were proposed. On the one hand the chloride can block the binding sites and on the other hand the chloride can interact with the precursor sites and thereby hinder the formation of the binding sites. [119]

2.2.3 HYDROGEN OXIDATION

At negative potentials hydrogen can be produced at the disc electrode and can influence the current at the ring electrode.

Hydrogen gas reduces the surface oxide of platinum [120].

In voltammetric measurements the anodic scan of platinized platinum shows three peaks in the presence of hydrogen in acidic, neutral and basic solution. Two of these peaks were identified as the oxidation of two different forms of adsorbed hydrogen, while the third at more positive potentials is the oxidation of the absorbed hydrogen. [121]

The crystal orientation of platinum influences the rate and the mechanism of the hydrogen oxidation reaction in 0.05 M H_2SO_4. At Pt(110) this reaction follows a Tafel-Volmer mechanism (28 mV dec^{-1}) with the atom-atom recombination as rate determining step. Pt(100) shows Tafel slopes of 37 mV dec^{-1} at low current density and 112 mV dec^{-1} at higher current densities indicating a Heyrovský-Volmer mechanism. The Tafel slope of 74 mV dec^{-1} found for Pt(111) could not be interpreted unambiguously. [122]

Using DFT a Tafel-Volmer mechanism was proposed for Pt(111) [123].

2.3 CATHODIC REACTIONS IN WATER

2.3.1 OXYGEN REDUCTION

This chapter summarizes the different parameters influencing the oxygen reduction reaction (ORR). More details about the mechanism of the oxygen reduction can be found in chapter 1.5.

2.3.1.1 SURFACE CONDITIONS

Different treated Pt surfaces have been compared in acidic (HClO$_4$, pH1-3) and alkaline (NaOH, pH13) solutions [124]. The electrodes were prepared chemically with concentrated HCl, by an anodic pulse at 1.7 V vs. SHE or thermally in H_2-atmosphere. All pretreated electrodes showed Tafel slopes of -60 mV dec^{-1} for the ORR [124]. The experimental results for chemically and thermally pretreated platinum almost overlap, while the anodic treatment increased the activity due to an increase of the

surface area [124]. A similar higher activity of the oxygen reduction has been found after treating platinum with concentrated nitric acid [125].

Organic impurities in the electrolyte increase the amount of peroxide formed during ORR [61, 72] or may hinder the ORR [126]. The same effect can be caused by inorganic adsorbents like Tl, Bi or Pb [63]. Adsorbed Br⁻ increases the amount of hydrogen peroxide by suppressing the adsorption of oxygen and reducing the pairs of platinum sites which are required for the oxygen dissociation [73]. The same effect was found with Cl⁻ [67]. Perchlorate decreases the kinetic of the ORR [127].

The half-wave potentials are depending on the acids (half wave potentials: $HClO_4$>H_2SO_4>HCl>HBr) [60]. Potassium iodide shifts the half-wave potential on pre-reduced platinum to more negative values due to the formation of PtI_2 [128]. In the presence of potassium cyanide no oxygen wave appeared on the platinum electrodes [128].

2.3.1.2 TEMPERATURE

According to Appleby the Tafel slopes of the ORR in 85 % orthophosphoric acid increase with temperature from 62 mV dec^{-1} at 25.1 °C to 82 mV dec^{-1} at 136.1 °C [129] at oxide-free platinum electrodes while Huang et al. [130] obtained Tafel slopes of 120 to 125 mV dec^{-1} in a temperature range between 25 °C and 150 °C on reduced platinum. The exchange current density increases from $3.8 \cdot 10^{-13}$ A cm^{-2} at 25.1 °C by a factor of 10^4 when the temperature is increased to 136.1°C [129].

Park et al. used a RDE to investigate the ORR in potassium hydroxide concentrations between 0.11 M and 6.0 M. The exchange current density and the Tafel slope depend also in alkaline electrolytes on the temperature. The Tafel slopes increased 10 mV dec^{-1} by increasing the temperature from 25 °C to 66 °C. The logarithm of the exchange current density showed a linear relation with the reciprocal of the temperature. [131]

With exception of the results of Huang et al. [130] the reported Tafel slopes show a linear relationship with the temperature with a slope of $2.3 \cdot R \cdot F^{-1}$. [129, 131, 132]

A linear relationship between the logarithmic exchange current density and the reciprocal of the temperature was found by several authors. [66, 133-135]

2.3.1.3 pH INFLUENCE

The influence of the pH on the oxygen reduction found in literature is inconsistent.

H. A. Laitinen and I. M. Kolthoff [136, 137] measured the current at a stationary and rotating platinum wire microelectrode in air saturated electrolyte. The variation of the pH showed no influence on the ORR and they wrote [136]: *"It is striking that, although the electrode reaction involves hydrogen ions, there is no pronounced pH effect on the potential at which oxygen reduction begins or on the shape of the current-voltage curve."*

Donald T. Sawyer [128, 138] found also no influence of the pH-values of 2 and 12 at pre-reduced platinum but the half-wave potentials of pre-oxidized electrodes showed a shift from +0.30 V at pH 2 to -0.32 V vs. SCE at pH 13. J. J. Lingane measured a shift of the beginning of the cathodic oxygen reduction wave from +0.40 V vs. SCE at pH 0 to -0.32 V vs. SCE at pH 14 on anodized platinum [80]. These potentials are 0.1 V more positive for pre-reduced electrodes [80]. In acidic electrolytes

changes in the OCP of -59 mV pH^{-1} [91], -100 mV pH^{-1} [108, 124] or -90 mV to -120 mV pH^{-1} [93] have been measured. Winkelmann [82] found a change in the OCP of -60 mV pH^{-1} for the whole pH range.

In 0.1 M borate buffered solutions (pH 8 and 10) potential shifts of -60 mV pH^{-1} for low current densities and -300 to -400 mV pH^{-1} for high current densities have been found [62] while in alkaline electrolytes (pH>10) these slopes were between -26 and -33 mV pH^{-1} [59, 99, 124].

2.3.1.4 Hydrogen peroxide formation

Hydrogen peroxide can be a stable product of the ORR but the Pt surface condition has a high influence on its formation [82]. It was produced by applying 100 μA between two large platinum electrodes separated by an agar gel [136]. In 0.1 M K_2SO_4 between 5.9 % and 10.0 % of the current is consumed by forming hydrogen peroxide at pre-oxidized Pt while this amount can be increased to 50 % using pre-reduced platinum [128]. Adsorbed organic impurities [61, 72] or inorganic adsorbates [63, 73, 128] on the Pt surface also increase the formation of peroxide.

According to the PhD thesis of M. A. Genshaw about 20 % of the total current was consumed by the production of peroxide in alkaline solution but Damjanovic and Brusic found no evidence for its formation in acidic or alkaline electrolytes even by applying 0.3 mA cm^{-2} between two platinum electrodes for 24 h [124]. More evidence for the formation of peroxide as an intermediate or a product of the ORR in alkaline solution has been also found by other authors [70, 131] while oxygen is almost completely reduced to water [98, 139] in acidic electrolytes. The formation of hydrogen peroxide in alakline solutions was explained by a second path parallel to the ORR [140].

Müller and Nekrassow found peroxide in acidic and alkaline electrolytes during the ORR in combination with the hydrogen evolution [60]. Further details about this effect can be found in the next chapter.

2.3.1.5 RRDE experiments

A rotating disc electrode (RDE) provides a well-defined diffusion profile with an increased mass transport of the oxygen. Intermediates formed at this electrode can be detected by a ring electrode placed around the disc.

With such a rotating ring disc electrode (RRDE) Müller and Nekrassow measured a distinct diffusion limiting current due to the complete 4 e^{-} reduction of oxygen in acidic and alkaline electrolytes [60]. In the hydrogen adsorption potential range and with the onset of the hydrogen evolution this limiting current decreases and the simultaneous appearance of a ring current indicated the formation of hydrogen peroxide [60]. Müller and Nekrassow explained this effect by the reduction of the catalytic activity of the platinum surface for the hydrogen reduction due to the reduction of the surface oxides [60].

The same decrease of the diffusion limiting current in the hydrogen adsorption region of Pt was also observed in sulfuric acid in a potential range between +0.2 V to 0 V vs. SHE [61]. In this potential range the charge associated with the amount of adsorbed hydrogen is 180 μC cm^{-2} [141]. The same decrease in the diffusion limited current density due to the hydrogen adsorption was found by many other authors [62-71].

Using rotating electrodes several authors found two Tafel slopes for the ORR at platinum in the range of -60 mV dec^{-1} at low current densities and -120 mV dec^{-1} at high current densities in acidic [64-66, 93, 132, 133, 135, 142-144], neutral [62, 93] and alkaline [62, 93, 99, 131, 134, 140, 145, 146] electrolytes. The change in the Tafel slope was explained by a change from Temkin adsorption at high potentials to Langmuir conditions at low potentials [93, 108, 133, 134, 140, 147, 148].

These two Tafel slopes have the same enthalpies of activation and therefore the change in the slopes does not arise from a change in the mechanism or the reaction products [133, 134]. These enthalpies are also independent of the pH [135].

2.3.1.6 SINGLE CRYSTALS

Damjanovic and Brusic [124] found no influence of the different crystal planes of platinum in perchloric acid. This was confirmed by El Kadiri et al. [142] but they also found that the ORR is structure sensitive in sulfuric acid, phosphoric acid and hydrochloric acid. Markovic et al. [64] found the highest activity for the complete ORR at Pt(110) while Pt(100) showed the slowest reaction rate in perchloric acid. Zinola et al. [143] concluded that the blockage by sulfate is favored on Pt(111) whereas peroxide is responsible for the low activity at Pt(100).

In combination with the HER the partial reduction of oxygen to H_2O_2 depends on the crystal orientation of the surface and is 100 % H_2O_2 at Pt(100) [65].

The activation energy was found to be independent of crystallographic orientation of the surface [66].

2.3.1.7 THEORETICAL APPROACH

Using an electron-correlation method Anderson and Albu predicted the following, lowest energy reaction path for the ORR [149]:

$$PtO_2 + H^+ + e^- \rightleftharpoons PtOOH \qquad \{2.30\}$$

$$PtOOH + H^+ + e^- \rightleftharpoons PtOHOH \qquad \{2.31\}$$

$$PtOHOH + H^+ + e^- \rightleftharpoons PtOH + H_2O \qquad \{2.32\}$$

$$PtOH + H^+ + e^- \rightleftharpoons PtH_2O \qquad \{2.33\}$$

It is possible to replace reaction {2.31} with reaction {2.34}, but the reduction of PtO requires a high activation energy [149].

$$PtOOH + H^+ + e^- \rightleftharpoons PtO + H_2O \qquad \{2.34\}$$

Panchenko et al. calculated the properties of oxygen and the intermediates OH, HO_2 and H_2O_2 on different Pt-surfaces using DFT-GGA (density functional theory with generalized gradient approximation). Oxygen atoms prefer the adsorption as a bridge between two Pt atoms on Pt(111) but it can also adsorb on a hollow between three surface Pt atoms. On Pt(100) and Pt(110) oxygen adsorbs mainly at bridge positions.

Hydroxyl adsorbs preferentially on one Pt-atom or in a bridge structure and shows the weakest adsorption on Pt(100). HO_2 adsorbs only in a bridge structure on Pt(111). H_2O_2 is unstable and dissociates into two adsorbed hydroxyls or water and atomic oxygen. [150]

Calculations by DFT-B3LYP (density functional theory with B3LYP hybrid approxiamtion) showed that the first electron transfer is rate determining and since the O_2^- has a high proton affinity the proton transfer is expected to be immediately after the rate determining step [151]. A possible source for the protons can be dissociated water on the surface [152]. The adsorbed OOH has a moderate potential-independent dissociation barrier which depends on the local surface environment [152].

2.3.1.8 TAFEL SLOPES

Table 2 shows the Tafel slopes found in literature. It contains the first slope of the ORR at low current densities and, since some authors reported a change in the kinetics, the second slope at higher current densities.

Table 2: Tafel slopes of the ORR

pH	Electrolyte	1. slope mV dec^{-1}	2. slope mV dec^{-1}	Reference
0	1 M HClO$_4$	-100	-	[59]
0	1 M H$_2$SO$_4$	-93 to -95	-	[98, 153]
0	1 M H$_2$SO$_4$	-65	-	[142]
0	1 M H$_2$SO$_4$	-64 to -67	-121 to -165	[143]
1	0.05 M H$_2$SO$_4$	-97	-	[81]
1	0.05 M H$_2$SO$_4$	-70	-	[61]
1-3	HClO$_4$	-60	-120	[108]
7	0.067 M phosphate buffer	-118	-	[81]
7.9-9.7	0.5 M NaClO$_4$+0.1M borate buffer	-68 to -84	-110 to -144	[62]
8.0-9.0	0.5 M NaCl+0.1M borate buffer	-66 to -89	-120 to -150	[62]
10-13	NaOH	-60	-120	[99]
13	0.1 M NaOH	-46 to -55	-	[81]
13	0.1 M NaOH	-60	-	[124]
13	0.1 M KOH	-60	-120	[140]
13	0.1 M KOH	-52	-180 to -400	[145]
13	0.11-0.30 M KOH	-64	-200 to -300	[131]
13-14	NaOH	-60	-	[99]
14	1 M KOH	-65	-	[59]
14	1 M KOH	-35 to -39	-	[95]

2.3.2 HYDROGEN PEROXIDE REDUCTION

The wave of the hydrogen peroxide reduction is more anodic than that of the ORR. Therefore the hydrogen peroxide would be immediately reduced if formed as an intermediate during the ORR [66, 69, 154]. During its reduction the platinum surface can be oxidized by the hydrogen peroxide [155].

2.3.3 HYDROGEN EVOLUTION

Julius Tafel [42] compared several electrode materials for the HER and platinum was the best catalyst for this reaction. Bowden and Rideal [47] found a Tafel slope of 120 mV dec^{-1} and a potential of -0.6 V vs. SCE at 1 mA cm^{-2} in 0.1 M H$_2$SO$_4$. The current density for the hydrogen evolution decreases with time of electrolysis at Pt cathodes [106].

Sigmund Schuldiner [52] found Tafel slopes of -22 to -27 mV dec^{-1} for the HER at low current densities in sulfuric acid and potassium sulfate. The values of these slopes are increasing at higher current densities from -91 to -120 mV dec^{-1}. In sulfuric acid with a pH below 1 only one slope of 26

mV dec^{-1} appears [156]. Other authors found slopes of -30 mV dec^{-1} under acidic conditions [157-163]. Two Tafel slopes were also found in alkaline electrolytes. At pH above 8 the Tafel slope of about -120 mV dec^{-1} increases at higher current densities to -240 mV dec^{-1} and analog to the acidic conditions only one Tafel slope of -120 mV dec^{-1} can be observed for electrolytes with a pH >11 [156]. The second slope disappears at pH-values above 7.6 when ammonium anions are used in the electrolyte [156]. This is explained by their buffering ability [156].

Reviews about the hydrogen evolution were written by K. Wirtz in the late 1930s [164] and by J. O'M. Bockris in the late 1940s [165].

The adsorption isotherms depend on the crystal orientation but the orientation has only a slight influence on the hydrogen evolution under acidic conditions [158]. In KOH the current measured on Pt(111) was one order of magnitude smaller than on Pt(100) or Pt(110) [54].

INPUT PARAMETERS FOR CALCULATIONS

The standard potentials of several reactions and the Pourbaix diagram for platinum are given in chapter 3.1.

To calculate the thickness of the diffusion layer at a rotating disc or ring-disc electrode several input parameters are required. In this chapter the necessary values from literature are compared. The values of the kinematic viscosity for different electrolytes found in literature are shown in chapter 3.2. In Chapter 3.3 the influence of the temperature, the partial pressure and the electrolyte on the oxygen solubility are reviewed. The diffusion coefficients for oxygen in water found in literature are summarized in chapter 3.4.

3.1 STANDARD POTENTIALS

The standard potentials of several, relevant reactions are listed in Table 3. Figure 10 shows the Pourbaix diagram for platinum.

Table 3: Standard potentials

| Reaction	E^0 / V	Reference
$H_2 \rightleftharpoons 2\,H^+ + 2\,e^-$	0.000	
$H_2 + 2\,OH^- \rightleftharpoons 2\,H_2O + 2\,e^-$	+0.828	[166]
$O_2^- \rightleftharpoons O_2 + e^-$	-0.56	[166]
$OH + 2\,OH^- \rightleftharpoons HO_2^- + H_2O + e^-$	-0.24	[166]
$HO_2 \rightleftharpoons O_2 + H^+ + e^-$	-0.13	[166]
$H_2O_2 + 2\,OH^- \rightleftharpoons O_2 + 2\,H_2O + 2\,e^-$	-0.146	[1]
$HO_2^- + OH^- \rightleftharpoons O_2 + H_2O + 2\,e^-$	-0.076	[1, 166]
$HO_2^- + OH^- \rightleftharpoons O_2^- + H_2O + e^-$	+0.4	[166]
$4\,OH^- \rightleftharpoons O_2 + 2\,H_2O + 4\,e^-$	+0.401	[1, 166]
$H_2O_2 \rightleftharpoons O_2 + 2\,H^+ + 2\,e^-$	+0.695	[1]
$4\,OH^- \rightleftharpoons O_2^- + 2\,H_2O + 3\,e^-$	+0.7	[166]
$OH + H_2O \rightleftharpoons H_2O_2 + H^+ + e^-$	+0.72	[166]
$3\,OH^- \rightleftharpoons HO_2^- + H_2O + 2\,e^-$	+0.878	[1]
$2\,H_2O \rightleftharpoons O_2 + 4\,H^+ + 4\,e^-$	+1.229	[1, 166]
$O_2 + 2\,OH^- \rightleftharpoons O_3 + H_2O + 2\,e^-$	+1.24	[1, 166]
$Cl^- + 6\,OH^- \rightleftharpoons ClO_3^- + 3\,H_2O + 6\,e^-$	+0.62	[1]
$Cl^- + 4\,OH^- \rightleftharpoons ClO_2^- + 2\,H_2O + 4\,e^-$	+0.76	[1]
$Cl^- + 2\,OH^- \rightleftharpoons ClO^- + H_2O + 2\,e^-$	+0.81	[1]
$2\,Cl^- \rightleftharpoons Cl_2 + 2\,e^-$	+1.358	[1]
$SO_3^{2-} + 2\,OH^- \rightleftharpoons SO_4^{2-} + H_2O + 2\,e^-$	-0.93	[1, 166]
$S_2O_6^{2-} + H_2O \rightleftharpoons 2\,SO_4^{2-} + 4\,H^+ + 2\,e^-$	-0.22	[1]
$H_2SO_3 + H_2O \rightleftharpoons H_2SO_4 + 2\,H^+ + 2\,e^-$	+0.172	[1]
$Pt + 2\,OH^- \rightleftharpoons Pt(OH)_2 + 2\,e^-$	+0.14	[1]
$Pt + 4\,Cl^- \rightleftharpoons PtCl_4{}^{2-} + 2\,e^-$	+0.755	[1]
$Pt + 2\,H_2O \rightleftharpoons Pt(OH)_2 + 2\,H^+ + 2\,e^-$	+0.98	[166]
$Pt + 2\,H_2O \rightleftharpoons PtO_2 + 4\,H^+ + 4\,e^-$	+1.00	[1]
$PtO + H_2O \rightleftharpoons PtO_2 + 2\,H^+ + 2\,e^-$	+1.01	[1]
$Pt(OH)_2 \rightleftharpoons PtO_2 + 2\,H^+ + 2\,e^-$	+1.1	[166]
$Pt \rightleftharpoons Pt^{2+} + 2\,e^-$	+1.18	[1]
$Pt + H_2O \rightleftharpoons PtOH^+ + H^+ + 2\,e^-$	+1.2	[1]
$PtO_2 + H_2O \rightleftharpoons PtO_3 + 2\,H^+ + 2\,e^-$	+1.7	[1]
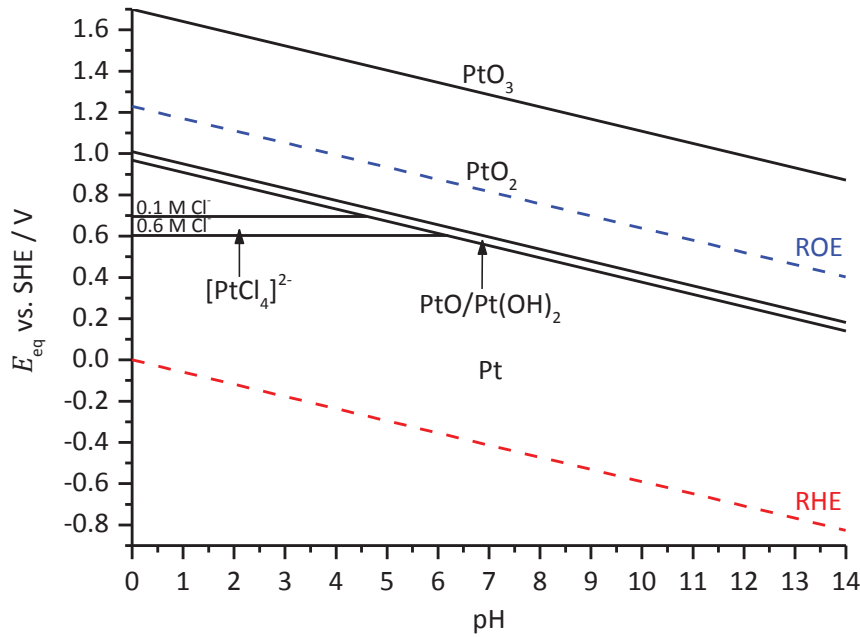
Figure 10: Pourbaix diagram; calculated with the standard potentials of Table 3 and 10^{-6} M $[PtCl_4]^{2-}$ with different chloride concentrations

3.2 KINEMATIC VISCOSITY

The kinematic viscosity influences the mobility of ions in a fluid. It is a function of electrolyte concentration and temperature [167] and therefore the viscosity of the different electrolyte solutions has to be taken into account.

Some older literature only stated the relative viscosity $\frac{\eta}{\eta_0}$. In these cases the electrolyte viscosities were calculated using the dynamic viscosity of water η_0 with 1.0016 mPa s at 293 K, 0.95001 mPa s at 295 K and 0.89002 mPa s at 298 K [1]. The kinematic viscosities of several electrolytes in water are listed in Table 4. The calculated kinematic viscosities in Table 4 were obtained by equation (3.1) published by Hefter et al. [167]. In this equation B and D are fitted parameters for aqueous electrolyte solutions and are given for several electrolytes. These results are in good agreement with the measured values of other authors.

$$\log \frac{\eta}{\eta_0} = B \cdot c + D \cdot c^2 \tag{3.1}$$

Table 4: Kinematic viscosity of different solutions

Electrolyte	Method	T / K	ν / 10^{-6} m^2 s^{-1}	Reference
water	-	293	1.0034	[1]
water	-	295	0.9998	[1]
water	-	298	0.8927	[1]
0.138 M HCl	-	293	1.0073	[1]
0.100 M HCl	calculated by (3.1)	293	1.0026	[167]
0.100 M HCl	calculated by (3.1)	295	0.9544	[167]
0.100 M HCl	calculated by (3.1)	298	0.8898	[167]
0.100 M HCl	Ostwald viscometer	298	0.8971	[168]
0.086 M NaCl	-	293	1.0092	[1]
0.100 M NaCl	calculated by (3.1)	293	1.0046	[167]
0.100 M NaCl	calculated by (3.1)	295	0.9564	[167]
0.100 M NaCl	calculated by (3.1)	298	0.8917	[167]
0.100 M NaCl	Ostwald viscometer	298	0.8974	[168]
0.933 M NaCl	Ubbelohde viscometer	298	0.8977	[169]
0.523 M NaCl	-	293	1.0318	[1]
0.600 M NaCl	calculated by (3.1)	293	1.0270	[167]
0.600 M NaCl	calculated by (3.1)	295	0.9784	[167]
0.600 M NaCl	calculated by (3.1)	298	0.9132	[167]
0.500 M NaCl	Ostwald viscometer	298	0.9149	[168]
0.561 M NaCl	Ubbelohde viscometer	298	0.9187	[169]
0.125 M NaOH	-	293	1.0230	[1]
0.100 M NaOH	calculated by (3.1)	293	0.9949	[167]
0.100 M NaOH	calculated by (3.1)	295	0.9507	[167]
0.100 M NaOH	calculated by (3.1)	298	0.8829	[167]
0.035 M Na$_2$SO$_4$	-	293	1.0103	[1]
0.050 M Na$_2$SO$_4$	calculated by (3.1)	293	1.0128	[167]
0.050 M Na$_2$SO$_4$	calculated by (3.1)	295	0.9640	[167]
0.050 M Na$_2$SO$_4$	calculated by (3.1)	298	0.8986	[167]
0.291 M Na$_2$SO$_4$	-	293	1.0887	[1]
0.300 M Na$_2$SO$_4$	calculated by (3.1)	293	1.0863	[167]
0.300 M Na$_2$SO$_4$	calculated by (3.1)	295	1.0340	[167]
0.300 M Na$_2$SO$_4$	calculated by (3.1)	298	0.9639	[167]
0.051 H$_2$SO$_4$	-	293	1.0084	[1]

3.3 OXYGEN SOLUBILITY

The oxygen solubility depends on temperature, oxygen partial pressure and the concentration of the electrolyte.

3.3.1 TEMPERATURE

One of the first equations to calculate the influence of the temperature and the chloride concentration on the oxygen solubility was published by Whipple [170]. This work is based on the measurements carried out by C. J. J. Fox using the Winkler titration [171].

Using a modified Winkler titration method Truesdale et al. found a lower oxygen concentration (about 6%) compared to these previous results [172]. From these data the empirical equation (3.2) was derived where S is the salinity in g per 1000 g, the temperature T in °C and the oxygen saturation concentration in mg L^{-1} under air [173, 174].

$$c_{O_2} = \frac{475 - (2.83 - 0.011 \cdot T) \cdot S}{33.5 + T} \tag{3.2}$$

More information can be found in the reviews of Rubin Battino et al. [175-177] and in the IUPAC solubility data series Volume 7 [178] and 10 [179].

In literature cc L^{-1} is an often used unit for the oxygen concentration. These data were converted assuming an ideal gas with the IUPAC standard conditions for temperature and pressure (STP). Figure 11 shows different models for the calculation of the oxygen solubility as function of the temperature compared with experimental values from literature. The models of Battino [178] and Benson [180] show the best correlation with the experimental values.
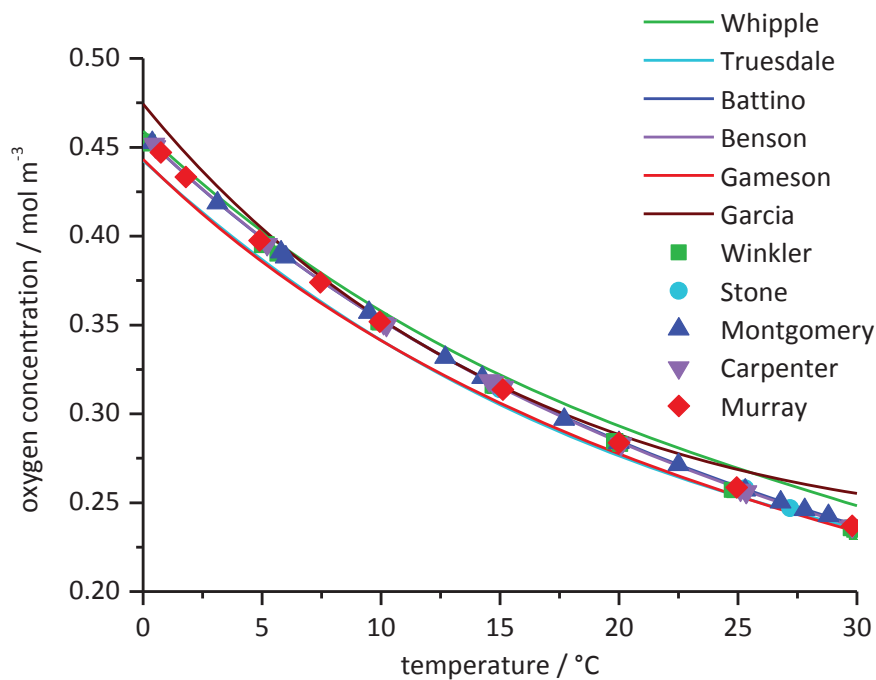
Figure 11: Oxygen solubility in water at 101.23 kPa total pressure and 20.95 % vol. O_2 as function of temperature; calculated [170, 174, 178, 180] (lines) and measured values [181-184] (points)

3.3.2 OXYGEN PARTIAL PRESSURE

Equation (3.3) describes the effect of the oxygen partial pressure on its solubility and was introduced by William Henry [185] with the following statement: *"… that, under equal circumstances of temperature, water takes up, in all cases, the same volume of condensed gas as of gas under ordinary pressure. But, as the spaces occupied by every gas are inversely as the compressing force, it follows, that water takes up, of gas condensed by one, two, or more additional atmospheres, a quantity which, ordinarily compressed, would be equal to twice, thrice, etc. the volume absorbed under the common pressure of the atmosphere."* In this equation k_H is the volatility constant and depends on the temperature.

$$p_{O_2} = k_H \cdot c_{O_2} \tag{3.3}$$

Under atmospheric conditions (20.95 % vol. oxygen at 101.23 kPa total pressures) the oxygen partial pressure is 21.3 kPa. According to Henry's law a pure oxygen atmosphere with 101.23 kPa should

increase the oxygen concentration by the ratio of the two partial pressures which is 4.75. The oxygen concentration for these two partial pressures is shown in Figure 12. The ratio of the two oxygen concentrations increases from 4.8 at 0°C to 5.0 at 30°C. The model of Battino [178] shows a good correlation with the experimental values.
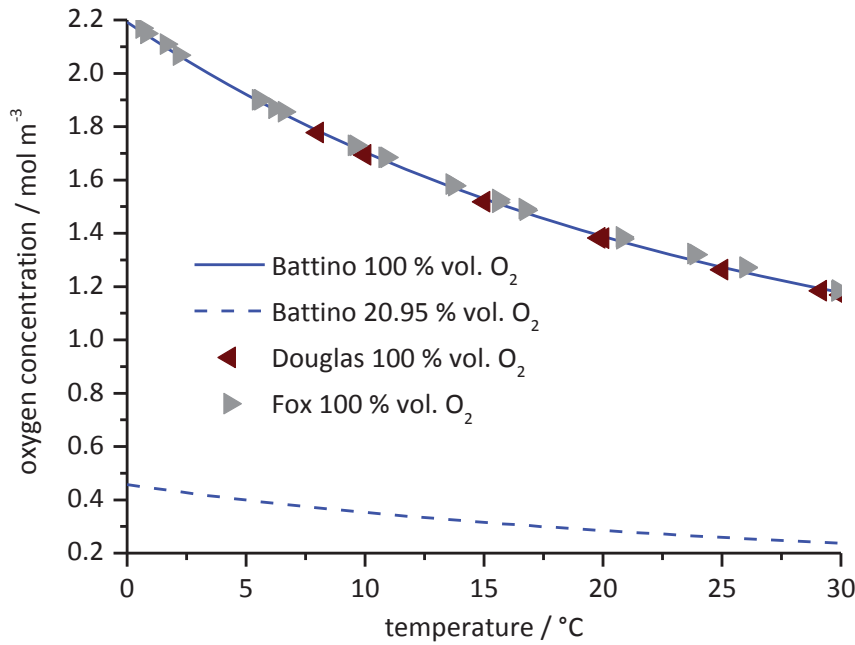

Figure 12: Oxygen solubility in water at 101.23 kPa total pressure with 20.95 % vol. O_2 (21.23 kPa) and 100 % vol. O_2 as function of temperature; calculated [178] (lines) and measured [171, 186] (points)

3.3.3 ELECTROLYTE

The oxygen solubility decreases by increasing the electrolyte concentration. This salting-out effect can be described by Sechenov equation (3.4) with the constant coefficient K_{Sech}. [187-189]

$$\ln \frac{c_{O_2,\text{water}}}{c_{O_2,\text{electolyte}}} = K_{Sech} \cdot c_{salt} \tag{3.4}$$

The experimental work in literature on this effect is mainly focused on the salinity and the chlorinity of seawater and therefore most models are only valid for sodium chloride electrolytes. Adrian Schumpe [188] separated the Sechenov coefficient into an ion-specific parameter h_{ion} and a gas-specific parameter h_{gas}.

$$K_{Sech} \cdot c_{salt} = \sum_{i=1}^{n} \left(h_{ion} + h_{gas} \right) \cdot c_i \tag{3.5}$$

Table 5: Specific parameters for oxygen solubility [188]

Cation	h_i L mol^{-1}	Anion	h_i L mol$^-$	Gas	h_g L mol
H$^+$	0.0000	OH$^-$	0.0756	O$_2$	0.0000
Na$^+$	0.1171	Cl$^-$	0.0334		
		SO$_4$$^{2-}$	0.1537		

Some of these values are listed in Table 5 so that the oxygen solubility in different electrolytes can be calculated by equation (3.5).

In Figure 13 several models for the calculation of the effect of sodium chloride are compared with experimental values found in literature. The salting out effect according to Schumpe was calculated using the oxygen solubility in pure water obtained by the equation given by Battino [178].
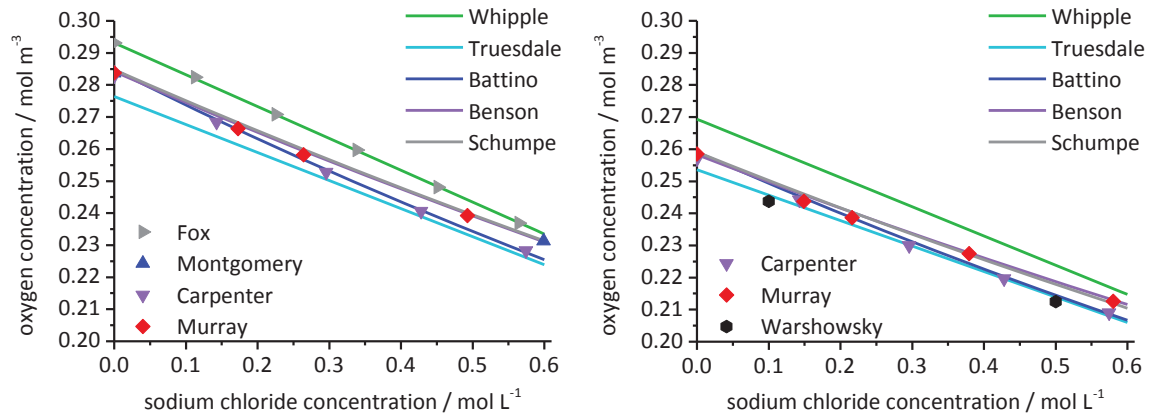

Figure 13: Oxygen solubility in water at 101.23 kPa total pressure with 20.95 % vol. O_2 as function of sodium chloride concentration at 20°C (left) and 25°C (right); calculated [170, 174, 178, 180, 188] (lines) and measured [171, 183, 184, 190] (points)

3.4 DIFFUSION COEFFICIENT OF OXYGEN IN WATER

Diffusion is the mass transport caused by concentration differences. According to equation (3.6) [191] the diffusion coefficient is a function of the association parameter of the solvent (x_{H_2O}=2.6 [191]), the molecular weight of the solvent (M_{g,H_2O}=18.015 g mol^{-1}), the dynamic viscosity of the solvent (chapter 3.2) and the molar volume of the solute (V_{O_2}=25.6 cm^3 g^{-1} [191-193]).

$$D = 7.4 \cdot 10^{-8} \cdot \frac{\left(x_{\text{solvent}} \cdot M_{\text{g,solvent}}\right)^{0.5} \cdot T}{\eta_{\text{solvent}} \cdot V_{\text{solute}}^{0.6}} \tag{3.6}$$

Himmelblau [192] compared several models between 15 °C and 35 °C with experimental values and found equation (3.7) [193] to be best fitting for the diffusion of gases in aqueous solution.

$$D = \frac{14.0}{\eta_{\text{solvent}}^{1.1} \cdot V_{\text{solute}}^{0.6}} \tag{3.7}$$

The diffusion coefficient decreases with increasing concentrations of potassium hydroxide [194, 195] and of several salts [196-199].

Table 6 shows the diffusion coefficients found in literature and calculated by equation (3.6) and (3.7).

Table 6: Diffusion coefficient of oxygen in water

Electrolyte	Method	T / K	D / 10^{-9} m^2 s^{-1}	Reference
water	volumetric mass transfer	293	1.98	[199]
water	calculated by (3.7)	293	2.00	[193]
water	-	293	2.01	[1]
water	calculated by (3.6)	293	2.12	[191]
water	gas bubble size	293	2.3	[200]
water	Taylor dispersion technique	294	1.78	[201]
water	oxygen flux	295	2.08	[196]
water	calculated by (3.7)	295	2.12	[193]
water	polarography	295	2.16 to 2.46	[192]
water	calculated by (3.6)	295	2.25	[191]
water	polarography	298	1.90	[195]
water	RDE	298	1.9 to 2.0	[194]
water	Taylor dispersion technique	298	1.96	[201]
water	laminar dispersion	298	2.20	[202]
water	mean value	298	2.35	[192]
water	calculated by (3.7)	298	2.27	[193]
water	-	298	2.42	[1]
water	calculated by (3.6)	298	2.42	[191]
0.100 M KCl	correction of [203]	298	2.0	[80]
0.100 M KCl	stationary Pt-wire	298	2.38	[136]
0.100 M KCl	polarography	298	2.62	[203]
0.085 M NaCl	transient pulse	293	1.95	[204]
0.103 M NaCl	volumetric mass transfer	293	1.44	[199]
0.552 M NaCl	volumetric mass transfer	293	1.46	[199]
0.564 M NaCl	transient pulse	293	1.91	[204]
1.0 M NaCl	oxygen flux	295	1.93	[197]
0.085 M NaCl	transient pulse	298	2.20	[204]
0.500 M NaCl	diaphragm cell method	298	2.08	[198]
0.564 M NaCl	transient pulse	298	2.17	[204]
0.10 M Na$_2$SO$_4$	oxygen flux	295	1.77	[196]
0.30 M Na$_2$SO$_4$	oxygen flux	295	1.47	[196]
0.38 M Na$_2$SO$_4$	oxygen flux	295	1.84	[197]
0.05 M Na$_2$SO$_4$	diaphragm cell method	298	3.00	[198]
0.30 M Na$_2$SO$_4$	diaphragm cell method	298	1.91	[198]

EXPERIMENTAL

4.1 EXPERIMENTAL SETUP

For the experimental work a rotating ring disc electrode (RRDE) made of polycrystalline platinum was used. The setup used for the experimental work is listed in Table 7. All experiments were carried out at 22°C.

Table 7: Experimental setup

Device	Name	Serial No.
Rotator	Rotator R/S Standard	200 297
Bi-Potentiostat	Jaissle Bi-Potentiostat PG100	200 284
Digital/Analog Converter	IPS-A8/PC104	200 300
Impedance spectroscope	PGU 10V-1A-IMP-S	200 281
Software	EcmWin 2.4.1 (Build 53)	-
Reference-Electrodes	KE 11NSK/7 (Hg/Hg_2Cl_2 sat. KCl)	1314271
	HgE11 (Hg/Hg_2SO_4 sat. K_2SO_4)	805291
	SE_11/NSK_7 (Ag/AgCl sat. KCl)	1310549
Counter-Electrode	Platinized titanium oxide	-

4.1.1 CALIBRATION OF THE BIPOTENTIOSTAT

The bipotentiostat was calibrated using a circuit according to Figure 14 built by metal film resistors with 0.1 % tolerance.

Figure 14: Circuit for calibration of the bipotentiostat

A potentiodynamic sweep was applied at the disc-current ranges 1 mA, 10 mA and 100 mA with a sweep rate of 10 mV s^{-1}. During the potentiodynamic sweep the ring potential was held at +0.50 V and at +1.00 V. The results are shown in Figure 15 and Figure 16 and follow the expected linear behavior according to Ohm's law.

The lowest Pearson's R of the data in Figure 15 is 0.99999 for the 100 mA range. The offset decreases using lower current ranges.

Table 8: Results of the bipotentiostat calibration

Disc range	Ring potential	R_Ω / Ω	E_{off} / mV
1 mA	+0.5 V	996.72±0.04	-0.65±0.02
	+1.0 V	996.83±0.04	-0.63±0.02
10 mA	+0.5 V	997.30±0.04	-1.26±0.03
	+1.0 V	996.44±0.04	-1.02±0.03
100 mA	+0.5 V	990.08±0.23	-10.0±0.2
	+1.0 V	991.18±0.22	-6.72±0.16

Figure 15: Measurement of the circuit shown in Figure 14; potentiodynamic polarization curves at the disc electrode: complete scan left, zoom right

Figure 16: Measurement of the circuit shown in Figure 14; hold potential at the ring: +0.500 V left, +1.000 V right

The offset of the hold potential at the ring electrode (Figure 16) is about -1 mV to -2 mV and the fluctuation is ±1 mV at the 1 mA and 10 mA disc current ranges.

4.1.2 CALIBRATION OF THE IMPEDANCE SPECTROMETER

To correct the ohmic drop the ohmic resistance of the electrolyte was measured with an impedance spectrometer. This device was tested using a circuit according to Figure 17.

Figure 17: Circuit for calibration of the impedance spectrometer

The electrical impedance of this circuit can be separated into a real part (4.1) and an imaginary part (4.2). Both terms are a function of the angular frequency of the alternating current ω_{AC}. The absolute value of the impedance is given by equation (4.3). The phase shift between the potential and the current can be calculated by equation (4.4). [57]

$$Re = R_{\Omega,S} + \frac{R_{\Omega,DL}}{1 + \omega_{AC}^2 \cdot R_{\Omega,DL}^2 \cdot C^2} \qquad (4.1)$$

$$Im = \frac{\omega_{AC} \cdot R_{\Omega,DL}^2 \cdot C}{1 + \omega_{AC}^2 \cdot R_{\Omega,DL}^2 \cdot C^2} \tag{4.2}$$

$$|Z| = \sqrt{Re^2 + Im^2} \tag{4.3}$$

$$phase = \frac{180°}{\pi} \cdot \tan^{-1}\frac{Im}{Re} \tag{4.4}$$

The impedance measurements were carried out between 200 kHz and 0.2 Hz. An inductive effect appears at frequencies above 20 kHz. Below 20 kHz the measurement is in good agreement with the calculation (Figure 18).

Figure 18: Bode plot of the measurement of the circuit shown in Figure 17 compared to calculated values

4.1.3 REFERENCE ELECTRODES

Figure 19: Potential stability of the used reference electrodes, the standard potentials of the reference electrodes vs. SHE were subtracted from the experimental values

To avoid a systematic error different reference electrodes have been used which were checked against other reference electrodes. In chloride and NaOH electrolytes a saturated calomel electrode (SCE, Hg/Hg_2Cl_2 sat. KCl) was used, while a Hg/Hg_2SO_4 sat. K_2SO_4 electrode was used in sulfate electrolytes.

Excluding the first five minutes of the measurements the error of the reference electrodes is below ±2 mV (Figure 19).

4.1.4 GEOMETRY OF THE RRDE AND THE COLLECTION EFFICIENCY

Figure 20: Geometry of the RRDE in mm

The collection efficiency depends on the geometry of the RRDE and can be calculated by equation (1.45). The RRDE used in this work (Figure 20) has a theoretical collection efficiency of 37.2 % according to equation (1.45). The collection efficiency was also determined by reducing potassium ferricyanide at the disc electrode and by reoxidizing the product at the ring electrode with a potential of +1.34 V vs. SHE (Figure 21).

Figure 21: Reduction and reoxidation of 2 mM potassium ferricyanide in N_2-purged 0.1 M NaCl; potentiodynamic scan at the disc electrode (10 mV s^{-1}); ring potential +1.340 V vs. SHE

The collection efficiency can be calculated using the ratio of the ring and the disc current. The ring currents were corrected for their background of up to 30 μA depending on the rotation rate. The collection efficiency is between 36.0 % and 36.5 % in the limiting current region (Figure 22).

The difference between the theoretical and the measured collection efficiency is about 1 %. This might be due to equation (1.45) which is ill conditioned for errors of the geometrical input factors. A

change of 0.1 mm in the inner or outer diameter of the ring causes a change of up to 0.7 % in the collection efficiency.
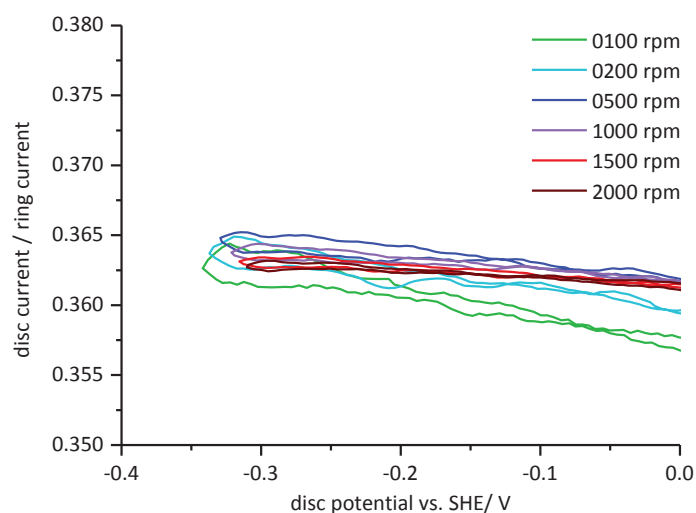

Figure 22: Collection efficiency calculated from the measured currents in Figure 21

4.2 ELECTRODE PREPARATION

The electrodes were grinded with abrasive paper up to grit 2000 and polished with 3 μm and 1 μm diamond paste. After each step the electrode was put into an ultrasonic bath for 3 minutes and rinsed with water. The polished and cleaned electrodes were stored in a desiccator for 4 days before the measurements were carried out.

Before each series of measurements the ring electrode was cycled between anodic and cathodic polarization with a scan rate of 50 mV s^{-1}. After that 10 cycles at the disc were measured at 1000 rpm while the ring was held at the hold potential. Then the potentiodynamic measurements were carried out at different rotation rates. After each measurement the electrodes were held at the OCP for 10 to 20 minutes.

4.3 CHEMICALS

The chemicals (Table 9) used in this work were of pro analysis grade and dissolved in 1.5 μS cm^{-1} water.

Table 9: Chemicals used in this work

Substance	Chemical formula	Trademark	Charge
Potassium ferricyanide	$K_3Fe(CN)_6$	Merck KGaA	A703173 547
Potassium hydrogen phthalate	$KC_8H_5O_4$	ACROS ORGANICS	177 121000
Sodium tetraborate decahydrate	$Na_2B_4O_7 \cdot 10\ H_2O$	Merck KGaA	K26663503 941
Sodium hydroxide 50 %	$NaOH$	VWR Int. SAS	0604391
Sodium chloride	$NaCl$	AppliChem GmbH	2J004144
Sodium sulfate decahydrate	$Na_2SO_4 \cdot 10\ H_2O$	AppliChem GmbH	1D002448
Hydrochloric acid 2 M	HCl	VWR Int. SAS	13F100516
Sulfuric acid 95-97 %	H_2SO_4	Merck KGaA	K40869531 012

The pH 4.5 buffer solution contained 1.74 mM sodium hydroxide and 0.01 M potassium hydrogen phthalate [205]. The pH 9.5 buffer was prepared with 7.04 mM sodium hydroxide and 0.01 M sodium tetraborate [206].

The buffered electrolytes contained also 0.05 M Sodium sulfate or 0.1 M sodium chloride.

4.4 DATA ANALYSIS

All data were corrected for the ohmic drop in the electrolyte according to equation (4.5) [50]. The ohmic resistances R_Ω of the electrolytes were measured at the OCP using impedance spectroscopy in a three-electrode configuration after the electrode was exposed to the electrolyte for one hour. The disc electrode was pretreated with ten cathodic cycles in the electrolyte. The amplitude was 10 mV and the measurements were carried out at 100 rpm, 1000 rpm and 2000 rpm. The corrected potential E is the measured potential E_Ω minus the current I multiplied by the ohmic resistance of the electrolyte.

$$E = E_\Omega - I \cdot R_\Omega \qquad (4.5)$$

The impedance measurements were analyzed with the ZView software using the simple equivalent circuit shown in Figure 17. An ideal capacitor ($cp = 1$) shows a phase of -90°. In real systems it is possible that this phase has values between 0° and -90°. This was considered for the analysis of the impedance measurements by a constant phase element with the exponent cp, which can have values between 0 and 1. The impedance of such a constant phase element can be calculated by equation (4.6) [207].

$$Z = \frac{1}{C_{DL} \cdot \left(\sqrt{-1} \cdot \omega_{AC}\right)^{cp}} \qquad (4.6)$$

The IR-corrected data was further analyzed. Usually in literature the Koutecký-Levich equation (1.30) is used for the interpretation of RDE experiments by extrapolating the reciprocal of the current density versus the reciprocal of the square root of the rotation rate. In chapter 1.3.1 it has been shown that this equation is very ill conditioned close to the diffusion limiting current density. This method is very susceptible for errors and therefore the data were directly fitted in this work.

All data were measured with a scan rate of 10 mV s^{-1} because a oxygen, with a diffusion coefficient of $2 \cdot 10^{-9}$ m^2 s^{-1}, would cover a mean distance of 63 μm in 1 second according to equation (1.16). This is the thickness of the diffusion layer at 100 rpm, the lowest used rotation rate. Therefore the influence of non-stationary (transient) mass transport effects on the measurements can be neglected.

A cathodic polarization curve in air saturated water involves the ORR and at more negative potentials the HER. Therefore at least two reactions must be considered for the calculation. The total current is the sum of all reactions.

Reactions with a limiting current density were calculated with the Koutecký-Levich equation in the form of equation (4.8) analogue to equation (1.66). The HER in the acidic electrolytes was considered using the simplified equation (4.7) for the Tafel equation (1.52). For pH-values of 4.5 and higher the experimental data show a change in the Tafel slope for the HER. The reason for this was described in chapter 1.4. These HERs were fitted by equation (4.9) which is analogous to equation (1.59). The HER

at pH 4.5 shows a limiting current density and also a change in the Tafel slope. Therefore the Koutecký-Levich equation was modified to form equation (4.10). The pre-exponential current densities are the current densities which could be expected for the reaction if the electrode is polarized to the potential of the reference electrode RE.

$$i = i^{\mathrm{RE}} \cdot \exp[s \cdot E_{\mathrm{RE}}] \tag{4.7}$$

$$i = \frac{i^{\mathrm{RE}} \cdot \exp(s \cdot E_{\mathrm{RE}})}{1 + \dfrac{i^{\mathrm{RE}}}{i_{\mathrm{lim}}} \cdot \exp(s \cdot E_{\mathrm{RE}})} \tag{4.8}$$

$$i = \frac{i^{\mathrm{RE}} \cdot \exp(s \cdot E_{\mathrm{RE}})}{1 + i_{\mathrm{b}}^{\mathrm{RE}} \cdot \exp(s_{\mathrm{b}} \cdot E_{\mathrm{RE}})} \tag{4.9}$$

$$i = \frac{i^{\mathrm{RE}} \cdot \exp(s \cdot E_{\mathrm{RE}})}{1 + \dfrac{i^{\mathrm{RE}}}{i_{\mathrm{lim}}} \cdot \exp(s \cdot E_{\mathrm{RE}})} \cdot \left[1 + i_{\mathrm{b}}^{\mathrm{RE}} \cdot \exp(s_{\mathrm{b}} \cdot E_{\mathrm{RE}})\right]^{-1} \tag{4.10}$$

Using this set of equations the parameters were fitted to the measured curves. For this a least square problem was defined using the difference between the measured and the calculated current densities as a function of the potential. The kinetic parameters were optimized by minimizing the squares with the "fminsearch" function of MATLAB R2013a. In the measured electrolytes up to 5 reactions must be considered so that it was necessary to optimize each reaction separately.

The obtained kinetic data are given in the following chapter.

Additionally the limiting current densities obtained by this method were analyzed using the Levich equation (1.27) and the diffusion coefficients were calculated from the slopes.

RESULTS AND DISCUSSION

5.1 CAPACITY AND OHMIC RESISTANCE

The open circuit potentials of the platinum disc after one hour exposed to the electrolyte are given in Table 10 and are compared with the thermodynamic equilibria of the Pourbaix diagram in Figure 23. The OCPs in sulfate, hydroxide and borate buffered (pH 9.5) electrolytes are close to the standard equilibrium potential of the reversible reaction {5.1}. The change of the OCP of platinum in these electrolytes is with -59.8 mV pH^{-1} close to the theoretical value of -58.4 mV pH^{-1}.

$$Pt + H_2O \rightleftharpoons PtO + 2\,H^+ + 2\,e^- \qquad \{5.1\}$$

The OCP measured in this work is higher in chloride containing neutral and acidic electrolytes. Previous authors [208, 209] found a smaller OCP in chloride containing electrolytes than in sulfuric acid. In acidic electrolytes containing chloride ions the oxide layer on platinum can be dissolved [85] and it is also known that the chloride ion adsorption competes with the adsorption of oxygen [210, 211]. It has been reported that the chlorine formation takes place in chloride solutions even when the oxidation of water should be the thermodynamically predominant anodic process [208, 210]. For this reason equilibrium {5.2} might shift the OCP to higher potentials.

$$Cl_2 + 2\,e^- \rightleftharpoons 2\,Cl^- \qquad \{5.2\}$$

At pH 9.5 the presence of chloride does not influence the OCP.

The measured double layer capacity of platinum was between 30 µS s^{cp} cm^{-2} and 121 µS s^{cp} cm^{-2} depending on the electrolyte. The obtained values are lower than the 200 to 300 µF cm^{-2} published by Hickling [102] but in the range of the 34 µF cm^{-2} found in 1 M H$_2$SO$_4$ at +1.20 V vs. NHE [103] and also comparable to those measured in neutral electrolytes [212]. The double layer capacity is lower in the sulfate than in the chloride electrolytes, which is in agreement with the tendency of less adsorption of these cations [212]. The only exception is the 0.60 M sodium chloride solution where platinum has almost the same capacity as in 0.1 M sodium chloride solution. The increase of the double layer capacity with higher chloride concentrations published by Popat and Hackerman [212] was not observed.

Table 10: Mean values of the double layer capacity and the ohmic resistance of a platinum disc in different air saturated electrolytes

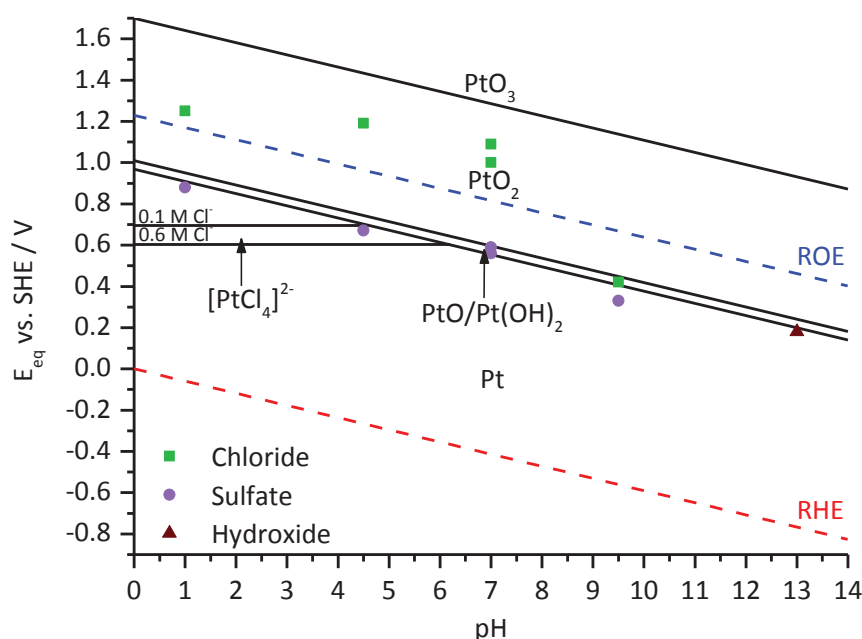| Electrolyte	OCP / V	C_{DL} / µS s^{cp} cm^{-2}	cp	$R_{\Omega,S}$ / Ω
0.05 M H$_2$SO$_4$	0.88	42.8	0.901	15.6
0.10 M HCl	1.25	65.4	0.921	10.5
0.05 M Na$_2$SO$_4$ at pH 4.5	0.67	74.9	0.824	34.1
0.10 M NaCl at pH 4.5	1.19	91.9	0.923	34.8
0.05 M Na$_2$SO$_4$	0.59	81.0	0.832	41.8
0.30 M Na$_2$SO$_4$	0.56	30.0	0.971	10.5
0.10 M NaCl	1.00	62.1	0.927	36.9
0.60 M NaCl	1.09	68.6	0.909	10.2
0.05 M Na$_2$SO$_4$ at pH 9.5	0.33	50.5	0.929	39.9
0.10 M NaCl at pH 9.5	0.42	94.4	0.867	32.2
0.10 M NaOH	0.18	120.6	0.898	19.1

Figure 23: OCPs of Table 10 (dots); lines calculated with the standard potentials of Table 3 and 10^{-6} M $[PtCl_4]^{2-}$ with different chloride concentrations

5.2 ACIDIC ELECTROLYTES
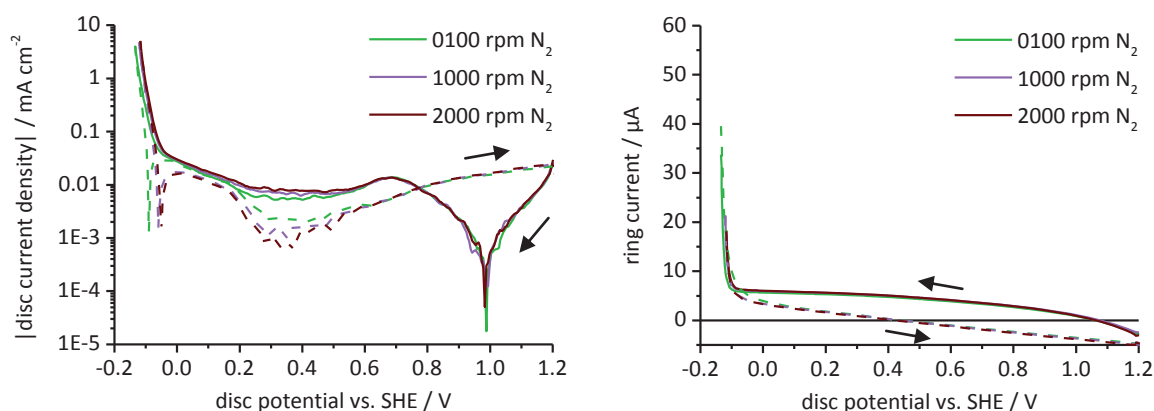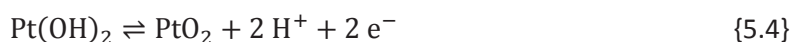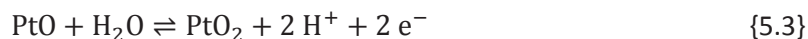
5.2.1 SULFURIC ACID 0.05 M

5.2.1.1 NITROGEN

Figure 24: Potentiodynamic polarization curves (10 mV s^{-1}) in N$_2$ saturated 0.05 M H$_2$SO$_4$ after 20 min OCP at different rotation rates; ring potential: +1.29 V vs. SHE; forward scan: solid lines, reverse scan: dashed lines

Figure 24 shows the potentiodynamic measurements on a platinum RRDE in deaerated 0.05 M H$_2$SO$_4$. The zero-current potential of the disc electrode measured during the forward scans are with +0.99 V very close to the OCPs found by previous authors in 0.5 M H$_2$SO$_4$ [213], 0.1 M H$_2$SO$_4$ [84] and 0.05 M H$_2$SO$_4$ [81]. These literature data show that the rest potential or OCP is independent of the sulfate ion concentration. The same zero-current potential was found in air saturated sulfuric acid. In acidic solutions the oxide film seems to be formed from the H$_2$O as the formed film is independent of the

presence or absence of oxygen [90, 214]. The measured zero-current potential is between equilibrium {5.3}, which has a potential of +0.951 V at pH 1 [1], and equilibrium {5.4} with a potential of +1.04 V at pH 1 [166].

$$PtO + H_2O \rightleftharpoons PtO_2 + 2\,H^+ + 2\,e^- \hspace{3cm} \{5.3\}$$

$$Pt(OH)_2 \rightleftharpoons PtO_2 + 2\,H^+ + 2\,e^- \hspace{3cm} \{5.4\}$$

The cathodic current peaks between the zero-current potential and +0.33 V are caused by the reduction of the oxide layer [50]. At more negative potentials the platinum surface becomes covered with a hydrogen layer [50] before the hydrogen evolution starts at -0.05 V. In the reverse scans the current densities at these potentials were caused by the oxidation of the adsorbed hydrogen and finally the formation of a new oxide layer.

The reduction peaks in the forward scan at +0.7 V have an area of 200±20 µC cm^{-2}, which corresponds to 48 % of a complete monolayer of PtO (420 µC cm^{-2} [86, 87, 110]). This value is close to the 47 % found by Hoare [87] in 1 M H_2SO_4 stirred by bubbling N_2 into the electrolyte. El Kadiri measured 230 µC cm^{-2} in 1 M H_2SO_4 [142] after some oxygen adsorption-desorption cycles. Laitinen [110] found 180 µC cm^{-2} in perchloric acid while Damjanovic [124] published a value of 115 µC cm^{-2} at 1 V vs. RHE in 0.1 M perchloric acid solution.

The ring current due to the hydrogen oxidation is smallest at the highest rotation rate. This effect was found in all investigated electrolytes under nitrogen and air. Only the oxidation of the hydrogen formed from protons at pH 4.5 at the disc electrode results in an increase of the ring current with higher rotation rates.

The hydrogen evolution shows an exponential Tafel behavior. Since no hydrogen is initially in the solution an equilibrium potential could not be determined. Therefore all kinetic data are given with respect to the SHE and the RHE. The mass transport influences the exchange current density of the hydrogen evolution [39] and the pre-exponential current density increases with higher rotation rates as has been shown in chapter 1.4.

Table 11: Kinetic data for the HER in 0.05 M H_2SO_4 for equation (4.7)

ω	forward scan			reverse scan		
	$i^{SHE}\,(i^{RHE})$	s	t_s	$i^{SHE}\,(i^{RHE})$	s	t_s
rpm	mA cm^{-2}	V^{-1}	mV dec^{-1}	mA cm^{-2}	V^{-1}	mV dec^{-1}
100	-15.42·10^{-6} (-3.969·10^{-3})			-3.936·10^{-6} (-1.373·10^{-3})		
1000	-40.71·10^{-6} (-10.48·10^{-3})	-94.81	-24.29	-21.96·10^{-6} (-7.660·10^{-3})	-100.0	-23.03
2000	-62.96·10^{-6} (-16.21·10^{-3})			-34.46·10^{-6} (-12.02·10^{-3})		

Although the Tafel slopes for the HER (Table 11) are smaller than the expected -29 mV dec^{-1} [40] a Tafel mechanism can still be assumed. Schuldiner [52, 156, 215] measured values between -22 and -30 mV dec^{-1} in sulfuric acid in this current density range. Hoare [157] found a Tafel slope of -27 mV dec^{-1} in 1 M H_2SO_4. Gomez et al. reported -30 mV dec^{-1} in 0.5 M H_2SO_4 at different oriented platinum electrodes while Protopopoff et al. [159] measured -35 mV dec^{-1} in 0.05 M H_2SO_4 at Pt(110). Other authors [158, 161-163] found values close to the theoretical -29 mV dec^{-1} in acidic electrolytes.

The current densities calculated by equation (4.7) with the kinetic data in Table 11 are compared with the measured values in Figure 25.
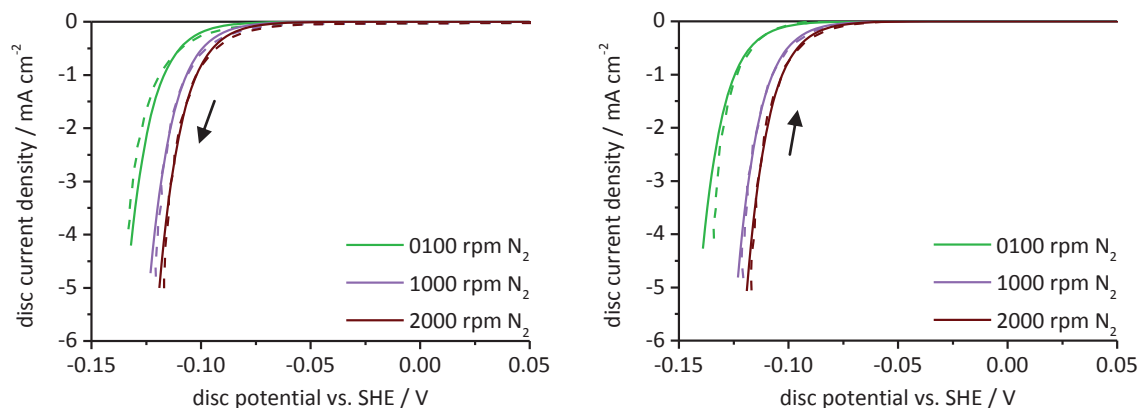

Figure 25: Potentiodynamic polarization curves (10 mV s^{-1}) in N$_2$ saturated 0.05 M H$_2$SO$_4$ after 20 min OCP at different rotation rates; measured (dashed) and calculated (solid); forward scan: left, reverse scan: right
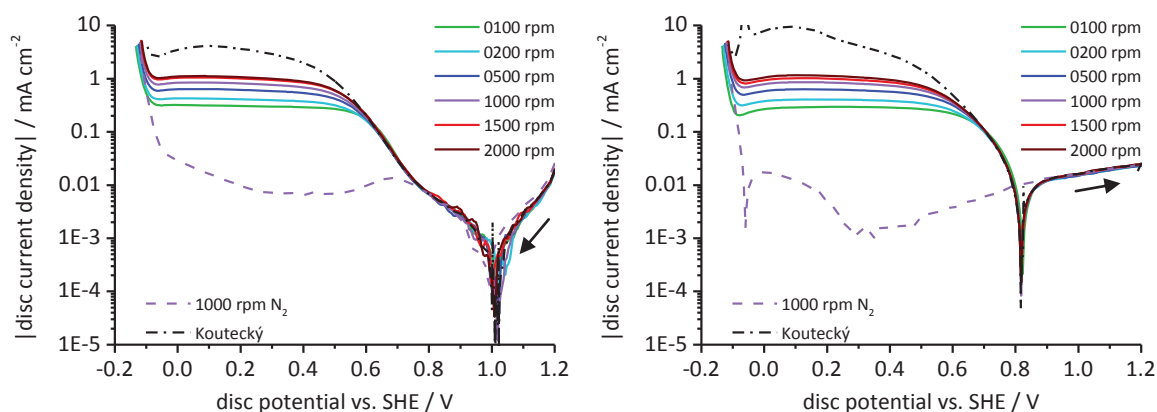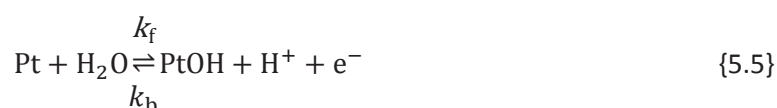
5.2.1.2 AIR

Figure 26: Potentiodynamic polarization curves (10 mV s^{-1}) in air saturated 0.05 M H$_2$SO$_4$ after 20 min OCP at different rotation rates and the evaluated Koutecký current density; forward scan: left, reverse scan: right

The zero-current potentials in the forward scans of +1.02 V (Figure 26) are close to the +0.99 V found under nitrogen. In the reverse scans the equilibrium between the ORR and the oxygen adsorption is at +0.82 V where the first oxygen species are adsorbed [86, 216]. The current densities at potentials above +0.8 V are identical in the air saturated and in the nitrogen purged electrolytes. This agrees with a similar oxygen coverage in an oxygen and in nitrogen atmosphere [124]. The ORR starts at +0.82 V when the oxide layer gets reduced. Lingane [80] observed the beginning of the reduction wave of oxygen at +0.74 V.

Several authors found a Tafel slope of -60 mV dec^{-1} [64-66, 93, 132, 133, 135, 142-144] at potentials more positive than +0.8 V which was explained by Temkin adsorption [93, 108, 133, 134, 140, 147, 148]. In the present work only the second Tafel slope reported in literature [64-66, 93, 132, 133, 135, 142-144] of -120 mV dec^{-1} due to the Langmuir adsorption was found since lower currents are overlapped by the formation and reduction of platinum oxide. It can be expected that at lower scan rates than the used 10 mV s^{-1} a slope of -60 mV dec^{-1} would appear.

Both Tafel slope regions show the same enthalpy of activation [133, 134]. For this reason the theory that the change in the slope is caused by a transition from Temkin to Langmuir conditions seems at least questionable. According to the Langmuir adsorption theory all surface sites are equal without interaction between the adsorbents. The Temkin model assumes that the adsorption enthalpy is a function of the surface coverage and considers an interaction between the adsorbed species. Even if the same reaction step, the first electron transfer [133, 134], is rate determining, it is unlikely that a difference in the adsorption enthalpy would have no influence on the activation enthalpy. For this reason a new approach should be considered similar to the one used for the change in the slope during the hydrogen evolution in chapter 1.4. In this case only the Langmuir adsorption is considered.

The ORR determines the current density at potentials below +0.7 V under air (Figure 26). At the same potential the oxide layer is reduced under nitrogen (Figure 24). The oxide film is independent of the presence or the absence of oxygen [90, 214] and therefore the ORR takes place at the same potentials at which the oxide layer is reduced. This has also been reported by other authors [80, 217]. This reduction peak is about 200 mV more negative than the standard potential of the PtO or Pt(OH)$_2$ reduction (see Table 3). The charge calculated from the area of the reduction peak is only 47 % of the charge expected for the reduction of a fully covered PtO or Pt(OH)$_2$ surface. The reason could be that the surface might be covered with PtOH in this potential range [218, 219]. For those reasons it is more likely that equilibrium {5.5} dominates this potential region. This reaction was also stated by Damjanovic and Bockris [59] as the rate-determining step in acidic solution. Under Langmuir conditions only free Pt sites are available for the adsorption of oxygen molecules {5.6}. The reduction of adsorbed oxygen {5.7} can be assumed to be irreversible at high overpotential.

$$\mathrm{Pt + H_2O} \underset{k_\mathrm{b}}{\overset{k_\mathrm{f}}{\rightleftharpoons}} \mathrm{PtOH + H^+ + e^-} \tag{5.5}$$

$$\mathrm{Pt + O_2 \rightarrow PtO_2} \tag{5.6}$$

$$\mathrm{PtO_2 + Pt + 2\,H_2O + 2\,e^- \rightarrow 2\,PtOH + 2\,OH^-} \tag{5.7}$$

Under steady state conditions the reduction of PtOH {5.5} is as fast as the formation of PtOH from water {5.5} and the oxygen adsorption {5.6} according to (5.1). The activity of the free platinum surface sites is therefore given by equation (5.2).

$$k_\mathrm{f} \cdot a_\mathrm{Pt} + \alpha_\mathrm{Lang} \cdot \mu_\mathrm{Lang} \cdot a_\mathrm{Pt} = k_\mathrm{b} \cdot a_\mathrm{PtOH} \tag{5.1}$$

$$a_\mathrm{Pt} = \frac{k_\mathrm{b}}{k_\mathrm{f} + \alpha_\mathrm{Lang} \cdot \mu_\mathrm{Lang}} \cdot a_\mathrm{PtOH} \tag{5.2}$$

If reaction {5.7} is relatively fast, which can be assumed due to the high difference (-400 mV) between the potentials were the ORR starts and the standard potential of equilibrium {2.1}, the oxygen reduction rate would only depend on the oxygen adsorption at the platinum surface according to equation (5.3). Equation (5.2) and equation (5.3) can be combined to (5.4).

$$j_\mathrm{ORR} = \alpha_\mathrm{Lang} \cdot \mu_\mathrm{Lang} \cdot a_\mathrm{Pt} \tag{5.3}$$

$$j_\mathrm{ORR} = \frac{k_\mathrm{b}}{1 + \frac{k_\mathrm{f}}{\alpha_\mathrm{Lang} \cdot \mu_\mathrm{Lang}}} \cdot a_\mathrm{PtOH} \tag{5.4}$$

$$i_{ORR} = i_b^0 \cdot \frac{\exp\left[-\frac{(1-\alpha)\cdot n \cdot F}{R_g \cdot T} \cdot E\right]}{1 + \frac{k_f^0}{\alpha_{Lang} \cdot \mu_{Lang}} \cdot \exp\left[\frac{\alpha \cdot n \cdot F}{R_g \cdot T} \cdot E\right]} \cdot a_{PtOH} \tag{5.5}$$

Equation (5.4) is similar to equation (1.56) derived for the HER and can be transformed into equation (5.5). According to equation (5.5) a change in the Tafel slope from -60 mV dec^{-1} at high potentials and low currents to -120 mV dec^{-1} at low potentials and high currents can be expected and can be seen in Figure 4.

After the onset of the diffusion limitation of the ORR at +0.6 V the Koutecký current density (the extrapolated current density at infinite rotation rate) does not show the expected discontinuity (see chapter 1.3.1). Instead a second slope appears between +0.5 V and +0.1 V, as can be seen in Figure 26. At the same potential a rotation rate depending increase of the ring current (Figure 27) indicates the formation of hydrogen peroxide at the disc electrode. In the experiments carried out by Bianchi and Mussini [209] hydrogen peroxide was formed at potentials below +0.680 V vs. NHE. Small amounts of hydrogen peroxide during the ORR were also found by other authors (see chapter 2.3.1.4). According to Damjanovic [37] this ring current indicates that the ORR follows two different reaction paths. A second ORR path was also stated by other authors [61, 72, 130, 131, 220]. This second path involves two steps, the formation of hydrogen peroxide {5.8} and its further dissociation to hydroxide {5.9}.
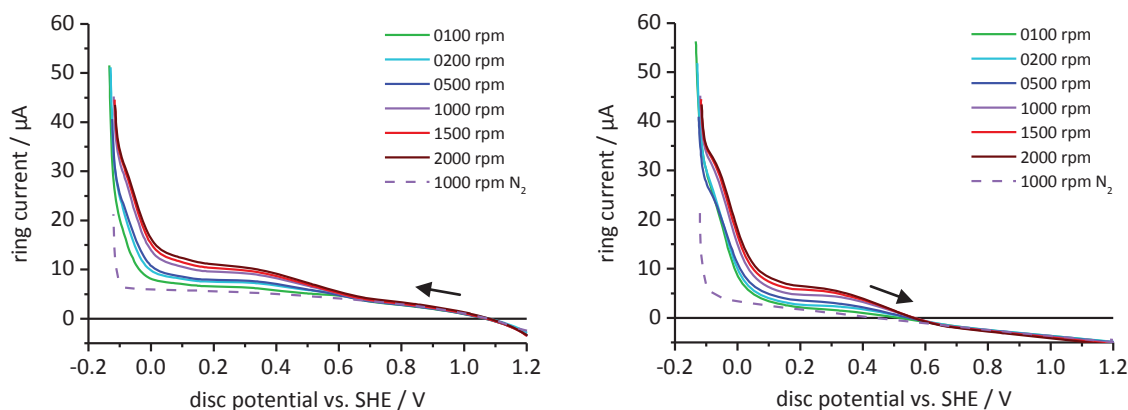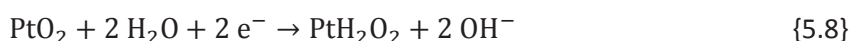
$$PtO_2 + 2\,H_2O + 2\,e^- \rightarrow PtH_2O_2 + 2\,OH^- \tag{5.8}$$

$$PtH_2O_2 + 2\,e^- \rightarrow Pt + 2\,OH^- \tag{5.9}$$

Figure 27: Ring currents measured during the potentiodynamic scan (10 mV s^{-1}) at the disc electrode in air saturated 0.05 M H$_2$SO$_4$ after 20 min OCP at different rotation rates; ring potential: +1.29 V vs. SHE; forward scan: left, reverse scan: right

The difference in the ring current at +0.200 V between the measurements under nitrogen and under air is between 1.2 µA and 7.2 µA depending on the rotation rate. Therefore less than 1 % of the disc current is consumed by forming peroxide desorbing from the disc electrode. The limiting current densities of the ORR path in which peroxide (2. ORR path) is formed as an intermediate (Table 13) are much higher than the ring current would indicate and therefore most of the peroxide gets further reduced to hydroxide at the disc electrode. The contribution of this 2. ORR path to the total ORR increases from just 2 % at low rotation rates to up to 27 %.

To study the cathodic reaction kinetic on platinum in air saturated 0.05 M H_2SO_4 four reactions have to be considered.

The direct ORR (1. ORR path) is the rate determining process between +0.8 V and +0.6 V. The kinetic data for this reaction obtained from the measured curves by equation (1.66) can be found in Table 12.

Table 12: Kinetic data for the 1. ORR path in air saturated 0.05 M H_2SO_4 for equation (4.8)

ω	i_{lim}	i^{SHE} (i^{ROE})	s	t_s	i_{lim}	i^{SHE} (i^{ROE})	s	t_s
	forward scan				reverse scan			
rpm	mA cm^{-2}	mA cm^{-2}	V^{-1}	mV dec^{-1}	mA cm^{-2}	mA cm^{-2}	V^{-1}	mV dec^{-1}
100	-0.3050				-0.2850			
200	-0.3576				-0.3446			
500	-0.5194	-29220	-19.42	-118.7	-0.5076	-20620	-17.20	-133.9
1000	-0.6798	(-3.851·10^{-6})			-0.6558	(-36.74·10^{-6})		
1500	-0.8040				-0.7635			
2000	-0.9018				-0.8487			

The same equation can be used for the second reaction path of the ORR in which peroxide is formed as an intermediate. The Tafel slope for this reaction is -180 mV dec^{-1} (Table 13).

Table 13: Kinetic data for the 2. ORR path in air saturated 0.05 M H_2SO_4 for equation (4.8)

ω	i_{lim}	i^{SHE} (i^{ROE})	s	t_s	i_{lim}	i^{SHE} (i^{ROE})	s	t_s
	forward scan				reverse scan			
rpm	mA cm^{-2}	mA cm^{-2}	V^{-1}	mV dec^{-1}	mA cm^{-2}	mA cm^{-2}	V^{-1}	mV dec^{-1}
100	-0.0069				-0.0097			
200	-0.0627				-0.0619			
500	-0.1217	-6.890	-12.24	-188.2	-0.1227	-32.77	-12.65	-182.1
1000	-0.1774	(-4.084·10^{-6})			-0.2027	(-12.01·10^{-6})		
1500	-0.2041				-0.2583			
2000	-0.2317				-0.3121			

At potentials below +0.1 V the diffusion limiting current density at the disc electrode decreases. Simultaneously a shoulder appears in the ring current prior to the hydrogen oxidation. This decrease in the diffusion limiting current density at the disc has been observed by several authors (chapter 2.3.1.5) and is caused by the formation of hydrogen peroxide during the oxygen reduction in combination with the hydrogen adsorption.

In chapter 1.6 it has been shown that the decrease of the limiting diffusion current density of the ORR, caused by the hydrogen adsorption, can be calculated using an exponential function. It is necessary to use a limiting current density in this case according to equation (1.66) since the hydrogen adsorption is limited by the amount of free platinum sites. According to Marković [65] the hydrogen adsorption can lead to the formation of 100 % peroxide by the ORR on platinum in sulfuric acid.

The amount of hydrogen peroxide formed with the onset of the HER during the forward scan is significantly smaller than the amount formed during the reverse scan (Table 14). The error due to the formation and oxidation of adsorbed hydrogen is 0.02 mA cm^{-2} as can be observed using measurements in nitrogen purged electrolytes.

The limiting current densities of the complete ORR are reduced by up to 20 % in the hydrogen adsorption region so that up to 40 % of the oxygen is consumed forming hydrogen peroxide. Other authors reported 70 % to 90 % [60] and up to 100 % [65] hydrogen peroxide formation on platinum during the ORR in sulfuric acid with the onset of the HER.

Table 14: Kinetic data for the ORR in combination with the hydrogen adsorption in air saturated 0.05 M H_2SO_4 for equation (4.8)

ω rpm	forward scan				reverse scan			
	i_{lim} mA cm^{-2}	$i^{SHE}\left(i^{RHE}\right)$ mA cm^{-2}	s V^{-1}	t_s mV dec^{-1}	i_{lim} mA cm^{-2}	$i^{SHE}\left(i^{RHE}\right)$ mA cm^{-2}	s V^{-1}	t_s mV dec^{-1}
100	0.0000				0.0748			
200	0.0000				0.0763			
500	0.0324	0.02490 (0.5860)	-53.95	-42.69	0.1148	0.1418 (2.213)	-46.93	-49.07
1000	0.0713				0.1674			
1500	0.1131				0.2166			
2000	0.1420				0.2517			

Figure 28: Potentiodynamic forward measurements (10 mV s^{-1}) in N$_2$ saturated 0.05 M H$_2$SO$_4$ after 20 min OCP at different rotation rates; measured (dashed) and calculated (solid); a) 1. ORR path, b) 1. ORR path and 2. ORR path, c) ORR in combination with the hydrogen adsorption, d) complete ORR with the HER

As can be seen in Figure 28 the 1. ORR path determines the current density at potentials higher than +0.5 V. At lower potentials the 2. ORR path has to be taken into account (Figure 28 b). The decrease of the diffusion limited ORR current density due to the hydrogen adsorption can be well fitted by equation (4.8) (Figure 28 c). The total current density shown in Figure 28 d and Figure 29 is the sum of the current densities of the two ORR steps and their reduction due to the hydrogen adsorption which can be all calculated using equation (4.8) and of the HER calculated by equation (4.7).

All limiting current densities of the ORRs and the pre-exponential current densities of the HER (Table 15) are in linear relationship with the square root of the rotation rate and show Pearson product-moment correlation coefficients of more than 0.98. The Tafel slopes of the HER are smaller in aerated 0.05 M H_2SO_4 than those found under nitrogen.

Table 15: Kinetic data for the HER in air saturated 0.05 M H_2SO_4 for equation (4.7)

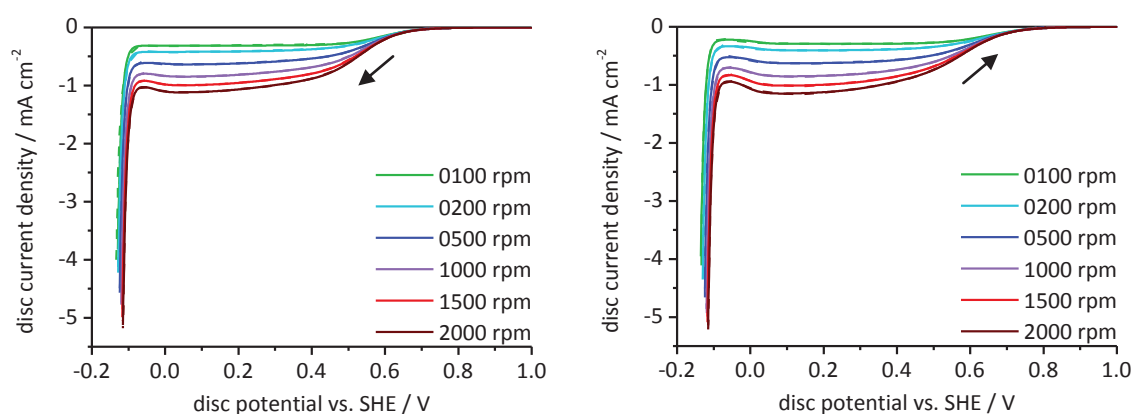| ω rpm	forward scan			reverse scan		
	$i^{SHE}\ (i^{RHE})$ mA cm^{-2}	s V^{-1}	t_s mV dec^{-1}	$i^{SHE}\ (i^{RHE})$ mA cm^{-2}	s V^{-1}	t_s mV dec^{-1}
100	$-4.432 \cdot 10^{-6}$ $(-2.108 \cdot 10^{-3})$			$-1.227 \cdot 10^{-6}$ $(-0.7960 \cdot 10^{-3})$		
200	$-5.328 \cdot 10^{-6}$ $(-2.535 \cdot 10^{-3})$			$-2.299 \cdot 10^{-6}$ $(-1.492 \cdot 10^{-3})$		
500	$-8.302 \cdot 10^{-6}$ $(-3.949 \cdot 10^{-3})$	-105.3	-21.87	$-4.425 \cdot 10^{-6}$ $(-2.871 \cdot 10^{-3})$	-110.6	-20.82
1000	$-12.99 \cdot 10^{-6}$ $(-6.179 \cdot 10^{-3})$			$-7.198 \cdot 10^{-6}$ $(-4.670 \cdot 10^{-3})$		
1500	$-18.29 \cdot 10^{-6}$ $(-8.701 \cdot 10^{-3})$			$-10.06 \cdot 10^{-6}$ $(-6.527 \cdot 10^{-3})$		
2000	$-22.79 \cdot 10^{-6}$ $(-10.84 \cdot 10^{-3})$			$-12.69 \cdot 10^{-6}$ $(-8.233 \cdot 10^{-3})$		

Figure 29: Potentiodynamic polarization curves (10 mV s^{-1}) in N_2 saturated 0.05 M H_2SO_4 after 20 min OCP at different rotation rates; measured (dashed) and complete calculated (solid); forward scan: left, reverse scan: right

5.2.2 HYDROCHLORIC ACID 0.10 M

5.2.2.1 NITROGEN

In N_2 saturated 0.1 M HCl the zero-current potential of the Pt-disc is between +1.00 V and +1.06 V in the forward scan (Figure 30). This is more positive than the zero-current potential measured in 0.05 M H_2SO_4. The charge required for the reduction of the surface layer obtained from the peak at +0.8 V in the forward scan is 145±5 µC cm-2 which is smaller than in sulfuric acid. This difference between HCl and H_2SO_4 was also found by Mayell and Langer [208] and Markovic et al. [221].

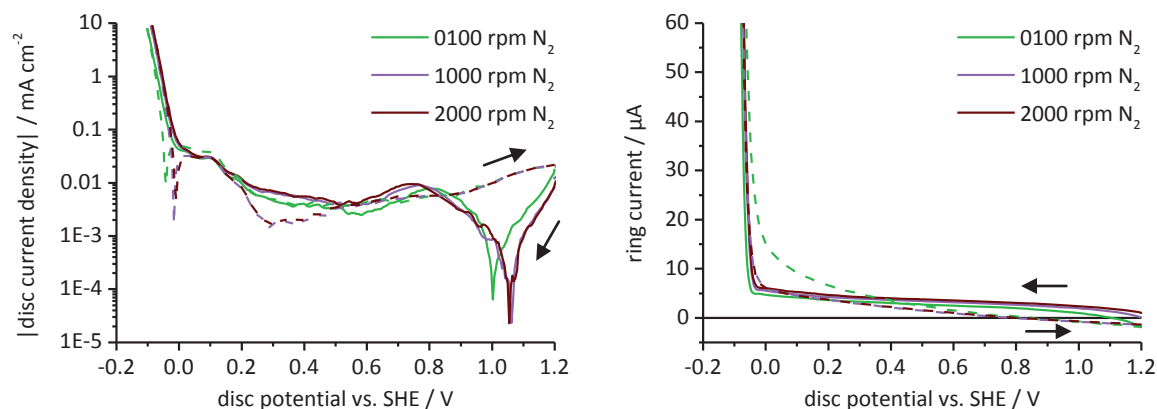Figure 30: Potentiodynamic polarization curves (10 mV s^{-1}) in N$_2$ saturated 0.10 M HCl after 20 min OCP at different rotation rates; ring potential: +1.29 V vs. SHE; forward scan: solid lines, reverse scan: dashed lines

The values of the Tafel slopes obtained for the HER (Table 16) are higher in hydrochloric acid than in sulfuric acid but due to greater pre-exponential current densities the reaction is faster. The measured slopes are larger than the -28 mV dec^{-1} reported by Bockris [163] and Parsons [162] in hydrochloric acid but a Tafel mechanism can still be assumed. Several authors found slopes close to these values in acidic electrolytes [52, 156-159, 161-163, 215].

Table 16: Kinetic data for the HER in N$_2$ saturated 0.10 M HCl for equation (4.7)

ω	forward scan			reverse scan		
	$i^{SHE}\left(i^{RHE}\right)$	s	t_s	$i^{SHE}\left(i^{RHE}\right)$	s	t_s
rpm	mA cm^{-2}	V^{-1}	mV dec^{-1}	mA cm^{-2}	V^{-1}	mV dec^{-1}
100	-0.00917 (-0.470)			-0.00578 (-0.324)		
1000	-0.02219 (-1.138)	-67.26	-34.24	-0.01864 (-1.072)	-69.21	-33.28
2000	-0.02926 (-1.501)			-0.02465 (-1.418)		

The current densities calculated for the HER using equation (4.7) with the kinetic data in Table 16 is shown in Figure 31 and fit well with the measured values. The pre-exponential current densities are even more influenced by the rotation rate than those measured in sulfuric acid.
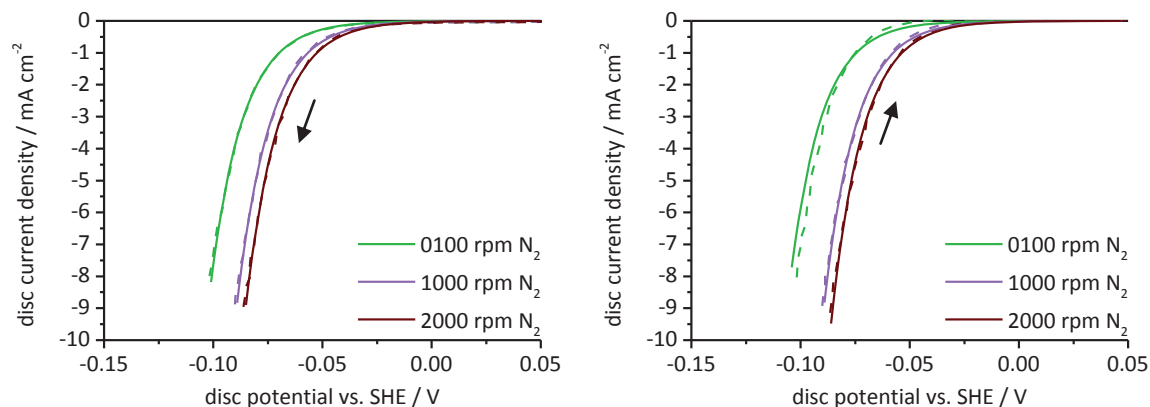

Figure 31: Potentiodynamic polarization curves (10 mV s^{-1}) in N$_2$ saturated 0.10 M HCl after 20 min OCP at different rotation rates; measured (dashed) and calculated (solid); forward scan: left, reverse scan: right
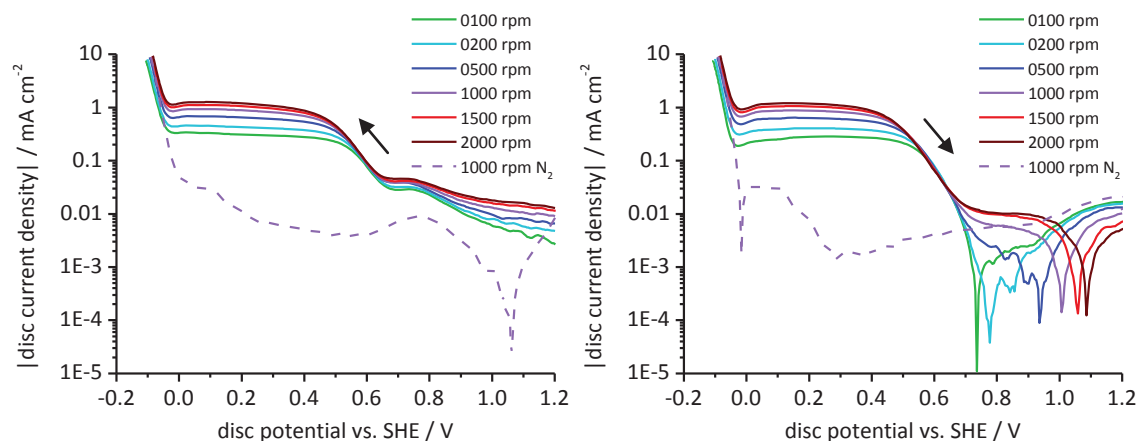
5.2.2.2 Air

Figure 32: Potentiodynamic polarization curves (10 mV s^{-1}) in air saturated 0.10 M HCl after 20 min OCP at different rotation rates; forward scan: left, reverse scan: right

While the measurements in N_2 saturated 0.10 M HCl are similar to those in 0.05 M H_2SO_4 there is a significant difference in aerated solutions. A cathodic step or peak prior to the ORR appears at +0.8 V (Figure 32) in the region where PtO or PtO_2 reduction/formation was measured in sulfuric acid. This cathodic step depends on the rotation rate and is not caused by the reduction of surface platinum chloride, as it also appears in the reverse scan. Hydrochloric acid has been used to strip oxides from a platinum surface [85]. This explains why the oxide film in HCl is smaller than in H_2SO_4. It might also inhibit the formation of a tight oxide film. The porous oxide layer formed instead would have free platinum surface sites which could be available for the ORR.

A shift of the ORR to more negative potentials in hydrochloric acid compared to sulfuric acid is observed and confirms the results of Müller [60]. In 0.05 M H_2SO_4 a current density of -0.100 mA cm^{-2} is reached at +0.58 V. This potential is 60 to 120 mV more negative in hydrochloric acid.

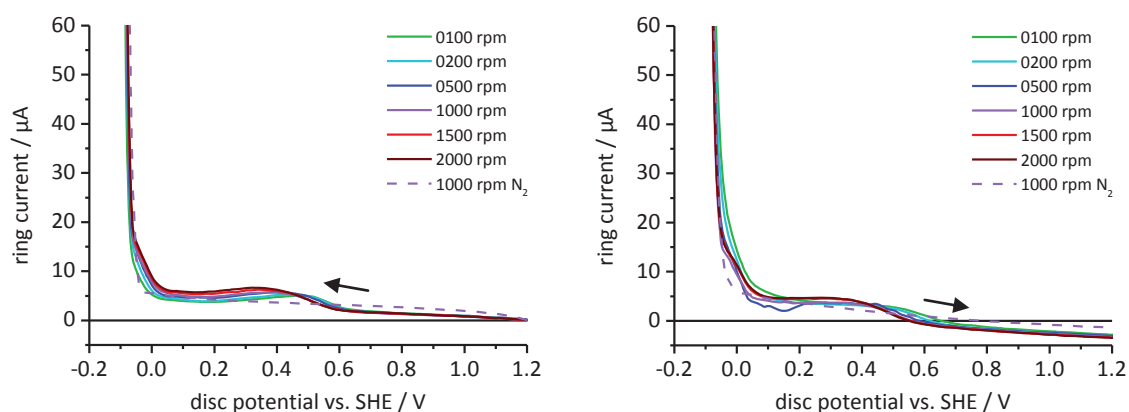Figure 33: Ring currents measured during the potentiodynamic scan (10 mV s^{-1}) at the disc electrode in air saturated 0.10 M HCl after 20 min OCP at different rotation rates; ring potential: +1.29 V vs. SHE; forward scan: left, reverse scan: right

Two current peaks were measured at the ring (Figure 33) similar to those observed in sulfuric acid. The first peak at +0.4 V indicates that the oxygen is also reduced by two different reaction paths in HCl. The peaks are in a range of 4 µA at +0.4 V and smaller than 10 µA with the hydrogen adsorption.

Table 17: Kinetic data for the 1. ORR path in air saturated 0.10 M HCl for equation (4.8)

	forward scan				reverse scan			
ω rpm	i_{lim} mA cm^{-2}	i^{SHE} (i^{ROE}) mA cm^{-2}	s V^{-1}	t_s mV dec^{-1}	i_{lim} mA cm^{-2}	i^{SHE} (i^{ROE}) mA cm^{-2}	s V^{-1}	t_s mV dec^{-1}
100	-0.2865				-0.2687			
200	-0.3927				-0.3889			
500	-0.5843	-15220	-19.69	-117.0	-0.5269	-44040	-22.06	-104.4
1000	-0.7811	(-1.462·10^{-6})			-0.6650	(-0.2634·10^{-6})		
1500	-0.9236				-0.7636			
2000	-1.0418				-0.8327			

The two ORR paths have similar slopes (Table 17 and Table 18), but can be separated by their different pre-exponential current densities at the ROE. As it was the case in sulfuric acid, the first ORR path dominates the total current for the ORR.

Table 18: Kinetic data for the 2. ORR path in air saturated 0.10 M HCl for equation (4.8)

	forward scan				reverse scan			
ω rpm	i_{lim} mA cm^{-2}	i^{SHE} (i^{ROE}) mA cm^{-2}	s V^{-1}	t_s mV dec^{-1}	i_{lim} mA cm^{-2}	i^{SHE} (i^{ROE}) mA cm^{-2}	s V^{-1}	t_s mV dec^{-1}
100	-0.0383				-0.0094			
200	-0.0542				-0.0143			
500	-0.0977	-58.12	-23.38	-98.51	-0.1029	-468.4	-19.77	-116.5
1000	-0.1482	(-7.406·10^{-11})			-0.2045	(-4.097·10^{-8})		
1500	-0.1874				-0.2819			
2000	-0.2131				-0.3510			

The diffusion limiting current densities of the ORR are 10 % to 48 % smaller at the onset of the hydrogen evolution which indicates up to nearly 96 % hydrogen peroxide formation for the ORR. The small currents at the ring electrode can be explained by the inhibition of the H_2O_2 oxidation by chloride as was found by Hall et al. [119].

Table 19: Kinetic data for the ORR in combination with the hydrogen adsorption in air saturated 0.10 M HCl for equation (4.8)
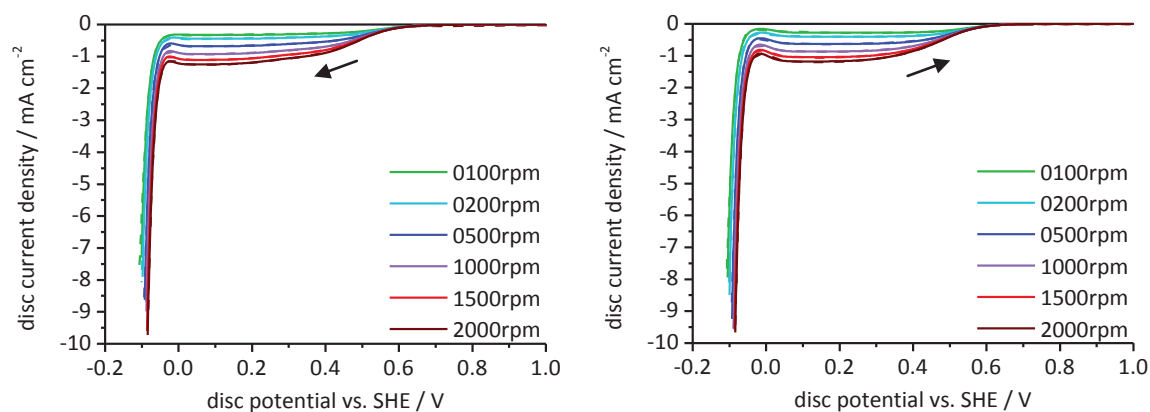
	forward scan				reverse scan			
ω rpm	i_{lim} mA cm^{-2}	i^{SHE} (i^{RHE}) mA cm^{-2}	s V^{-1}	t_s mV dec^{-1}	i_{lim} mA cm^{-2}	i^{SHE} (i^{RHE}) mA cm^{-2}	s V^{-1}	t_s mV dec^{-1}
100	0.0304				0.1616			
200	0.0927				0.1831			
500	0.2613	0.07867	-79.06	-29.13	0.2996	0.4032	-56.28	-40.92
1000	0.3672	(8.053)			0.3944	(10.88)		
1500	0.4921				0.4533			
2000	0.5423				0.5200			

The kinetics of the HER are unaffected by the ORR and only slightly higher pre-exponential current densities were observed (Table 20) compared to those measured in deaerated solution. This is in agreement with the observation of Hickling and Slat [222] that the presence of oxygen does not influence the HER in hydrochloric acid.

As can be seen in Figure 34 the calculated current densities are in good agreement with the measured values.
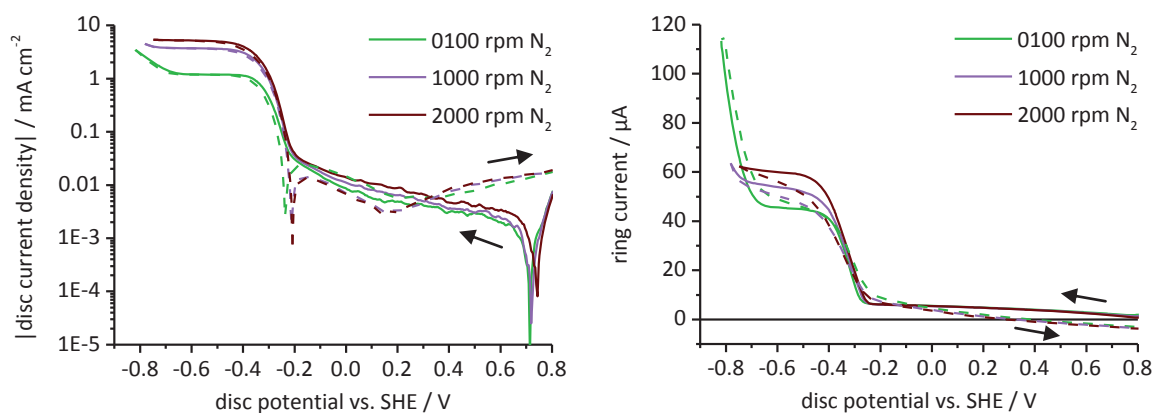
Table 20: Kinetic data for the HER adsorption in air saturated 0.10 M HCl for equation (4.7)

ω	forward scan			reverse scan		
	$i^{SHE}\ (i^{RHE})$	s	t_s	$i^{SHE}\ (i^{RHE})$	s	t_s
rpm	mA cm^{-2}	V^{-1}	mV dec^{-1}	mA cm^{-2}	V^{-1}	mV dec^{-1}
100	-0.00834 (-0.413)			-0.00646 (-0.338)		
200	-0.01097 (-0.545)			-0.00956 (-0.501)		
500	-0.01778 (-0.881)	-66.67	-34.54	-0.01654 (-0.867)	-67.63	-34.05
1000	-0.02383 (-1.181)			-0.02206 (-1.157)		
1500	-0.02902 (-1.438)			-0.02676 (-1.403)		
2000	-0.03328 (-1.649)			-0.03069 (-1.609)		

Figure 34: Potentiodynamic polarization curves (10 mV s^{-1}) in air saturated 0.10 M HCl after 20 min OCP at different rotation rates; measured (dashed) and calculated (solid); forward scan: left, reverse scan: right

5.2.3 SODIUM SULFATE 0.05 M BUFFERED AT PH 4.5

5.2.3.1 NITROGEN

Figure 35: Potentiodynamic polarization curves (10 mV s^{-1}) in N$_2$ saturated 0.05 M Na$_2$SO$_4$ pH 4.5 after 20 min OCP at different rotation rates; ring potential: +1.29 V vs. SHE; forward scan: solid lines, reverse scan: dashed lines

The zero-current potentials of the disc electrode in deaerated 0.05 M Na_2SO_4 buffered with 0.01 M potassium hydrogen phthalate at pH 4.5 are between +0.71 V and +0.74 V in the forward scan (Figure 35). This value is 250 mV more negative than in 0.05 M sulfuric acid and is in good agreement with the potential shift expected from the Nernst equation of -210 mV. In the reverse scan the zero-current potentials show a difference of 150 mV to that measured in sulfuric acid. No oxide reduction peak can be seen in the forward scans but the reverse scans show the expected oxide formation which starts at +0.18 V.

The diffusion limited HER {5.10} starts around -0.2 V while the onset of the HER from water {5.11} is at -0.6 V.

$$2\,H^+ + 2\,e^- \rightleftharpoons H_2 \qquad\qquad \{5.10\}$$

$$H_2O + 2\,e^- \rightleftharpoons H_2 + 2\,OH^- \qquad\qquad \{5.11\}$$

The HER {5.10} does not show the straight Tafel slope and therefore it is necessary to consider the reversible HER without hydrogen in the solution as has been shown in chapter 1.4. This effect will be further discussed for the alkaline electrolytes (chapter 5.3) since this effect is more pronounced at higher pH-values. For the fitting of the diffusion limited HER equation (4.8) is used. Both HER paths {5.10} and {5.11} in this electrolyte follow a Heyrovský mechanism (Table 21 and Table 22). Schuldiner [156] showed a change from a Tafel mechanism to a Heyrovský mechanism at pH-values between 2 and 3.
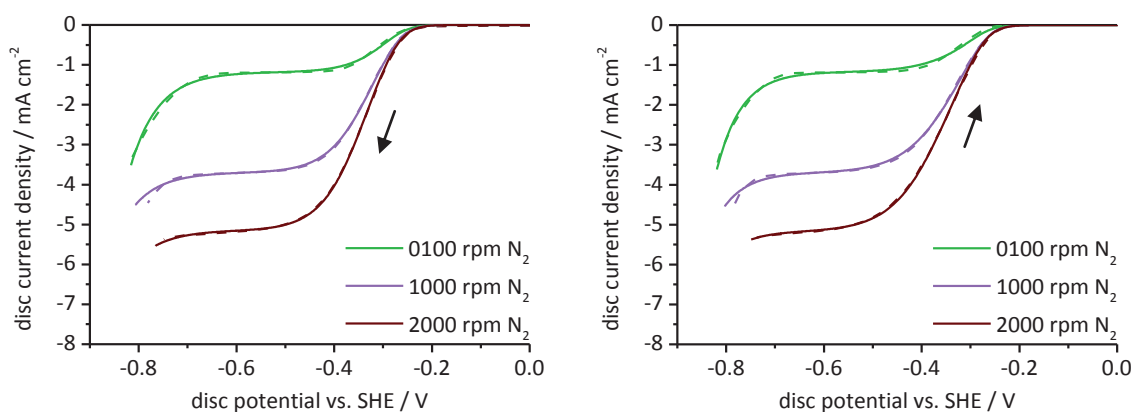
The kinetic data obtained for the HER from water {5.11} is not very accurate as a significant current was only measured at the lowest rotation rate. This leads to a poor fit at high potentials between the current densities calculated by the sum of equation (4.8) and equation (4.10) for the HER and the measured values (Figure 36).

Table 21: Kinetic data for the diffusion limited HER in 0.05 M Na_2SO_4 pH 4.5 for equation (4.10)
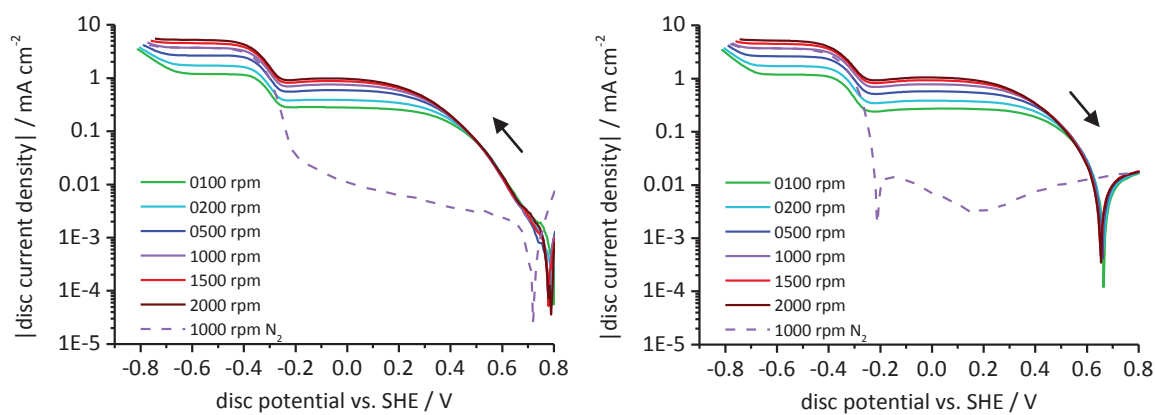
		forward scan					
ω rpm	i_{lim} mA cm^{-2}	$i^{SHE}\,(i^{RHE})$ mA cm^{-2}	s V^{-1}	t_s mV dec^{-1}	$i_b^{SHE}\,(i_b^{RHE})$ mA cm^{-2}	s_b V^{-1}	t_b mV dec^{-1}
100	-1.181	$-1.695 \cdot 10^{-3}$ (-0.5878)					
1000	-3.698	$-2.431 \cdot 10^{-3}$ (-0.8430)	-22.20	-103.7	30640 (1.088)	38.89	59.23
2000	-5.150	$-2.648 \cdot 10^{-3}$ (-0.9182)					
		reverse scan					
ω rpm	i_{lim} mA cm^{-2}	$i^{SHE}\,(i^{RHE})$ mA cm^{-2}	s V^{-1}	t_s mV dec^{-1}	$i_b^{SHE}\,(i_b^{RHE})$ mA cm^{-2}	s_b V^{-1}	t_b mV dec^{-1}
100	-1.240	$-3.573 \cdot 10^{-3}$ (-0.4901)					
1000	-3.908	$-6.691 \cdot 10^{-3}$ (-0.9179)	-18.68	-123.3	80350 (1.577)	41.14	55.98
2000	-5.463	$-6.626 \cdot 10^{-3}$ (-0.9090)					

Table 22: Kinetic data for the HER in 0.05 M Na_2SO_4 at pH 4.5 for equation (4.8)

ω rpm	forward scan			reverse scan		
	$i^{SHE} \left(i^{RHE}\right)$ mA cm^{-2}	s V^{-1}	t_s mV dec^{-1}	$i^{SHE} \left(i^{RHE}\right)$ mA cm^{-2}	s V^{-1}	t_s mV dec^{-1}
100	$-1.494 \cdot 10^{-6}$ $(-14.94 \cdot 10^{-5})$			$-0.2084 \cdot 10^{-6}$ $(-4.178 \cdot 10^{-5})$		
1000	$-0.6077 \cdot 10^{-6}$ $(-6.077 \cdot 10^{-5})$	-17.48	-131.7	$-0.09905 \cdot 10^{-6}$ $(-1.986 \cdot 10^{-5})$	-20.12	-114.4
2000	$-0.5905 \cdot 10^{-6}$ $(-5.905 \cdot 10^{-5})$			$-0.06976 \cdot 10^{-6}$ $(-1.399 \cdot 10^{-5})$		

Figure 36: Potentiodynamic polarization curves (10 mV s^{-1}) in N_2 saturated 0.05 M Na_2SO_4 at pH 4.5 after 20 min OCP at different rotation rates; measured (dashed) and calculated (solid); forward scan: left, reverse scan: right

5.2.3.2 AIR

Figure 37: Potentiodynamic polarization curves (10 mV s^{-1}) in air saturated 0.05 M Na_2SO_4 at pH 4.5 after 20 min OCP at different rotation rates; forward scan: left, reverse scan: right

In aerated 0.05 M Na_2SO_4 solutions buffered at pH 4.5 the zero-current potentials are at +0.79 V in the forward scan and at +0.66 V in the reverse scan (Figure 37). Compared to the values in 0.05 M H_2SO_4 the zero-current potentials are 230 mV and 170 mV more negative. The ORR shows a limiting current density at 0.0 V while at more negative potentials (-0.5 V) a second limiting current density caused by the mass transport limited reduction of protons appears.

The limiting current densities of the HER under nitrogen almost overlap with the sum of the limiting current densities of the ORR and that of the proton reduction {5.10} under air (Figure 38). This can be explained by the fact that the hydrogen ions consumed by reaction {1.15} or {5.12} are not any longer available for the HER.
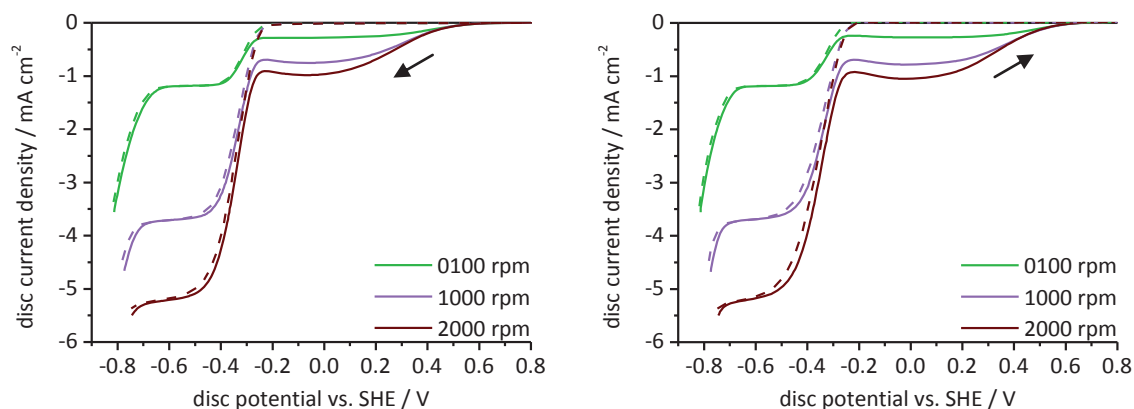
$$O_2 + 2\,H^+ + 2\,e^- \rightleftharpoons H_2O_2 \qquad\qquad \{5.12\}$$

Figure 38: Potentiodynamic polarization curves (10 mV s^{-1}) in air (solid) and N$_2$ (dashed) saturated 0.05 M Na$_2$SO$_4$ at pH 4.5 after 20 min OCP at different rotation rates; forward scan: left, reverse scan: right

At the ring electrode two peaks appear prior to the hydrogen oxidation at -0.25 V (Figure 39). The first peak reaches currents between 1.1 µA and 4.8 µA at -0.1 V and can be explained by a second ORR path at the disc in which hydrogen peroxide is formed as an intermediate. The second peak is caused by the hydrogen peroxide formed with the hydrogen adsorption at the disc at -0.23 V where it reaches currents between 2.0 µA and 7.6 µA.

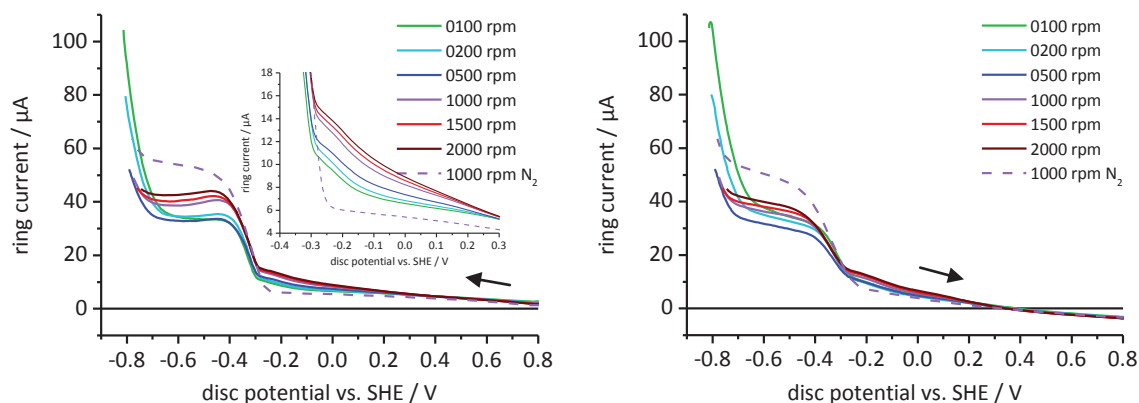

Figure 39: Ring currents measured during the potentiodynamic scan (10 mV s^{-1}) at the disc electrode in air saturated 0.05 M Na$_2$SO$_4$ at pH 4.5 after 20 min OCP at different rotation rates; ring potential: +1.29 V vs. SHE; forward scan: left, reverse scan: right

The forward scan shows a peak at -0.4 V in the ring current atop the step of the hydrogen oxidation. This additional current might be due to the oxidation of the ring electrode by hydrogen peroxide, formed during the forward scan at the disc electrode. Such an oxidized and thereby passivated ring electrode would also explain why the ring currents in the reverse scan are lower under air than under nitrogen.

Table 23: Kinetic data for the 1. ORR path in air saturated 0.05 M Na$_2$SO$_4$ at pH 4.5 for equation (4.8)

	forward scan				reverse scan			
ω rpm	i_{lim} mA cm^{-2}	$i^{\text{SHE}}\left(i^{\text{ROE}}\right)$ mA cm^{-2}	s V^{-1}	t_{s} mV dec^{-1}	i_{lim} mA cm^{-2}	$i^{\text{SHE}}\left(i^{\text{ROE}}\right)$ mA cm^{-2}	s V^{-1}	t_{s} mV dec^{-1}
100	-0.2800				-0.2733			
200	-0.3665				-0.3864			
500	-0.5488	-40.87 (-2.041·10^{-4})	-12.63	-182.4	-0.5764	-82.69 (-4.727·10^{-4})	-12.49	-184.4
1000	-0.6691				-0.7836			
1500	-0.7611				-0.8092			
2000	-0.8302				-0.8683			

The limiting current densities of both ORR paths in the forward scans are in a linear relationship with the square root of the rotation rate (Table 23 and Table 24). This correlation is poor in the reverse scan as the 2. ORR path has no significant current density contribution up to 1000 rpm. The 1. ORR path shows Tafel slopes of about -180 mV dec^{-1} while the Tafel slopes of the 2. ORR path are closer to the expected -120 mV dec^{-1} for a one electron transfer reaction with a charge transfer coefficient of 0.5.

Table 24: Kinetic data for the 2. ORR path in air saturated 0.05 M Na$_2$SO$_4$ at pH 4.5 for equation (4.8)

	forward scan				reverse scan			
ω rpm	i_{lim} mA cm^{-2}	$i^{\text{SHE}}\left(i^{\text{ROE}}\right)$ mA cm^{-2}	s V^{-1}	t_{s} mV dec^{-1}	i_{lim} mA cm^{-2}	$i^{\text{SHE}}\left(i^{\text{ROE}}\right)$ mA cm^{-2}	s V^{-1}	t_{s} mV dec^{-1}
100	-0.0002				-0.0028			
200	-0.0251				-0.0032			
500	-0.0467	-2.488 (-1.341·10^{-9})	-22.08	-104.3	-0.0042	-14.02 (-53.24·10^{-9})	-20.06	-114.8
1000	-0.0866				-0.0055			
1500	-0.1225				-0.1201			
2000	-0.1584				-0.1779			

The decrease in the limited current density at the disc due to the hydrogen adsorption (Table 25) is lower in the pH 4.5 buffered sodium sulfate solution compared to the sulfuric acid (chapter 5.2.1.2).

Table 25: Kinetic data for the ORR in combination with the hydrogen adsorption in air saturated 0.05 M Na$_2$SO$_4$ at pH 4.5 for equation (4.8)

	forward scan				reverse scan			
ω rpm	i_{lim} mA cm^{-2}	$i^{\text{SHE}}\left(i^{\text{RHE}}\right)$ mA cm^{-2}	s V^{-1}	t_{s} mV dec^{-1}	i_{lim} mA cm^{-2}	$i^{\text{SHE}}\left(i^{\text{RHE}}\right)$ mA cm^{-2}	s V^{-1}	t_{s} mV dec^{-1}
100	0.00982				0.0622			
200	0.03528				0.0894			
500	0.07353	1.195·10^{-5} (4.414)	-48.66	-47.33	0.1361	0.8370·10^{-5} (0.01965)	-29.46	-78.16
1000	0.08047				0.1755			
1500	0.08458				0.1746			
2000	0.08573				0.1719			

The cathodic pre-exponential current densities of the diffusion limited HER are only diffusion controlled at low rotation rates (Table 26). With the larger set of data measured under air it is possible to determine the kinetic values of the HER from water more exact than with the measurements under nitrogen (Table 27).

Table 26: Kinetic data of the diffusion limited HER in 0.05 M Na_2SO_4 at pH 4.5 for equation (4.10)

			forward scan				
ω rpm	i_{lim} mA cm^{-2}	$i^{SHE}\ (i^{RHE})$ mA cm^{-2}	s V^{-1}	t_s mV dec^{-1}	$i_b^{SHE}\ (i_b^{RHE})$ mA cm^{-2}	s_b V^{-1}	t_b mV dec^{-1}
100	-0.928	$-0.6531 \cdot 10^{-3}$ (-0.3877)					
200	-1.364	$-0.7418 \cdot 10^{-3}$ (-0.4403)					
500	-2.148	$-0.9678 \cdot 10^{-3}$ (-0.5745)	-24.19	-95.19	$3.903 \cdot 10^{5}$ (3.118)	44.46	51.80
1000	-3.033	$-1.034 \cdot 10^{-3}$ (-0.6138)					
1500	-3.720	$-1.062 \cdot 10^{-3}$ (-0.6304)					
2000	-4.291	$-1.063 \cdot 10^{-3}$ (-0.6310)					
			reverse scan				
ω rpm	i_{lim} mA cm^{-2}	$i^{SHE}\ (i^{RHE})$ mA cm^{-2}	s V^{-1}	t_s mV dec^{-1}	$i_b^{SHE}\ (i_b^{RHE})$ mA cm^{-2}	s_b V^{-1}	t_b mV dec^{-1}
100	-0.991	-0.00800 (-0.7702)					
200	-1.431	-0.01206 (-1.161)					
500	-2.195	-0.01528 (-1.471)	-17.30	-133.1	$2.545 \cdot 10^{4}$ (4.200)	32.99	69.81
1000	-3.101	-0.01546 (-1.488)					
1500	-3.774	-0.01431 (-1.378)					
2000	-4.343	-0.01304 (-1.255)					

In the aerated solution at high current densities and low rotation rates the total current densities do not fit the measured values (Figure 40). Such a poor fit at low rotation rates was only found in the two pH 4.5 electrolytes and in the 0.05 M Na_2SO_4 at pH 9.5 (chapter 5.3.2).
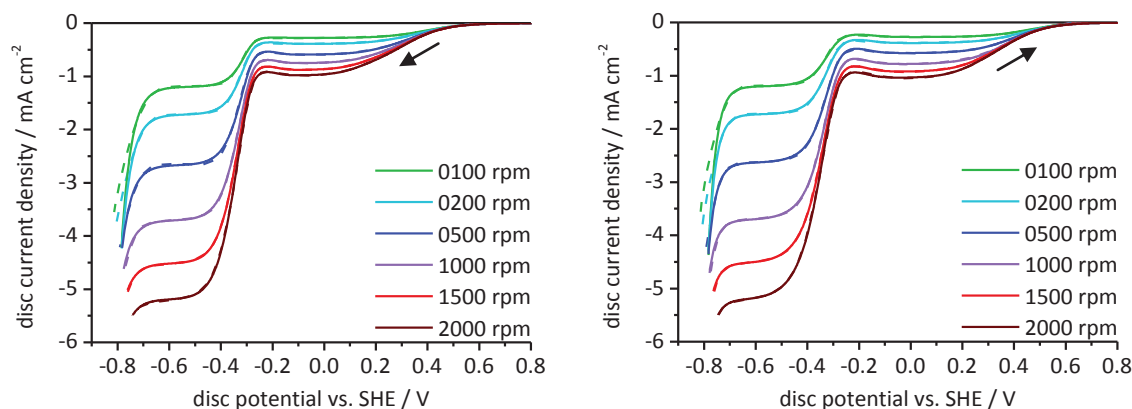

Figure 40: Potentiodynamic polarization curves (10 mV s^{-1}) in air saturated 0.05 M Na_2SO_4 at pH 4.5 after 20 min OCP at different rotation rates; measured (dashed) and calculated (solid); forward scan: left, reverse scan: right

Table 27: Kinetic data for the HER from water in air saturated 0.05 M Na_2SO_4 at pH 4.5 for equation (4.7)

ω rpm	forward scan			reverse scan		
	$i^{SHE}\ (i^{RHE})$ mA cm^{-2}	s V^{-1}	t_s mV dec^{-1}	$i^{SHE}\ (i^{RHE})$ mA cm^{-2}	s V^{-1}	t_s mV dec^{-1}
100	$-3.772 \cdot 10^{-9}$ $(-3.674 \cdot 10^{-6})$			$-4.797 \cdot 10^{-12}$ $(-4.551 \cdot 10^{-8})$		
200	$-3.221 \cdot 10^{-9}$ $(-3.137 \cdot 10^{-6})$			$-3.876 \cdot 10^{-12}$ $(-3.677 \cdot 10^{-8})$		
500	$-2.100 \cdot 10^{-9}$ $(-2.045 \cdot 10^{-6})$	-26.12	-88.18	$-2.598 \cdot 10^{-12}$ $(-2.465 \cdot 10^{-8})$	-34.76	-66.26
1000	$-1.440 \cdot 10^{-9}$ $(-1.403 \cdot 10^{-6})$			$-1.726 \cdot 10^{-12}$ $(-1.637 \cdot 10^{-8})$		
1500	$-1.163 \cdot 10^{-9}$ $(-1.133 \cdot 10^{-6})$			$-1.542 \cdot 10^{-12}$ $(-1.463 \cdot 10^{-8})$		
2000	$-1.149 \cdot 10^{-9}$ $(-1.119 \cdot 10^{-6})$			$-1.601 \cdot 10^{-12}$ $(-1.519 \cdot 10^{-8})$		

5.2.4 SODIUM CHLORIDE 0.10 M BUFFERED AT PH 4.5

5.2.4.1 NITROGEN

In the sodium chloride solution buffered with 0.01 M potassium hydrogen phthalate at pH 4.5 a reduction peak of 702±11 µC cm^{-2} with a maximum at +0.48 V appeared (Figure 41) while no peak appeared in the sodium sulfate solution at pH 4.5. The large peak area is much higher than the 420 µC cm^{-2} [86, 87, 110] which would be expected for the reduction of a complete PtO monolayer. Therefore the dominant oxide specie must be the PtO_2.

At higher rotation rates the reverse scans show a cathodic current density at the disc electrode over the measured potential range while no zero-current potential appears. At 100 rpm a hydrogen oxidation peak forms at -0.1 V. This is followed by a reaction causing a cathodic current up to +0.66 V. A possible explanation would be the reduction of rest oxygen in the solution. This ORR would also, as observed, lead to an increase of the cathodic current at higher rotation rates.
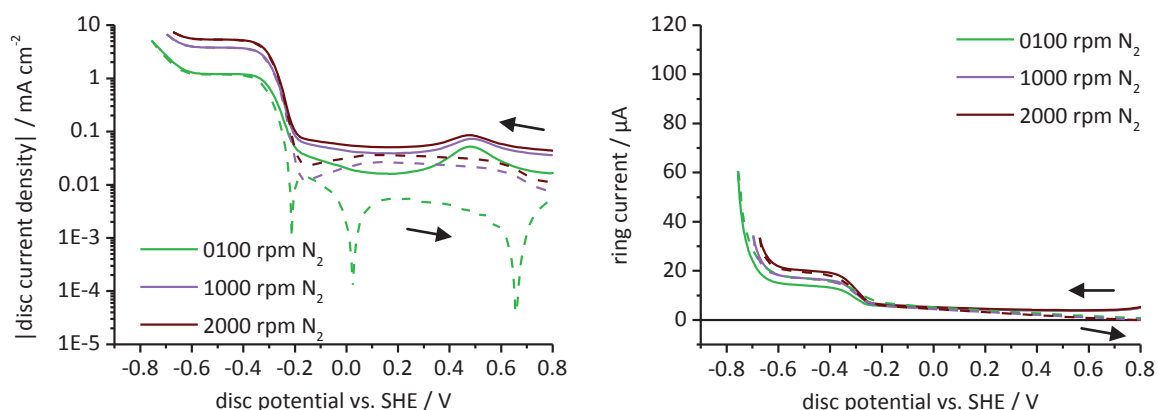

Figure 41: Potentiodynamic polarization curves (10 mV s^{-1}) in N_2 saturated 0.10 M NaCl pH 4.5 after 20 min OCP at different rotation rates; ring potential: +1.29 V vs. SHE; forward scan: solid lines, reverse scan: dashed lines

The hydrogen evolution from protons {5.10} starts around -0.2 V at the disc electrode and leads to a positive current due to the hydrogen oxidation at the ring electrode. Both currents show a limited

current density caused by mass transport. At about -0.5 V reaction {5.11} takes place at the disc electrode which also leads to a further increase of the ring current.

Table 28: Kinetic data for the HER in 0.10 M NaCl pH 4.5 for equation (4.7)

ω rpm	forward scan $i^{\mathrm{SHE}}\left(i^{\mathrm{RHE}}\right)$ mA cm^{-2}	s V^{-1}	t_{s} mV dec^{-1}	reverse scan $i^{\mathrm{SHE}}\left(i^{\mathrm{RHE}}\right)$ mA cm^{-2}	s V^{-1}	t_{s} mV dec^{-1}
100	-1.804·10^{-6} (-3.008·10^{-4})			-0.2101·10^{-6} (0.7355·10^{-4})		
1000	-3.579·10^{-6} (-5.967·10^{-4})	-19.38	-118.9	-0.5101·10^{-6} (-1.786·10^{-4})	-22.19	-103.8
2000	-3.872·10^{-6} (-6.455·10^{-4})			-0.6100·10^{-6} (-2.135·10^{-4})		

The Tafel slope of the HER from water shows the expected -118 mV dec^{-1} for a Heyrovský mechanism (Table 28). The diffusion limited HER has slopes close to -60 mV dec^{-1} (Table 29) which indicates neither a Heyrovský mechanism nor a Tafel mechanism. This slope is close to the -59 mV dec^{-1} expected for a reversible system which is always in equilibrium due to a fast charge-transfer process.

The current densities for the two HERs calculated by the sum of equation (4.7) and equation (4.10) using the kinetic data from Table 29 and Table 28 fit well with the measured values (Figure 42).

Table 29: Kinetic data of the diffusion limited HER in 0.10 NaCl pH 4.5 for equation (4.10)

ω rpm	i_{lim} mA cm^{-2}	forward scan $i^{\mathrm{SHE}}\left(i^{\mathrm{RHE}}\right)$ mA cm^{-2}	s V^{-1}	t_{s} mV dec^{-1}	$i_{\mathrm{b}}^{\mathrm{SHE}}\left(i_{\mathrm{b}}^{\mathrm{RHE}}\right)$ mA cm^{-2}	s_{b} V^{-1}	t_{b} mV dec^{-1}
100	-1.155	-2.046·10^{-5} (-0.4520)					
1000	-3.684	-4.833·10^{-5} (-1.068)	-37.89	-60.79	441.4 (0.06234)	33.58	68.58
2000	-5.272	-6.676·10^{-5} (-1.475)					

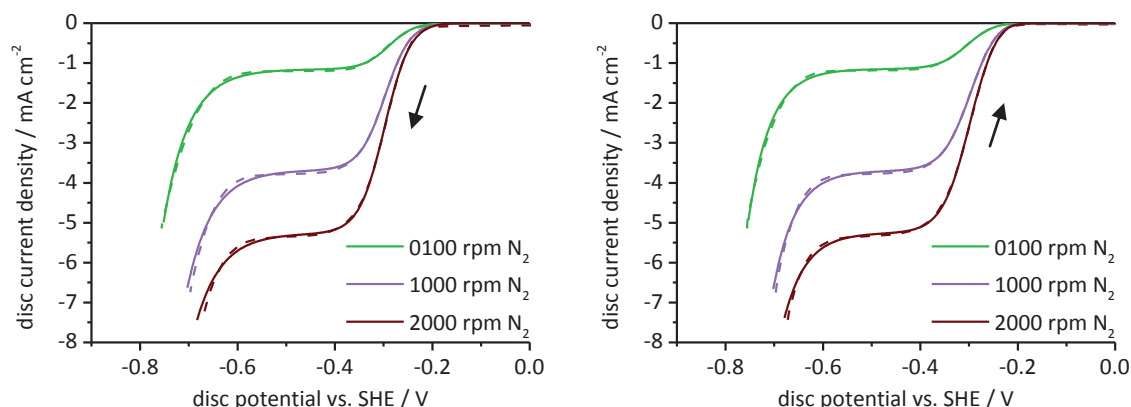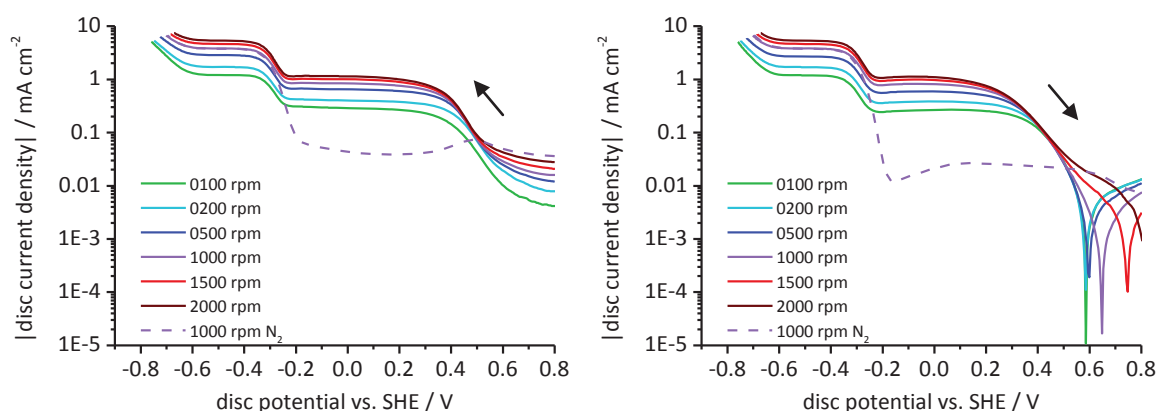| ω rpm	i_{lim} mA cm^{-2}	reverse scan $i^{\mathrm{SHE}}\left(i^{\mathrm{RHE}}\right)$ mA cm^{-2}	s V^{-1}	t_{s} mV dec^{-1}	$i_{\mathrm{b}}^{\mathrm{SHE}}\left(i_{\mathrm{b}}^{\mathrm{RHE}}\right)$ mA cm^{-2}	s_{b} V^{-1}	t_{b} mV dec^{-1}
100	-1.146	-2.361·10^{-5} (-0.2605)					
1000	-3.699	-9.722·10^{-5} (-1.073)	-35.26	-65.32	218800 (0.1193)	54.63	42.16
2000	-5.257	-13.37·10^{-5} (-1.475)					

Figure 42: Potentiodynamic polarization curves (10 mV s^{-1}) in N$_2$ saturated 0.10 M NaCl pH 4.5 after 20 min OCP at different rotation rates; measured (dashed) and calculated (solid); forward scan: left, reverse scan: right

5.2.4.2 Air

As it has been seen in the hydrochloric acid solution a step appeared prior to the ORR in buffered 0.1 M NaCl solution with pH 4.5 (Figure 43). The ORR starts at +0.6 V. As observed in sulfate solutions (chapter 5.2.3.2) the limited current densities of the HER under nitrogen almost overlap with the sum of the limiting current densities of the ORR and that of the proton reduction {5.10} under air.

As observed in the sulfate solutions at pH 4.5 the ring currents in the buffered sodium chloride solution at pH 4.5 (Figure 44) show two peaks prior to the HER. The first one is caused by a second ORR path becoming rate determining below +0.4 V and causing ring currents smaller than 2 µA at -0.1 V. The second peak in the hydrogen adsorption region is barely visible in the forward scan and reaches currents between 2.6 µA and 5.5 µA at -0.23 V but is more pronounced in the reverse scan.

Figure 43: Potentiodynamic polarization curves (10 mV s^{-1}) in air saturated 0.10 M NaCl pH 4.5 after 20 min OCP at different rotation rates; forward scan: left, reverse scan: right

The pre-exponential current density caused by the 1. ORR path in the forward scan measured at 100 rpm is significantly smaller than the pre-exponential current densities measured at higher rotation rates (Table 30), which are almost equal.
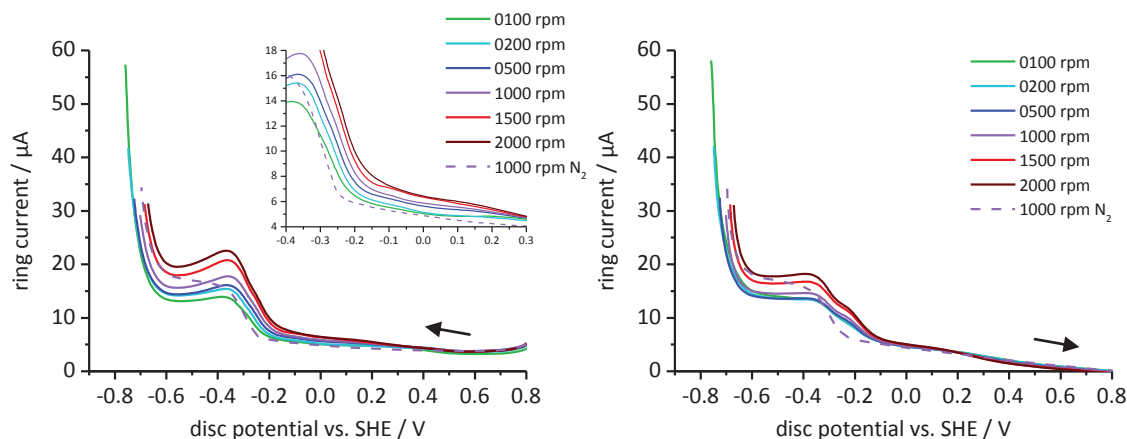
Figure 44: Ring currents measured during the potentiodynamic scan (10 mV s^{-1}) at the disc electrode in air saturated 0.10 M NaCl at pH 4.5 after 20 min OCP at different rotation rates; ring potential: +1.29 V vs. SHE; forward scan: left, reverse scan: right

In the forward scan 14 % to 29 % of the oxygen is reduced by the 2. ORR path. During the reverse scan this path can be neglected at low rotation rates but its contribution to the total ORR increases to 23 % at 2000 rpm.

Table 30: Kinetic data for the 1. ORR path in air saturated 0.10 M NaCl at pH 4.5 for equation (4.8)

		forward scan				reverse scan		
ω rpm	i_{lim} mA cm^{-2}	$i^{\text{SHE}}\left(i^{\text{ROE}}\right)$ mA cm^{-2}	s V^{-1}	t_s mV dec^{-1}	i_{lim} mA cm^{-2}	$i^{\text{SHE}}\left(i^{\text{ROE}}\right)$ mA cm^{-2}	s V^{-1}	t_s mV dec^{-1}
100	-0.2094	-1714 (-2.817·10^{-6})			-0.2678			
200	-0.3224	-3282 (-5.394·10^{-6})			-0.3831			
500	-0.5022	-3259 (-5.356·10^{-6})	-20.96	-109.9	-0.5472	-89.91 (-26.31·10^{-6})	-15.59	-147.8
1000	-0.6716	-3280 (-5.391·10^{-6})			-0.6891			
1500	-0.7957	-3202 (-5.263·10^{-6})			-0.7902			
2000	-0.8949	-3230 (-5.309·10^{-6})			-0.8720			

The limiting current densities of the two ORR paths show a linear relationship with the square root of the rotation rate. Only the limited current densities at 100 rpm in the 2. ORR path (Table 31) deviate from this linearity.

Table 31: Kinetic data for the 2. ORR path in air saturated 0.10 M NaCl at pH 4.5 for equation (4.8)

		forward scan				reverse scan		
ω rpm	i_{lim} mA cm^{-2}	$i^{\text{SHE}}\left(i^{\text{ROE}}\right)$ mA cm^{-2}	s V^{-1}	t_s mV dec^{-1}	i_{lim} mA cm^{-2}	$i^{\text{SHE}}\left(i^{\text{ROE}}\right)$ mA cm^{-2}	s V^{-1}	t_s mV dec^{-1}
100	-0.0849				-0.0019			
200	-0.0832				-0.0026			
500	-0.1183	-4.331 (-2.034·10^{-6})	-15.10	-152.5	-0.0471	-2.154 (-2.050·10^{-8})	-19.14	-120.3
1000	-0.1762				-0.1383			
1500	-0.2208				-0.2062			
2000	-0.2607				-0.2651			

Similar to the sodium sulfate electrolyte at pH 4.5 the amount of hydrogen peroxide formed in the hydrogen adsorption region in the sodium chloride solution at pH 4.5 is higher in the reverse scan than in the forward scan (Table 32).

Table 32: Kinetic data for the ORR in combination with the hydrogen adsorption in air saturated 0.10 M NaCl at pH 4.5 for equation (4.8)

ω rpm	i_{lim} mA cm^{-2}	forward scan			i_{lim} mA cm^{-2}	reverse scan		
		$i^{\text{SHE}}\left(i^{\text{RHE}}\right)$ mA cm^{-2}	s V^{-1}	t_s mV dec^{-1}		$i^{\text{SHE}}\left(i^{\text{RHE}}\right)$ mA cm^{-2}	s V^{-1}	t_s mV dec^{-1}
100	0.0009				0.0279			
200	0.0060				0.0338			
500	0.0342	$4.009 \cdot 10^{-15}$	-148.1	-15.54	0.0565	$1.229 \cdot 10^{-4}$	-35.93	-64.09
1000	0.0771	(382.0)			0.1078	(1.618)		
1500	0.1104				0.1513			
2000	0.1290				0.1942			

The Tafel slopes of the diffusion limited HER are close to -60 mV dec^{-1} (Table 33). As has been stated in chapter 1.4, the pre-exponential and the limiting current densities for this reaction (Table 34) are increasing linearly with the square root of the rotation rate.

Table 33: Kinetic data of the diffusion limited HER in air saturated 0.10 M NaCl at pH 4.5 for equation (4.10)

ω rpm	i_{lim} mA cm^{-2}	forward scan					
		$i^{\text{SHE}}\left(i^{\text{RHE}}\right)$ mA cm^{-2}	s V^{-1}	t_s mV dec^{-1}	$i_b^{\text{SHE}}\left(i_b^{\text{RHE}}\right)$ mA cm^{-2}	s_b V^{-1}	t_b mV dec^{-1}
100	-0.909	$-2.551 \cdot 10^{-6}$ (-0.2082)					
200	-1.301	$-3.260 \cdot 10^{-6}$ (-0.2661)					
500	-2.100	$-5.000 \cdot 10^{-6}$ (-0.4081)	-42.84	-53.75	34.80 (0.2200)	19.18	120.1
1000	-3.015	$-7.537 \cdot 10^{-6}$ (-0.6151)					
1500	-3.711	$-9.676 \cdot 10^{-6}$ (-0.7897)					
2000	-4.304	$-11.49 \cdot 10^{-6}$ (-0.9377)					
ω rpm	i_{lim} mA cm^{-2}	reverse scan					
		$i^{\text{SHE}}\left(i^{\text{RHE}}\right)$ mA cm^{-2}	s V^{-1}	t_s mV dec^{-1}	$i_b^{\text{SHE}}\left(i_b^{\text{RHE}}\right)$ mA cm^{-2}	s_b V^{-1}	t_b mV dec^{-1}
100	-0.943	$-7.131 \cdot 10^{-6}$ (-0.3387)					
200	-1.339	$-13.93 \cdot 10^{-6}$ (-0.6617)					
500	-2.146	$-28.23 \cdot 10^{-6}$ (-1.341)	-40.79	-56.45	6704 (2.113)	30.54	75.41
1000	-3.080	$-48.89 \cdot 10^{-6}$ (-2.322)					
1500	-3.781	$-66.77 \cdot 10^{-6}$ (-3.172)					
2000	-4.390	$-82.76 \cdot 10^{-6}$ (-3.931)					

The calculated current densities (Figure 45) fit well with the measured values except the high current densities at low rotation rates.

Table 34: Kinetic data for the HER from water in air saturated 0.10 M NaCl at pH 4.5 for equation (4.7)

ω	forward scan			reverse scan		
	$i^{SHE}\,(i^{RHE})$	s	t_s	$i^{SHE}\,(i^{RHE})$	s	t_s
rpm	mA cm^{-2}	V^{-1}	mV dec^{-1}	mA cm^{-2}	V^{-1}	mV dec^{-1}
100	$-0.9685\cdot10^{-8}$ ($-12.93\cdot10^{-6}$)			$-2.528\cdot10^{-10}$ ($-1.293\cdot10^{-6}$)		
200	$-1.097\cdot10^{-8}$ ($-14.64\cdot10^{-6}$)			$-2.983\cdot10^{-10}$ ($-1.444\cdot10^{-6}$)		
500	$-1.386\cdot10^{-8}$ ($-18.50\cdot10^{-6}$)	-27.26	-84.47	$-4.071\cdot10^{-10}$ ($-1.971\cdot10^{-6}$)	-32.14	-71.65
1000	$-1.759\cdot10^{-8}$ ($-23.48\cdot10^{-6}$)			$-5.586\cdot10^{-10}$ ($-2.704\cdot10^{-6}$)		
1500	$-2.149\cdot10^{-8}$ ($-28.69\cdot10^{-6}$)			$-7.375\cdot10^{-10}$ ($-3.571\cdot10^{-6}$)		
2000	$-2.529\cdot10^{-8}$ ($-33.76\cdot10^{-6}$)			$-9.339\cdot10^{-10}$ ($-4.521\cdot10^{-6}$)		

Neither the HER from water nor the diffusion limited HER show the expected slopes for a Heyrovský or a Tafel mechanism. The Tafel slope close to -60 mV dec^{-1} of the HER from protons can be explained by a reversible system as was done for this reaction under nitrogen in chapter 5.2.4.1.

Figure 45: Potentiodynamic polarization curves (10 mV s^{-1}) in air saturated 0.10 M NaCl at pH 4.5 after 20 min OCP at different rotation rates; measured (dashed) and calculated (solid); forward scan: left, reverse scan: right

5.3 ALKALINE ELECTROLYTES

5.3.1 SODIUM HYDROXIDE 0.10 M

5.3.1.1 NITROGEN

The zero-current potential of the platinum disc electrode in 0.10 M sodium hydroxide is +0.42 V in the forward scan, which is close to the potential of the reversible oxygen electrode and shifts to values between -0.73 V and -0.71 V in the reverse scan (Figure 46). The peak caused by the oxide

layer reduction has the maximum at -0.07 V and an area of 323±6 µC cm^{-2}. This is 77 % of the charge required for the reduction of a fully covered PtO surface.
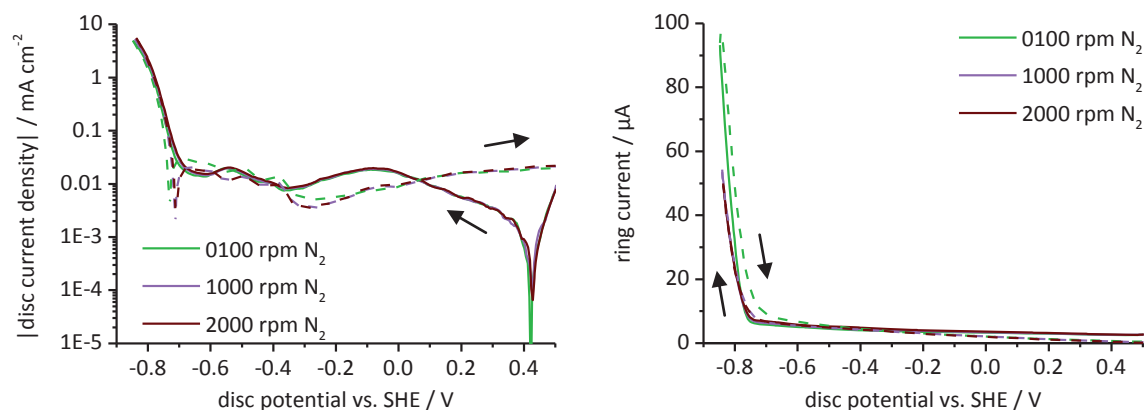

Figure 46: Potentiodynamic polarization curves (10 mV s^{-1}) in N$_2$ saturated 0.10 M NaOH after 20 min OCP at different rotation rates; ring potential: +0.80 V vs. SHE; forward scan: solid lines, reverse scan: dashed lines

The HER starts at -0.7 V and shows a change in its current potential relation at -0.8 V. Such a change in the slope could be caused by an ohmic drop in the electrolyte, but all disc currents densities have been manually corrected for it. The ohmic resistance of the 0.1 M NaOH in this cell measured by impedance is 19 Ω. It was additionally calculated by equation (5.6) [223] using the conductivity κ and the geometrical factors of the cell. A 0.125 M (5 %) sodium hydroxide solution has a specific conductivity of 24.8 mS cm^{-1} [1] which is a molar conductivity of 198 mS cm^{-1} M^{-1}. The specific conductivity of a 0.10 M NaOH solution would therefore be 19.8 mS cm^{-1} which is close to the measured 19.7 mS cm^{-1}. The distance between the working electrode and the reference electrode z was 20 mm. The ohmic resistance of a disc electrode with the radius R of 0.58 cm in this set up is 17.9 Ω according to equation (5.6).

$$R_\Omega = \frac{\tan^{-1}\left(z \cdot R^{-1}\right)}{2 \cdot \pi \cdot \kappa \cdot R} \tag{5.6}$$

An additional 9 Ω to 10 Ω would be required to compensate the change in the slope at potentials more negative than -0.8 V. The change in the current potential relation is therefore not due to an ohmic drop in the electrolyte. The proposed reason for the change in the slope is outlined in chapter 1.4 and leads to equation (4.9) which fits well with the measured current-potential curves.

The slope of the HER in Table 35 indicates a Heyrovský mechanism. A Tafel slope of about -120 mV dec^{-1} for the HER in alkaline electrolytes has also been published by Schuldiner [156] who found only one slope at pH-values above 11. Markovic [54] used a RRDE to measure the influence of the diffusion on the kinetic of the HER and found two Tafel slopes in 0.1 M KOH. These Tafel slopes have values of -55 mV dec^{-1} and -65 mV dec^{-1} at high potentials and -140 mV dec^{-1} at low potentials. Conway [224, 225] found a single slope of -125 mV dec^{-1} on cathodic reduced platinum and a change in the slope at anodic activated platinum in 0.5 M NaOH.

The current densities calculated by equation (4.9) using the kinetic data from Table 35 fit well with the measured values (Figure 47).

Table 35: Kinetic data for the HER in 0.10 M NaOH for equation (4.9)

ω rpm	$i^{\text{SHE}}\left(i^{\text{RHE}}\right)$ mA cm^{-2}	s V^{-1}	t_s mV dec^{-1}	$i_b^{\text{SHE}}\left(i_b^{\text{RHE}}\right)$ mA cm^{-2}	s_b V^{-1}	t_b mV dec^{-1}
			forward scan			
100	-1.562·10^{-6} (-1.193)					
1000	-1.829·10^{-6} (-1.397)	-17.73	-129.9	1.559·10^{16} (1.672)	48.13	47.85
2000	-2.039·10^{-6} (-1.557)					
			reverse scan			
100	-1.158·10^{-8} (-0.7373)					
1000	-1.425·10^{-8} (-0.9073)	-23.52	-97.93	1.580·10^{17} (1.108)	51.70	44.54
2000	-1.615·10^{-8} (-1.028)					

Figure 47: Potentiodynamic polarization curves in N$_2$ saturated 0.10 M NaOH after 20 min OCP at different rotation rates; measured (dashed) and calculated (solid); forward scan: left, reverse scan: right

5.3.1.2 Air
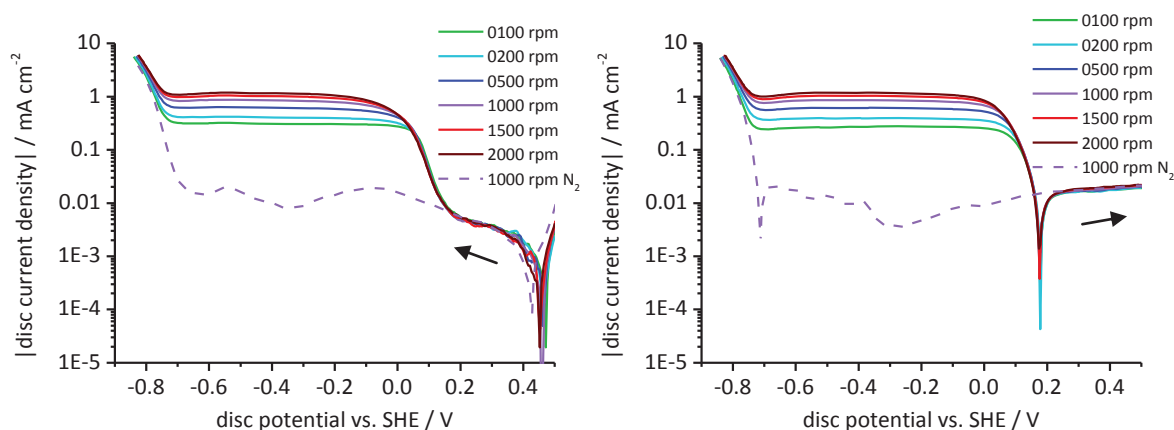
Figure 48: Potentiodynamic polarization curves in air saturated 0.10 M NaOH after 20 min OCP at different rotation rates; forward scan: left, reverse scan: right

The zero-current potentials measured during the potentiodynamic scans on a rotating platinum disc are independent of the rotation speed in 0.10 M sodium hydroxide (Figure 48). The zero-current potentials in the forward scans are with +0.46 V just slightly more positive than those measured under nitrogen (+0.42 V). In the reverse scan the zero-current potentials are at +0.18 V.

The ORR starts in the forward scan at the same potential at which the oxide reduction peak appears in the nitrogen purged solutions. The HER appears at the same potential (-0.71 V) as under nitrogen and is therefore not influenced by the ORR.

During the forward scan a peak in the ring current appeared with the beginning of the ORR at the disc electrode (Figure 49). Its height increases with the rotation rate. The peak at the ring reaches a maximum at a disc potential of 0.0 V when the diffusion limitation of the 1. ORR path takes place. The peak maxima are between 3.3 µA (100 rpm) and 14.4 µA (2000 rpm) higher than the current measured under nitrogen and therefore only 3 % to 7 % of the disc current are consumed forming desorbing hydrogen peroxide at 0.0 V. This happens only in the forward scan. In 0.1 M NaOH the hydrogen peroxide oxidation is diffusion controlled at +0.5 V vs. SCE [226] and therefore all the peroxide reaching the ring electrode should be oxidized. The 100 % H_2O_2 formation in 0.1 M KOH solution in the PtO region (+0.2 V) stated by Fischer and Heitbaum [70] could not be confirmed.
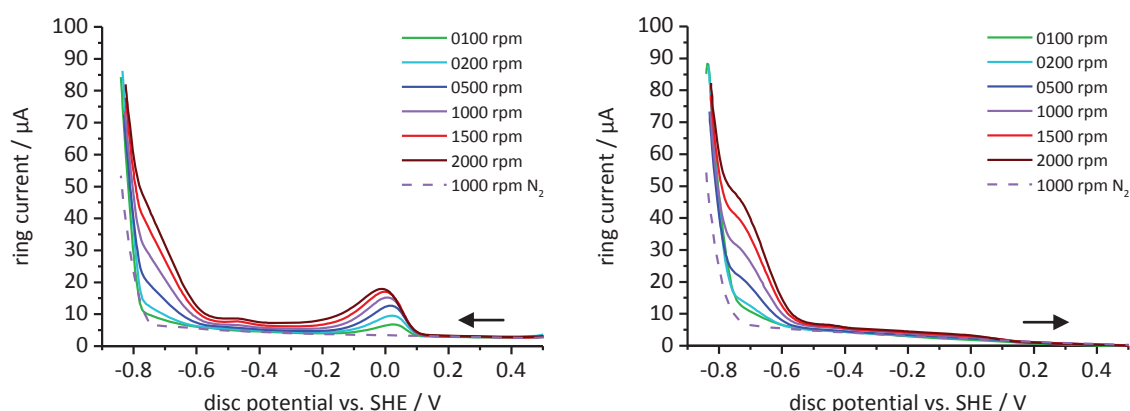

Figure 49: Ring currents measured during the potentiodynamic scan (10 mV s^{-1}) at the disc electrode in air saturated 0.10 M NaCl after 20 min OCP at different rotation rates; ring potential: +0.80 V vs. SHE; forward scan: left, reverse scan: right

When the disc potential reaches the hydrogen adsorption region, the current at the ring increases and forms a shoulder with maxima between 4.7 µA and 37.7 µA. At more negative disc potentials the ring current is further increased due to the hydrogen oxidation at the ring.

Table 36: Kinetic data for the 1. ORR path in air saturated 0.10 M NaOH for equation (4.8)

ω	forward scan				reverse scan			
	i_{lim}	$i^{\text{SHE}}\left(i^{\text{ROE}}\right)$	s	t_s	i_{lim}	$i^{\text{SHE}}\left(i^{\text{ROE}}\right)$	s	t_s
rpm	mA cm^{-2}	mA cm^{-2}	V^{-1}	mV dec^{-1}	mA cm^{-2}	mA cm^{-2}	V^{-1}	mV dec^{-1}
100	-0.2275				-0.2400			
200	-0.2694				-0.3327			
500	-0.3441	-1.985	-42.23	-54.53	-0.4983	-7.770	-35.91	-64.13
1000	-0.3958	($-5.882\cdot10^{-9}$)			-0.6610	($-4.350\cdot10^{-7}$)		
1500	-0.4321				-0.7705			
2000	-0.4513				-0.8491			

As it was the case for acidic electrolytes the peak in the ring current indicates two different reaction paths for the ORR. The 1. ORR path dominates the ORR in the reverse scan and at low rotation rates in the forward scan (Table 36). The limiting current densities of the two ORR paths show a linear relationship with the square root of the rotation rate. The obtained Tafel slopes for the first path are similar to those found in literature for sodium or potassium hydroxide solutions with values between -50 mV dec^{-1} and -65 mV dec^{-1} [59, 81, 99, 124, 131, 140, 145]. The Tafel slopes of the second ORR path (Table 37) are between -143 mV dec^{-1} and -154 mV dec^{-1}. In literature [71, 99, 131, 140, 145] values from -116 mV dec^{-1} to -400 mV dec^{-1} can be found. Similar results can be obtained using the classical method, the Koutecký-Levich plot, for evaluation of the kinetic data (Figure 50).

Table 37: Kinetic data for the 2. ORR path in air saturated 0.10 M NaOH for equation (4.8)

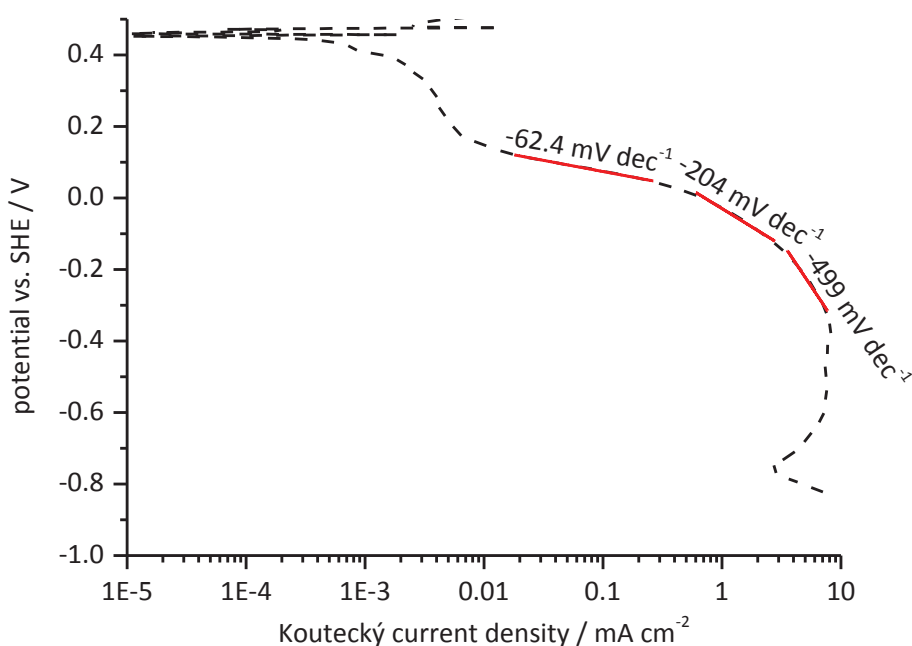| ω | forward scan | | | | reverse scan | | | |
rpm	i_{lim} mA cm^{-2}	$i^{SHE}\left(i^{ROE}\right)$ mA cm^{-2}	s V^{-1}	t_s mV dec^{-1}	i_{lim} mA cm^{-2}	$i^{SHE}\left(i^{ROE}\right)$ mA cm^{-2}	s V^{-1}	t_s mV dec^{-1}
100	-0.0662				-0.0315			
200	-0.1367				-0.0592			
500	-0.2742	-0.1632 ($-9.364\cdot10^{-5}$)	-16.05	-143.4	-0.1124	-0.1201 ($-11.44\cdot10^{-5}$)	-14.96	-153.9
1000	-0.4581				-0.1923			
1500	-0.5917				-0.2608			
2000	-0.7124				-0.3289			

Figure 50: Koutecký current density obtained from the Koutecký-Levich plot (intercept in the linear relationship between the inverse current density and ω-0.5) of the current densities in Figure 48

With the onset of the HER at the disc electrode the limiting current density of the ORR becomes smaller and a ring current due to the oxidation of peroxide appears. This decrease is due to the formation of hydrogen peroxide (chapter 2.3.1.5). The kinetic data obtained by multi curve fit for this reaction at the disc is given in Table 38.

The two slopes of the current density caused by the HER found in air saturated 0.10 M NaOH (Table 39) are close to those measured under nitrogen.

Table 38: Kinetic data for the ORR in combination with the hydrogen adsorption in air saturated 0.10 M NaOH for equation (4.8)

ω	forward scan				reverse scan			
	i_{lim}	$i^{SHE}\left(i^{RHE}\right)$	s	t_s	i_{lim}	$i^{SHE}\left(i^{RHE}\right)$	s	t_s
rpm	mA cm^{-2}	mA cm^{-2}	V^{-1}	mV dec^{-1}	mA cm^{-2}	mA cm^{-2}	V^{-1}	mV dec^{-1}
100	0.00000				0.0491			
200	0.00000				0.0344			
500	0.00570	$1.903 \cdot 10^{-24}$	-80.26	-28.69	0.0488	$3.440 \cdot 10^{-15}$	-49.28	-46.73
1000	0.02630	(812.4)			0.0900	(77.22)		
1500	0.05418				0.1364			
2000	0.08412				0.1847			

In Figure 51 the fitted curves are compared to the measured data and a good correlation was obtained.

Table 39: Kinetic data for the HER in air saturated 0.10 M NaOH for equation (4.9)

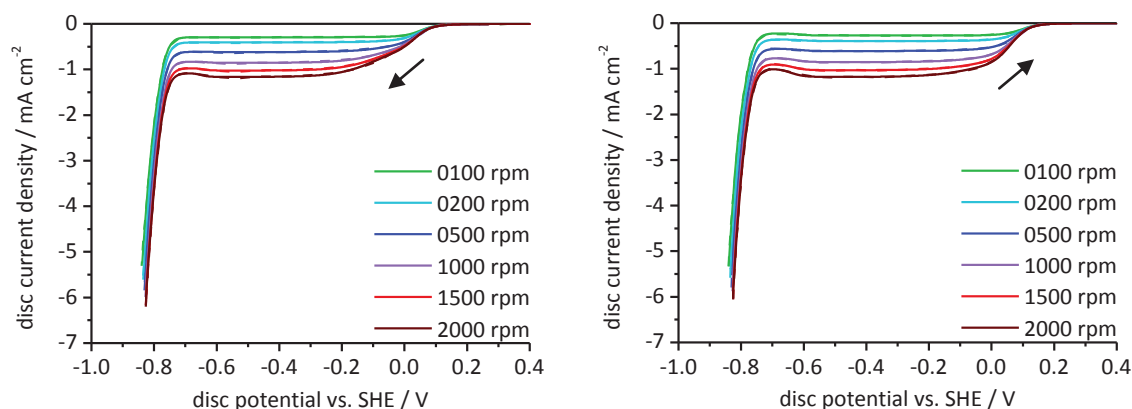| ω	forward scan					
	$i^{SHE}\left(i^{RHE}\right)$	s	t_s	$i_b^{SHE}\left(i_b^{RHE}\right)$	s_b	t_b
rpm	mA cm^{-2}	V^{-1}	mV dec^{-1}	mA cm^{-2}	V^{-1}	mV dec^{-1}
100	$-3.847 \cdot 10^{-7}$ (-1.198)					
200	$-4.312 \cdot 10^{-7}$ (-1.343)					
500	$-4.726 \cdot 10^{-7}$ (-1.472)	-19.57	-117.8	$1.537 \cdot 10^{18}$ (1.608)	54.19	42.50
1000	$-4.983 \cdot 10^{-7}$ (-1.552)					
1500	$-5.128 \cdot 10^{-7}$ (-1.597)					
2000	$-5.056 \cdot 10^{-7}$ (-1.575)					
ω	reverse scan					
	$i^{SHE}\left(i^{RHE}\right)$	s	t_s	$i_b^{SHE}\left(i_b^{RHE}\right)$	s_b	t_b
rpm	mA cm^{-2}	V^{-1}	mV dec^{-1}	mA cm^{-2}	V^{-1}	mV dec^{-1}
100	$-3.796 \cdot 10^{-8}$ (-0.9663)					
200	$-4.317 \cdot 10^{-8}$ (-1.099)					
500	$-4.803 \cdot 10^{-8}$ (-1.223)	-22.32	-103.2	$1.887 \cdot 10^{17}$ (1.293)	51.73	44.52
1000	$-5.131 \cdot 10^{-8}$ (-1.306)					
1500	$-5.258 \cdot 10^{-8}$ (-1.339)					
2000	$-5.246 \cdot 10^{-8}$ (-1.335)					

Figure 51: Potentiodynamic polarization curves (10 mV s^{-1}) in air saturated 0.10 M NaOH after 20 min OCP at different rotation rates; measured (dashed) and calculated (solid); forward scan: left, reverse scan: right

5.3.2 SODIUM SULFATE 0.05 M BUFFERED AT PH 9.5

5.3.2.1 NITROGEN

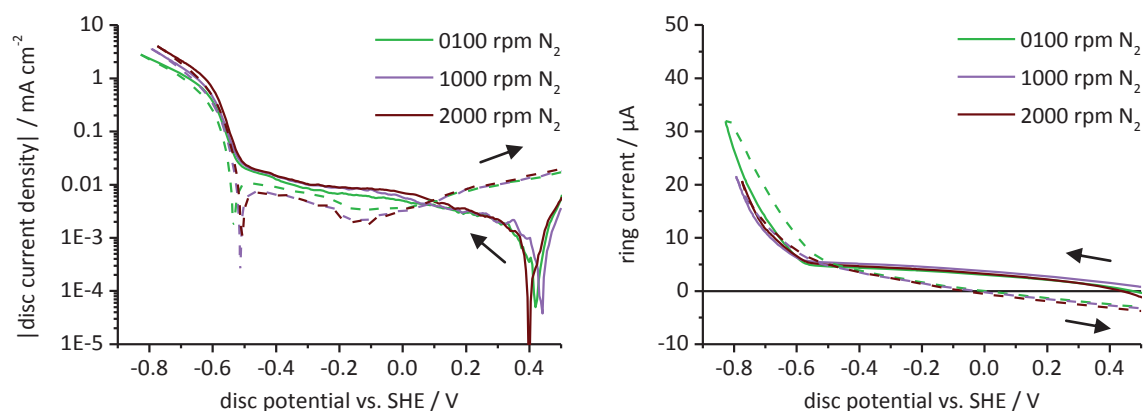Figure 52: Potentiodynamic polarization curves (10 mV s^{-1}) in N$_2$ saturated 0.05 M Na$_2$SO$_4$ at pH 9.5 after 20 min OCP at different rotation rates; ring potential: +0.99 V vs. SHE; forward scan: solid lines, reverse scan: dashed lines

The zero-current potentials observed during the potentiodynamic measurements in 0.05 M Na$_2$SO$_4$ buffered with 0.01 M sodium borate at pH 9.5 are between +0.44 V and +0.40 V in the forward scans (Figure 52). This is nearly the same potential as in 0.1 M sodium hydroxide (+0.42 V) despite the pH-difference of 3.5. The zero-current potentials in the reverse scans are between -0.50 V and -0.54 V. No reduction peak appears in the forward scans.

The HER starts at -0.5 V and shows a change in the Tafel slope at -0.6 V (Figure 53) as has been discussed in chapter 5.3.1.1. The kinetic data of this reaction can be found in Table 40. The Tafel slopes of the HER measured in deaerated 0.05 M Na$_2$SO$_4$ at pH 9.5 are similar to the -252 mV dec^{-1} measured by Schuldiner [156] at pH 9.4 and 9.6. These high Tafel slopes can be explained by a high charge transfer coefficient. The cathodic Tafel slope for a 1 e$^-$ transfer reaction with a charge transfer coefficient of 0.75 would be -244 mV dec^{-1} while the reversible anodic reaction would show a Tafel slope of 77 mV dec^{-1}, which is within the range of the obtained slopes of the reverse reaction.
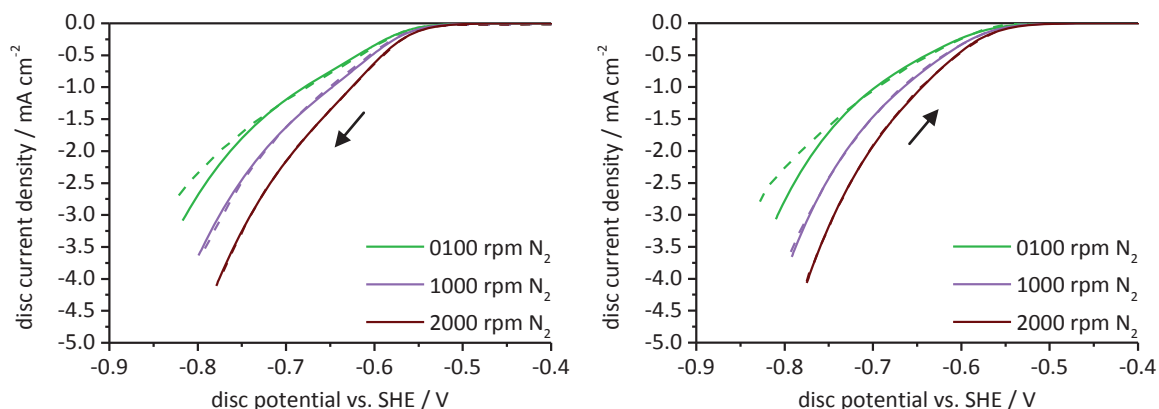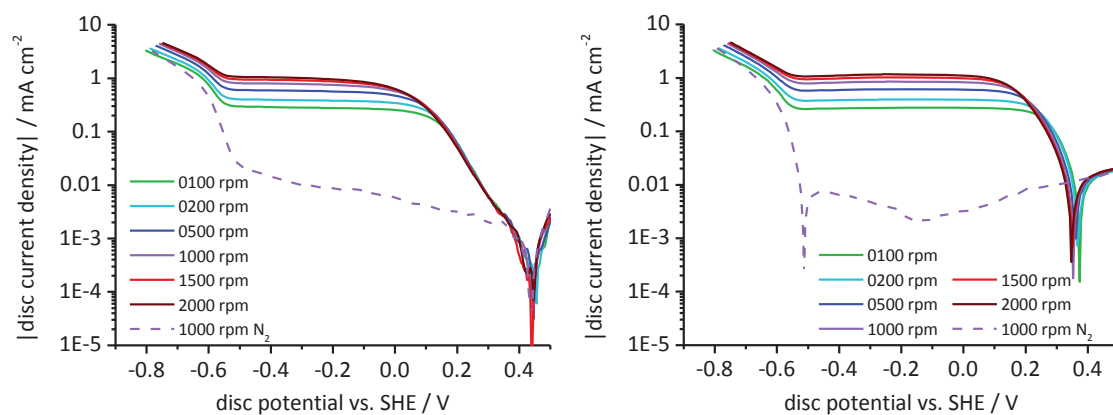
Figure 53: Potentiodynamic polarization curves (10 mV s^{-1}) in N$_2$ saturated 0.05 M Na$_2$SO$_4$ at pH 9.5 after 20 min OCP at different rotation rates; measured (dashed) and calculated (solid); forward scan: left, reverse scan: right

The current densities calculated by equation (4.9) with the kinetic data in Table 40 are shown in Figure 53. The calculated values fit poorly to the measured current densities in the high current density region at 100 rpm but at higher rotation rates the correlation is very good. The reason might be a poor mass transport of the hydrogen at this low rotation rate. This was also observed in the electrolytes with pH 4.5.

Table 40: Kinetic data for the HER in 0.05 M Na$_2$SO$_4$ at pH 9.5 for equation (4.9)

ω rpm	i^{SHE} (i^{RHE}) mA cm^{-2}	s V^{-1}	t_s mV dec^{-1}	i_b^{SHE} (i_b^{RHE}) mA cm^{-2}	s_b V^{-1}	t_b mV dec^{-1}
			forward scan			
100	-4.349·10^{-3} (-0.3853)					
1000	-5.917·10^{-3} (-0.5242)	-8.036	-286.6	2.395·10^{10} (2.986)	40.87	56.34
2000	-7.857·10^{-3} (-0.6961)					

ω rpm	i^{SHE} (i^{RHE}) mA cm^{-2}	s V^{-1}	t_s mV dec^{-1}	i_b^{SHE} (i_b^{RHE}) mA cm^{-2}	s_b V^{-1}	t_b mV dec^{-1}
			reverse scan			
100	-1.153·10^{-3} (-0.2638)					
1000	-1.640·10^{-3} (-0.3752)	-9.736	-236.5	1.259·10^{9} (2.889)	35.65	64.60
2000	-2.152·10^{-3} (-0.4923)					

5.3.2.2 AIR

Borate has been used as a buffer in previous investigations of the ORR on platinum [62, 99] and it has been shown that borate species present (e. g. B(OH)$_3$ and B(OH)$_4^-$) do not undergo any redox reaction in a potential range between +0.8 V vs. SCE and -0.8 V vs. SCE even at a concentration of 0.1 M [62].

The zero-current potential in the buffered air saturated 0.05 M Na$_2$SO$_4$ with pH 9.5 is +0.45 V in the forward scan and +0.35 V to +0.37 V in the reverse scan (Figure 54). The pre-exponential current density of the ORR is influenced by the rotation rate in the reverse scan. This effect can be explained

by the same effect as has been done for the HER in chapter 1.4. The only difference is that the pre-exponential current density decreases with an increase of the rotation rate while it is the opposite way for the HER. This can be explained by the fact that the HER depends on the diffusion of the product from the surface into the electrolyte. For the ORR the opposite is the case. In buffered solution the pH is constant and under alkaline conditions the overall reaction {1.16} takes place. In this reaction the educt of the ORR depends on the diffusion.

Figure 54: Potentiodynamic polarization curves (10 mV s^{-1}) in air saturated 0.05 M Na$_2$SO$_4$ at pH 9.5 after 20 min OCP at different rotation rates; forward scan: left, reverse scan: right

The slope of the current density caused by the HER changes at -0.6 V as has been observed under nitrogen.

The ORR starts at +0.4 V and small ring currents at potentials below +0.2 V (Figure 55) indicate a second ORR path. At the same potential Kaska [62] and Sepa [99] observed a change in the Tafel slope of the ORR at in a solution with a similar pH. These currents reach values between 1.0 and 4.5 µA when corrected by the currents measured under nitrogen and are close to the values between 1.17 µA and 4.0 µA found by Kaska et al. [62] using a ring potential of +0.62 V vs. SCE at 2500 rpm.
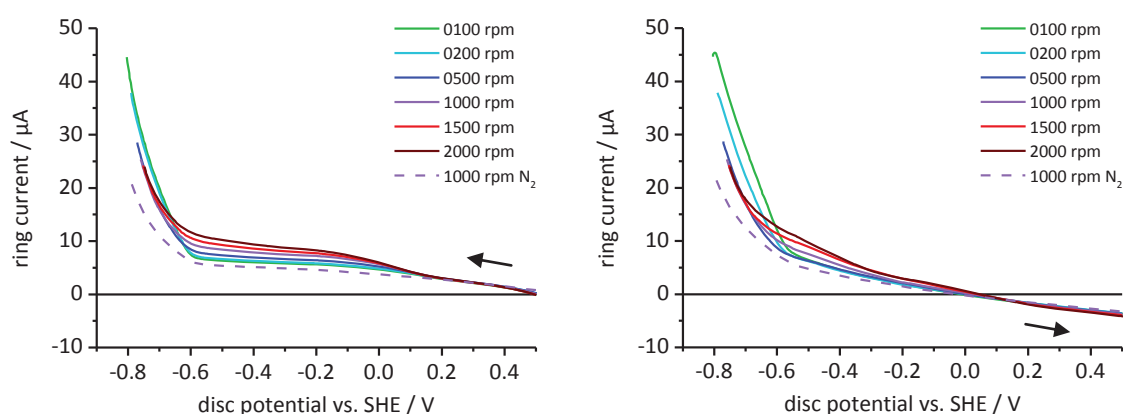

Figure 55: Ring currents measured during the potentiodynamic scan (10 mV s^{-1}) at the disc electrode in air saturated 0.05 M Na$_2$SO$_4$ at pH 9.5 after 20 min OCP at different rotation rates; ring potential: +0.99 V vs. SHE; forward scan: left, reverse scan: right

The 1. ORR path does not form any detectable peroxide and dominates at low rotation rates and in the reverse scan (Table 41).

Table 41: Kinetic data for the 1. ORR path in air saturated 0.05 M Na_2SO_4 at pH 9.5 for equation (4.8)

		forward scan				reverse scan		
ω rpm	i_{lim} mA cm^{-2}	i^{SHE} (i^{ROE}) mA cm^{-2}	s V^{-1}	t_s mV dec^{-1}	i_{lim} mA cm^{-2}	i^{SHE} (i^{ROE}) mA cm^{-2}	s V^{-1}	t_s mV dec^{-1}
100	-0.2217				-0.2595	-399.8 (-7.425·10^{-6})		
200	-0.3181				-0.3633	-343.2 (-6.374·10^{-6})		
500	-0.4272	-4.299 (-1.539·10^{-6})	-22.12	-104.1	-0.5486	-238.2 (-4.424·10^{-6})	-26.53	-86.80
1000	-0.5067				-0.7385	-171.4 (-3.183·10^{-6})		
1500	-0.5460				-0.8609	-139.4 (-2.589·10^{-6})		
2000	-0.5586				-0.9514	-116.6 (-2.165·10^{-6})		

The limiting current densities of the two ORR paths are in a linear relationship with the square root of the rotation rate only in the reverse scan. The kinetic data for the 2. ORR path is given in Table 42. The Tafel slopes obtained during the reverse scans are close to the -70 mV dec^{-1} to -90 mV dec^{-1} at low current densities and the -110 mV dec^{-1} to -150 mV dec^{-1} at high current densities reported by Kaska et al. [62].

Table 42: Kinetic data for the 2. ORR path in air saturated 0.05 M Na_2SO_4 at pH 9.5 for equation (4.8)

		forward scan				reverse scan		
ω rpm	i_{lim} mA cm^{-2}	i^{SHE} (i^{ROE}) mA cm^{-2}	s V^{-1}	t_s mV dec^{-1}	i_{lim} mA cm^{-2}	i^{SHE} (i^{ROE}) mA cm^{-2}	s V^{-1}	t_s mV dec^{-1}
100	-0.0646				-0.01873			
200	-0.0721				-0.03273			
500	-0.1572	-0.1961 (-42.60·10^{-6})	-12.57	-183.3	-0.06715	-0.8897 (-9.321·10^{-7})	-20.52	-112.2
1000	-0.2821				-0.1063			
1500	-0.3855				-0.1534			
2000	-0.4822				-0.1972			

During the forward scan no decrease in the liming current density of the ORR was observed in the hydrogen adsorption region. In the reverse scans the hydrogen peroxide formation in this region has to be considered since the limited current density is smaller compared to the current densities at higher potentials. The kinetic data for this decrease during the reverse scan are given in Table 43.

Table 43: Kinetic data for the ORR in combination with the hydrogen adsorption in air saturated 0.05 M Na_2SO_4 at pH 9.5 for equation (4.8)

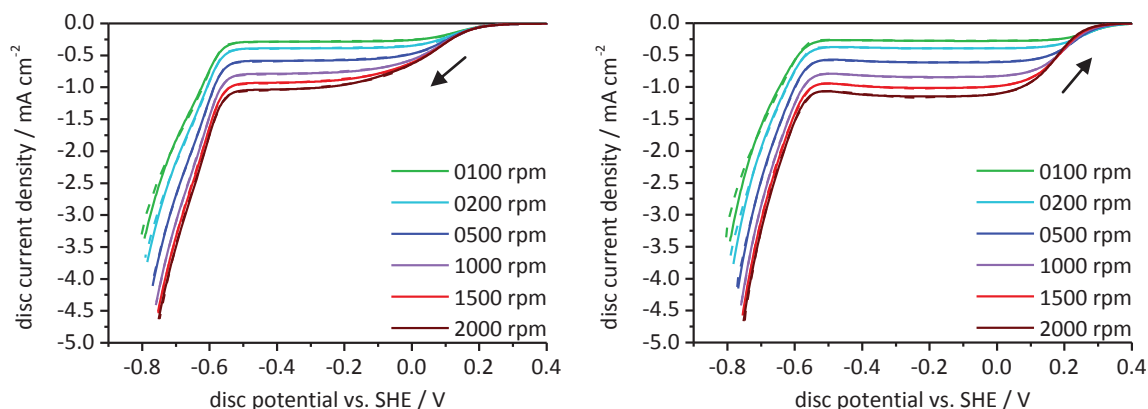|		forward scan				reverse scan		
ω rpm	i_{lim} mA cm^{-2}	i^{SHE} (i^{RHE}) mA cm^{-2}	s V^{-1}	t_s mV dec^{-1}	i_{lim} mA cm^{-2}	i^{SHE} (i^{RHE}) mA cm^{-2}	s V^{-1}	t_s mV dec^{-1}
100	-				0.0192			
200	-				0.0315			
500	-	-	-	-	0.0728	4.449·10^{-5} (-0.5272)	-16.81	-137.0
1000	-				0.0943			
1500	-				0.1392			
2000	-				0.1830			

Figure 56: Potentiodynamic polarization curves (10 mV s^{-1}) in air saturated 0.05 M Na$_2$SO$_4$ at pH 9.5 after 20 min OCP at different rotation rates; measured (dashed) and calculated (solid); forward scan: left, reverse scan: right

The Tafel slopes of the HER measured during the forward scan under air (Table 44) are higher than those found in the deaerated solution. The value obtained during the reverse scan is almost identical with the -252 mV dec^{-1} measured by Schuldiner [156] at pH 9.4 and 9.6.

Table 44: Kinetic data for the HER in air saturated 0.05 M Na$_2$SO$_4$ at pH 9.5 for equation (4.9)

ω rpm	$i^{SHE} (i^{ROE})$ mA cm^{-2}	s V^{-1}	t_s mV dec^{-1}	$i_b^{SHE} (i_b^{RHE})$ mA cm^{-2}	s_b V^{-1}	t_b mV dec^{-1}
	forward scan					
100	-9.33·10^{-3} (-0.5525)					
200	-10.75·10^{-3} (-0.6366)					
500	-12.73·10^{-3} (-0.7538)	-7.314	-314.9	1.439·10^{11} (4.112)	43.51	52.94
1000	-14.00·10^{-3} (-0.8290)					
1500	-14.55·10^{-3} (-0.8616)					
2000	-14.79·10^{-3} (-0.8758)					
ω rpm	$i^{SHE} (i^{ROE})$ mA cm^{-2}	s V^{-1}	t_s mV dec^{-1}	$i_b^{SHE} (i_b^{RHE})$ mA cm^{-2}	s_b V^{-1}	t_b mV dec^{-1}
	reverse scan					
100	-2.402·10^{-3} (-0.3785)					
200	-2.839·10^{-3} (-0.4474)					
500	-3.416·10^{-3} (-0.5383)	-9.068	-254.0	3.504·10^{9} (3.330)	37.23	61.85
1000	-3.755·10^{-3} (-0.5917)					
1500	-3.943·10^{-3} (-0.6213)					
2000	-4.051·10^{-3} (-0.6384)					

The calculated current densities fit well to the measured values except at high current densities for slow rotation rates (Figure 56).

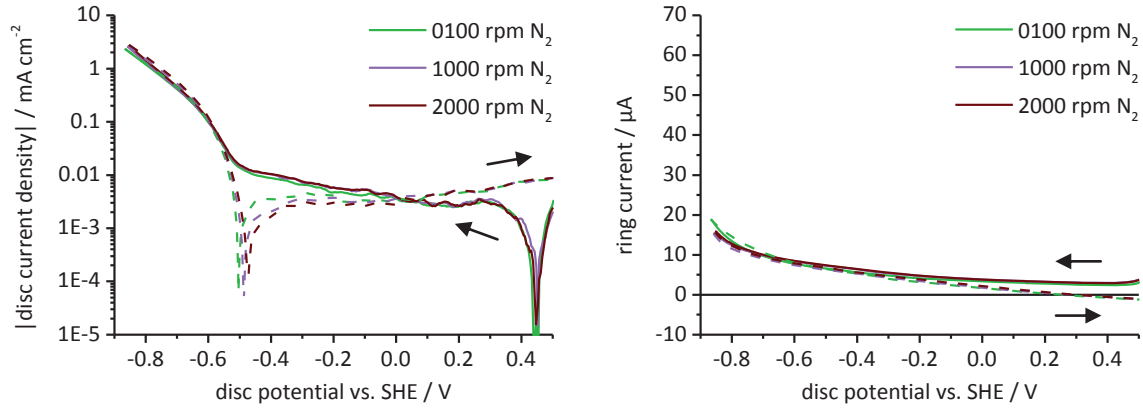## 5.3.3 SODIUM CHLORIDE 0.10 M BUFFERED AT PH 9.5

5.3.3.1 NITROGEN

Figure 57: Potentiodynamic polarization curves (10 mV s^{-1}) in N$_2$ saturated 0.10 M NaCl at pH 9.5 after 20 min OCP at different rotation rates; ring potential: +0.99 V vs. SHE; forward scan: solid lines, reverse scan: dashed lines

The platinum disc shows no distinct oxide reduction peak in the 0.10 M NaCl electrolyte buffered with 0.01 M sodium borate at pH 9.5 (Figure 57). The zero-current potential is at +0.45 V in the forward scan and around -0.50 V in the reverse scan independent of the rotation rate.

The Tafel slopes for the HER (Table 45) are smaller than those measured in the sulfate electrolyte and in the same range as the -252 mV dec^{-1} found by Schuldiner [156].

In Figure 58 the current densities calculated by equation (4.7) with the kinetic data from Table 45 are compared with the measured values.

Table 45: Kinetic data for the HER in 0.10 M NaCl at pH 9.5 for equation (4.9)

ω rpm	$i^{\text{SHE}}\left(i^{\text{ROE}}\right)$ mA cm^{-2}	s V^{-1}	t_s mV dec^{-1}	$i_b^{\text{SHE}}\left(i_b^{\text{RHE}}\right)$ mA cm^{-2}	s_b V^{-1}	t_b mV dec^{-1}
	forward scan					
100	-0.1717·10^{-3} (-0.08269)					
1000	-0.1868·10^{-3} (-0.08996)	-11.07	-208.1	6.791·10^6	27.98 (1.126)	82.30
2000	-0.2060·10^{-3} (-0.09920)					
	reverse scan					
100	-0.4982·10^{-3} (-0.1173)					
1000	-0.5977·10^{-3} (-0.1407)	-9.787	-235.3	1.909·10^6	24.33 (2.425)	94.67
2000	-0.6647·10^{-3} (-0.1564)					

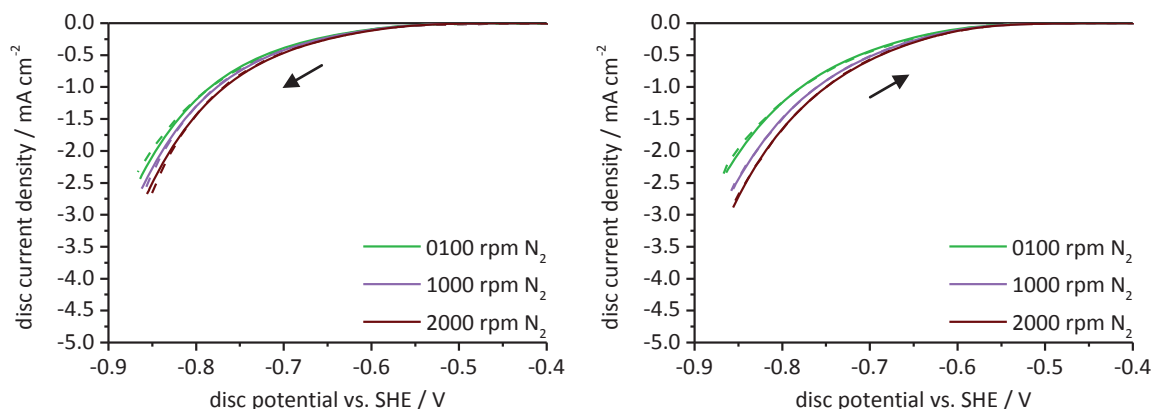Figure 58: Potentiodynamic polarization curves (10 mV s^{-1}) in N$_2$ saturated 0.10 M NaCl at pH 9.5 after 20 min OCP at different rotation rates; measured (dashed) and calculated (solid); forward scan: left, reverse scan: right
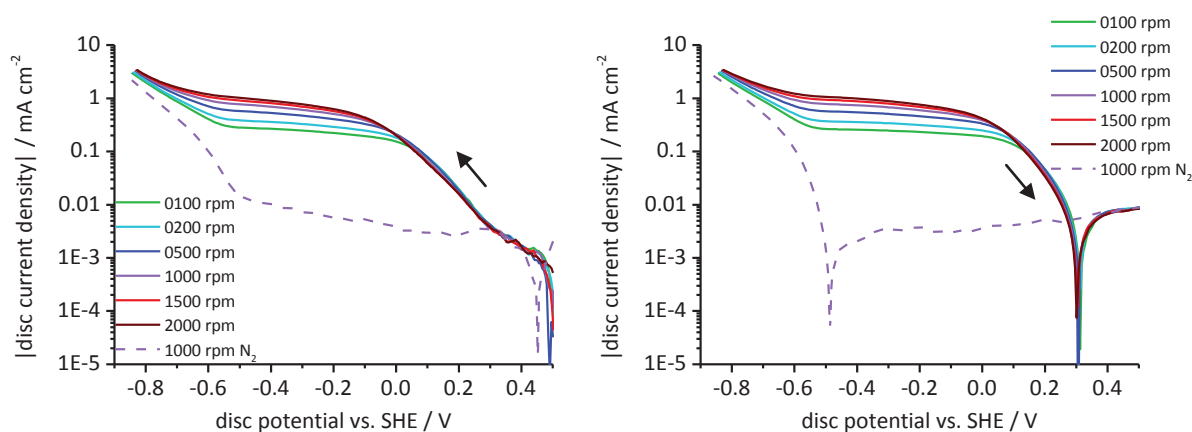
5.3.3.2 AIR

Figure 59: Potentiodynamic polarization curves (10 mV s^{-1}) in air saturated 0.10 M NaCl at pH 9.5 after 20 min OCP at different rotation rates; forward scan: left, reverse scan: right

The zero-current potential of the platinum disc electrode in an aerated buffered 0.10 M NaCl solution at pH 9.5 is +0.50 V in the forward scan and +0.31 V in the reverse scan (Figure 59). The ORR does not reach its diffusion limiting current density before the HER starts and no evidence for a hydrogen peroxide formation caused by the hydrogen adsorption can be found in the disc or the ring currents.

When the disc potential reached +0.2 V, high current peaks appeared at the ring electrode (Figure 60). The maxima between 19.5 µA and 61.4 µA are caused by the oxidation of hydrogen peroxide formed at the disc. These peak maxima increasing linear with an increase of the square root of the rotation rate. With a collection efficiency of 0.37 the corresponding disc current densities are between 0.048 mA cm^{-2} (100 rpm) and 0.157 mA cm^{-2} (2000 rpm). This is the highest amount of hydrogen peroxide detected at the ring electrode in all electrolytes studied in this work.

This is a significant increase of desorbing hydrogen peroxide compared to the much smaller amount found in buffered Na$_2$SO$_4$ at pH 9.5 and must be caused by chloride adsorption. An increase of the amount of hydrogen peroxide due to the presence of chloride has also been found by Kaska [62].
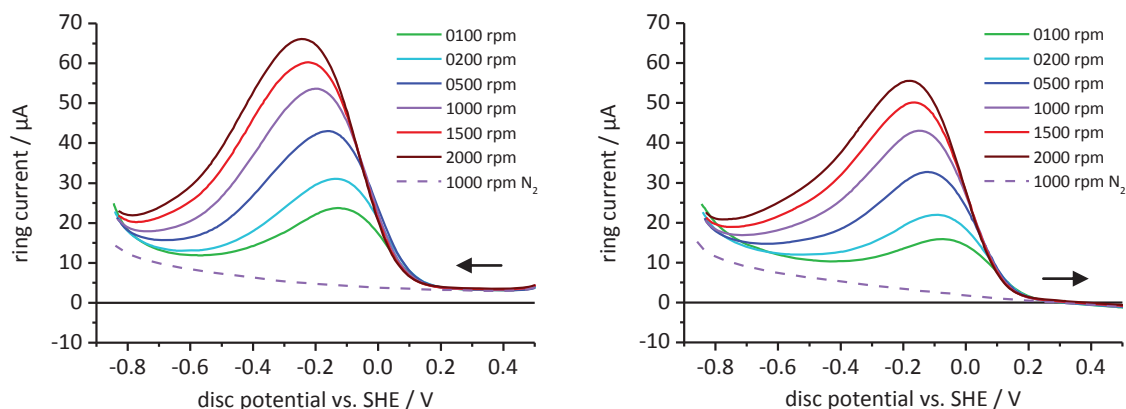
Figure 60: Ring currents measured during the potentiodynamic scan (10 mV s^{-1}) at the disc electrode in air saturated 0.10 M NaCl at pH 9.5 after 20 min OCP at different rotation rates; ring potential: +0.99 V vs. SHE; forward scan: left, reverse scan: right

The increase of the ring currents when the ORR proceeds at the disc indicates two ORR reaction paths in the 0.10 M NaCl at pH 9.5. The same was observed in 0.05 M Na$_2$SO$_4$ at pH 9.5. The kinetic data of the first ORR path is given in Table 46.

Table 46: Kinetic data for the 1. ORR path in air saturated 0.10 M NaCl at pH 9.5 for equation (4.8)

	forward scan				reverse scan			
ω	i_{lim}	$i^{SHE}\left(i^{ROE}\right)$	s	t_s	i_{lim}	$i^{SHE}\left(i^{ROE}\right)$	s	t_s
rpm	mA cm^{-2}	mA cm^{-2}	V^{-1}	mV dec^{-1}	mA cm^{-2}	mA cm^{-2}	V^{-1}	mV dec^{-1}
100	-0.1620				-0.1587			
200	-0.2173				-0.2137			
500	-0.3106	-0.3126	-15.40	-149.6	-0.3079	-1.469	-19.05	-120.9
1000	-0.3886	(-1.017·10^{-5})			-0.3855	(-4.127·10^{-6})		
1500	-0.4425				-0.4355			
2000	-0.4902				-0.4738			

The share of the second ORR path on the total ORR increases at higher rotation rates (Table 47). The Tafel slopes of these two ORR paths are higher than those found in 0.05 M Na$_2$SO$_4$ at pH 9.5 and therefore also higher than those published by Kaska [62].

Table 47: Kinetic data for the 2. ORR path in air saturated 0.10 M NaCl at pH 9.5 for equation (4.8)

	forward scan				reverse scan			
ω	i_{lim}	$i^{SHE}\left(i^{ROE}\right)$	s	t_s	i_{lim}	$i^{SHE}\left(i^{ROE}\right)$	s	t_s
rpm	mA cm^{-2}	mA cm^{-2}	V^{-1}	mV dec^{-1}	mA cm^{-2}	mA cm^{-2}	V^{-1}	mV dec^{-1}
100	-0.1140				-0.0979			
200	-0.1557				-0.1428			
500	-0.2577	-0.03459	-9.215	-249.9	-0.2471	-0.08860	-8.709	-264.4
1000	-0.3955	(-7.138·10^{-5})			-0.3931	(-2.568·10^{-4})		
1500	-0.5049				-0.5159			
2000	-0.5917				-0.6214			

Neither current at the disc nor the ring show any evidence for a formation of hydrogen peroxide in the hydrogen adsorption region. Therefore no such reaction was considered.

The slopes of the HER under air (Table 48) are equal to those under nitrogen.

As can be seen in Figure 61, the calculated current densities are in good agreement with the measured data.

Table 48: Kinetic data for the HER in air saturated 0.10 M NaCl at pH 9.5 for equation (4.8)

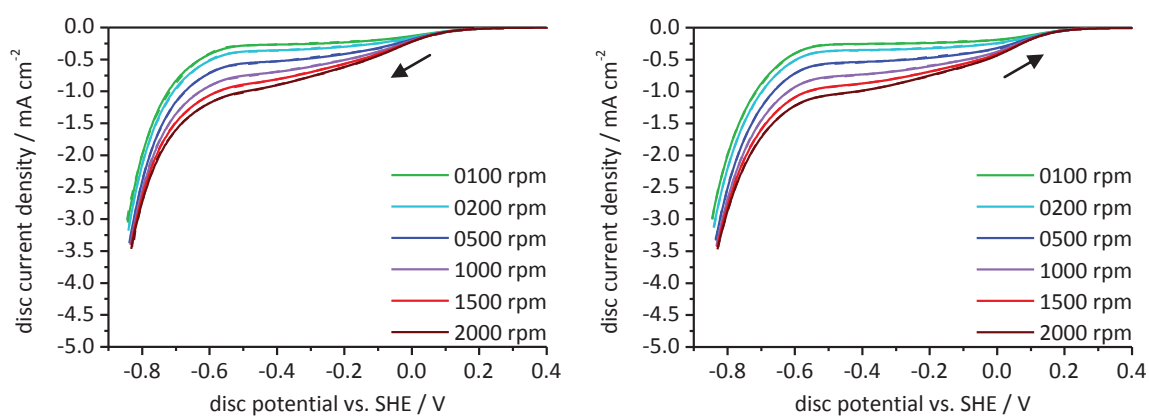| ω rpm	$i^{SHE}\,(i^{RHE})$ mA cm^{-2}	s V^{-1}	t_s mV dec^{-1}	$i_b^{SHE}\,(i_b^{RHE})$ mA cm^{-2}	s_b V^{-1}	t_b mV dec^{-1}
			forward scan			
100	$-2.450\cdot10^{-4}$ (-0.1180)					
200	$-2.533\cdot10^{-4}$ (-0.1220)					
500	$-2.623\cdot10^{-4}$ (-0.1263)	-11.07	-208.0	$3.405\cdot10^{6}$ (0.9068)	27.13	84.90
1000	$-2.526\cdot10^{-4}$ (-0.1216)					
1500	$-2.420\cdot10^{-4}$ (-0.1165)					
2000	$-2.355\cdot10^{-4}$ (-0.1134)					
			reverse scan			
100	$-7.991\cdot10^{-4}$ (-0.1717)					
200	$-8.493\cdot10^{-4}$ (-0.1825)					
500	$-8.979\cdot10^{-4}$ (-0.1930)	-9.624	-239.3	$3.306\cdot10^{5}$ (1.772)	21.75	105.9
1000	$-8.758\cdot10^{-4}$ (-0.1882)					
1500	$-8.411\cdot10^{-4}$ (-0.1808)					
2000	$-8.149\cdot10^{-4}$ (-0.1751)					

Figure 61: Potentiodynamic polarization curves (10 mV s^{-1}) in air saturated 0.10 M NaCl at pH 9.5 after 20 min OCP at different rotation rates; measured (dashed) and calculated (solid); forward scan: left, reverse scan: right

5.4 NEUTRAL ELECTROLYTES
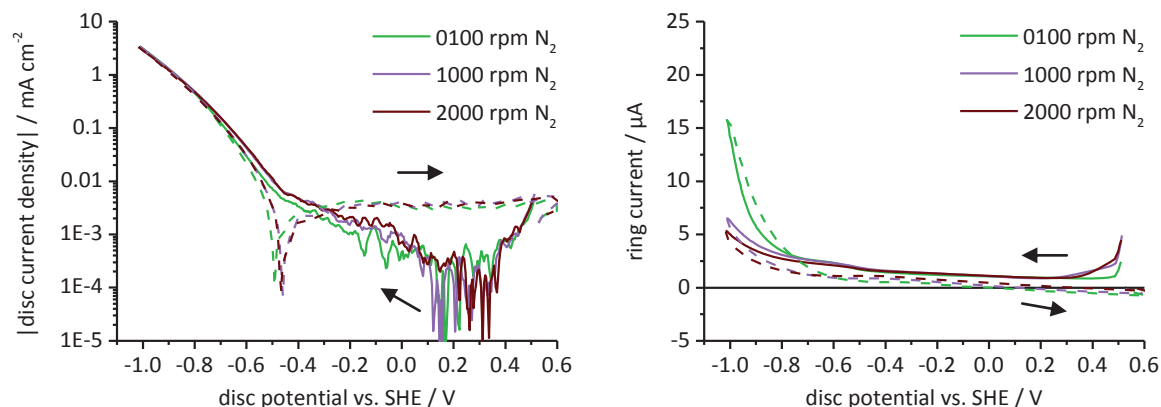
5.4.1 SODIUM SULFATE 0.05 M

5.4.1.1 NITROGEN

Figure 62: Potentiodynamic polarization curves (10 mV s^{-1}) in N_2 saturated 0.05 M Na_2SO_4 after 10 min OCP at different rotation rates; ring potential: +0.80 V vs. SHE; forward scan: solid lines, reverse scan: dashed lines

The zero-current potentials of the disc electrode in deaerated 0.05 M Na_2SO_4 are between +0.12 V and +0.34 V in the forward scan and show no clear value (Figure 62). This might be due to a shorter OCP period in neutral electrolytes. The zero-current potentials in the reverse scan are between -0.49 V and -0.46 V. At more negative potentials the hydrogen evolution takes place.

Table 49: Kinetic data for the HER in N_2 saturated 0.05 M Na_2SO_4 for equation (4.9)

ω rpm	$i^{SHE}\left(i^{RHE}\right)$ mA cm^{-2}	s V^{-1}	t_s mV dec^{-1}	$i_b^{SHE}\left(i_b^{RHE}\right)$ mA cm^{-2}	s_b V^{-1}	t_b mV dec^{-1}
	forward scan					
100	-5.799·10^{-4} (-0.01999)					
1000	-5.911·10^{-4} (-0.02037)	-8.613	-267.4	1432 (14.53)	11.17	206.2
2000	-5.570·10^{-4} (-0.01920)					
ω rpm	$i^{SHE}\left(i^{RHE}\right)$ mA cm^{-2}	s V^{-1}	t_s mV dec^{-1}	$i_b^{SHE}\left(i_b^{RHE}\right)$ mA cm^{-2}	s_b V^{-1}	t_b mV dec^{-1}
	reverse scan					
100	-4.184·10^{-4} (-0.01656)					
1000	-4.168·10^{-4} (-0.01649)	-8.949	-257.3	3868 (24.46)	12.32	186.9
2000	-3.853·10^{-4} (-0.01525)					

The Tafel slopes of the HER are comparable to those measured in 0.05 M Na_2SO_4 at pH 9.5 but the change in the slope at more negative potentials is smaller in the neutral electrolyte (Table 49). The

current densities calculated by equation (4.9) using the kinetic data in Table 49 are compared with the measured values in Figure 63. The rotation rate has almost no effect on the HER.
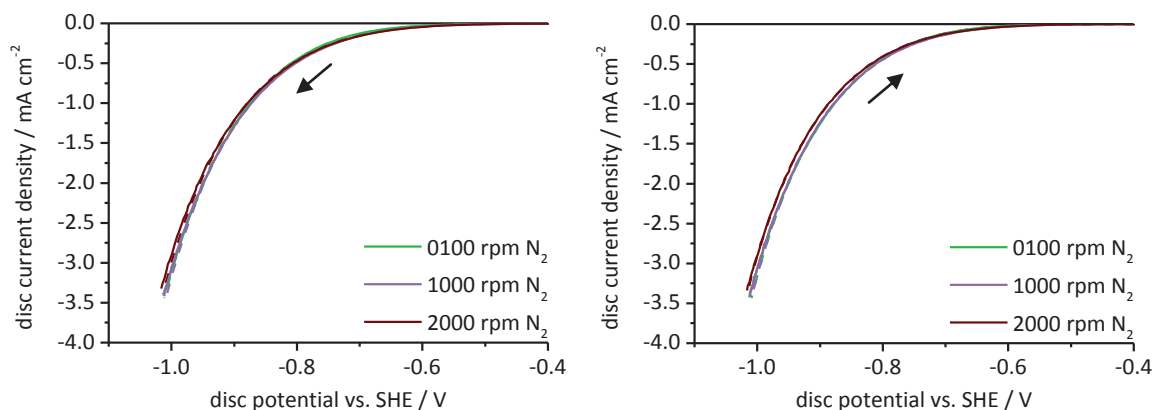

Figure 63: Potentiodynamic polarization curves (10 mV s^{-1}) in N$_2$ saturated 0.05 M Na$_2$SO$_4$ after 10 min OCP at different rotation rates; measured (dashed) and calculated (solid); forward scan: left, reverse scan: right
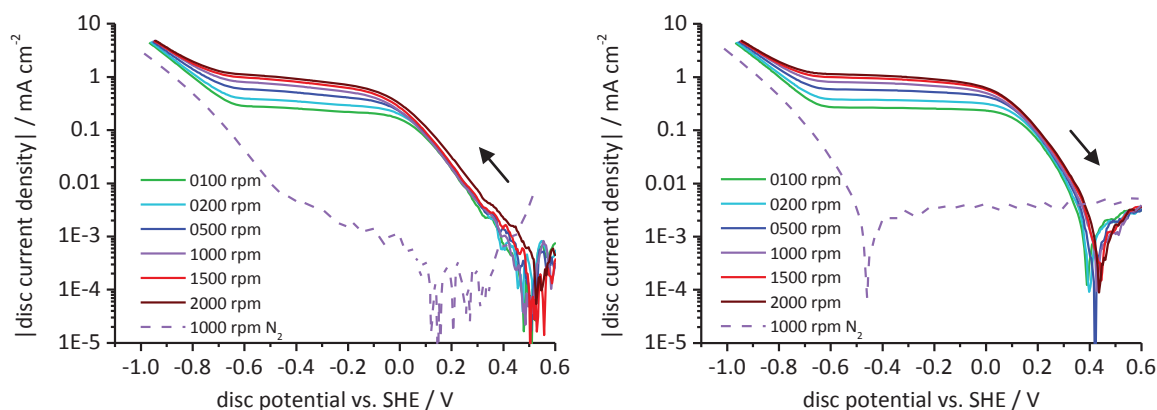
5.4.1.2 Air

Figure 64: Potentiodynamic polarization curves (10 mV s^{-1}) in air saturated 0.05 M Na$_2$SO$_4$ after 10 min OCP at different rotation rates; forward scan: left, reverse scan: right

The zero-current potentials of the disc electrode in the aerated 0.05 M Na$_2$SO$_4$ are between +0.48 V and +0.56 V in the forward scan and, depending on the rotation rate, between +0.38 V and +0.44 V in the reverse scan (Figure 64). The ORR does not reach a limiting current density before the HER starts and no decrease in the current density appears in the hydrogen adsorption range.

At disc potentials between +0.2 V and -0.7 V a peak in the ring current indicates the formation of hydrogen peroxide at the disc electrode. The peak maxima at the ring indicate, that the disc current densities between -0.027 mA cm^{-2} and -0.055 mA cm^{-2} are caused by the formation of hydrogen peroxides which desorbs from the disc electrode.

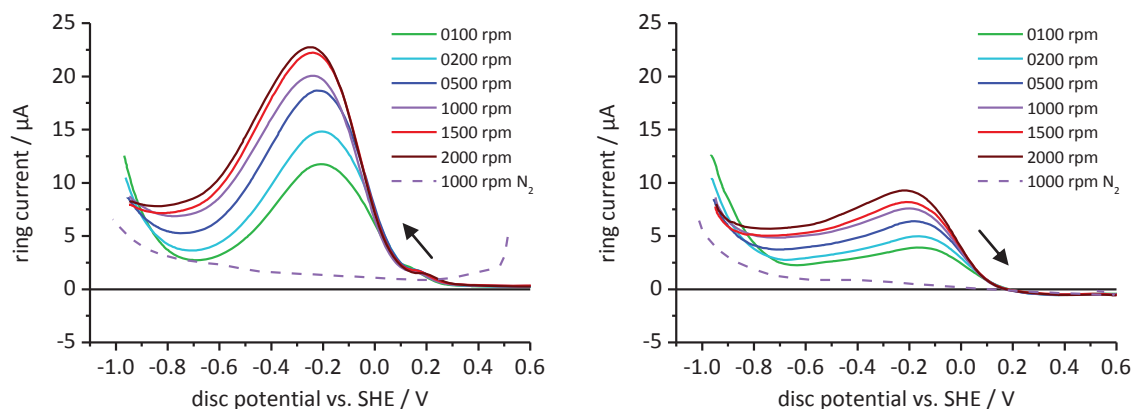Figure 65: Ring currents measured during the potentiodynamic scan (10 mV s^{-1}) at the disc electrode in air saturated 0.05 M Na$_2$SO$_4$ after 10 min OCP at different rotation rates; ring potential: +0.80 V vs. SHE; forward scan: left, reverse scan: right

The Tafel slopes of the first path of the ORR given in Table 50 are close to the values between −110 mV dec^{-1} and -150 mV dec^{-1} published by other authors [62, 81, 99] for neutral electrolytes.

Table 50: Kinetic data for the 1. ORR path in air saturated 0.05 M Na$_2$SO$_4$ for equation (4.8)

ω rpm	forward scan				reverse scan			
	i_{lim} mA cm^{-2}	i^{SHE} (i^{ROE}) mA cm^{-2}	s V^{-1}	t_s mV dec^{-1}	i_{lim} mA cm^{-2}	i^{SHE} (i^{ROE}) mA cm^{-2}	s V^{-1}	t_s mV dec^{-1}
100	-0.2041				-0.2456			
200	-0.2731				-0.3084			
500	-0.3837	-0.4801 ($-2.974 \cdot 10^{-6}$)	-14.66	-157.1	-0.4301	-2.877 ($-2.160 \cdot 10^{-6}$)	-17.24	-133.6
1000	-0.4973				-0.5310			
1500	-0.6112				-0.6468			
2000	-0.7130				-0.7204			

Due to the appearance of a ring current at disc potentials below +0.20 V a second path for the ORR has to be considered in 0.05 M Na$_2$SO$_4$ (Table 51). The limiting current densities of both ORR paths are in a linear relationship with the square root of the rotation rate.

Table 51: Kinetic data for the 2. ORR path in air saturated 0.05 M Na$_2$SO$_4$ for equation (4.8)

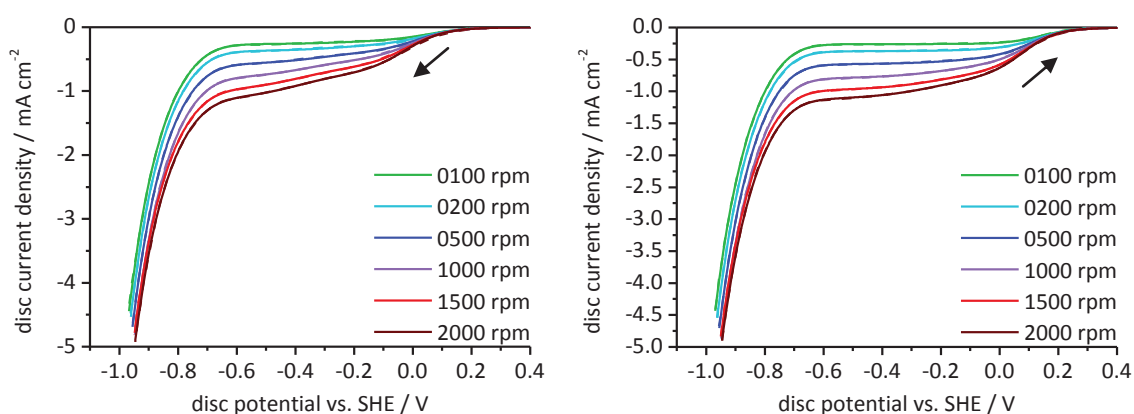| ω rpm	forward scan				reverse scan			
	i_{lim} mA cm^{-2}	i^{SHE} (i^{ROE}) mA cm^{-2}	s V^{-1}	t_s mV dec^{-1}	i_{lim} mA cm^{-2}	i^{SHE} (i^{ROE}) mA cm^{-2}	s V^{-1}	t_s mV dec^{-1}
100	-0.0592				-0.0133			
200	-0.0989				-0.0620			
500	-0.1951	$-6.181 \cdot 10^{-3}$ ($-1.078 \cdot 10^{-6}$)	-10.58	-217.6	-0.1451	$-63.87 \cdot 10^{-3}$ ($-52.56 \cdot 10^{-6}$)	-8.683	-265.2
1000	-0.2979				-0.2644			
1500	-0.3749				-0.3362			
2000	-0.4132				-0.4039			

No reduction of the limited current density due to hydrogen adsorption can be observed. Therefore no peroxide formation is considered in this potential range.

The slopes of the HER are similar in both scan directions (Table 52) and are comparable to those found in the deaerated solution.

Figure 66 shows that the model fits well to the measured values.

Table 52: Kinetic data for the HER in air saturated 0.05 M Na$_2$SO$_4$ for equation (4.9)

ω rpm	i^{SHE} (i^{RHE}) mA cm^{-2}	s V^{-1}	t_s mV dec^{-1}	i_b^{SHE} (i_b^{RHE}) mA cm^{-2}	s_b V^{-1}	t_b mV dec^{-1}
	forward scan					
100	-5.158·10^{-4} (-0.02377)					
200	-5.432·10^{-4} (-0.02503)					
500	-5.686·10^{-4} (-0.02620)	-9.320	-247.1	1.289·10^5 (128.2)	16.82	136.9
1000	-5.997·10^{-4} (-0.02764)					
1500	-5.612·10^{-4} (-0.02586)					
2000	-5.725·10^{-4} (-0.02638)					
	reverse scan					
ω rpm	i^{SHE} (i^{RHE}) mA cm^{-2}	s V^{-1}	t_s mV dec^{-1}	i_b^{SHE} (i_b^{RHE}) mA cm^{-2}	s_b V^{-1}	t_b mV dec^{-1}
100	-7.916·10^{-4} (-0.03021)					
200	-8.428·10^{-4} (-0.03216)					
500	-8.894·10^{-4} (-0.03394)	-8.861	-259.9	2.130·10^5 (193.6)	17.04	135.1
1000	-9.351·10^{-4} (-0.03569)					
1500	-8.697·10^{-4} (-0.03319)					
2000	-8.844·10^{-4} (-0.03375)					

Figure 66: Potentiodynamic polarization curves (10 mV s^{-1}) in air saturated 0.05 M Na$_2$SO$_4$ after 10 min OCP at different rotation rates; measured (dashed) and calculated (solid); forward scan: left, reverse scan: right

5.4.2 SODIUM CHLORIDE 0.10 M
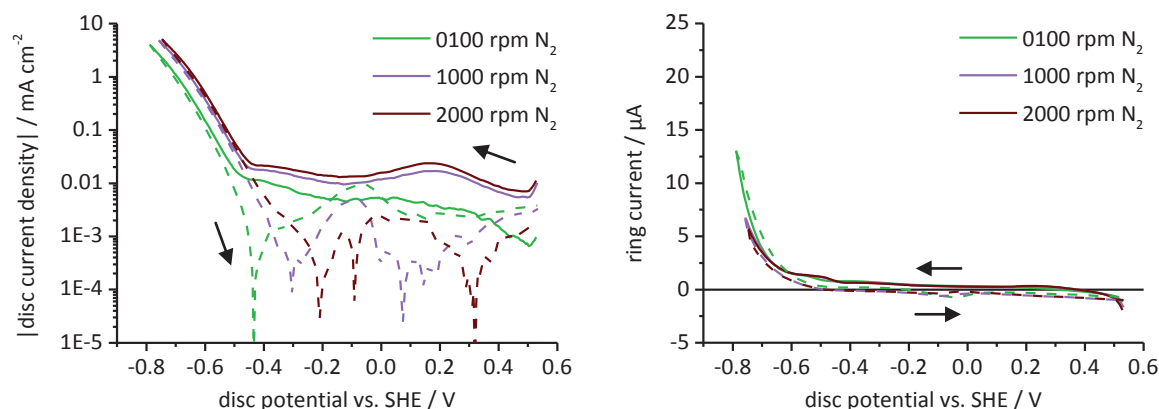
5.4.2.1 NITROGEN

Figure 67: Potentiodynamic polarization curves (10 mV s^{-1}) in N$_2$ saturated 0.10 M NaCl after 10 min OCP at different rotation rates; ring potential: +0.80 V vs. SHE; forward scan: solid lines, reverse scan: dashed lines

The potentiodynamic measurements at the disc electrode at 1000 rpm and 2000 rpm in 0.10 M NaCl show a reduction peak in the forward scan with an area of 300±50 µC cm^{-2} (Figure 67). This peak is supposedly the reduction of the surface oxide layer which is thicker than in sulfuric acid (200±20 µC cm^{-2}) but similar to the oxide layer in sodium hydroxide (323±6 µC cm^{-2}). The HER starts at -0.4 V and has a pre-exponential current density that depends on the rotation rate. A clear zero-current potential appears only in the reverse scan at 100 rpm. The measurements at the higher rotation rates show more than one zero-current potential. The reason for this is an anodic peak at -0.1 V, which may be caused by the oxidation of adsorbed or absorbed hydrogen.

Table 53: Kinetic data for the HER in N$_2$ saturated 0.10 M NaCl for equation (4.9)

ω rpm	$i^{\mathrm{SHE}}\ (i^{\mathrm{RHE}})$ mA cm^{-2}	s V^{-1}	t_s mV dec^{-1}	$i_b^{\mathrm{SHE}}\ (i_b^{\mathrm{RHE}})$ mA cm^{-2}	s_b V^{-1}	t_b mV dec^{-1}
			forward scan			
100	-1.909·10^{-4} (-0.03458)					
1000	-3.519·10^{-4} (-0.06374)	-12.65	-182.1	8.253·10^{4} (28.32)	19.41	118.7
2000	-4.328·10^{-4} (-0.07839)					
			reverse scan			
100	-0.3420·10^{-4} (-0.01480)					
1000	-0.6711·10^{-4} (-0.02905)	-14.77	-155.9	2.702·10^{4} (12.21)	18.74	122.9
2000	-0.8276·10^{-4} (-0.03583)					

The kinetic data for the HER is given in Table 53. The Tafel slopes for the HER in 0.10 M NaCl are lower than those found in 0.05 M Na$_2$SO$_4$. In Figure 68 the current densities calculated by equation

(4.9) using the kinetic data in Table 53 are compared with the measured values. The model fits well with the measured data.
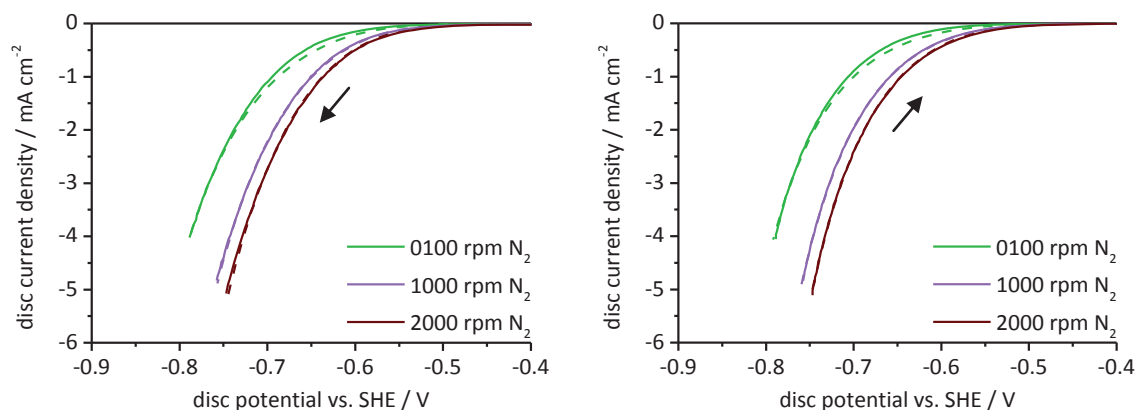

Figure 68: Potentiodynamic polarization curves (10 mV s^{-1}) in N$_2$ saturated 0.10 M NaCl after 10 min OCP at different rotation rates; measured (dashed) and calculated (solid); forward scan: left, reverse scan: right

5.4.2.2 AIR
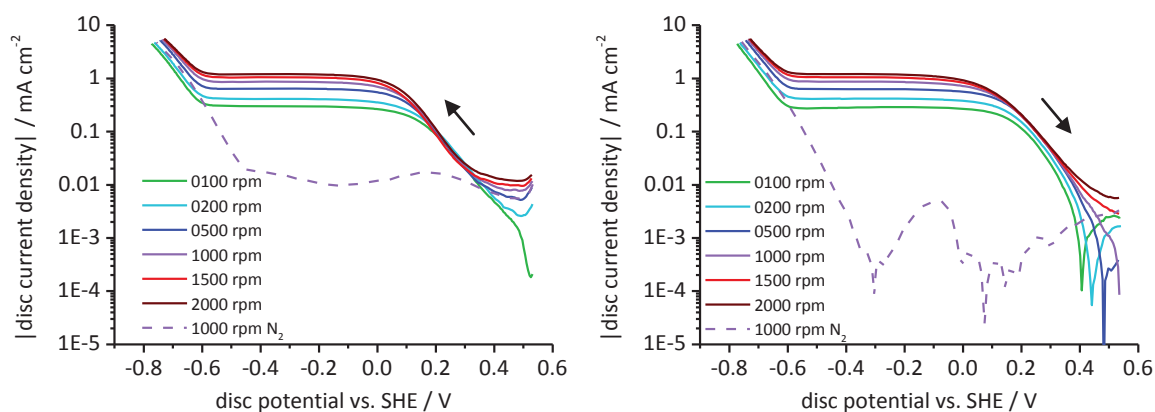
Figure 69: Potentiodynamic polarization curves (10 mV s^{-1}) in air saturated 0.10 M NaCl after 10 min OCP at different rotation rates; forward scan: left, reverse scan: right

A diffusion dependent current density step prior to the ORR (Figure 69) appeared, as has been observed in all other chloride electrolytes, in the aerated 0.10 M NaCl. The zero-current potential shifted from +0.41 V to more positive potential with an increase of the rotation rate.

A diffusion independent peak with an area of 16 µC cm^{-2} appears between +0.3 V and +0.2 V at the ring during the forward scan (Figure 70). A second diffusion dependent peak with a maximum at +0.1 V indicates the formation of hydrogen peroxide as an intermediate at the disc electrode.
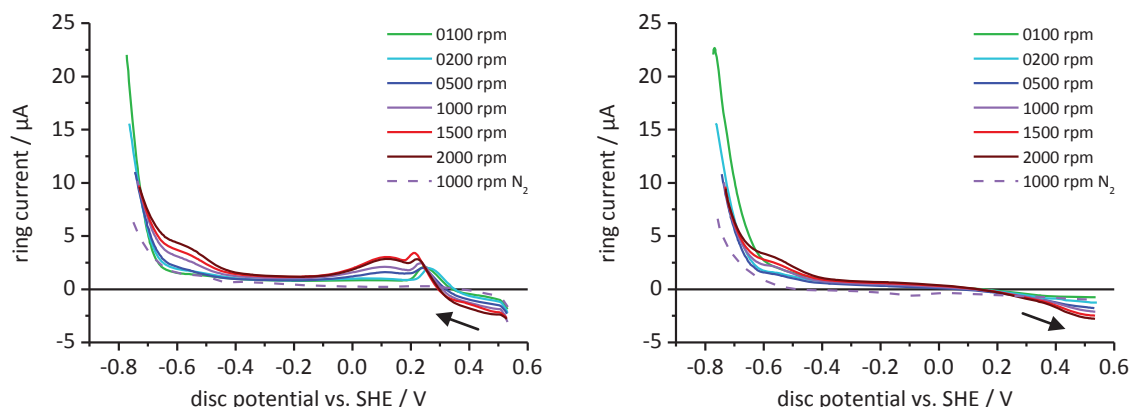
Figure 70: Ring currents measured during the potentiodynamic scan (10 mV s^{-1}) at the disc electrode in air saturated 0.10 M NaCl after 10 min OCP at different rotation rates; ring potential: +0.80 V vs. SHE; forward scan: left, reverse scan: right

The values for the potentiodynamic forward scan in 0.10 M NaCl can be sufficiently fitted using just one ORR path. In the reverse scan the ORR depends on the rotation rate which was taken into account in the multi curve fit by a variable pre-exponential current density (Table 54) but no clear tendency was obtained for these values. The Tafel slopes of the 1. ORR path are close to the values between -110 mV dec^{-1} and -150 mV dec^{-1} found by other authors [62, 81, 99] in neutral electrolytes.

Table 54: Kinetic data for the 1. ORR path in air saturated 0.10 M NaCl for equation (4.8)

ω rpm	forward scan i_{lim} mA cm^{-2}	i^{SHE} (i^{ROE}) mA cm^{-2}	s V^{-1}	t_s mV dec^{-1}	reverse scan i_{lim} mA cm^{-2}	i^{SHE} (i^{ROE}) mA cm^{-2}	s V^{-1}	t_s mV dec^{-1}
100	-0.2913				-0.2795	-5.610 (-6.936·10^{-6})		
200	-0.4027				-0.3864	-6.324 (-7.819·10^{-6})		
500	-0.6311	-4.134 (-2.931·10^{-6})	-17.31	-133.0	-0.5635	-8.224 (-10.17·10^{-6})	-16.63	-138.5
1000	-0.8564				-0.7234	-7.194 (-8.894·10^{-6})		
1500	-1.0440				-0.8586	-6.698 (-8.281·10^{-6})		
2000	-1.1990				-0.9787	-6.590 (-8.148·10^{-6})		

To obtain a sufficient fit a second ORR path has to be considered (Table 55) in the reverse scan for higher rotation rates while the ring currents do not give any hint of the formation of hydrogen peroxide. The limiting current densities of all ORR paths have a linear relationship with the square root of the rotation rate.

Peaks with less than 5 µA have been measured at the ring electrode in the hydrogen adsorption region but no decrease in the limiting current densities at the disc electrode was found. Therefore the peroxide formation in combination with the hydrogen adsorption was neglected in 0.10 M NaCl.

Table 55: Kinetic data for the 2. ORR path in air saturated 0.10 M NaCl for equation (4.8)

| ω | forward scan | | | | reverse scan | | | |
rpm	i_{lim} mA cm^{-2}	$i^{SHE}\left(i^{ROE}\right)$ mA cm^{-2}	s V^{-1}	t_s mV dec^{-1}	i_{lim} mA cm^{-2}	$i^{SHE}\left(i^{ROE}\right)$ mA cm^{-2}	s V^{-1}	t_s mV dec^{-1}
100	-				-0.0000			
200	-				-0.0245			
500	-	-	-	-	-0.0619	-0.09969 (-4.053·10^{-6})	-12.36	-186.3
1000	-				-0.1479			
1500	-				-0.1994			
2000	-				-0.2346			

The Tafel slopes of the HER (Table 56) are, as it was the case in the deaerated solutions, smaller in 0.10 M NaCl than in 0.05 M Na$_2$SO$_4$. Additionally a higher influence of the rotation rate on the HER is observed in NaCl. The pre-exponential current densities have no linear relationship with the square root of the rotation rate but their values increase with a decrease in the diffusion layer thickness due to a higher mass transport.

Table 56: Kinetic data for the HER in air saturated 0.10 M NaCl for equation (4.9)

| ω | forward scan | | | | | |
rpm	$i^{SHE}\left(i^{RHE}\right)$ mA cm^{-2}	s V^{-1}	t_s mV dec^{-1}	$i_b^{SHE}\left(i_b^{RHE}\right)$ mA cm^{-2}	s_b V^{-1}	t_b mV dec^{-1}
100	-35.71·10^{-6} (-17.49·10^{-3})					
200	-43.71·10^{-6} (-21.40·10^{-3})					
500	-63.56·10^{-6} (-31.12·10^{-3})	-15.07	-152.8	1.174·10^{10} (3783)	36.37	63.32
1000	-72.92·10^{-6} (-35.71·10^{-3})					
1500	-77.57·10^{-6} (-37.99·10^{-3})					
2000	-78.54·10^{-6} (-38.46·10^{-3})					

| ω | reverse scan | | | | | |
rpm	$i^{SHE}\left(i^{RHE}\right)$ mA cm^{-2}	s V^{-1}	t_s mV dec^{-1}	$i_b^{SHE}\left(i_b^{RHE}\right)$ mA cm^{-2}	s_b V^{-1}	t_b mV dec^{-1}
100	-3.768·10^{-6} (-6.077·10^{-3})					
200	-4.778·10^{-6} (-7.706·10^{-3})					
500	-7.303·10^{-6} (-11.78·10^{-3})	-17.97	-128.2	10.68·10^{10} (6225)	40.53	56.82
1000	-8.410·10^{-6} (-13.56·10^{-3})					
1500	-8.985·10^{-6} (-14.49·10^{-3})					
2000	-9.072·10^{-6} (-14.63·10^{-3})					

Figure 71 shows fitted curves compared to the measured values.
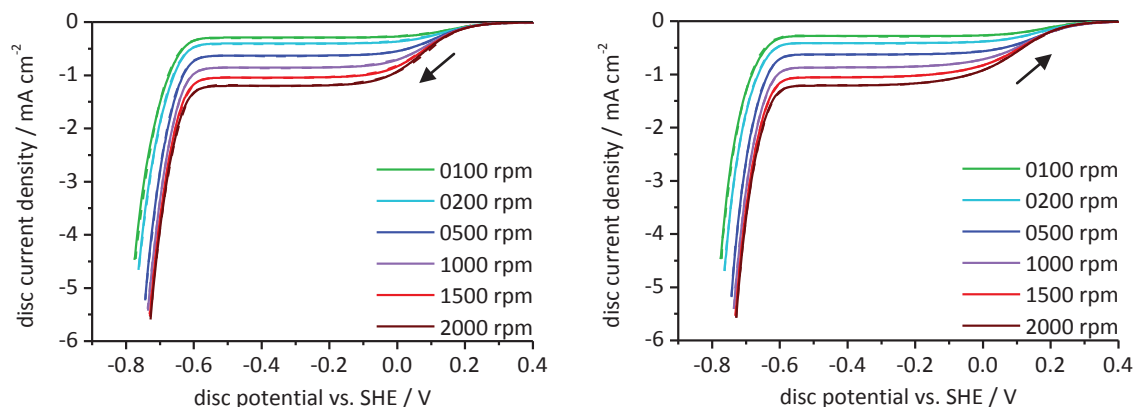
Figure 71: Potentiodynamic polarization curves (10 mV s^{-1}) in air saturated 0.10 M NaCl after 10 min OCP at different rotation rates; measured (dashed) and calculated (solid); forward scan: left, reverse scan: right
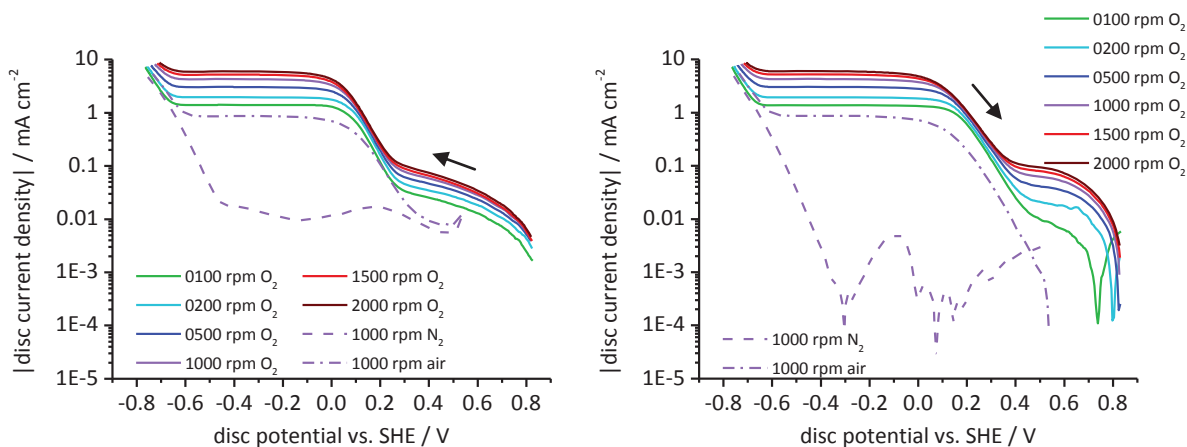
5.4.2.3 OXYGEN

Figure 72: Potentiodynamic polarization curves (10 mV s^{-1}) in O$_2$ saturated 0.10 M NaCl after 20 min OCP at different rotation rates; forward scan: left, reverse scan: right

To investigate the current step prior to the ORR, measurements under oxygen were carried out (Figure 72). The current densities of this step are higher in the oxygen saturated electrolyte than in the aerated electrolyte (Figure 73). The current densities of this step in hydrochloric acid and 0.10 M NaCl electrolyte buffered at pH 4.5 are also smaller than in the oxygen saturated 0.10 M NaCl. In the 0.10 M NaCl solution buffered at pH 9.5 no such step was found while the increase of hydrogen peroxide in this electrolyte due to the presence of chloride indicates a chloride adsorption. The step appears in neutral or acidic solutions only in the presence of chloride but no change was observed by increasing the chloride concentration from 0.1 M to 0.6 M. The chloride adsorption is competitive to the oxide film formation [227, 228] and the platinum surface oxide might be dissolved by chloride [85]. Therefore it can be assumed that this prior current step is due to the oxygen reduction taking place at free platinum sites formed by desorption of chloride or by the dissolution of the platinum oxide layer.
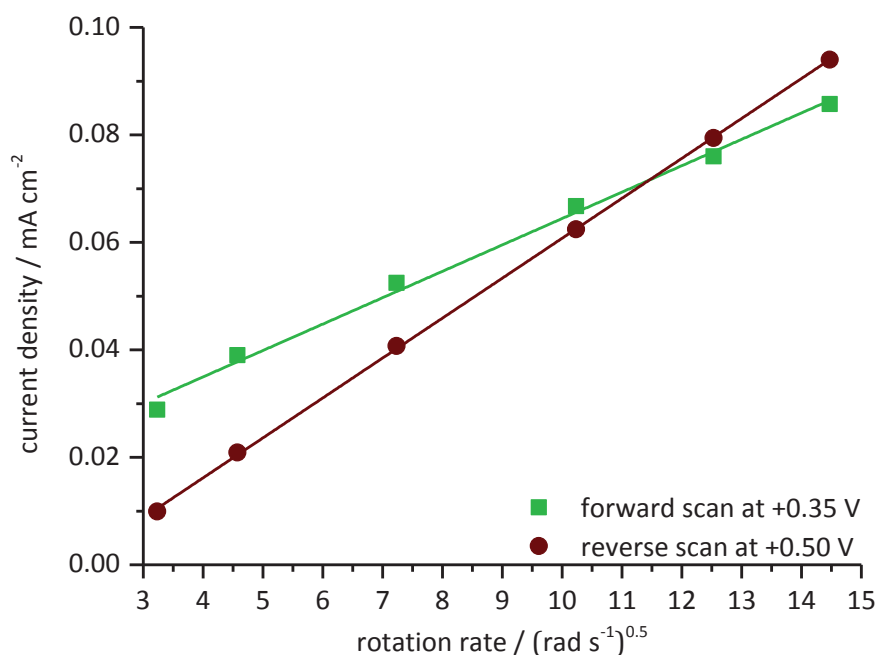
Figure 73: Current densities of the pre-ORR step in O_2 saturated 0.10 M NaCl after 20 min OCP at different rotation rates with linear fit

The beginning of the ORR in the forward scans at the disc electrode is accompanied by a high peak at the ring. This peak maximum at +0.1 V is about five times higher than that in air saturated electrolytes. Also the shoulders in the ring currents caused by the hydrogen peroxide formation due to the hydrogen adsorption at the disc are about five times higher than those found in air. Therefore the amount of hydrogen peroxide, detected at the ring electrode, increases linearly with the oxygen concentration according to Henry's law.
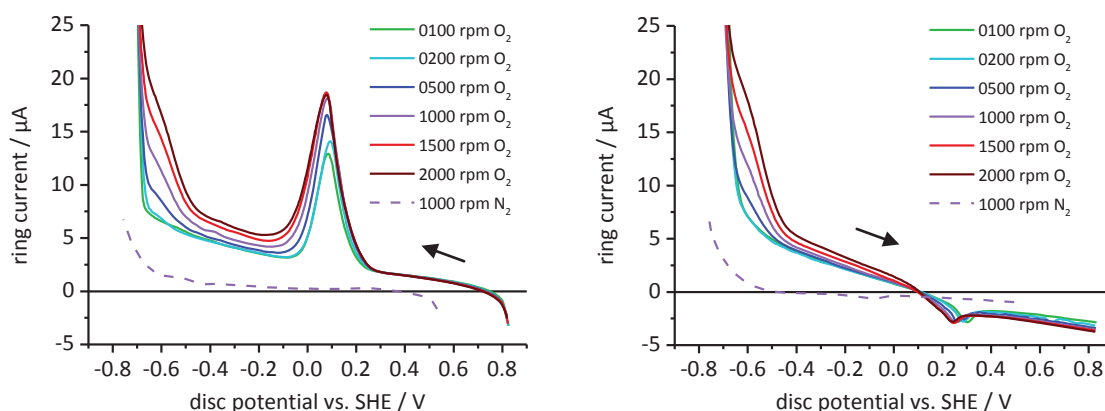
Figure 74: Ring currents measured during the potentiodynamic scan (10 mV s^{-1}) at the disc electrode in O_2 saturated 0.10 M NaCl after 10 min OCP at different rotation rates; ring potential: +0.80 V vs. SHE; forward scan: left, reverse scan: right

There is an influence of the rotation rate on the kinetics of the ORR in oxygen saturated 0.10 M NaCl as was the case in aerated 0.10 M NaCl (chapter 5.4.2.2) and in aerated 0.05 M Na$_2$SO$_4$ buffered at pH 4.5 (chapter 5.2.3.2). For this reason the pre-exponential current densities were set as a variable parameter for this fit. While the pre-exponential current densities show an increase at higher

rotation rates in the forward scan it seems to be the other way for the reverse scan (Table 57). The fit of these values might also be disturbed by the prior current step.

The Tafel slopes measured for the 1. ORR path are in the same range as in aerated solution and therefore also similar to the published values of other authors [62, 81, 99] in neutral solutions. In the forward scan the pre-exponential current densities increase linearly with the square root of the rotation rate. In the reverse scan the pre-exponential current densities, except that at 100 rpm, also shows a linear relationship with the square root of the rotation rate. In contrast to the forward scan the values are decreasing when the rotation rate is increased.

Table 57: Kinetic data for the 1. ORR path in O_2 saturated 0.10 M NaCl for equation (4.8)

ω	i_{lim}	$i^{SHE}\left(i^{ROE}\right)$	s	t_s	i_{lim}	$i^{SHE}\left(i^{ROE}\right)$	s	t_s
	forward scan				reverse scan			
rpm	mA cm^{-2}	mA cm^{-2}	V^{-1}	mV dec^{-1}	mA cm^{-2}	mA cm^{-2}	V^{-1}	mV dec^{-1}
100	-1.404	-11.49 (-1.986·10^{-7})			-1.371	-46.67 (-174.8·10^{-7})		
200	-1.950	-15.62 (-2.700·10^{-7})			-1.927	-49.37 (-184.9·10^{-7})		
500	-2.930	-16.64 (-2.877·10^{-7})	-21.85	-105.4	-2.970	-45.96 (-172.1·10^{-7})	-18.09	-127.3
1000	-3.990	-17.75 (-3.068·10^{-7})			-3.687	-43.29 (-162.1·10^{-7})		
1500	-4.804	-17.48 (-3.022·10^{-7})			-4.295	-42.14 (-157.8·10^{-7})		
2000	-5.455	-19.00 (-3.285·10^{-7})			-4.802	-40.61 (-151.0·10^{-7})		

At rotation rates higher than 200 rpm a second ORR path has to be considered (Table 58). Neglecting the 2. ORR path at low rotation rates the limiting current densities of both ORR paths show a linear relationship with the square root of the rotation rate.

Table 58: Kinetic data for the 2. ORR path in O_2 saturated 0.10 M NaCl for equation (4.8)

ω	i_{lim}	$i^{SHE}\left(i^{ROE}\right)$	s	t_s	i_{lim}	$i^{SHE}\left(i^{ROE}\right)$	s	t_s
	forward scan				reverse scan			
rpm	mA cm^{-2}	mA cm^{-2}	V^{-1}	mV dec^{-1}	mA cm^{-2}	mA cm^{-2}	V^{-1}	mV dec^{-1}
100	-0.0000				-0.0000			
200	-0.0000				-0.0000			
500	-0.1046	-0.04160 (-2.925·10^{-8})	-17.32	-133.0	-0.0503	-0.9357 (-4.595·10^{-4})	-9.314	-247.3
1000	-0.2743				-0.5823			
1500	-0.4012				-0.9438			
2000	-0.5295				-1.2380			

With the hydrogen adsorption the limited current densities of the ORR decrease in oxygen saturated 0.10 M NaCl which cannot be neglected in this electrolyte. The kinetic data is given in Table 59. The amount of this decrease is very low and if the amount of oxygen would be only a fifth, as was the case under air, it is obvious that it could be neglected under air.

The kinetic data for the HER given in Table 60 show smaller Tafel slopes in pure oxygen than in the air saturated electrolyte and under nitrogen.

Table 59: Kinetic data for the ORR in combination with the hydrogen adsorption in O_2 saturated 0.10 M NaCl for equation (4.8)

		forward scan				reverse scan		
ω	i_{lim}	$i^{SHE}\left(i^{RHE}\right)$	s	t_s	i_{lim}	$i^{SHE}\left(i^{RHE}\right)$	s	t_s
rpm	mA cm^{-2}	mA cm^{-2}	V^{-1}	mV dec^{-1}	mA cm^{-2}	mA cm^{-2}	V^{-1}	mV dec^{-1}
100	0.0224				0.0198			
200	0.0160				0.0100			
500	0.0396	$3.509 \cdot 10^{-26}$	-109.6	-21.02	0.0140	$1.696 \cdot 10^{-44}$	-183.4	-12.5
1000	0.0659	$(1.283 \cdot 10^{-6})$			0.0254	$(9.235 \cdot 10^{-12})$		
1500	0.0846				0.0410			
2000	0.0975				0.0553			

As can be seen in Figure 75 the model fits well to the measured data.

Table 60: Kinetic data for the HER in O_2 saturated 0.10 M NaCl for equation (4.9)

		forward scan					
ω	$i^{SHE}\left(i^{RHE}\right)$	s	t_s	$i_b^{SHE}\left(i_b^{RHE}\right)$	s_b	t_b
rpm	mA cm^{-2}	V^{-1}	mV dec^{-1}	mA cm^{-2}	V^{-1}	mV dec^{-1}
100	$-37.30 \cdot 10^{-9}$ $(-0.9562 \cdot 10^{-3})$					
200	$-45.29 \cdot 10^{-9}$ $(-1.161 \cdot 10^{-3})$					
500	$-58.41 \cdot 10^{-9}$ $(-1.497 \cdot 10^{-3})$	-24.70	-93.24	$4.979 \cdot 10^{12}$ (4455)	45.09	51.07
1000	$-69.57 \cdot 10^{-9}$ $(-1.783 \cdot 10^{-3})$					
1500	$-76.68 \cdot 10^{-9}$ $(-1.966 \cdot 10^{-3})$					
2000	$-82.44 \cdot 10^{-9}$ $(-2.113 \cdot 10^{-3})$					
		reverse scan					
ω	$i^{SHE}\left(i^{RHE}\right)$	s	t_s	$i_b^{SHE}\left(i_b^{RHE}\right)$	s_b	t_b
rpm	mA cm^{-2}	V^{-1}	mV dec^{-1}	mA cm^{-2}	V^{-1}	mV dec^{-1}
100	$-2.102 \cdot 10^{-9}$ $(-0.2517 \cdot 10^{-3})$					
200	$-2.645 \cdot 10^{-9}$ $(-0.3167 \cdot 10^{-3})$					
500	$-3.479 \cdot 10^{-9}$ $(-0.4165 \cdot 10^{-3})$	-28.56	-80.63	$3.027 \cdot 10^{14}$ (17250)	51.79	44.47
1000	$-4.120 \cdot 10^{-9}$ $(-0.4933 \cdot 10^{-3})$					
1500	$-4.561 \cdot 10^{-9}$ $(-0.5461 \cdot 10^{-3})$					
2000	$-4.956 \cdot 10^{-9}$ $(-0.5934 \cdot 10^{-3})$					
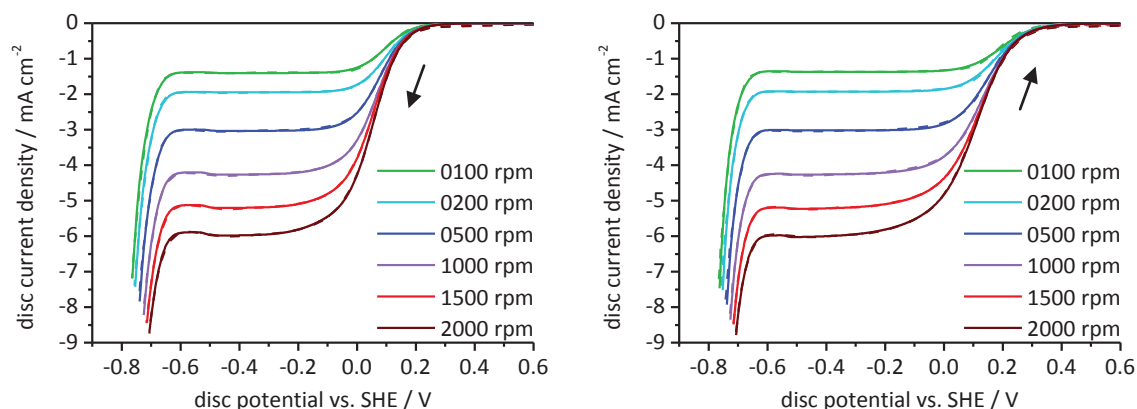
Figure 75: Potentiodynamic polarization curves (10 mV s^{-1}) in O$_2$ saturated 0.10 M NaCl after 20 min OCP at different rotation rates; measured (dashed) and calculated (solid); forward scan: left, reverse scan: right
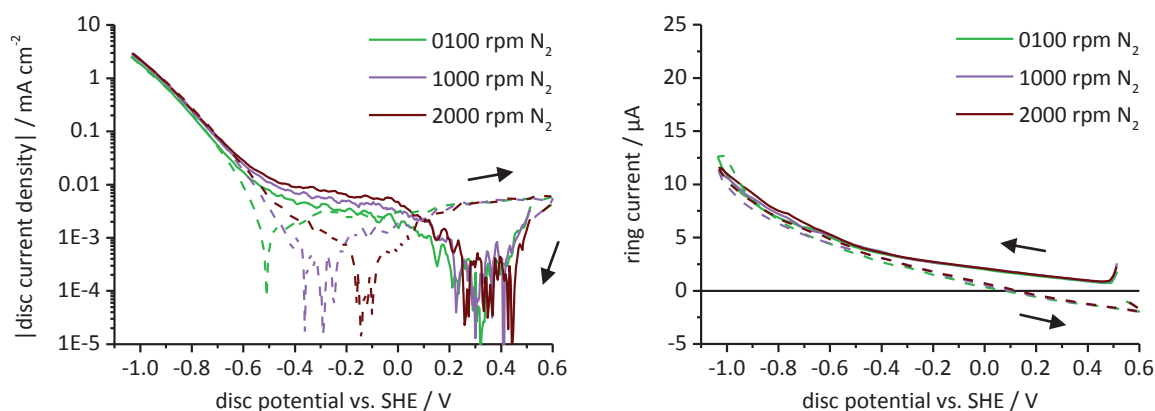
5.4.3 SODIUM SULFATE 0.30 M

5.4.3.1 NITROGEN

Figure 76: Potentiodynamic polarization curves (10 mV s^{-1}) in N$_2$ saturated 0.30 M Na$_2$SO$_4$ after 10 min OCP at different rotation rates; ring potential: +0.80 V vs. SHE; forward scan: solid lines, reverse scan: dashed lines

Analogous to the measurements in 0.05 M Na$_2$SO$_4$, no distinct zero-current potential appears at the disc electrode during the potentiodynamic forward scans in deaerated 0.30 M Na$_2$SO$_4$ (Figure 76) and no oxide peak can be found. The zero-current potentials are between +0.44 V and +0.23 V in the forward scan and between -0.51 V and -0.09 V in the reverse scan.

The slope of the HER in 0.30 M Na$_2$SO$_4$ is similar to that found in 0.05 M Na$_2$SO$_4$ and the pre-exponential current densities of the HER are more strongly influenced by the rotation rate. The kinetic data is given in Table 61.

Figure 77 shows the current densities calculated by equation (4.9) using the kinetic data in Table 61. As it can be seen the calculated values fit well with the measured values.

Table 61: Kinetic data for the HER in N_2 saturated 0.30 M Na_2SO_4 for equation (4.9)

| ω rpm	$i^{SHE}\left(i^{RHE}\right)$ mA cm^{-2}	s V^{-1}	t_s mV dec^{-1}	$i_b^{SHE}\left(i_b^{RHE}\right)$ mA cm^{-2}	s_b V^{-1}	t_b mV dec^{-1}
	forward scan					
100	-3.777·10^{-4} (-0.01293)					
1000	-4.329·10^{-4} (-0.01482)	-8.596	-267.9	1598 (29.47)	9.716	237.0
2000	-4.576·10^{-4} (-0.01566)					

ω rpm	$i^{SHE}\left(i^{RHE}\right)$ mA cm^{-2}	s V^{-1}	t_s mV dec^{-1}	$i_b^{SHE}\left(i_b^{RHE}\right)$ mA cm^{-2}	s_b V^{-1}	t_b mV dec^{-1}
	reverse scan					
100	-4.863·10^{-4} (-0.01471)					
1000	-5.795·10^{-4} (-0.01753)	-8.295	-277.6	1099 (24.02)	9.302	247.6
2000	-6.162·10^{-4} (-0.01864)					
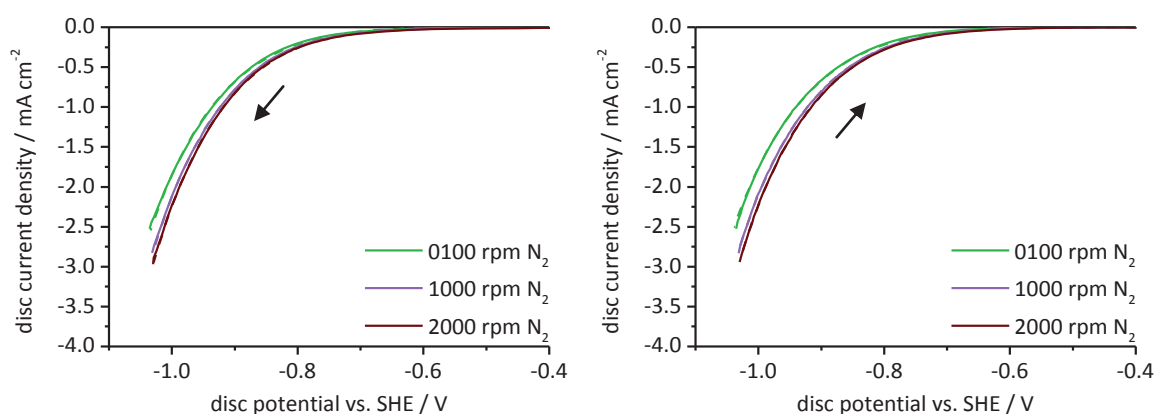
Figure 77: Potentiodynamic polarization curves (10 mV s^{-1}) in N_2 saturated 0.30 M Na_2SO_4 after 10 min OCP at different rotation rates; measured (dashed) and calculated (solid); forward scan: left, reverse scan: right

5.4.3.2 AIR
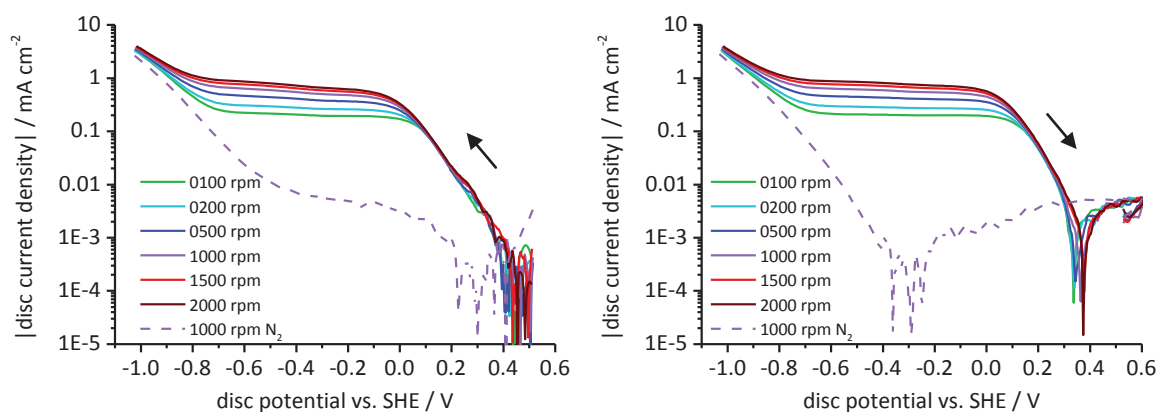
Figure 78: Potentiodynamic polarization curves (10 mV s^{-1}) in air saturated 0.30 M Na_2SO_4 after 10 min OCP at different rotation rates; forward scan: left, reverse scan: right

The zero-current potentials of a rotating platinum disc electrode in aerated 0.30 M Na_2SO_4 are between +0.51 V and +0.40 V in the forward scan and shift to +0.34 V at 100 rpm and +0.38 V at 2000 rpm in the reverse scan (Figure 78).

At a disc potential below +0.2 V a peak current peak appears at the ring (Figure 79) in 0.30 M Na_2SO_4 with a similar height as in 0.05 M Na_2SO_4. This peak consists of two or even three overlapping peaks which are most pronounced in the forward scan.
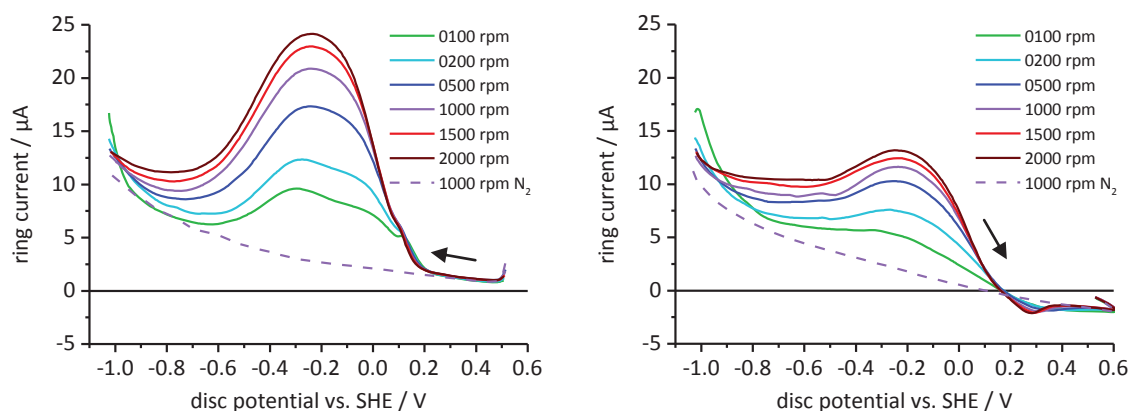

Figure 79: Ring currents measured during the potentiodynamic scan (10 mV s^{-1}) at the disc electrode in air saturated 0.30 M Na_2SO_4 after 20 min OCP at different rotation rates; ring potential: +0.80 V vs. SHE; forward scan: left, reverse scan: right

The kinetic data for the 1. ORR path is given in Table 62. The Tafel slopes of the 1. ORR path are smaller than in 0.05 M Na_2SO_4 but still in the range of the published values [62, 81, 99] for neutral electrolytes.

Table 62: Kinetic data for the 1. ORR path in air saturated 0.30 M Na_2SO_4 for equation (4.8)

ω	forward scan				reverse scan			
	i_{lim}	$i^{SHE}\left(i^{ROE}\right)$	s	t_s	i_{lim}	$i^{SHE}\left(i^{ROE}\right)$	s	t_s
rpm	mA cm^{-2}	mA cm^{-2}	V^{-1}	mV dec^{-1}	mA cm^{-2}	mA cm^{-2}	V^{-1}	mV dec^{-1}
100	-0.1970				-0.2039			
200	-0.2579				-0.2653			
500	-0.3643	-0.7019	-16.96	-135.8	-0.3870	-2.983	-19.58	-117.6
1000	-0.4809	(-6.625·10^{-7})			-0.5174	(-3.302·10^{-7})		
1500	-0.5664				-0.6196			
2000	-0.6363				-0.7032			

The 2. ORR path (Table 63) has a smaller contribution to the total ORR and lower Tafel slopes than in 0.05 M Na_2SO_4. All limiting current densities of the ORRs are increasing linearly with the square root of the rotation rate.

The diffusion limited current density does not decrease due to hydrogen adsorption and no peak in the ring current indicating an additional formation of hydrogen peroxide was observed in this potential region.

Table 63: Kinetic data for the 2. ORR path in air saturated 0.30 M Na_2SO_4 for equation (4.8)

ω rpm	i_{lim} mA cm^{-2}	$i^{SHE}\left(i^{ROE}\right)$ mA cm^{-2}	s V^{-1}	t_s mV dec^{-1}	i_{lim} mA cm^{-2}	$i^{SHE}\left(i^{ROE}\right)$ mA cm^{-2}	s V^{-1}	t_s mV dec^{-1}
	forward scan				reverse scan			
100	-0.0189				-0.0004			
200	-0.0430				-0.0228			
500	-0.0973	-2.775·10^{-4} (-1.323·10^{-9})	-14.98	-153.7	-0.0622	-25.37·10^{-4} (-1.905·10^{-7})	-11.61	-198.4
1000	-0.1580				-0.1115			
1500	-0.2041				-0.1440			
2000	-0.2423				-0.1718			

The kinetic data of the HER in air saturated 0.30 M Na_2SO_4 is given in Table 39. The pre-exponential current densities show a linear relationship with the square root of the rotation rate for all rotation rates higher than 100 rpm.

Table 64: Kinetic data for the HER in air saturated 0.30 M Na_2SO_4 for equation (4.9)

ω rpm	$i^{SHE}\left(i^{RHE}\right)$ mA cm^{-2}	s V^{-1}	t_s mV dec^{-1}	$i_b^{SHE}\left(i_b^{RHE}\right)$ mA cm^{-2}	s_b V^{-1}	t_b mV dec^{-1}
	forward scan					
100	-7.477·10^{-4} (-0.02193)					
200	-7.343·10^{-4} (-0.02153)					
500	-7.435·10^{-4} (-0.02180)	-8.220	-280.2	6.203·10^{4} (239.5)	13.52	-170.4
1000	-7.520·10^{-4} (-0.02205)					
1500	-7.677·10^{-4} (-0.02251)					
2000	-7.819·10^{-4} (-0.02293)					
	reverse scan					
100	-2.521·10^{-4} (-0.01104)					
200	-2.530·10^{-4} (-0.01108)					
500	-2.603·10^{-4} (-0.01140)	-9.196	-250.4	4.615·10^{4} (130.4)	14.28	161.2
1000	-2.639·10^{-4} (-0.01156)					
1500	-2.706·10^{-4} (-0.01185)					
2000	-2.759·10^{-4} (-0.01208)					

The polarization curves shown in Figure 80 are calculated from the sum of the current densities for the two ORR paths and for the HER. The calculated values fit well with the measured values.
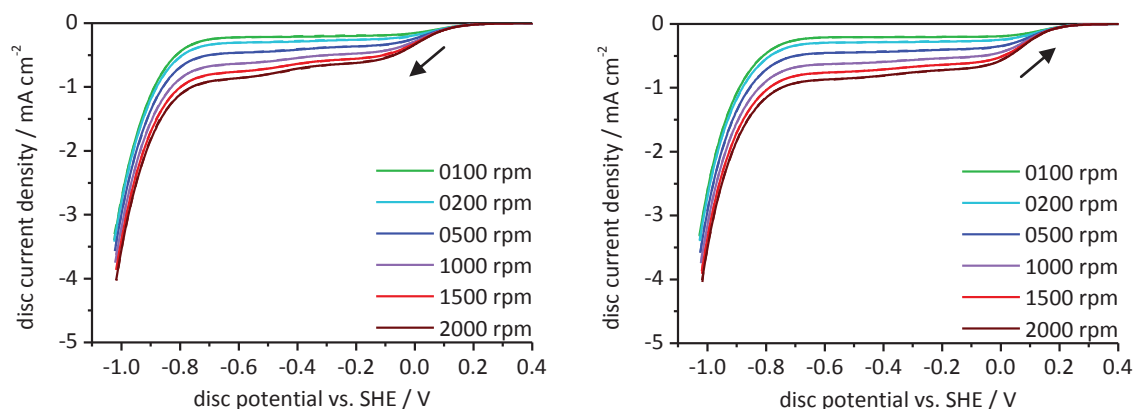
Figure 80: Potentiodynamic polarization curves (10 mV s^{-1}) in air saturated 0.30 M Na$_2$SO$_4$ after 10 min OCP at different rotation rates; measured (dashed) and calculated (solid); forward scan: left, reverse scan: right

5.4.4 SODIUM CHLORIDE 0.60 M

5.4.4.1 NITROGEN
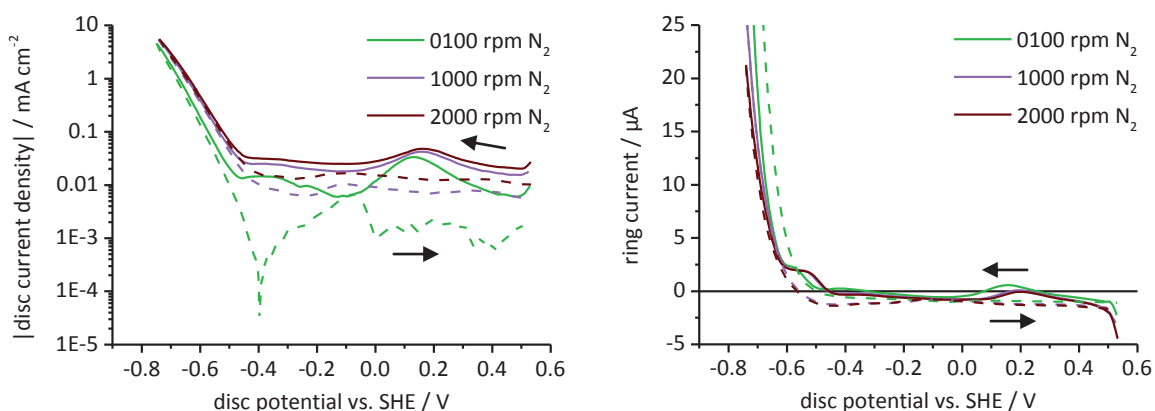
Figure 81: Potentiodynamic polarization curves (10 mV s^{-1}) in N$_2$ saturated 0.60 M NaCl after 10 min OCP at different rotation rates; ring potential: +0.80 V vs. SHE; forward scan: solid lines, reverse scan: dashed lines

In 0.60 M NaCl the platinum disc shows a reduction peak with a maximum between +0.14 V and +0.15 V during the forward scan (Figure 81). The charge consumed for this peak is 528±18 μC cm^{-2} which is higher than the 300 μC cm^{-2} found in 0.10 M NaCl. The HER starts at the same potential (-0.4 V) as in 0.10 M NaCl. Only the reverse scan at 100 rpm shows a zero-current potential at -0.40 V. In the reverse scans the current remains cathodic at higher rotation rates. This might be caused by the reduction of residual oxygen in the electrolyte.

The kinetic data for the HER in 0.60 M NaCl is given in Table 65. The Tafel slopes for the HER in 0.60 M NaCl are comparable with those found in 0.10 M NaCl.

The current densities calculated by equation (4.9) using the kinetic data in Table 65 are in good agreement with the measurements (Figure 82).

Table 65: Kinetic data for the HER in N_2 saturated 0.60 M NaCl for equation (4.9)

| ω rpm	$i^{SHE}\,(i^{RHE})$ mA cm^{-2}	s V^{-1}	t_s mV dec^{-1}	$i_b^{SHE}\,(i_b^{RHE})$ mA cm^{-2}	s_b V^{-1}	t_b mV dec^{-1}
	forward scan					
100	-50.88·10^{-6} (-0.02639)					
1000	-74.44·10^{-6} (-0.03861)	-15.21	-151.1	11370 (14.71)	16.18	142.3
2000	-80.20·10^{-6} (-0.04160)					
ω rpm	$i^{SHE}\,(i^{RHE})$ mA cm^{-2}	s V^{-1}	t_s mV dec^{-1}	$i_b^{SHE}\,(i_b^{RHE})$ mA cm^{-2}	s_b V^{-1}	t_b mV dec^{-1}
	reverse scan					
100	-3.547·10^{-6} (-0.007290)					
1000	-5.640·10^{-6} (-0.01159)	-18.56	-124.1	3263 (2.270)	17.69	130.2
2000	-6.058·10^{-6} (-0.01245)					
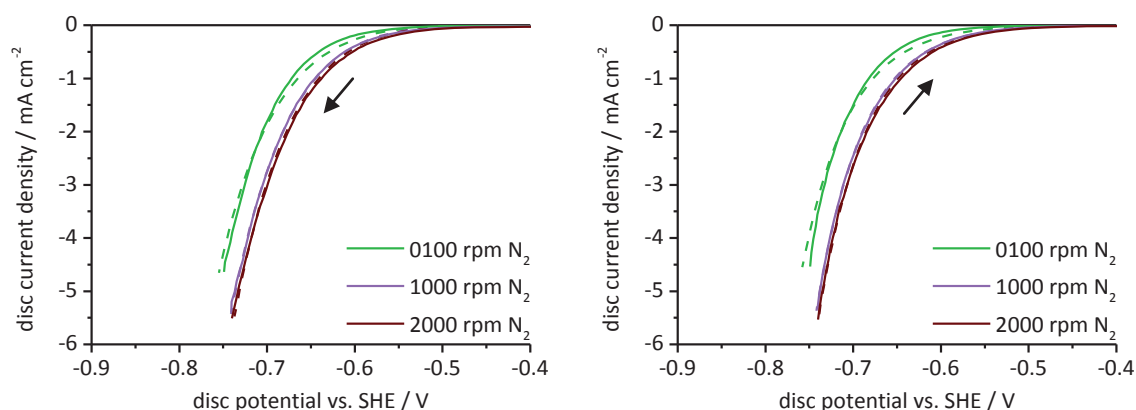
Figure 82: Potentiodynamic polarization curves (10 mV s^{-1}) in N_2 saturated 0.60 M NaCl after 10 min OCP at different rotation rates; measured (dashed) and calculated (solid); forward scan: left, reverse scan: right

5.4.4.2 Air
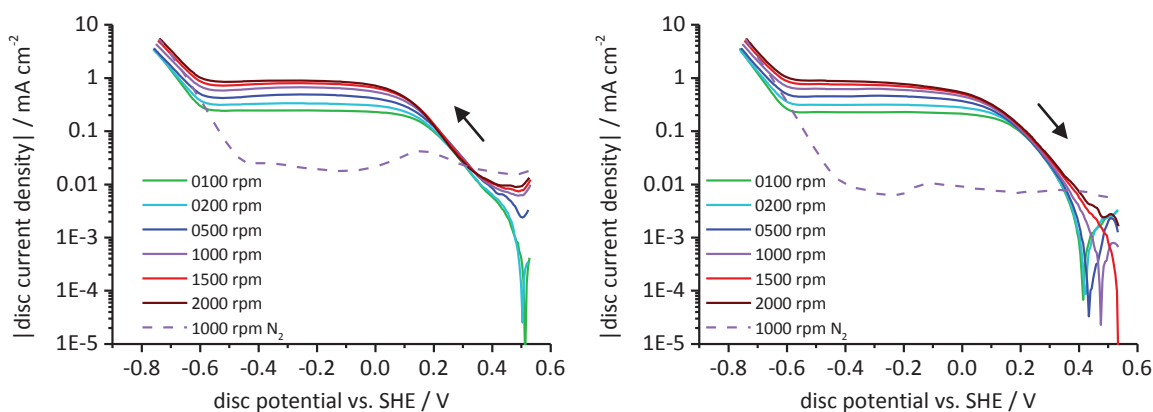
Figure 83: Potentiodynamic polarization curves (10 mV s^{-1}) in air saturated 0.60 M NaCl after 10 min OCP at different rotation rates; forward scan: left, reverse scan: right

The typical step in chloride solutions prior to the ORR appeared also in 0.60 M NaCl (Figure 83). The zero-current potentials of the disc electrode during the potentiodynamic scans at 100 rpm and 200 rpm are +0.5 V in the forward scan. In the reverse scan the zero-current potential shifts from +0.4 V at 100 rpm to higher potentials by increase of the rotation rate similar to the zero-current potentials in 0.10 M NaCl.

The limited current densities of the forward scans get reduced at -0.5 V with the hydrogen adsorption.

The ring current shows, similar to the measurements in the 0.10 M NaCl electrolyte, three peaks in the forward scans (Figure 84). The first peak with a maximum at +0.20 V is independent of rotation rate and has an area of 92 μC cm^{-2}. This charge density is 5.8 times higher than the 16 μC cm^{-2} measured in 0.10 M NaCl. The second peak depends on the rotation rate and its maximum is between -0.1 V (100 rpm) and +0.11 V (2000 rpm). These peaks are higher than in 0.10 M NaCl and disappear when the limiting current density at the disc electrode is reached at -0.3 V. The third peak in the ring current below -0.4 V also appears in the reverse scan and is caused by hydrogen peroxide formed due to the adsorption of hydrogen at the disc electrode. In contrast to the measurements in 0.10 M NaCl small diffusion dependent currents at the ring remain at disc potentials between -0.4 V and +0.2 V in 0.60 M NaCl.
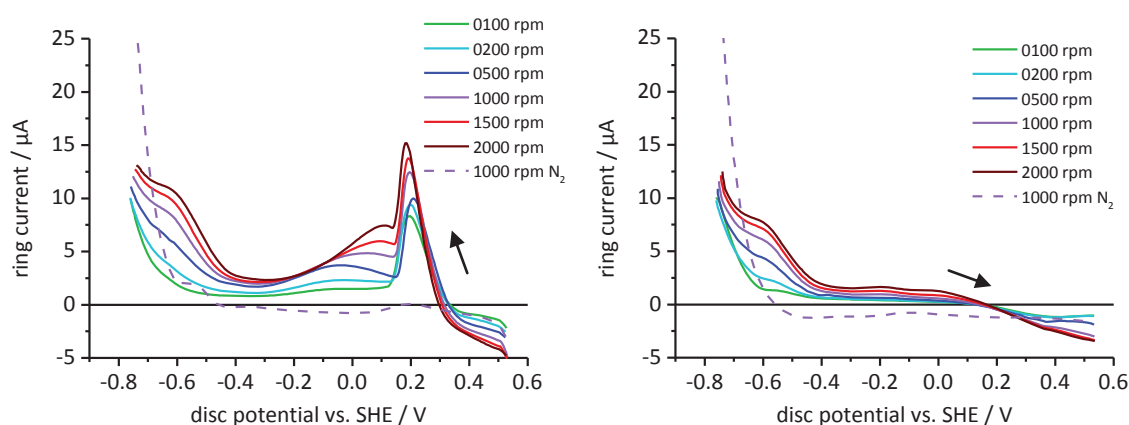
Figure 84: Ring currents measured during potentiodynamic scan (10 mV s^{-1}) at the disc electrode in air saturated 0.60 M NaCl after 10 min OCP at different rotation rates; ring potential: +0.80 V vs. SHE; forward scan: left, reverse scan: right

Table 66: Kinetic data for the 1. ORR path in air saturated 0.60 M NaCl for equation (4.8)

ω	forward scan				reverse scan			
	i_{lim}	$i^{\text{SHE}}\left(i^{\text{ROE}}\right)$	s	t_s	i_{lim}	$i^{\text{SHE}}\left(i^{\text{ROE}}\right)$	s	t_s
rpm	mA cm^{-2}	mA cm^{-2}	V^{-1}	mV dec^{-1}	mA cm^{-2}	mA cm^{-2}	V^{-1}	mV dec^{-1}
100	-0.2472				-0.2009			
200	-0.3313				-0.2753			
500	-0.4786	-3.854	-15.63	-147.3	-0.3195	-3.500	-17.09	-134.8
1000	-0.6570	(-10.80·10^{-6})			-0.3900	(-2.970·10^{-6})		
1500	-0.7914				-0.4300			
2000	-0.8892				-0.4488			

As it was the case for the ORR in 0.10 M NaCl only one step needs to be considered for a sufficient fit of the ORR in 0.60 M NaCl in the forward scan. The Tafel slopes (Table 66) are also within the range of those measured in 0.10 M NaCl and the values found by other authors [62, 81, 99] in neutral electrolytes.

In the reverse scan a second ORR path has to be considered. It has a high Tafel slope and its contribution to the total ORR increases from just 10 % at 100 rpm to 50 % at high rotation rates (Table 67). The limiting current densities increasing linearly with the square root of the rotation rate in the forward scan while in the reverse scan the 100 rpm limiting current density does not fit to this relation.

Table 67: Kinetic data for the 2. ORR path in air saturated 0.60 M NaCl for equation (4.8)

ω rpm	$i_{\lim}$ mA cm^{-2}	forward scan $i^{SHE}\left(i^{ROE}\right)$ mA cm^{-2}	s V^{-1}	t_s mV dec^{-1}	$i_{\lim}$ mA cm^{-2}	reverse scan $i^{SHE}\left(i^{ROE}\right)$ mA cm^{-2}	s V^{-1}	t_s mV dec^{-1}
100	-				-0.0235			
200	-				-0.0361			
500	-	-	-	-	-0.1361	-0.1747 (-71.31·10^{-6})	-9.540	-241.4
1000	-				-0.2412			
1500	-				-0.3435			
2000	-				-0.4494			

A decrease in the limited current density due to the hydrogen adsorption appears only in the forward scan. The kinetic data of this reaction is given in Table 68. The limiting current densities for this reaction did not increase linear with the square root of the rotation rates but reaching a maximum at 1000 rpm. A further increase of the rotation rate reduces this decrease of the limiting current density.

Table 68: Kinetic data for the ORR in combination with the hydrogen adsorption in air saturated 0.60 M NaCl for equation (4.8)

ω rpm	$i_{\lim}$ mA cm^{-2}	forward scan $i^{SHE}\left(i^{RHE}\right)$ mA cm^{-2}	s V^{-1}	t_s mV dec^{-1}	$i_{\lim}$ mA cm^{-2}	reverse scan $i^{SHE}\left(i^{RHE}\right)$ mA cm^{-2}	s V^{-1}	t_s mV dec^{-1}
100	0.02254				-			
200	0.02430				-			
500	0.05506	1.429·10^{-10} (0.02462)	-46.24	-49.81	-	-	-	-
1000	0.07163				-			
1500	0.06846				-			
2000	0.03934				-			

The kinetic data for the HER in air saturated 0.60 M NaCl is shown in Table 69. At low rotation rates the current due the HER seems to be independent of the rotation rate but at rotation rates above 200 rpm the pre-exponential current densities increase linearly with the square root of the rotation. The Tafel slopes are similar to those found in the deaerated solution.

Figure 85 shows a good correlation between the model and the measured values.

Table 69: Kinetic data for the HER in air saturated 0.60 M NaCl for equation (4.9)

ω rpm	$i^{SHE}\ (i^{RHE})$ mA cm^{-2}	s V^{-1}	t_s mV dec^{-1}	$i_b^{SHE}\ (i_b^{RHE})$ mA cm^{-2}	s_b V^{-1}	t_b mV dec^{-1}
	forward scan					
100	-29.28·10^{-6} (-0.01576)					
200	-28.36·10^{-6} (-0.01526)					
500	-30.22·10^{-6} (-0.01627)	-15.30	-150.6	1.416·10^{9} (1350)	33.73	68.28
1000	-39.84·10^{-6} (-0.02144)					
1500	-50.75·10^{-6}					
2000	-59.17·10^{-6} (-0.03185)					
	reverse scan					
100	-2.711·10^{-6} (-0.005132)					
200	-2.707·10^{-6} (-0.005125)					
500	-2.997·10^{-6} (-0.005674)	-18.36	-125.4	1.281·10^{11} (5201)	41.41	55.62
1000	-3.842·10^{-6} (-0.007273)					
1500	-4.987·10^{-6} (-0.009441)					
2000	-5.915·10^{-6} (-0.01120)					
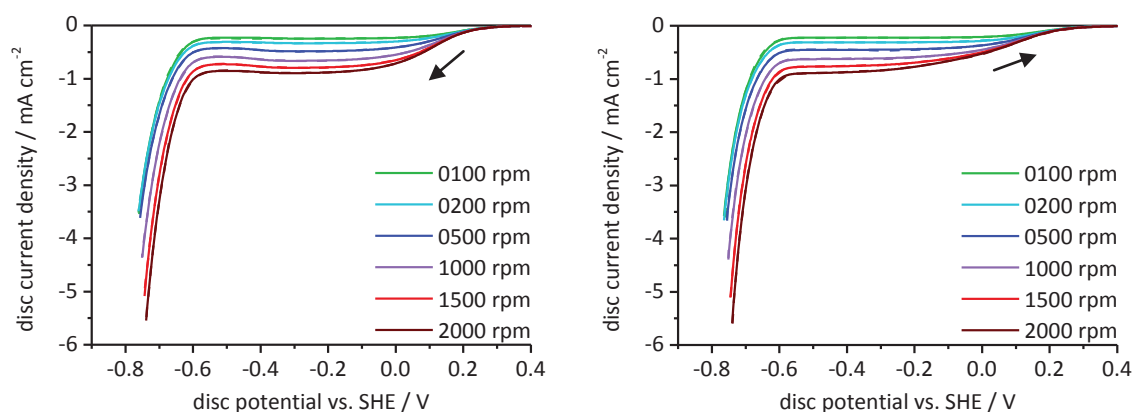
Figure 85: Potentiodynamic polarization curves (10 mV s^{-1}) in air saturated 0.60 M NaCl after 10 min OCP at different rotation rates; measured (dashed) and calculated (solid); forward scan: left, reverse scan: right

5.5 ZERO-CURRENT POTENTIALS

Figure 86 shows the pH-dependency of the zero-current potentials measured at a platinum disc electrode during a potentiodynamic scan at 1000 rpm. These zero-current potentials are close to the formation of PtO (equilibrium {5.1}) and PtO_2 (equilibrium {5.3}) in aerated solutions and in the forward scan measured in the deaerated electrolytes in the whole pH range except the neutral electrolytes. This fully agrees with the results of Lingane [80]. Only in deaerated solutions the zero-current potentials measured during the reverse scans are close to the RHE.

In sulfate electrolytes the pH dependence of this potential is -54.3 mV pH^{-1} under air. Excluding the value measured in 0.10 M HCl a similar value of -57.2 mV pH^{-1} has been found for chloride containing solution. In 0.10 M HCl the zero-current potential with +1.01 V is significant higher than the 0.95 V calculated for equilibrium {5.3}. The reason might be the corrosion of platinum which forms $[PtCl_4]^{2-}$ under acidic conditions. Similar results have been found for the OCP measured after the platinum disc electrode was exposed for one hour to sulfate electrolytes (chapter 5.1).

In the reverse scans for deaerated solutions the electrode shows zero-current potentials close to the reversible hydrogen electrode ({1.7} and {1.8}). For this case the slopes are -55.0 mV pH^{-1} in sulfate solutions and -57.6 mV in the chloride electrolytes.

Figure 86: Zero-current potentials during potentiodynamic measurements (10 mV s^{-1}) at 1000 rpm; sulfate and hydroxide: left, chloride and hydroxide: right; lines calculated with the standard potentials of Table 3 and 10^{-6} M $[PtCl_4]^{2-}$ with different chloride concentrations

The slopes obtained in the reverse scans under air and under nitrogen are close to the theoretical value of -58.5 mV pH^{-1}. These results are in good agreement with the potential-pH-dependence of -60 mV pH^{-1} measured by Winkelmann 30 min after cathodic polarization [82].

5.6 POTENTIALS AT -100 µA CM^{-2} DISC CURRENT DENSITY

To analyze the pH dependency of the ORR and the HER, the potentials at which the current density reaches a value of -100 µA cm^{-2} at 1000 rpm are plotted in Figure 87.

Under nitrogen these potentials are close to the potential of the reversible hydrogen electrode ({1.7} and {1.8}) and almost identical for the two scan directions. The slope of the pH dependency of the potentials at which -100 µA cm^{-2} is reached are in both cases -56.3 mV pH^{-1} for the sulfate

electrolytes and -62 mV pH^{-1} in chloride solutions. These values are close to the theoretical value of -58.5 mV pH^{-1}.

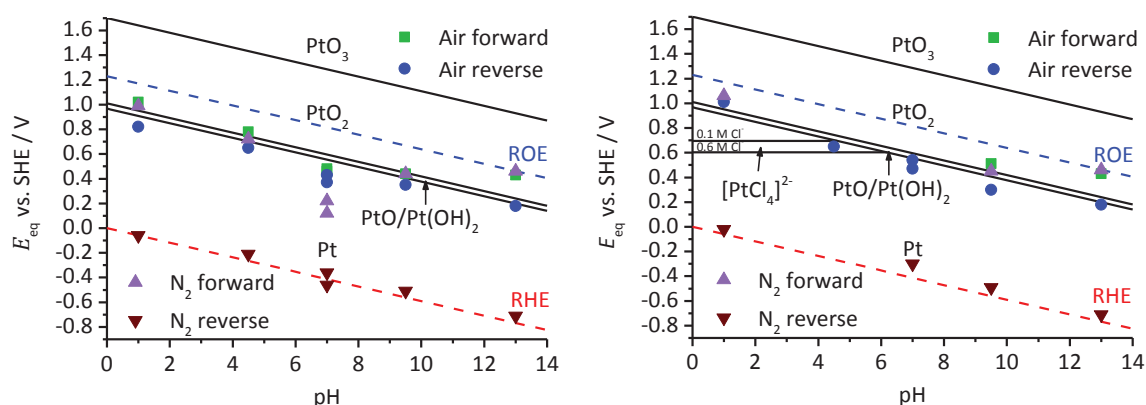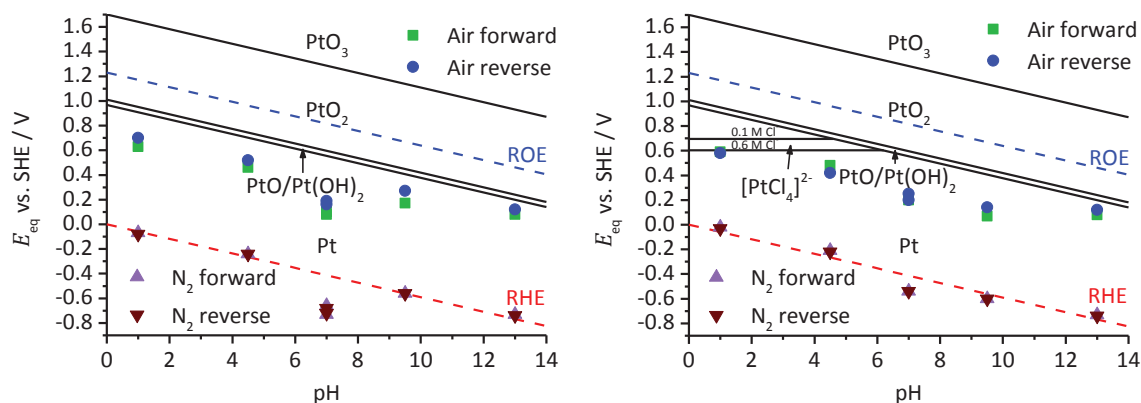Figure 87: Potentials at -100 µA cm^{-2} disc current density during potentiodynamic measurements (10 mV s^{-1}) at 1000 rpm; sulfate and hydroxide: left, chloride and hydroxide: right; lines calculated with the standard potentials of Table 3 and 10^{-6} M [PtCl$_4$]$^{2-}$ with different chloride concentrations

The potentials at which a current density of -100 µA cm^{-2} is reached show also a linear decrease with increasing pH in aerated solutions. In the sulfate electrolytes combined with the values obtained in 0.10 M NaOH these potentials show a change of -48 mV pH^{-1}. In chloride electrolytes these slopes are -48.3 mV pH^{-1} for the forward scan and -41.0 mV pH^{-1} for the reverse scan. Neglecting the potentials measured in sodium hydroxide at pH 13 slopes of -65.2 mV pH^{-1} and -55.0 mV pH^{-1} can be obtained.

The measured slopes of the pH dependency of the ORR are significantly lower in sulfuric acid than the theoretical value of -58.5 mV pH^{-1}. The results obtained in chloride electrolytes without hydrogen peroxide are closer to this theoretical value. These slopes fit well with the pH dependency of the half-wave potential and the quarter wave potential of the ORR found by chronopotentiometry between -58 mV pH^{-1} and -63 mV pH^{-1} by Sawyer [128]. Sepa [93] also found a potential pH relationship of -60 mV pH^{-1} at low current densities.

5.7 ANALYSIS OF THE LIMITING CURRENT DENSITIES

5.7.1 OXYGEN REDUCTION

The Levich equation (1.27) requires the kinematic viscosity, the concentration in the solution and the diffusion coefficient as input parameters. In chapter 3 a short review of the input parameters required for calculating the limiting current densities of the ORR is given. Especially the data for the diffusion coefficient in literature [1, 80, 136, 191-195, 200, 202-204] (Table 6) show a high spread between 1.9·10^{-9} m^2 s^{-1} and 2.6·10^{-9} m^2 s^{-1}. Therefore the diffusion coefficient is calculated from the slope of the limiting current densities as a function of the square root of the rotation rate.

The kinematic viscosity can be calculated by the equation and data given by Hefter et al. [167] as a function of the electrolyte, its concentration and the temperature. These calculated values are in good agreement with the measured values found in the literature given in Table 4. For these reasons the kinematic viscosity calculated according to Hefter is used for the analysis of the limiting current densities. No value for the kinematic viscosity of 0.05 M H$_2$SO$_4$ solution was found and therefore the

kinematic viscosity of 0.05 M Na_2SO_4 is used. Possible influences of the buffers on the kinematic viscosity are neglected considering their low concentration of 0.01 M.

In chapter 3.3 it has been shown that the oxygen concentration is well studied in sodium chloride solutions and in water at different temperatures. The available literature for other electrolytes is sparse. Equation (3.5) published by Adrian Schumpe [188] provides the opportunity to calculate the salting out effect as a function of the temperature and the electrolyte concentration for different ions. The combination of equation (3.5) with the model published by Battino [178] gives the highest oxygen concentration of the different models shown in chapter 3.3.3 neglecting that of the Whipples [170]. The relative difference between this model and the results calculated according to Truesdale [174], which gives the lowest oxygen concentration, are below 3 %. The oxygen concentrations for the analysis of the limiting current densities are therefore calculated by equation (3.5) using an oxygen solubility of 0.2740 mol m^{-3} in pure water [178].

The ratio between the limiting current densities measured in aerated and oxygen saturated 0.10 M NaCl is 0.2046±0.0040. This value is close the ratio of the oxygen partial pressure (0.2095) in the two atmospheres and therefore agrees with Henry's law (3.3). The calculated ratio using equation (3.5) is 0.2046, which is exactly the value found in the measurements.
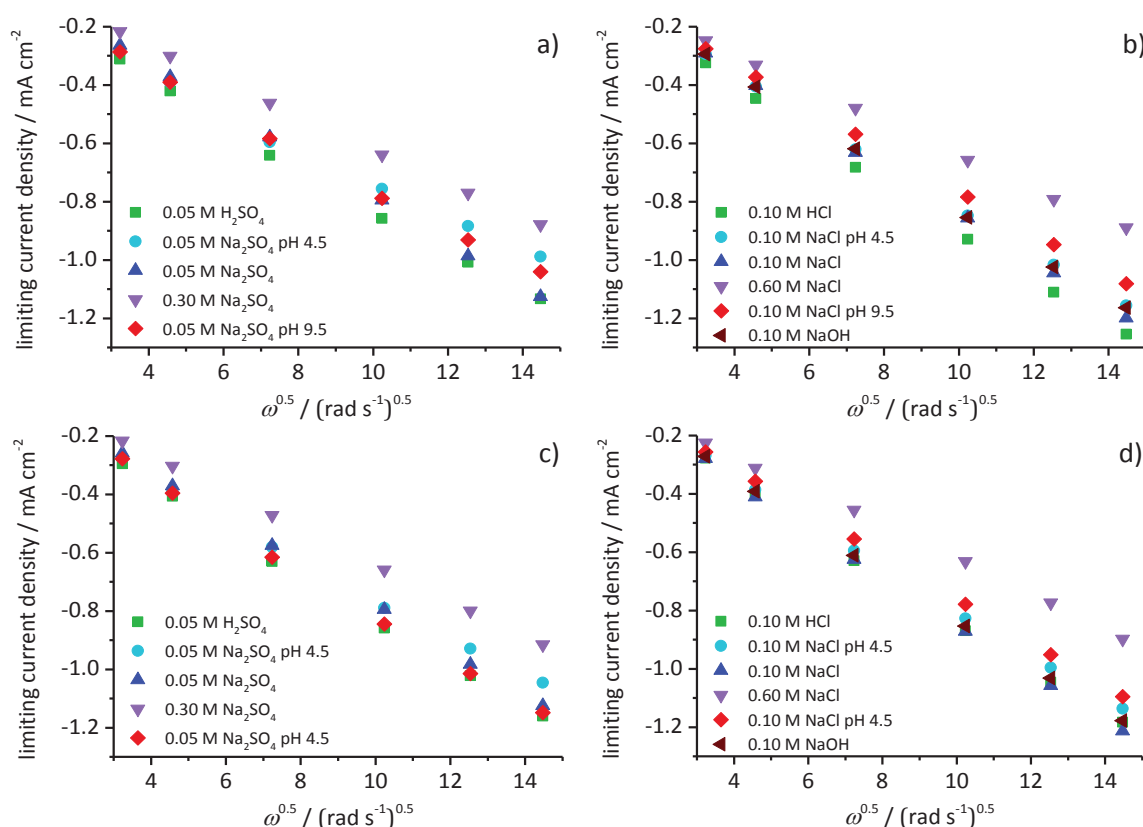
Figure 88: Limiting current densities for the complete ORR in different air saturated solutions; a) sulfate electrolytes forward scan, b) chloride and hydroxid electrolytes forward scan, c) sulfate electrolytes reverse scan, d) chloride and hydroxid electrolytes forward scan

The limiting current densities of the complete ORR, which is the sum of the limiting current densities of the two ORR paths, are shown in Figure 88. All limiting current densities show the linear behavior expected from the Levich equation (1.27). The lowest Pearson R is 0.9964 and was found for the liming current densities of the forward scan in 0.05 M Na_2SO_4 at pH 4.5.

The slope and the intercept of the linear fit are shown in Table 70 for the forward scans and Table 71 for the reverse scans. The diffusion coefficients were calculated according to equation (1.27) using the input parameters in these tables and assuming a complete 4 e$^-$ ORR.

The diffusion coefficients in neutral sodium chloride solutions are very close to the $1.4 \cdot 10^{-9}$ m^2 s^{-1} measured by Jamnongwong et al. [199] which are also the smallest values found in literature (Table 6). Diffusion coefficients between $1.78 \cdot 10^{-9}$ m^2 s^{-1} and $2.46 \cdot 10^{-9}$ m^2 s^{-1} have been published (Table 6) for oxygen in pure water. It has also been found, that diffusion coefficients decrease with higher electrolyte concentrations [194-199]. Several authors [196-198] found a lower diffusion coefficient in the presence of sulfate compared to chloride. For these reasons the small diffusion coefficients found in this work seem reasonable even if they are at the lower limit compared to the available literature data.

Table 70: Diffusion coefficients calculated from the slope the limiting current densities of the ORR in the forward scan by the Levich equation (1.27)

Electrolyte	Intercept mA cm^{-2}	Slope mA s$^{0.5}$ rad$^{-0.5}$ cm^{-2}	ν [167] 10^{-6} m^2 s^{-1}	c [178, 188] mol m^{-3}	D 10^{-9} m^2 s^{-1}
0.05 M H$_2$SO$_4$	-0.08997	-0.07329	0.9640	0.2724	1.181
0.10 M HCl	-0.06855	-0.08295	0.9544	0.2731	1.414
0.05 M Na$_2$SO$_4$ at pH 4.5	-0.10740	-0.06217	0.9640	0.2708	0.931
0.10 M NaCl at pH 4.5	-0.05550	-0.07664	0.9564	0.2699	1.278
0.05 M Na$_2$SO$_4$	-0.01866	-0.07669	0.9640	0.2708	1.276
0.30 M Na$_2$SO$_4$	-0.03033	-0.05899	1.0340	0.2553	0.957
0.10 M NaCl	-0.03593	-0.08051	0.9564	0.2699	1.376
0.10 M NaCl O$_2$	-0.08278	-0.40820	0.9564	1.3190	1.455
0.60 M NaCl	-0.06526	-0.05744	0.9564	0.2503	0.929
0.05 M Na$_2$SO$_4$ at pH 9.5	-0.08262	-0.06744	0.9640	0.2708	1.052
0.10 M NaCl at pH 9.5	-0.04536	-0.07188	0.9564	0.2699	1.161
0.10 M NaOH	-0.05098	-0.07753	0.9507	0.2688	1.307

Table 71: Diffusion coefficients calculated from the slope the limiting current densities of the ORR in the reverse scan by the Levich equation (1.27)

Electrolyte	Intercept mA cm^{-2}	Slope mA s$^{0.5}$ rad$^{-0.5}$ cm^{-2}	ν [167] 10^{-6} m^2 s^{-1}	c [178, 188] mol m^{-3}	D 10^{-9} m^2 s^{-1}
0.05 M H$_2$SO$_4$	-0.05689	-0.07710	0.9640	0.2724	1.275
0.10 M HCl	-0.03293	-0.08056	0.9544	0.2731	1.353
0.05 M Na$_2$SO$_4$ at pH 4.5	-0.07329	-0.06830	0.9640	0.2708	1.072
0.10 M NaCl at pH 4.5	-0.03028	-0.07705	0.9564	0.2699	1.289
0.05 M Na$_2$SO$_4$	-0.01505	-0.07682	0.9640	0.2708	1.279
0.30 M Na$_2$SO$_4$	-0.01802	-0.06224	1.0340	0.2553	1.037
0.10 M NaCl	-0.02449	-0.08245	0.9564	0.2699	1.427
0.10 M NaCl O$_2$	-0.02110	-0.41580	0.9564	1.3190	1.495
0.60 M NaCl	-0.03233	-0.05930	0.9564	0.2503	0.974
0.05 M Na$_2$SO$_4$ at pH 9.5	-0.04127	-0.07746	0.9640	0.2708	1.295
0.10 M NaCl at pH 9.5	-0.01475	-0.07468	0.9564	0.2699	1.230
0.10 M NaOH	-0.02073	-0.08056	0.9507	0.2688	1.384

5.7.2 HYDROGEN EVOLUTION

The limiting current densities measured for the hydrogen evolution at pH 4.5 show, similar to the limiting current densities of the ORR, a linear behavior with the square root of the rotation rate

(Figure 89). The proton concentration at pH 4.5 is 0.03162 mol m^{-3}. Using the same kinematic viscosity as has been used for the analysis of the limiting current densities caused by the ORR and a diffusion coefficient for protons of $9.311 \cdot 10^{-9}$ m^2 s^{-1} [1] the linear slope of the Levich equation (1.27) should be 0.008 mA s$^{0.5}$ rad$^{-0.5}$ cm^{-2}. This slope is a factor 50 lower than those measured for the HER at pH 4.5 Table 72 so that it can be assumed, that the limiting currents are not caused by the mass transport limitation of the protons from the bulk.

Table 72: Diffusion coefficients calculated from the slope of the limiting current densities of the HER according to Levich equation (1.27) under nitrogen

Electrolyte	Intercept mA cm^{-2}	Slope mA s$^{0.5}$ rad$^{-0.5}$ cm^{-2}	D 10^{-9} m^2 s^{-1}
0.05 M Na$_2$SO$_4$ at pH 4.5 forward	-0.04919	-0.3740	0.5934
0.05 M Na$_2$SO$_4$ at pH 4.5 reverse	-0.03148	-0.3764	0.5991
0.10 M NaCl at pH 4.5 forward	+0.04014	-0.3867	0.6226
0.10 M NaCl at pH 4.5 reverse	+0.04137	-0.3866	0.6224

The measurements were carried out in a buffered 0.01 M potassium hydrogen phthalate solution. In such a solution the hydrogen phthalate acts as a proton donor which determines the pH-value of the solution. The diffusion coefficient of phthalic acid is $0.811 \cdot 10^{-9}$ m^2 s^{-1} [229]. With these data a Levich slope for phthalate of 0.52411 mA s$^{0.5}$ rad$^{-0.5}$ cm^{-2} can be calculated which is in the range of the measured data given in Table 72.

The dissociation constants of the ortho-phthalic (H$_2$C$_8$H$_4$O$_4$) acid are $1.3 \cdot 10^{-3}$ [1] for the first proton and $3.9 \cdot 10^{-5}$ [1] for the second proton. Considering the Henderson-Hasselbalch equation [230, 231] the amount of the hydrogen phthalate ion (HC$_8$H$_4$O$_4^-$) at pH 4.5 is only 88.8 % of the total amount of phthalate in the solution. The Levich slope (0.46512 mA s$^{0.5}$ rad$^{-0.5}$ cm^{-2}) for this corrected concentration of 0.00888 M is even closer to the measured values. The diffusion coefficient calculated from the Levich slopes is 0.609 ± 0.015 m^2 s^{-1} for the phthalate, which is smaller than the $0.811 \cdot 10^{-9}$ m^2 s^{-1} published by Wen et al. [229] for phthalic acid.

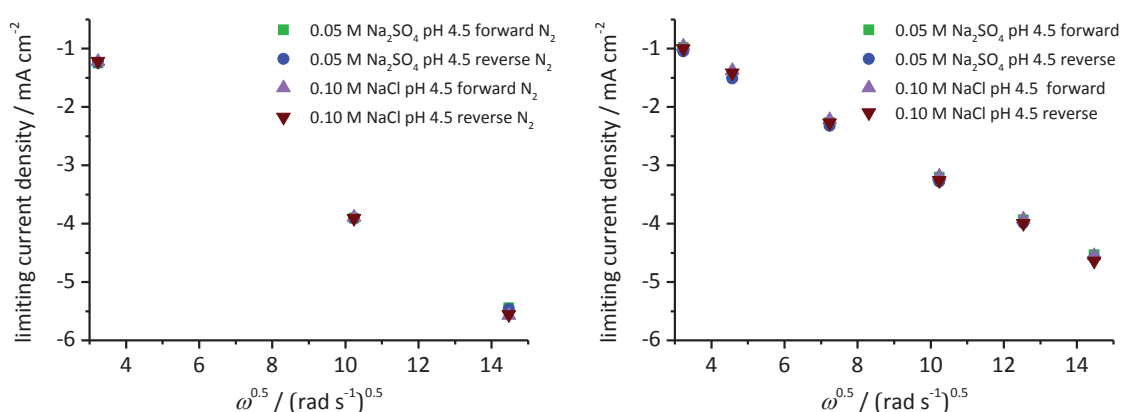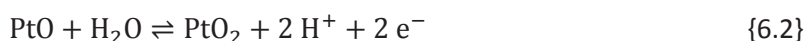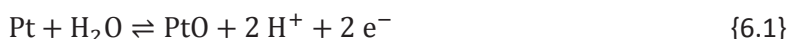Figure 89: Limiting current densities for the HER in different deaerated (left) and aerated (right) solutions at pH 4.5

The limiting current densities caused by the HER show also a linear increase with the square root of the rotation rate in aerated solutions (Figure 89) but since the proton donor is partly depleted due to the ORR less hydrogen phthalate remains for the HER and therefore lower Tafel slopes have been measured.

SUMMARY

In course of this work the important equilibriums responsible for the OCP and zero-current potentials of platinum in sulfate and chloride electrolytes were identified. After one hour exposure to different solutions containing sulfate or hydroxide the OCP is close to the standard potential of equilibrium {6.1}. It can be assumed that the shift of the OCPs to higher potentials in acidic electrolytes containing chloride is due to the influence of equilibrium {5.2}. The zero-current potentials during the forward scans are similar under nitrogen and in aerated electrolytes and close to the standard potentials of equilibrium {6.1} and {6.2}. The zero-current potentials obtained during the reverse scan under nitrogen are close to the standard potential of the reversible hydrogen electrode ({1.7} and {1.8}).
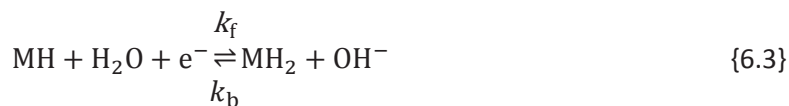
$$Pt + H_2O \rightleftharpoons PtO + 2\,H^+ + 2\,e^- \qquad\qquad \{6.1\}$$

$$PtO + H_2O \rightleftharpoons PtO_2 + 2\,H^+ + 2\,e^- \qquad\qquad \{6.2\}$$

The pH dependency of the OCP, the rest potential and the potentials where a current density of -100 µA cm^{-2} is reached was measured. It is close to 60 mV pH^{-1} in nearly all solutions. Only in sulfate electrolytes the potentials at a current density of -100 µA cm^{-2} shows a different pH-dependency with slopes of -48 mV pH^{-1}.

The mechanisms of the HER reaction on Pt was clarified over a wide pH range. The HER follows a Tafel mechanism in acidic electrolytes with a pH of 1 which is in agreement with the results of several other authors [40, 52, 156-159, 161-163, 215]. In sulfate electrolyte buffered at pH 4.5 the HER follows a Heyrovský mechanism with slopes around -120 mV dec^{-1} while it seems that in the presence of chloride at pH 4.5 the hydrogen evolution acts as a reversible system. A Heyrovský mechanism was found in 0.1 M NaOH which agrees with the literature [54, 156]. The HER follows also a Heyrovský mechanism in neutral, chloride electrolytes but Tafel slopes in the range of -240 mV dec^{-1} for the HER measured in sulfate containing neutral electrolytes and those buffered at pH 9.5 are more difficult to interpret. Similar slopes have been measured by Schuldiner [156]. Such high cathodic Tafel slopes might be explained by a high charge transfer coefficient of about 0.75 which would also lead to anodic Tafel slopes of 77 mV dec^{-1}. This is close to the Tafel slopes obtained for the reverse reaction decreasing the current density at low overpotential in the pH 9.5 electrolytes but for the neutral, sulfate electrolytes these Tafel slopes are too small.

In all measured electrolytes with a pH above 1 the HER shows a change in the slope during the polarization which confirms the findings of several authors [49, 54, 156]. For this reason a new kinetic model for the HER was developed in chapter 1.4. According to reaction {6.3} the platinum surface would be covered by atomic hydrogen at high positive overpotentials. At high negative overpotentials platinum is mainly covered by adsorbed hydrogen. At low overpotentials the activity of atomic hydrogen and molecular hydrogen is given by the Nernst equation (1.50). The steady state current is proportional to the amount of molecular hydrogen which desorbs from the platinum surface. The current would therefore increase with a higher amount of adsorbed molecular hydrogen at more negative potentials until reaction {6.3} becomes irreversible with a Tafel slope of -120 mV dec^{-1}. The current-potential relation of such a reaction in which only the product is initially in the solution can be calculated by equation (6.1).

$$\text{MH} + \text{H}_2\text{O} + \text{e}^- \underset{k_\text{b}}{\overset{k_\text{f}}{\rightleftharpoons}} \text{MH}_2 + \text{OH}^- \qquad \{6.3\}$$

$$i = i_\text{f}^0 \cdot \frac{\exp\left[-\frac{(1-\alpha)\cdot n\cdot F}{R_\text{g}\cdot T}\cdot E\right]}{1 + \frac{k_\text{b}^0}{\nu_\text{Lang}}\cdot \exp\left[\frac{\alpha\cdot n\cdot F}{R_\text{g}\cdot T}\cdot E\right]}\cdot a_\text{MH} \qquad (6.1)$$

At pH 4.5 the hydrogen evolution has a limiting current density due to the reduction of protons and an exponential current density caused by the hydrogen evolution from water. These limiting current densities for the HER are not caused by the mass transport of the protons from the bulk solution to the electrode surface but by the hydrogen phthalate ions which act as a proton donor.

The ORR on Pt was studied over a wide pH range in this work. The ORR usually follows two different reaction paths confirming the results of several other authors [61, 72, 130, 131, 220]. The first path takes place at the same potential at which the platinum surface gets reduced under nitrogen and is a complete reduction of oxygen to hydroxide. At more negative potentials a second ORR path becomes rate determining which is accompanied by the appearance of small ring currents indicating the formation of hydrogen peroxide as an intermediate. The small ring currents indicate that the main part of the hydrogen peroxide gets further reduced to hydroxide or water at the disc electrode which is in agreement with the results of other authors [66, 69, 154]. Within this work the kinetic data of both reactions have been determined.

A new model was developed for a better understanding of the ORR. Several authors [61, 62, 64-66, 93, 99, 131-135, 140, 142-146] found two Tafel slopes of -60 mV dec^{-1} at low current densities and of -120 mV dec^{-1} at high current densities for the ORR. This was explained by a change from Temkin to Langmuir adsorption [93, 108, 133, 134, 140, 147, 148]. For both slopes the same activation enthalpies have been found [133, 134]. It seems unlikely that the interaction between the adsorbates should have no effect on the activation enthalpy. For this reason a new model was derived in chapter 5.2.1.2 considering only Langmuir adsorption. The first electron transfer is usually accepted as the rate determining step [61, 66, 67, 93, 124, 132, 133, 143, 148, 151] but considering this new model there is evidence that reaction {6.4} is the rate determining step for the first ORR reduction path. Schmidt et al. [71] has also assumed that adsorbed hydroxide might determine the ORR on platinum in alkaline solutions. The measurements carried out in this work show that the ORR appears in most electrolytes at the same potential as the surface reduction peak under nitrogen which is in agreement with the results of other authors [80, 217]. This gives further evidence that reaction {6.4} is rate determining for the first ORR path. The change in the Tafel slope from -60 mV dec^{-1} to -120 mV dec^{-1} is therefore most likely caused by the reduction of PtOH which leads to an increase of free platinum sites available for the ORR. If equilibrium {6.4} is the rate determining step for the ORR it would be reversible at low overpotentials which would result in Tafel slopes of -60 mV dec^{-1}. At more negative potentials equilibrium {6.4} would become irreversible with a Tafel slope of -120 mV dec^{-1}.

$$\text{Pt} + \text{H}_2\text{O} \underset{k_\text{b}}{\overset{k_\text{f}}{\rightleftharpoons}} \text{PtOH} + \text{H}^+ + \text{e}^- \qquad \{6.4\}$$
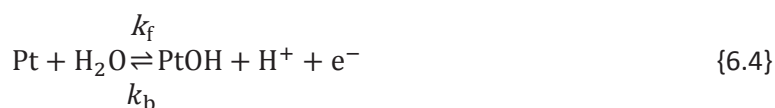
The diffusion coefficient of oxygen in water has the highest uncertainty of all input parameters required for the Levich equation (1.27). Values between $1.78\cdot10^{-9}$ m^2 s^{-1} [201] and $2.46\cdot10^{-9}$ m^2 s^{-1}

[192] for the diffusion coefficient of oxygen in pure water can be found in literature (Table 6). For this reason the diffusion coefficients were calculated from the slopes of the limiting current densities of the complete ORR against the square root of the rotation in chapter 5.7.1. The obtained diffusion coefficients in neutral sodium chloride solutions are very close to the $1.4 \cdot 10^{-9}$ m^2 s^{-1} measured by Jamnongwong et al. [199] in similar solutions. The obtained diffusion coefficients of oxygen in neutral sodium sulfate solution are higher than the values found in literature [196-198] but since several authors [196-198] found a lower diffusion coefficients in the presence of sulfate compared to chloride the data might still within the range of the values expected from the literature data. It has to be mentioned that all obtained diffusion coefficients are at the lower limit of the literature data.

The diffusion coefficient of phthalate was found to be 0.609 ± 0.015 m^2 s^{-1} which is smaller than the $0.811 \cdot 10^{-9}$ m^2 s^{-1} published by Wen et al. [229] for phthalic acid.

By using a least square multi-curve fit on the polarization curves obtained at the RDE it was possible to obtain the kinetic data of the ORR and the HER at the platinum electrode. This work is the first to give all kinetic data of both ORR paths, the formation of hydrogen peroxide due to the hydrogen adsorption and the HER. The kinetic data are given with respect to the SHE, RHE and ROE and can be used to calculate the whole polarization curves with the equations given in chapter 4.4.

Bibliography

[1]   Haynes, W. M., and D. R. Lide. 2010. CRC Handbook of Chemistry and Physics 2010-2011. CRC press.

[2]   Volta, A. 1800. On the electricity excited by the mere contact of conducting substances of different kinds. Philosophical Transactions of the Royal Society of London 90, 403-431.

[3]   Grove, W. R. 1843. On the gas Voltaic battery. Experiments made with a view of ascertaining the rationale of its action and its application to eudiometry. Philosophical Transactions of the Royal Society of London 133, 91-112.

[4]   Schönbein, L. F. 1842. Elektrochemische Untersuchungen. Annalen der Physik 132, 235-251.

[5]   Koutecký, J., and V. G. Levich. 1958. Применение вращающегося дискового электрода к изучению кинетических и каталитических процессов в электрохимии. Zhurnal Fizicheskoi Khimii 32, 1565-1575.

[6]   Vidal-Iglesias, F. J., J. Solla-Gullón, V. Montiel, and A. Aldaz. 2012. Errors in the use of the Koutecký–Levich plots. Electrochemistry Communications 15, 42-45.

[7]   Levich, V. G. 1942. The theory of concentration polarization. Acta Physicochimica U. R. S. S 17, 257-307.

[8]   Langmuir, I. 1916. The constitution and fundamental properties of solids and liquids. Part I. Solids. Journal of the American Chemical Society 38, 2221-2295.

[9]   Langmuir, I. 1932. Surface chemistry. Nobel Lecture.

[10]   Langmuir, I. 1932. Vapor pressures, evaporation, condensation and adsorption. Journal of the American Chemical Society 54, 2798-2832.

[11]   Temkin, M. I. 1940. О кинетике гетерогенных каталитических процессов. Zhurnal Fizicheskoi Khimii 14, 1153-1159.

[12]   Fick, A. 1855. Ueber Diffusion. Annalen der Physik 170, 59-86.

[13]   Einstein, A. 1905. Über die von der molekularkinetischen Theorie der Wärme geforderte Bewegung von in ruhenden Flüssigkeiten suspendierten Teilchen. Annalen der Physik 322, 549-560.

[14]   Saito, Y. 1968. A theoretical study on the diffusion current at the stationary electrodes of circular and narrow band types. Review of Polarography (Japan) 15, 177-187.

[15]   Bowman, F. 1968. Introduction to Bessel functions. Courier Dover Publications.

[16]   Gregory, D. P., and A. C. Riddiford. 1956. Transport to the surface of a rotating disc. Journal of the Chemical Society, 3756-3764.

[17]   Levich, V. G. 1962. Physicochemical Hydrodynamics. Englewood Cliffs, N. J.: Prentice-Hall, Inc.

[18]   Smyrl, W. H., and J. Newman. 1971. Limiting current on a rotating disk with radial diffusion. Journal of the Electrochemical Society 118, 1079-1081.

[19]   Hanke-Bourgeois, M. 2009. Grundlagen der Numerischen Mathematik und des Wissenschaftlichen Rechnens. Wiesbaden: Vieweg+Teubner GWV Fachverlage GmbH.

[20]   Sauvigny, F. 2014. Analysis - Grundlagen, Differentiation, Interationstheorie, Differentialgleichungen, Variationsmethodem. Berlin Heidelberg: Springer-Verlag.

[21]   Jahn, D., and W. Vielstich. 1962. Rates of electrode processes by the rotating disk method. Journal of the Electrochemical Society 109, 849-852.

[22]   Albery, W. J., and S. Bruckenstein. 1966. Ring-disk electrodes. 2. Theoretical and experimental collection efficiencies. Transactions of the Faraday Society 62, 1920-1931.

[23]   Albery, W. J. 1966. Ring-disk electrodes. 1. A new approach to the theory. Transactions of the Faraday Society 62, 1915-1919.

[24]   Albery, W. J., S. Bruckenstein, and D. T. Napp. 1966. Ring-disk electrodes. 3. Current-voltage curves at the ring electrode with simultaneous currents at the disk electrode. Transactions of the Faraday Society 62, 1932-1937.

[25]   Albery, W. J., S. Bruckenstein, and D. C. Johnson. 1966. Ring-disk electrodes. 4. Diffusion layer titration curves. Transactions of the Faraday Society 62, 1938-1945.

[26]   Albery, W. J., and S. Bruckenstein. 1966. Ring-disk electrodes. 5. First-order kinetic collection efficiencies at the ring electrode. Transactions of the Faraday Society 62, 1946-1954.

[27] Albery, W. J., and S. Bruckenstein. 1966. Ring-disk electrodes. 6. Second-order reactions. Transactions of the Faraday Society 62, 2584-2595.

[28] Albery, W. J., and S. Bruckenstein. 1966. Ring-disk electrodes. 7. Homogeneous and heterogeneous kinetics. Transactions of the Faraday Society 62, 2596-2606.

[29] Albery, W. J. 1967. Ring-disk electrodes. 8. Transient currents and first-order kinetics. Transactions of the Faraday Society 63, 1771-1781.

[30] Albery, W. J., M. L. Hitchman, and J. Ulstrup. 1968. Ring-disk electrodes. 9. Application to first-order kinetics. Transactions of the Faraday Society 64, 2831-2840.

[31] Albery, W. J., M. L. Hitchman, and J. Ulstrup. 1969. Ring-disk electrodes. 10. Application to second-order kinetics. Transactions of the Faraday Society 65, 1101-1112.

[32] Albery, W. J. 1971. Ring-disk electrodes. 11. General theory of transient currents. Transactions of the Faraday Society 67, 153-160.

[33] Albery, W. J., J. S. Drury, and M. L. Hitchman. 1971. Ring-disk electrodes. 12. Application to ring current transients. Transactions of the Faraday Society 67, 161-165.

[34] Albery, W. J., J. S. Drury, and M. L. Hitchman. 1971. Ring-disk electrodes. 13. Laplace transformation of transients. Transactions of the Faraday Society 67, 166-169.

[35] Albery, W. J., J. S. Drury, and M. L. Hitchman. 1971. Ring disk electrodes. 14. Kinetic and transient parameters. Transactions of the Faraday Society 67, 2162-2166.

[36] Albery, W. J., J. S. Drury, and A. P. Hutchinson. 1971. Ring disk electrodes. 15. Alternating current measurements. Transactions of the Faraday Society 67, 2414-2418.

[37] Damjanovic, A., M. A. Genshaw, and J. O. M. Bockris. 1966. Distinction between intermediates produced in main and side electrodic reactions. The Journal of Chemical Physics 45, 4057-4059.

[38] Guha, S. 2013. Simulation studies on a rotating ring disk electrode system: Role of supporting electrolyte in determination of relevance of ionic migration. American Institute of Chemical Engineers Journal 59, 1390-1399.

[39] Knorr, C. A. 1955. Kinetik der kathodischen Wasserstoffentwicklung. Zeitschrift für Elektrochemie, Berichte der Bunsengesellschaft für physikalische Chemie 59, 647-659.

[40] Erdey-Gruz, T., and M. Volmer. 1930. Zur Theorie der Wasserstoffüberspannung. Zeitschrift für physikalische Chemie 150, 203-213.

[41] Heyrovský, J. 1925. Researches with the dropping mercury cathode: Part I. General introduction. Recueil des Travaux Chimiques des Pays-Bas 44, 488-495.

[42] Tafel, J. 1905. Über die Polarisation bei der kathodischen Wasserstoffentwicklung. Zeitschrift für physikalische Chemie, Stöchiometrie und Verwandtschaftslehre 50, 641-712.

[43] Tafel, J., and K. Naumann. 1905. Beziehungen zwischen Kathodenpotential und elektrolytischer Reduktionswirkung. Zeitschrift für physikalische Chemie, Stöchiometrie und Verwandtschaftslehre 50, 713-752.

[44] Nernst, W. 1889. Die elektromotorische Wirksamkeit der Ionen. Zeitschrift für physikalische Chemie, Stöchiometrie und Verwandtschaftslehre 4, 129-181.

[45] Nernst, W. 1921. Studies in chemical thermodynamics. Nobel Lecture.

[46] Butler, J. A. V. 1932. The mechanism of overvoltage and its relation to the combination of hydrogen atoms at metal electrodes. Transactions of the Faraday Society 28, 379-382.

[47] Bowden, F. P., and E. K. Rideal. 1928. The electrolytic behaviour of thin films. Part I. Hydrogen. Proceedings of the Royal Society of London. Series A 120, 59-79.

[48] Bowden, F. P., and E. K. Rideal. 1928. On the electrolytic behaviour of thin films. Part II. The areas of catalytically active surfaces. Proceedings of the Royal Society of London. Series A 120, 80-89.

[49] Bockris, J. O. M., and E. C. Potter. 1952. The mechanism of the cathodic hydrogen evolution reaction. Journal of The Electrochemical Society 99, 169-186.

[50] Hamann, C. H., and W. Vielstich. 2005. Elektrochemie. Weinheim: WILEY-VCH Verlag GmbH & Co. KGaA.

[51] Kandler, C., C. A. Knorr, and C. Schwitzer. 1937. Über die maßgebenden Vorgänge bei der elektrolytischen Wasserstoffabscheidung an aktiven Palladium- und Platinelektroden. Zeitschrift für physikalische Chemie 180, 281-304.

[52]   Schuldiner, S. 1952. Hydrogen overvoltage on bright platinum. Journal of The Electrochemical Society 99**,** 488-494.

[53]   Schuldiner, S. 1959. Hydrogen overvoltage on bright platinum. III. Effect of hydrogen pressure. Journal of The Electrochemical Society 106**,** 891-895.

[54]   Markovic, N. M., S. T. Sarraf, H. A. Gasteiger, and P. N. Ross. 1996. Hydrogen electrochemistry on platinum low-index single-crystal surfaces in alkaline solution. Journal of the Chemical Society, Faraday Transactions 92**,** 3719-3725.

[55]   Lewis, F. A., R. C. Johnston, M. C. Witherspoon, and A. Obermann. 1983. Palladium and platinum hydrogen electrodes I: Hydrogen chemical potentials, molecular hydrogen diffusion and local cell hydrogen transfer effects at palladium and platinum electrodes under open-circuit conditions and during constant current and pulsed current electrolysis in hydrogen-saturated solutions. Surface Technology 18**,** 147-166.

[56]   Wroblowa, H. S., Y.-C. Pan, and G. Razumney. 1976. Electroreduction of oxygen. A new mechanistic criterion. Journal of Electroanalytical Chemistry and Interfacial Electrochemistry 69**,** 195-201.

[57]   Bard, A. J., and L. R. Faulkner. 2001. Electrochemical Methodes - Fundamentals and Applications. John Wiley & Sons, Inc.

[58]   Gnanamuthu, D. S., and J. V. Petrocelli. 1967. A generalized expression for the tafel slope and the kinetics of oxygen reduction on noble metals and alloys. Journal of the Electrochemical Society 114**,** 1036-1041.

[59]   Damjanovic, A., A. Dey, and J. O. M. Bockris. 1966. Kinetics of oxygen evolution and dissolution on platinum electrodes. Electrochimica Acta 11**,** 791-814.

[60]   Müller, L., and L. Nekrassow. 1964. Untersuchung des elektrochemischen Reduktionsprozesses von Sauerstoff an Platin mit Hilfe der rotierenden Scheibenelektrode mit Ring. Electrochimica Acta 9**,** 1015-1023.

[61]   Damjanovic, A., M. A. Genshaw, and J. O. M. Bockris. 1967. The role of hydrogen peroxide in oxygen reduction at platinum in H_2SO_4 solution. Journal of the Electrochemical Society 114**,** 466-472.

[62]   Kaska, S. M., S. Sarangapani, and J. Giner. 1989. Oxygen reduction on platinum in borate-buffered saline solutions. Journal of the Electrochemical Society 136**,** 75-83.

[63]   Kokkinidis, G., and D. Jannakoudakis. 1984. Oxygen reduction on Pt and Cu surfaces modified by underpotential adsorbates. Journal of Electroanalytical Chemistry and Interfacial Electrochemistry 162**,** 163-173.

[64]   Marković, N. M., R. R. Adžić, B. D. Cahan, and E. B. Yeager. 1994. Structural effects in electrocatalysis: oxygen reduction on platinum low index single-crystal surfaces in perchloric acid solutions. Journal of Electroanalytical Chemistry 377**,** 249-259.

[65]   Markovic, N. M., H. A. Gasteiger, and P. N. Ross. 1995. Oxygen reduction on platinum low-index single-crystal surfaces in sulfuric acid solution: Rotating ring-Pt(hkl) disk studies. The Journal of Physical Chemistry 99**,** 3411-3415.

[66]   Grgur, B. N., N. M. Marković, and P. N. Ross. 1997. Temperature-dependent oxygen electrochemistry on platinum low-index single crystal surfaces in acid solutions. Canadian Journal of Chemistry 75**,** 1465-1471.

[67]   Markovic, N. M., T. J. Schmidt, V. Stamenkovic, and P. N. Ross. 2001. Oxygen reduction reaction on Pt and Pt bimetallic surfaces: A selective review. Fuel Cells 1**,** 105-116.

[68]   Alexeyeva, N., K. Tammeveski, A. Lopez-Cudero, J. Solla-Gullon, and J. M. Feliu. 2009. Electroreduction of oxygen on Pt nanoparticle/carbon nanotube nanocomposites in acid and alkaline solutions. Electrochimica Acta 55**,** 794-803.

[69]   Gómez-Marín, A. M., R. Rizo, and J. M. Feliu. 2013. Some reflections on the understanding of the oxygen reduction reaction at Pt(111). Beilstein Journal of Nanotechnology 4**,** 956-967.

[70]   Fischer, P., and J. Heitbaum. 1980. Mechanistic aspects of cathodic oxygen reduction. Journal of Electroanalytical Chemistry and Interfacial Electrochemistry 112**,** 231-238.

[71] Schmidt, T. J., V. Stamenkovic, J. P. N. Ross, and N. M. Markovic. 2003. Temperature dependent surface electrochemistry on Pt single crystals in alkaline electrolyte Part 3. The oxygen reduction reaction. Physical Chemistry Chemical Physics 5, 400-406.

[72] Damjanovic, A., M. A. Genshaw, and J. O. M. Bockris. 1966. The role of hydrogen peroxide in the reduction of oxygen at platinum electrodes. The Journal of Physical Chemistry 70, 3761-3762.

[73] Marković, N. M., H. A. Gasteiger, B. N. Grgur, and P. N. Ross. 1999. Oxygen reduction reaction on Pt(111): effects of bromide. Journal of Electroanalytical Chemistry 467, 157-163.

[74] Crank, J., and P. Nicolson. 1996. A practical method for numerical evaluation of solutions of partial differential equations of the heat-conduction type. Adv Comput Math 6, 207-226.

[75] Liss, P. S. 1973. Processes of gas exchange across an air-water interface. Deep Sea Research and Oceanographic Abstracts 20, 221-238.

[76] Davis, H. S., and G. S. Crandall. 1930. The role of the liquid stationary film in batch absorptions of gases. I. Absorption involving no irreversible chemical reactions. Journal of the American Chemical Society 52, 3757-3768.

[77] Sidgwick, N. V. 1950. The Chemical Elements and Their Compounds. Volume 2. Oxford University Press.

[78] Wöhler, L., and F. Martin. 1909. Das Platintrioxyd, eine neue Oxydationsstufe des Platins. Berichte der deutschen chemischen Gesellschaft 42, 3326-3333.

[79] Bornemann, K. 1909. Einfluss des Wasserstoffsuperoxyds auf die Eigenschaften des Platins. Zeitschrift für Elektrochemie und angewandte physikalische Chemie 15, 673-678.

[80] Lingane, J. J. 1961. Chronopotentiometric study of oxygen reduction at a platinum wire cathode. Journal of Electroanalytical Chemistry 2, 296-309.

[81] Hoar, T. P. 1933. The mechanism of the oxygen electrode. Proceedings of the Royal Society of London. Series A 142, 628-646.

[82] Winkelmann, D. 1956. Untersuchungen über das elektrochemische Verhalten von O_2-H_2O_2-H_2O am blanken und platinierten Platin. Zeitschrift für Elektrochemie, Berichte der Bunsengesellschaft für physikalische Chemie 60, 731-740.

[83] Nagel, K., and H. Dietz. 1961. Elektrochemisches Verhalten anodisch hergestellter Oxidschichten auf Platin. Electrochimica Acta 4, 1-11.

[84] Grube, G. 1910. Zur Theorie der Sauerstoffelektrode. Das Elektromotorische Verhalten der Platinoxyde. Zeitschrift für Elektrochemie und angewandte physikalische Chemie 16, 621-632.

[85] Anson, F. C., and J. J. Lingane. 1957. Chemical evidence for oxide films on platinum electrometric electrodes. Journal of the American Chemical Society 79, 4901-4904.

[86] Thacker, R., and J. P. Hoare. 1971. Sorption of oxygen from solution by noble metals. I. Bright platinum. Journal of Electroanalytical Chemistry and Interfacial Electrochemistry 30, 1-14.

[87] Hoare, J. P., R. Thacker, and C. R. Wiese. 1971. Sorption of oxygen from solution by noble metals. II. Nitric acid-passivated bright platinum. Journal of Electroanalytical Chemistry and Interfacial Electrochemistry 30, 15-23.

[88] Biegler, T., and R. Woods. 1969. Limiting oxygen coverage on smooth platinum anodes in acid solution. Journal of Electroanalytical Chemistry and Interfacial Electrochemistry 20, 73-78.

[89] Biegler, T., D. A. J. Rand, and R. Woods. 1971. Limiting oxygen coverage on platinized platinum; Relevance to determination of real platinum area by hydrogen adsorption. Journal of Electroanalytical Chemistry and Interfacial Electrochemistry 29, 269-277.

[90] Wroblowa, H., M. L. B. Rao, A. Damjanovic, and J. O. M. Bockris. 1967. Adsorption and kinetics at platinum electrodes in the presence of oxygen at zero net current. Journal of Electroanalytical Chemistry and Interfacial Electrochemistry 15, 139-150.

[91] Schuldiner, S., and R. M. Roe. 1963. The Pt/O_2 electrode in sulfuric acid solution. Journal of the Electrochemical Society 110, 1142-1146.

[92] Bockris, J. O. M., and L. F. Oldfield. 1955. The oxidation-reduction reactions of hydrogen peroxide at inert metal electrodes and mercury cathodes. Transactions of the Faraday Society 51, 249-259.

[93] Sepa, D. B., M. V. Vojnovic, and A. Damjanovic. 1981. Reaction intermediates as a controlling factor in the kinetics and mechanism of oxygen reduction at platinum electrodes. Electrochimica Acta 26, 781-793.

[94] Bowen, R. J., H. B. Urbach, and J. H. Harrison. 1967. Oxygen–peroxide couple on platinum. Nature, 592-593.

[95] Bowen, R. J., and H. B. Urbach. 1968. Dynamic behavior of the oxygen–peroxide couple on platinum. The Journal of Chemical Physics 49, 1206-1213.

[96] Urbach, H. B., and R. J. Bowen. 1969. Behaviour of the oxygen-peroxide couple on platinum. Electrochimica Acta 14, 927-940.

[97] Warner, T. B., and S. Schuldiner. 1965. Potential of a platinum electrode at low partial pressures of hydrogen or oxygen. Journal of The Electrochemical Society 112, 853-856.

[98] Hoare, J. P. 1965. Oxygen overvoltage measurements on bright platinum in acid solutions. I. Bright platinum. Journal of The Electrochemical Society 112, 602-607.

[99] Sepa, D. B., M. V. Vojnovic, and A. Damjanovic. 1980. Kinetics and mechanism of O_2 reduction at Pt in alkaline solutions. Electrochimica Acta 25, 1491-1496.

[100] Gerischer, R., and H. Gerischer. 1956. Über die katalytische Zersetzung von Wasserstoffsuperoxyd an metallischem Platin. Zeitschrift für physikalische Chemie 6, 178-200.

[101] Hoare, J. P. 1965. Oxygen overvoltage measurements on bright platinum in acid solutions. II. Bright platinum in stabilized acid solutions. Journal of The Electrochemical Society 112, 608-611.

[102] Hickling, A. 1945. The anodic behaviour of metals. Part I.-Platinum. Transactions of the Faraday Society 41, 333-339.

[103] Rosen, M., D. R. Flinn, and S. Schuldiner. 1969. Double layer capacitance on platinum in 1 M H_2SO_4 from the reversible hydrogen potential to the oxygen formation region. Journal of The Electrochemical Society 116, 1112-1116.

[104] Kolthoff, I. M., and N. Tanaka. 1954. Rotated and stationary platinum wire electrodes. Analytical Chemistry 26, 632-636.

[105] Bowden, F. P. 1929. The amount of hydrogen and oxygen present on the surface of a metallic electrode. Proceedings of the Royal Society of London. Series A 125, 446-462.

[106] Bowden, F. P. 1929. The kinetics of the electro-deposition of hydrogen and oxygen. Proceedings of the Royal Society of London. Series A 126, 107-125.

[107] Armstrong, G., F. R. Himsworth, and J. A. V. Butler. 1933. The kinetics of electrode processes. Part III. The behaviour of platinum and gold electrodes in sulphuric acid and alkaline solutions containing oxygen. Proceedings of the Royal Society of London. Series A 143, 89-103.

[108] Paucirova, M., D. M. Drazic, and A. Damjanovic. 1973. The effect of surface coverage by adsorbed oxygen on the kinetics of oxygen reduction at oxide free platinum. Electrochimica Acta 18, 945-951.

[109] Bockris, J. O. M., and A. K. M. Shamshul Huq. 1956. The mechanism of the electrolytic evolution of oxygen on platinum. Proceedings of the Royal Society of London. Series A 237, 277-296.

[110] Laitinen, H., and C. Enke. 1960. The electrolytic formation and dissolution of oxide films on platinum. Journal of the Electrochemical Society 107, 773-781.

[111] Scarr, R. F. 1969. The mechanism of oxygen evolution on nickel, platinum, and other metals and alloys. Journal of the Electrochemical Society 116, 1526-1532.

[112] Berl, W. G. 1943. A reversible oxygen electrode. Transactions of The Electrochemical Society 83, 253-270.

[113] Hickling, A., and W. H. Wilson. 1951. The anodic decomposition of hydrogen peroxide. Journal of the Electrochemical Society 98, 425-433.

[114] Honda, M., T. Kodera, and H. Kita. 1986. Electrochemical behavior of H_2O_2 at Ag in $HClO_4$ aqueous solution. Electrochimica Acta 31, 377-383.

[115] Hall, S. B., E. A. Khudaish, and A. L. Hart. 1997. Electrochemical oxidation of hydrogen peroxide at platinum electrodes. Part I: An adsorption-controlled mechanism. Electrochimica Acta 43, 579-588.

[116] Hall, S. B., E. A. Khudaish, and A. L. Hart. 1998. Electrochemical oxidation of hydrogen peroxide at platinum electrodes. Part II: Effect of potential. Electrochimica Acta 43, 2015-2024.

[117] Hall, S. B., E. A. Khudaish, and A. L. Hart. 1999. Electrochemical oxidation of hydrogen peroxide at platinum electrodes. Part III: Effect of temperature. Electrochimica Acta 44, 2455-2462.

[118] Hall, S. B., E. A. Khudaish, and A. L. Hart. 1999. Electrochemical oxidation of hydrogen peroxide at platinum electrodes. Part IV: Phosphate buffer dependence. Electrochimica Acta 44, 4573-4582.

[119] Hall, S. B., E. A. Khudaish, and A. L. Hart. 2000. Electrochemical oxidation of hydrogen peroxide at platinum electrodes. Part V: Inhibition by chloride. Electrochimica Acta 45, 3573-3579.

[120] Sawyer, D. T., and E. T. Seo. 1963. Electrochemistry of dissolved gases. III. Oxidation of hydrogen at platinum electrodes. Journal of Electroanalytical Chemistry 5, 23-34.

[121] Franklin, T. C., and S. L. Cooke. 1960. A study of the oxidation of hydrogen at platinized platinum electrodes. Journal of The Electrochemical Society 107, 556-560.

[122] Marković, N. M., B. N. Grgur, and P. N. Ross. 1997. Temperature-dependent hydrogen electrochemistry on platinum low-index single-crystal surfaces in acid solutions. The Journal of Physical Chemistry B 101, 5405-5413.

[123] Skúlason, E., V. Tripković, M. E. Björketun, S. d. Gudmundsdóttir, G. Karlberg, J. Rossmeisl, T. Bligaard, H. Jónsson, and J. K. Nørskov. 2010. Modeling the electrochemical hydrogen oxidation and evolution reactions on the basis of density functional theory calculations. The Journal of Physical Chemistry C 114, 18182-18197.

[124] Damjanovic, A., and V. Brusic. 1967. Electrode kinetics of oxygen reduction on oxide-free platinum electrodes. Electrochimica Acta 12, 615-628.

[125] Hoare, J. P. 1965. Oxygen overvoltage measurements on bright platinum in acid solutions. III. Nitric acid-passivated bright platinum. Journal of The Electrochemical Society 112, 849-853.

[126] Srejić, I., M. Smiljanić, Z. Rakočevic, and S. Štrbac. 2011. Oxygen reduction on polycrystalline Pt and Au electrodes in perchloric acid solution in the presence of acetonitrile. International Journal of Electrochemical Science 6, 3344-3354.

[127] Omura, J., H. Yano, M. Watanabe, and H. Uchida. 2011. Electrochemical quartz crystal microbalance analysis of the oxygen reduction reaction on Pt-based electrodes. Part 1: Effect of adsorbed anions on the oxygen reduction activities of Pt in HF, $HClO_4$, and H_2SO_4 Solutions. Langmuir 27, 6464-6470.

[128] Sawyer, D. T., and L. V. Interrante. 1961. Electrochemistry of dissolved gases. II. Reduction of oxygen at platinum, palladium, nickel and other metal electrodes. Journal of Electroanalytical Chemistry 2, 310-327.

[129] Appleby, A. J. 1970. Oxygen reduction on oxide-free platinum in 85 % orthophosphoric acid: Temperature and impurity dependence. Journal of the Electrochemical Society 117, 328-335.

[130] Huang, J. C., R. K. Sen, and E. Yeager. 1979. Oxygen reduction on platinum in 85 % orthophosphoric acid. Journal of the Electrochemical Society 126, 786-792.

[131] Park, S. M., S. Ho, S. Aruliah, M. F. Weber, C. A. Ward, R. D. Venter, and S. Srinivasan. 1986. Electrochemical reduction of oxygen at platinum electrodes in KOH solutions - Temperature and concentration effects. Journal of the Electrochemical Society 133, 1641-1649.

[132] Sepa, D. B., L. M. Vracar, M. V. Vojnovic, and A. Damjanovic. 1986. Symmetry factor and transfer coefficient in analysis of enthalpies of activation and mechanisms of oxygen reduction at platinum electrodes. Electrochimica Acta 31, 1401-1402.

[133] Sepa, D. B., M. V. Vojnovic, L. M. Vracar, and A. Damjanovic. 1986. Apparent enthalpies of activation of electrodic oxygen reduction at platinum in different current density regions - I. Acid solution. Electrochimica Acta 31, 91-96.

[134] Sepa, D. B., M. V. Vojnovic, L. M. Vracar, and A. Damjanovic. 1986. Apparent enthalpies of activation of electrodic oxygen reduction at platinum in different current density regions - II. Alkaline solution. Electrochimica Acta 31, 97-101.

[135] Sepa, D. B., M. V. Vojnovic, L. M. Vracar, and A. Damjanovic. 1986. Invariance with pH of enthalpies of activation for O_2 reduction at Pt electrodes in acid solutions. Electrochimica Acta 31, 1105-1111.

[136] Laitinen, H. A., and I. M. Kolthoff. 1941. Voltammetry with stationary microelectrodes of platinum wire. The Journal of Physical Chemistry 45, 1061-1079.

[137] Laitinen, H. A., and I. M. Kolthoff. 1941. Voltammetric determinations and amperometric titrations with a rotating microelectrode of platinum wire. The Journal of Physical Chemistry 45, 1079-1093.

[138] Sawyer, D. T., and R. J. Day. 1963. Kinetics for oxygen reduction at platinum, palladium and silver electrodes. Electrochimica Acta 8, 589-594.

[139] Postlethwaite, T. A., J. E. Hutchison, R. Murray, B. Fosset, and C. Amatore. 1996. Interdigitated array electrode as an alternative to the rotated ring-disk electrode for determination of the reaction products of dioxygen reduction. Analytical Chemistry 68, 2951-2958.

[140] Damjanovic, A., M. A. Genshaw, and J. O. M. Bockris. 1967. The mechanism of oxygen reduction at platinum in alkaline solutions with special reference to H_2O_2. Journal of the Electrochemical Society 114, 1107-1112.

[141] Will, F. G., and C. A. Knorr. 1960. Untersuchung von Adsorptionserscheinungen an Rhodium, Iridium, Palladium und Gold mit der potentiostatischen Dreieckmethode. Zeitschrift für Elektrochemie, Berichte der Bunsengesellschaft für physikalische Chemie 64, 270-275.

[142] El Kadiri, F., R. Faure, and R. Durand. 1991. Electrochemical reduction of molecular oxygen on platinum single crystals. Journal of Electroanalytical Chemistry and Interfacial Electrochemistry 301, 177-188.

[143] Zinola, C. F., A. M. Castro Luna, W. E. Triaca, and A. J. Arvia. 1994. Electroreduction of molecular oxygen on preferentially oriented platinum electrodes in acid solution. Journal of Applied Electrochemistry 24, 119-125.

[144] Pasti, I. A., Nemanja M. Gavrilov, and S. V. Mentus. 2012. Potentiodynamic investigation of oxygen reduction reaction on polycrystalline platinum surface in acidic solutions: The effect of the polarization rate on the kinetic parameters. International Journal of Electrochemical Science 7, 11076-11090.

[145] Zinola, C. F., A. M. Castro Luna, W. E. Triaca, and A. J. Arvia. 1994. Kinetics and mechanism of the electrochemical reduction of molecular oxygen on platinum in KOH: Influence of preferred crystallographic orientation. Journal of Applied Electrochemistry 24, 531-541.

[146] Jiang, L., A. Hsu, D. Chu, and R. Chen. 2009. Oxygen reduction on carbon supported Pt and PtRu catalysts in alkaline solutions. Journal of Electroanalytical Chemistry 629, 87-93.

[147] Damjanovic, A., and M. A. Genshaw. 1970. Dependence of the kinetics of O_2 dissolution at Pt on the conditions for adsorption of reaction intermediates. Electrochimica Acta 15, 1281-1283.

[148] Sepa, D. B., M. V. Vojnovic, L. M. Vracar, and A. Damjanovic. 1984. A confirmation of the O_2 reduction mechanism at Pt electrodes from temperature studies. Electrochimica Acta 29, 1169-1170.

[149] Anderson, A. B., and T. V. Albu. 2000. Catalytic effect of platinum on oxygen reduction an ab initio model including electrode potential dependence. Journal of the Electrochemical Society 147, 4229-4238.

[150] Panchenko, A., M. T. M. Koper, T. E. Shubina, S. J. Mitchell, and E. Roduner. 2004. Ab initio calculations of intermediates of oxygen reduction on low-index platinum surfaces. Journal of the Electrochemical Society 151, A2016-A2027.

[151] Sidik, R. A., and A. B. Anderson. 2002. Density functional theory study of O_2 electroreduction when bonded to a Pt dual site. Journal of Electroanalytical Chemistry 528, 69-76.

[152] Tripković, V., E. Skúlason, S. Siahrostami, J. K. Nørskov, and J. Rossmeisl. 2010. The oxygen reduction reaction mechanism on Pt(111) from density functional theory calculations. Electrochimica Acta 55, 7975-7981.

[153] Hoare, J. P. 1975. On the reduction of oxygen at platinum - oxygen alloy diaphragm electrodes. Electrochimica Acta 20, 267-272.

[154] Katsounaros, I., W. B. Schneider, J. C. Meier, U. Benedikt, P. U. Biedermann, A. A. Auer, and K. J. Mayrhofer. 2012. Hydrogen peroxide electrochemistry on platinum: towards understanding the oxygen reduction reaction mechanism. Physical Chemistry Chemical Physics 14, 7384-7391.

[155] Lingane, J. J., and P. J. Lingane. 1963. Chronopotentiometry of hydrogen peroxide with a platinum wire electrode. Journal of Electroanalytical Chemistry 5, 411-419.

[156] Schuldiner, S. 1954. Hydrogen overvoltage on bright platinum. II. pH and salt effects in acid, neutral, and alkaline solutions. Journal of The Electrochemical Society 101, 426-432.

[157] Hoare, J. P. 1969. On dissolved oxygen in bulk platinum. Journal of The Electrochemical Society 116, 612-614.

[158] Seto, K., A. Iannelli, B. Love, and J. Lipkowski. 1987. The influence of surface crystallography on the rate of hydrogen evolution at Pt electrodes. Journal of Electroanalytical Chemistry and Interfacial Electrochemistry 226, 351-360.

[159] Protopopoff, E., and P. Marcus. 1988. Poisoning of the cathodic hydrogen evolution reaction by sulfur chemisorbed on platinum (110). Journal of The Electrochemical Society 135, 3073-3075.

[160] Gomez, R., A. Fernandez-Vega, J. M. Feliu, and A. Aldaz. 1993. Hydrogen evolution on platinum single crystal surfaces. Effects of irreversibly adsorbed bismuth and antimony on hydrogen adsorption and evolution on Pt(100). The Journal of Physical Chemistry 97, 4769-4776.

[161] Adžić, R. R., M. D. Spasojević, and A. R. Despić. 1979. Hydrogen evolution on platinum in the presence of lead, cadmium and thallium adatoms. Electrochimica Acta 24, 569-576.

[162] Parsons, R. 1960. Hydrogen evolution on platinum electrodes. The heats of activation for the component reactions. Transactions of the Faraday Society 56, 1340-1350.

[163] Bockris, J. O. M., I. A. Ammar, and A. K. M. S. Huq. 1957. The mechanism of the hydrogen evolution reaction on platinum, silver and tungsten surfaces in acid solutions. The Journal of Physical Chemistry 61, 879-886.

[164] Wirtz, K. 1938. Sammelreferat. Überspannung und Mechanismus der elektrolytischen Wasserstoffabscheidung. Zeitschrift für Elektrochemie und angewandte physikalische Chemie 44, 303-326.

[165] Bockris, J. O. M. 1948. Recent developments in the study of hydrogen overpotential. Chemical Reviews 43, 525-577.

[166] Latimer, W. M. 1952. The oxidation states of the elements and their potentials in aqueous solutions. Prentice-Hall New York.

[167] Hefter, G., P. M. May, P. Sipos, and A. Stanley. 2003. Viscosities of concentrated electrolyte solutions. Journal of Molecular Liquids 103–104, 261-273.

[168] Ruby, C. E., and J. Kawai. 1926. The densities, equivalent conductances and relative viscosities at 25°, of solutions of hydrochloric acid, potassium chloride and sodium chloride, and of their binary and ternary mixtures of constant chloride-ion-constituent content. Journal of the American Chemical Society 48, 1119-1128.

[169] Zhang, and Han. 1996. Viscosity and density of water + sodium chloride + potassium chloride solutions at 298.15 K. Journal of Chemical & Engineering Data 41, 516-520.

[170] Whipple, G. C., and M. C. Whipple. 1911. Solubility of oxygen in sea water. Journal of the American Chemical Society 33, 362-365.

[171] Fox, C. J. J. 1909. On the coefficients of absorption of nitrogen and oxygen in distilled water and sea-water, and of atmospheric carbonic acid in sea-water. Transactions of the Faraday Society 5, 68-86.

[172] Truesdale, G. A., A. L. Downing, and G. F. Lowden. 1955. The solubility of oxygen in pure water and sea-water. Journal of Applied Chemistry 5, 53-62.

[173] Gameson, A. L. H., and K. G. Robertson. 1955. The solubility of oxygen in pure water and sea-water. Journal of Applied Chemistry 5, 502-502.

[174] Truesdale, G. A., and A. L. H. Gameson. 1957. The solubility of oxygen in saline water. Journal du Conseil / Conseil Permanent International pour l'Exploration de la Mer 22, 163-166.

[175] Battino, R., and H. L. Clever. 1966. The solubility of gases in liquids. Chemical Reviews 66, 395-463.

[176] Battino, R., T. R. Rettich, and T. Tominaga. 1984. The solubility of nitrogen and air in liquids. Journal of Physical and Chemical Reference Data 13, 563-600.

[177] Wilhelm, E., R. Battino, and R. J. Wilcock. 1977. Low-pressure solubility of gases in liquid water. Chemical Reviews 77, 219-262.

[178] Battino, R. 1981. Oxygen and ozone. IUPAC solubility data series 7.

[179] Battino, R., H. L. Cleve, and C. L. Young. 1982. Nitrogen and air. IUPAC Solubility Data Series 10.

[180] Benson, B. B., and D. Krause Jr. 1984. The concentration and isotopic fractionation of oxygen dissolved in freshwater and seawater in equilibrium with the atmosphere. Limnology and Oceanography 29, 620-632.

[181] Winkler, L. W. 1889. Die Löslichkeit des Sauerstoffs in Wasser. Berichte der deutschen chemischen Gesellschaft 22, 1764-1774.

[182] Stone, H. W., R. Eichelberger, and S. E. Wiberley. 1951. Titration of dissoved oxygen using acid-chromous reagent. Analytical Chemistry 23, 868-871.

[183] Montgomery, H. A. C., N. S. Thom, and A. Cockburn. 1964. Determination of dissolved oxygen by the winkler method and the solubility of oxygen in pure water and sea water. Journal of Applied Chemistry 14, 280-296.

[184] Carpenter, J. H. 1966. New measurements of oxygen solubility in pure and natural water. Limnology and Oceanography 11, 264-277.

[185] Henry, W. 1803. Experiments on the quantity of gases absorbed by water, at different temperatures, and under different pressures. Philosophical Transactions of the Royal Society of London 93, 29-43.

[186] Douglas, E. 1964. Solubilities of oxygen, argon, and nitrogen in distilled water. The Journal of Physical Chemistry 68, 169-174.

[187] Green, E. J., and D. E. Carritt. 1967. Oxygen solubility in sea water: thermodynamic influence of sea salt. Science 157, 191-193.

[188] Schumpe, A. 1993. The estimation of gas solubilities in salt solutions. Chemical Engineering Science 48, 153-158.

[189] Schumpe, A., I. Adler, and W. D. Deckwer. 1978. Solubility of oxygen in electrolyte solutions. Biotechnology and Bioengineering 20, 145-150.

[190] Murray, C. N., and J. P. Riley. 1969. Solubility of gases in distilled water and sea water. II. Oxygen. Deep Sea Research and Oceanographic Abstracts 16, 311-320.

[191] Wilke, C. R., and P. Chang. 1955. Correlation of diffusion coefficients in dilute solutions. American Institute of Chemical Engineers Jorunal 1, 264-270.

[192] Himmelblau, D. M. 1964. Diffusion of dissolved gases in liquids. Chemical Reviews 64, 527-550.

[193] Othmer, D. F., and M. S. Thakar. 1953. Correlating diffusion coefficient in liquids. Industrial & Engineering Chemistry 45, 589-593.

[194] Davis, R. E., G. L. Horvath, and C. W. Tobias. 1967. The solubility and diffusion coefficient of oxygen in potassium hydroxide solutions. Electrochimica Acta 12, 287-297.

[195] Gubbins, K. E., and R. D. Walker. 1965. The solubility and diffusivity of oxygen in electrolytic solutions. Journal of The Electrochemical Society 112, 469-471.

[196] Ju, L.-K., and C. S. Ho. 1985. Measuring oxygen diffusion coefficients with polarographic oxygen electrodes: I. Electrolyte solutions. Biotechnology and Bioengineering 27, 1495-1499.

[197] Ho, C. S., L.-K. Ju, R. F. Baddour, and D. I. C. Wang. 1988. Simultaneous measurement of oxygen diffusion coefficients and solubilities in electrolyte solutions with a polarographic oxygen electrode. Chemical Engineering Science 43, 3093-3107.

[198] Hung, G. W., and R. H. Dinius. 1972. Diffusivity of oxygen in electrolyte solutions. Journal of Chemical & Engineering Data 17, 449-451.

[199] Jamnongwong, M., K. Loubiere, N. Dietrich, and G. Hébrard. 2010. Experimental study of oxygen diffusion coefficients in clean water containing salt, glucose or surfactant: Consequences on the liquid-side mass transfer coefficients. Chemical Engineering Journal 165, 758-768.

[200] Wise, D. L., and G. Houghton. 1966. The diffusion coefficients of ten slightly soluble gases in water at 10–60°C. Chemical Engineering Science 21, 999-1010.

[201] Han, P., and D. M. Bartels. 1996. Temperature dependence of oxygen diffusion in H_2O and D_2O. The Journal of Physical Chemistry 100, 5597-5602.

[202] Ferrell, R. T., and D. M. Himmelblau. 1967. Diffusion coefficients of nitrogen and oxygen in water. Journal of Chemical & Engineering Data 12, 111-115.

[203] Kolthoff, I. M., and C. S. Miller. 1941. The reduction of oxygen at the dropping mercury electrode. Journal of the American Chemical Society 63, 1013-1017.

[204] van Stroe, A. J., and L. J. J. Janssen. 1993. Determination of the diffusion coefficient of oxygen in sodium chloride solutions with a transient pulse technique. Analytica Chimica Acta 279, 213-219.

[205] Bower, V. E., and R. G. Bates. 1955. pH-values of the Clark and Lubs buffer solutions at 25°C. Journal of Research of the National Bureau of Standards 55, 197-200.

[206] Bates, R. G., and V. E. Bower. 1956. Alkaline solutions for pH control. Analytical Chemistry 28, 1322-1324.

[207] Jorcin, J.-B., M. E. Orazem, N. Pébère, and B. Tribollet. 2006. CPE analysis by local electrochemical impedance spectroscopy. Electrochimica Acta 51, 1473-1479.

[208] Mayell, J. S., and S. H. Langer. 1964. Effect of dilute chloride ion on platinum electrodes. Journal of Electroanalytical Chemistry 7, 288-296.

[209] Bianchi, G., and T. Mussini. 1965. Cathodic reduction of oxygen on smooth platinum in acid solutions. Electrochimica Acta 10, 445-455.

[210] Littauer, E. L., and L. L. Shreir. 1966. Anodic polarization of platinum in sodium chloride solutions. Electrochimica Acta 11, 527-536.

[211] Birss, V. I., M. Chang, and J. Segal. 1993. Platinum oxide film formation - reduction: An in-situ mass measurement study. Journal of Electroanalytical Chemistry 355, 181-191.

[212] Popat, P. V., and N. Hackerman. 1958. Capacity of the electrical double layer and adsorption at polarized platinum electrodes. I. Adsorption of anions. The Journal of Physical Chemistry 62, 1198-1203.

[213] Lorenz, R., and P. E. Spielmann. 1909. Die Oxydtheorie der Sauerstoffelektrode (Vierte Mitteilung). Zeitschrift für Elektrochemie 15, 293-297.

[214] Damjanovic, A., L. S. R. Yeh, and J. F. Wolf. 1981. Evidence for the rate determining step at the solution - oxide film interface in the anodic growth of thin oxide films at platinum and nickel electrodes in aqueous solutions. Electrochimica Acta 26, 825-827.

[215] Hoare, J. P., and S. Schuldiner. 1955. Mechanisms of hydrogen producing reactions on palladium. Journal of The Electrochemical Society 102, 485-489.

[216] Mayell, J. S., and S. H. Longer. 1964. A study of surface oxides on platinum electrodes. Journal of The Electrochemical Society 111, 438-446.

[217] Bagotskii, V. S., L. N. Nekrasov, and N. A. Shumilova. 1965. Electrochemical reduction of oxygen. Russian Chemical Reviews 34, 717-730.

[218] Marinković, N. S., N. M. Marković, and R. R. Adžić. 1992. Hydrogen adsorption on single-crystal platinum electrodes in alkaline solutions. Journal of Electroanalytical Chemistry 330, 433-452.

[219] Bagotzky, V. S., and M. R. Tarasevich. 1979. Oxygen adsorption on platinum and platinum metals. Part I. Investigation of the adsorption mechanism by the potentiodynamic method. Journal of Electroanalytical Chemistry and Interfacial Electrochemistry 101, 1-17.

[220] Hsueh, K. L., D. T. Chin, and S. Srinivasan. 1983. Electrode kinetics of oxygen reduction. A theoretical and experimental analysis of the rotating ring-disc electrode method. Journal of Electroanalytical Chemistry and Interfacial Electrochemistry 153, 79-95.

[221] Markovic, N., M. Hanson, G. McDougall, and E. Yeager. 1986. The effects of anions on hydrogen electrosorption on platinum single-crystal electrodes. Journal of Electroanalytical Chemistry and Interfacial Electrochemistry 214, 555-566.

[222] Hickling, A., and F. W. Salt. 1941. Studies in hydrogen overvoltage at high current densities. Part III. The influence of oxygen. Transactions of the Faraday Society 37, 319-321.

[223] Oelßner, W., F. Berthold, and U. Guth. 2006. The iR drop – well-known but often underestimated in electrochemical polarization measurements and corrosion testing. Materials and Corrosion 57, 455-466.

[224] Conway, B. E., and L. Bai. 1986. State of adsorption and coverage by overpotential-deposited H in the H_2 evolution reaction at Au and Pt. Electrochimica Acta 31, 1013-1024.

[225] Conway, B. E., and L. Bai. 1986. Determination of adsorption of OPD H species in the cathodic hydrogen evolution reaction at Pt in relation to electrocatalysis. Journal of Electroanalytical Chemistry and Interfacial Electrochemistry 198, 149-175.

[226] Jiang, R., and S. Dong. 1989. RRDE theory dealing with nondiffusion-controlled process at ring electrode. Study of the mechanism of dioxygen electroreduction. Journal of the Electrochemical Society 136, 3325-3332.

[227] Conway, B. E., and D. M. Novak. 1979. Chloride ion adsorption effects in the recombination-controlled kinetics of anodic chlorine evolution at Pt electrodes. Journal of the Chemical Society, Faraday Transactions 1: Physical Chemistry in Condensed Phases 75, 2454-2472.

[228] Breiter, M. W. 1963. Voltammetric study of halide ion adsorption on platinum in perchloric acid solutions. Electrochimica Acta 8, 925-935.

[229] Wen, W., H. Zhao, S. Zhang, and V. Pires. 2008. Rapid photoelectrochemical method for in situ determination of effective diffusion coefficient of organic compounds. The Journal of Physical Chemistry C 112, 3875-3880.

[230] Henderson, L. J. 1908. Concerning the relationship between the strength of acids and their capacity to preserve neutrality. American Journal of Physiology 21, 173-179.

[231] Hasselbalch, K. A. 1917. Die Berechnung der Wasserstoffzahl des Blutes aus der freien und gebundenen Kohlensäure desselben, und die Sauerstoffbindung des Blutes als Funktion der Wasserstoffzahl. Biochemische Zeitschrift 78, 112-144.